Tectonics of Continental Convergence in Central and West Asia

Ben Johnson

Supervisors: Prof. Richard Walker, Prof. Mike Kendall, Prof. Alex Copley

St Anne's College

University of Oxford

April 2025

Declaration

The contents of this thesis are all my own work, except where otherwise stated. The views and opinions expressed herein are mine and not necessarily those of any other person or body unless so attributed.

This thesis is dedicated to Libby for telling me all I ever needed to do was my best.

Abstract

Tectonics of Continental Convergence in Central and West Asia

Benedict Johnson

St. Anne's College

Trinity Term, 2025

This thesis presents three case studies of tectonically converging mountain ranges across West and Central Asia, examining how and whether this convergence is accommodated by earthquakes. In northern Tajikistan, where the Pamir and Tian Shan have fully converged, I use calibrated earthquake relocations and analysis of tectonic geomorphology to find that the 1949 M_w 7.6 Khait Earthquake occurred not on the geomorphically well expressed boundary fault, but within a previously unmapped structure in the Tian Shan basement. I show vertical axis rotations within the Tian Shan accommodate up to half the convergence rate between the Pamir and Tian Shan, demonstrating the greatest seismic hazard can lie on cryptic faults. In the Kura Basin of Azerbaijan, I use time series InSAR to reveal that the convergence between the Turkish Iranian Plateau and Greater Caucasus is accommodated by rapid creep on faults in the sedimentary cover, and hypothesise gravitational collapse of basin sediments into the South Caspian Basin as an additional driving force of this creep. Finally, I use calibrated earthquake relocation to demonstrate that the 1985 M_w 6.9 Wuqia Earthquake occurred beneath the sedimentary cover of the Tarim Basin, northwest China. I find that the earthquake occurred on a buried, slow moving transpressive strike slip fault formed during more rapid strike-slip motion between the Pamir and Tarim Basin. Overall this thesis extends our knowledge of how converging zones in continental interiors behave, and demonstrates that the greatest seismic hazard in a region is not necessarily on the most geomorphically well-expressed faults.

Extended Abstract

This thesis is concerned with how the large scale convergence within the continents is accommodated on faults and released in earthquakes. In particular, the thesis examines both the incipient and advanced convergence between mountain ranges, using the Pamir and Turkish Iranian Plateaux as case studies. In Chapter 2 I examine the advanced stage of convergence, where the Pamir and Tian Shan are in contact and the intervening space between them is fully closed. In Chapter 3 I examine the incipient case, where the Kura Basin still separates the converging Greater Caucasus and Turkish Iranian Plateau. Finally in Chapter 4 I turn to an intermediate case in the north-eastern Pamir, where the Tarim Basin still separates the Tian Shan from the converging Pamir. A uniting theme in these case studies is how earthquake hazard cannot always be deduced from geodetic observation and geomorphology.

Chapter 2 focusses on the 1949 M_w 7.6 Khait earthquake, Tajikistan, which took place at the boundary between the converging Pamir and Tian Shan. I anlayse the tectonic geomorphology using high resolution optical satellite imagery and photogrammetry to find and characterise surface ruptures caused by this earthquake. I use calibrated earthquake relocation methods to obtain accurate epicentres for the 1949 mainshock, its immediate aftershocks, and moderate seismicity in the region between 1949 and 2017. I find the earthquake ruptured a previously unknown fault in the Tian Shan basement, rather than the geomorphically well expressed Vakhsh Fault, as previously thought. Using alignments of well located earthquakes, focal mechanisms, and surface ruptures, I propose the Tian Shan is internally deforming due to its convergence with the Pamir via vertical axis rotations. These rotations are accommodated by right-lateral strike-slip faults, which ruptured to produce the 1949 earthquake. Using previous geochronology of tectonically offset glacial moraines, I conclude the prominent Vakhsh Fault accommodates around half the geodetically observed convergence between the Pamir and Tian Shan. The rest is distributed across other structures and accommodated within the Tian Shan.

In Chapter 3, I use Interferometric Synthetic Aperture Radar (InSAR) time series anal-

ysis of the Kura Basin, Azerbaijan, to assess how the convergence between the Greater Caucasus and Turkish Iranian Plateau are accommodated on faults within the basin. I find evidence for rapid creep along many of the basin faults, including at least ∼5 mm/yr uplift of the prominent Kura Fold and Thrust Belt. I find evidence of rapid creep on two strike-slip faults: ∼7 mm/yr right-lateral creep on the Alat Fault, and ∼1.5–2.5 mm/yr left-lateral creep on the Sumquayit Fault. Together these appear to form pincers pushing out a wedge of material I term the Gobustan wedge into the South Caspian Basin, which I suggest is responding to both tectonic convergence, and gravitational collapse along a detatchment of fluidised mud at depth. This raises the question of how much surficial motion of basin sediments is correlated to interseismic accumulation in the basement.

In Chapter 4 returns to the Pamir to examine the 1985 M_w 6.9 Wuqia earthquake, which appeared to produce a set of surface ruptures incongruous with the seismologically determined focal mechanism. As in Chapter 2, I use calibrated earthquake relocation methods to relocate the 1985 mainshock epicentre, along with the immediate aftershocks and moderate magnitude seismicity in the region. I find that the mainshock and subsequent aftershocks align well with macroseismic contours, and all occurred at depths greater than 10 km within the Tarim Basin basement beneath the sedimentary cover. The alignment of epicentres and mechanisms suggests a north-east dipping focal plane, which is incongruous with the south-west dipping structures in the basin sediments. I propose this earthquake occurred on a buried strike-slip transpressional structure which used to accommodate significantly faster motion between the Pamir and Tarim Basin, but has since slowed. This suggests the primary source of seismic hazard in the region is not visible in the geomorphology of the basin sediments.

In Chapter 5, I present my concluding thoughts and recommendations for further work.

Acknowledgements

Firstly I would like to thank my supervisors: Richard Walker, Mike Kendall and Alex Copley. Richard's patient support at every stage has been invaluable. During times of disillusionment and difficulty I invariably came away from a chat with him energised and encouraged. Without that support I definitely wouldn't have persisted to this point. Similar gratitude goes to Eric Bergman, who has been an unofficial supervisor to me and has spent a lot of time on Zoom guiding me though the intricacies of *mloc* and providing encouragement. Tamarah King kindly spent a lot of time on Zoom with me in the early stages of the DPhil, showing me the ropes of QGIS and giving general life advice.

Thanks to Ian Pierce I was able to join fieldwork to Kyrgyzstan just after COVID regulations had relaxed enough to make it possible in mid-2021, and to Azerbaijan in 2022. Ian taught me all I know about paleoseismology and he has my gratitude for this. Those field trips would never have happened without our colleagues in Kyrgyzstan and Azerbaijan. My thanks to Sultan Baikulov, Erkin Rakhmedinov, Gulkaiyr Tilek Kyzy, Sabina Kazimov, and Ilyas Kazimov.

I would like to thank the people of Oxford Earth Sciences, in particular Neill Marshall, Wendy Tsai, Roberta Wilkinson, Yangfan Huang and Emma Greenough, and Matt Sutton.

My thanks go to the COMET group at Leeds: John Elliott, Jack McGrath, Andrew Watson, and Qi Ou. Jack, Andrew and Qi have fielded many of my basic questions about InSAR over the past few years. James Hollingsworth allowed me to crash in his office for a week to learn the basics of ASP when other methods of photogrammetry failed, my thanks to him. I am grateful to the researchers associated with GFZ and the University of Potsdam, in particular Bernd Schurr and Wasja Bloch, for their speedy replies to requests for data, and to Sabrina Metzger, Magda Patyniak, and Sylvia Crosetto for useful discussions about the Pamir.

I owe a great deal to James Jackson and Alex Copley at Cambridge, who supervised me during my masters project and instilled in me a fascination for tectonics that has lasted me this far. James' first year Introduction to Earth Sciences lecture series encouraged me

to defect to Earth Sciences from Physics, for which I will be eternally thankful.

I would like to thank my friends and family. Thank you to Lucy, Libby, and Rich for your love and support, I would not have made it to this point without you.

Finally, I thank my partner Kostja, who has shared my burdens, provided unconditional love, and shown tireless dedication to graphic design.

Contents

Contents viii

List of Figures xi

List of Tables xiv

1 Introduction 1

1.1 Continental Deformation . . . 1
1.2 Links between topography and earthquakes . . . 5
1.3 The Arabia-Eurasia Collision . . . 7
1.4 The India-Eurasia Collision . . . 9
1.5 Barriers to earthquake hazard mitigation . . . 10
1.6 Overview of the text . . . 12
1.7 Publications arising from this thesis . . . 14

2 Rupture of the 1949 Khait earthquake on a cryptic fault: implications for earthquake hazard 15

2.1 Introduction . . . 16
2.2 Seismotectonic Setting . . . 22
2.3 Materials and Methods . . . 25
2.3.1 1949 Source Parameters Determination using analogue seismic data 25
2.3.2 Calibrated Earthquake Relocations . . . 30
2.3.3 Depth Control and Velocity Model . . . 34
2.3.4 Geomorphic Analysis . . . 36
2.4 Results . . . 40
2.4.1 Regional seismicity and source parameters of the 10th July 1949 Khait earthquake . . . 40
2.4.2 Geomorphology of the 1949 Khait epicentral zone . . . 45
2.5 Discussion . . . 54
2.5.1 Causative fault of the 1949 Earthquake . . . 54

2.5.2 Seismicity of the Vakhsh Fault . . . 57
2.5.3 Slip rate of the Vakhsh Fault . . . 58
2.5.4 Implications for hazard in the region . . . 59
2.5.5 Do observations of small earthquakes elucidate sources of large earthquakes? . . . 60
2.6 Conclusions . . . 61

3 Rapid fault creep in the fluid-rich Kura Basin, Azerbaijan, imaged with InSAR 64
3.1 Introduction . . . 66
3.2 Materials and Methods . . . 70
3.3 Results . . . 74
3.3.1 West Caspian Fault zone . . . 76
3.3.2 West of the Absheron Peninsula (the Sumquayit Fault) . . . 83
3.3.3 Kura fold-and-thrust belt . . . 84
3.4 Discussion . . . 85
3.4.1 Observations of creeping faults . . . 85
3.4.2 Fault kinematics: extrusion towards the South Caspian Basin . . . 89
3.5 Conclusions . . . 91

4 The 1985 Wuqia Earthquake: rupture beneath the sedimentary cover on a strike-slip transpressive structure 94
4.1 Introduction . . . 94
4.1.1 The 1985 Wuqia Earthquake . . . 94
4.1.2 Tectonic background . . . 95
4.1.3 Seismicity in the north-west Tarim . . . 100
4.2 The 1985 Wuqia Earthquake . . . 102
4.2.1 Macroseismic data . . . 102
4.2.2 Source parameters from seismology . . . 103
4.2.3 Surface ruptures . . . 105
4.3 Methods – Calibratated Earthquake Relocations . . . 107
4.3.1 Overview . . . 107

4.3.2 Treatment of Errors . . . 109
4.3.3 Depth Control and Velocity Model . . . 110
4.3.4 Event Selection . . . 111
4.3.5 Relocation Strategy . . . 112
4.4 Results . . . 112
4.4.1 Location and depth of the 1985 mainshock . . . 113
4.4.2 1985 Aftershock Distribtion . . . 114
4.4.3 Depth distribution of the cluster . . . 119
4.5 Discussion . . . 120
4.5.1 Source of the surface ruptures . . . 120
4.5.2 Structure involved in the 1985 Mainshock . . . 122
4.5.3 An earthquake double-event? . . . 123
4.5.4 Is the sedimentary cover seismogenic? . . . 125
4.5.5 Implications for seismic hazard . . . 126
4.6 Conclusions . . . 127

5 Concluding Remarks **129**
5.1 Thesis conclusions . . . 129
5.2 Further work . . . 131

6 Appendix **165**
6.1 Appendix to Chapter 2: Rupture of the 1949 Khait earthquake on a cryptic fault: implications for earthquake hazard . . . 165
6.2 Appendix to Chapter 3: Rapid fault creep in the fluid-rich Kura Basin, Azerbaijan, imaged with InSAR . . . 173
6.3 Appendix to Chapter 4: The 1985 Wuqia Earthquake: rupture beneath the sedimentary cover on a strike-slip transpressive structure . . . 179

List of Figures

1.1 Map of global plate boundaries and earthquakes . . . 3
1.2 Convergence between Arabia and Eurasia . . . 8
1.3 Convergence between India and Eurasia . . . 10
1.4 Locations studied in this thesis . . . 13

2.1 Earthquake mechanisms of the Pamir and surroundings . . . 18
2.1 Earthquake mechanisms of the Pamir and surroundings . . . 19
2.2 Isoseismals from the earthquake . . . 20
2.2 Isoseismals from the earthquake . . . 21
2.2 Isoseismals from the earthquake . . . 22
2.3 Azimuthal distribution of all seismic stations which recorded the 1949 Khait earthquake . . . 27
2.4 Flowchart for the Hypocentroidal Decomposition Algorithm . . . 33
2.5 (A)Mapped surface ruptures in the Vakhsh Valley . . . 42
2.6 Dip-slip and right-lateral strike-slip ruptures in the upper western end of the Yasman Valley . . . 44
2.6 Dip-slip and right-lateral strike-slip ruptures in the upper western end of the Yasman Valley . . . 45
2.7 MLOC-relocated epicentres and mechanisms and interpretation . . . 46
2.7 MLOC-relocated epicentres and mechanisms and interpretation . . . 47
2.8 Vakhsh Valley Digital Elevation Model (DEM) . . . 48
2.9 LGM moraine complex near Dzhaligan . . . 51
2.10 South-facing perspective Google Earth Imagery of a section of the Vakhsh Valley . . . 52

3.1 Location map with Shuttle Radar Topography Mission (Farr and Kobrick 2000) (SRTM) topography, focal mechanisms of earthquakesfrom the Global Centroid Moment Tensor Catalog (Ekström et al. 2012) (gCMT) and Global Waveform Catalog (Wimpenny and Watson 2020) (gWFM) catalogs with ISC-EHB hypocenters from 1976 to present . . . 67

3.1 (Previous page.) GNSS velocities relative to Eurasia from Kadirov et al. (2014), with 95% confidence ellipses, and active fault traces visible in the geomorphology (mapped by the authors). Swath profiles of GNSS velocities, as shown in Fig. 3.2, are represented by black rectangles. Profile 1 is orthogonal to the Salyan fault (West Caspian fault zone) and Profile 2 is orthogonal to the Kura fold-and-thrust belt. A geologic uplift rate from Pierce et al. (2024) is shown, as is the trench site from Marshall (2023). Bottom: footprints of ascending and descending Sentinal 1A radar images used in this study, labelled with the prefix of the Frame ID (Table 3.1) . . 68
3.2 Fault parallel and fault perpendicular components of Global Navigation Satellite System (GNSS) velocities for the Salyan and Alat faults in the West Caspian fault zone 69
3.3 Ascending and Descending Sentinel 1A velocity fields. 71
3.4 Decomposed vU (vertical) component of the velocity field 75
3.5 Decomposed vE (eastward) component of the velocity field 76
3.6 East velocity on the Alat Fault 77
3.7 Decomposed eastward velocity for the Salyan Fault 78
3.8 Vertical velocity and topography at a transpressional fault bend along the Salyan fault 79
3.9 East velocity field showing apparent east-west left-lateral fault creep in the region west of the Absheron Peninsula 82
3.10 Vertical velocity field for the Kura Fold and Thrust Belt (KFTB) 86
3.11 Perspective view showing merged topography and bathymetry for the South Caspian Basin and its surroundings 90

4.1 Focal mechanisms and GNSS vectors for the Pamir-Tian Shan-Tarim Basin intersection. 97
4.2 Geological map adapted from Li et al. (2019) 98
4.3 Relationship between relocated earthquakes and subsurface geology 101
4.4 Map of surface ruptures for the 1985 Wuqia Earthquake 106
4.5 Statistics for the cluster of 111 earthquakes analysed with *mloc* 112

4.6 Aftershocks within 20 days of the 23^{rd} August 1985 Moment Magnitude (M_w) 6.9 Wuqia mainshock color coded by time since the mainshock, with formal uncertainty error ellipses from the *mloc* relocation 115
4.7 Tectonic model for the 23^{rd} August 1985 M_w 6.9 Wuqia mainshock. 124

A4 Possible rupture near Khurramshahr, about half way down the Yasman Valley 167
A5 Bedding plane slip north-east of Khait 168
A6 Offsets visible west of Musofiron 169
A7 Surface ruptures near Safebod. 170
A8 False colour image of fault trace south of Yasman Valley 171
A9 Seismic phase travel time residuals from the modified ak135 velocity model 172
A10 Close up view of the vertical velocity over agricultural land just south of the KFTB. The unmasked vertical velocity field shows the degree to which land use affects the signal. The pixels within the settlement are close to 0 mm/yr, by contrast the surrounding fields show highly negative vertical velocities reaching ∼-20 mm/yr. This can be attributed to phase bias, but also potentially to subsidence from water abstraction for agriculture. 173
A11 Vertical velocity field near the Lesser Caucasus 174
A12 Salt pan uplift in the Kura Basin 175
A13 Time series of line-of-sight displacements for 108D pixel centred on the Salyan Fault uplift (Figure 3.8a). The jump in velocity in 2023 is likely related to the M_w 7.8 Kahramanmaraş earthquake in Turkey, around 1000 km away. 176
A14 Decomposed vertical velocity west of the Absheron Peninsula 177
A15 East-west velocity field for the KFTB 178
A16 Burtman and Molnar (1993) figures. 185
A17 Figures taken from Fan et al. (1994) figure 186
A20 Direct calibration stations used for the *mloc* cluster, most of which are from the 8H seismic network deployed between 2015 and 2017 188

List of Tables

2.1 Previous estimes of the 1949 Khait earthquake source parameters 17

2.2 *mloc* relocated events 38

3.1 Statistics for the LiCSAR frames used in this analysis 70

4.1 Focal mechanism determinations compiled by Ainscoe (2018) for the 23^{rd} August M_w6.9 Wuqia Mainshock. SV Az. = Slip vector azimuth. B+M93 = (Burtman and Molnar 1993); F94 = (Fan et al. 1994); W87 = (Wang et al. 1987). Values in italics show the conjugate fault planes. Ranges for parameters are also shown. 103

4.2 Focal mechanism determinations compiled by Ainscoe (2018) for the 11^{th} September M_w6.1 earthquake, the largest aftershock of the 1985 Wuqia earthquake. SV Az. = Slip vector azimuth. B+M93 = Burtman and Molnar (1993); F94 = Fan et al. (1994). Values in italics show the conjugate fault planes. Ranges for parameters are also shown. 104

4.3 Earthquakes relocated using *mloc* with mechanisms where available 116

A1 1949 digitized arrivals and Body Wave Magnitude (m_B) estimates 165

A2 1949 surface wave magnitude estimates 166

A3 1949 scalar moment and moment magnitude M_w estimates for each seismic station. This was done by fitting synthetic seismograms generated from the modelled focal mechanism and varying the seismic moment until the observed and synthetic seismogram amplitudes agreed. A more detailed account of the method can be found in a more detailed account of this method see Kulikova and Krüger (2015) and Ou et al. (2020). 166

A18 Surface rupture measurements compiled by Ainscoe (2018) from Feng et al. (1986) and Feng et al. (1988) 187

A19 Cumulative scarp height measurements from Ainscoe (2018) 189

Acronyms

DEM Digital Elevation Model

FTB Fold and Thrust Belt

GACOS Generic Atmospheric Correction Online Service (Yu et al. 2018a)

gCMT Global Centroid Moment Tensor Catalog (Ekström et al. 2012)

gWFM Global Waveform Catalog (Wimpenny and Watson 2020)

GCCEL Global Catalog of Calibrated Earthquake Locations

GNSS Global Navigation Satellite System

HDC Hypocentroidal Decomposition

ISC-EHB Catalog of well particularly well located earthquake hypocentres (Weston et al. 2018)

InSAR Interferometric Synthetic Aperture Radar

KFTB Kura Fold and Thrust Belt

KYTS Kashgar Yecheng Transfer System

LGM Last Glacial Maximum

$\mathbf{m}_B$ Body Wave Magnitude

$\mathbf{M}_{LH}$ Soviet Surface Wave Magnitude (Bindi et al. 2013; Bormann 2002)

MPT Main Pamir Thrust

$\mathbf{M}_S$ Surface Wave Magnitude

$\mathbf{M}_w$ Moment Magnitude

NDVI Normalised Difference Vegetation Index

NIR Near-Infrared

PFT Pamir Frontal Thrust

RMS Root Mean Squared

RPC Rational Polynomial Coefficients

SCB South Caspian Basin

SRTM Shuttle Radar Topography Mission (Farr and Kobrick 2000)

SYF Shache-Yangdaman Fault

UD Up-Down

1 | Introduction

1.1 Continental Deformation

Continental deformation differs from the plate tectonic model valid in the oceans and at their margins. This model predicts tightly delineated zones of deformation, with earthquake activity and tectonic structures concentrated over a narrow area (Isacks et al. 1968). For example, the boundary between the Pacific and Eurasian Plates in Japan accommodates $\sim$ 9 cm/yr convergence over a $\sim$ 500 km zone. The model breaks down in the continents due to the differing rheological properties of continental and oceanic lithosphere; while oceanic plates remain rigid when undergoing high stress, continents can be thought of as having a yield stress beyond which they stop behaving as rigid plates and exhibit more ductile behaviour. A physical explanation for this is that while oceanic lithosphere is younger than $\sim$ 350 Myr (Seton et al. 2020), homogenous, and contains few pre-existing lines of weakness, continental lithosphere is freqently older than 1 Byr, very heterogenous, and contains many existing lines of weakness (Cawood et al. 2013; Schwab et al. 2004). Ductile behaviour in the continents can be seen at the boundary between the Indian and Eurasian plates, which accommodates $\sim$ 3.5 cm/yr convergence over a $\sim$ 3000 km wide zone (Figure 1.3)(Altamimi et al. 2023). The difference in distribution of deformation translates into a difference in distribution of earthquakes which accommodate it (Figure 1.1). Furthermore, due to these pre-existing weaknesses in the continents, the style of deformation cannot be inferred through Andersonian fault mechanics, where a homogenous elastic medium breaks along planes of maximum shear stress (Anderson 1905; Jackson and McKenzie 1988). Sedimentary basins present additional problems, as these have their own responses to tectonic strains which may be different to those of the crystalline basement.

The forces which drive continental deformation are the same as those which drive plate tectonic motion in the oceans, namely ridge push and slab pull. Ridge push is the force arising from contrasts in gravitational potential energy between mid-ocean ridges and the seawater around them. As the mid-ocean ridge collapses under gravity, it spreads laterally

imposing a force on the surrounding oceanic plate directed away from the ridge. Slab pull arises from gravitational potential energy contrasts at subduction zones: between cold oceanic slabs and the hot mantle they are descending into. This exerts a downward force on the slab, acting to pull the connected oceanic plate towards the subduction zone. Of the two, slab pull is thought to be the stronger force (Forsyth and Uyeda 1975; Goes et al. 2008). These forces drive continental motion because oceanic plates are connected to continents via passive margins.

Over large lengthscales (>1000 km) and long timescales (>10 kyr) continental deformation can be modelled as a viscous fluid responding to contasts in graviational potential energy (Copley 2008; England and Houseman 1986; England and Jackson 1989; England and Molnar 2005; Thatcher 2009). While long faults with strong geomorphic traces do exist, they do not move at rates fast enough to be considered plate boundary faults (Avouac and Tapponnier 1993; Cowgill et al. 2009; Elliott et al. 2008). These large-scale tectonic models provide insight into why stress fields are the way they are, and tell us we might expect the large scale stress field to be expressed across a distributed network of faults. For this thesis, I am concerned with how these stresses express themselves on far smaller timescales and length scales in the form of earthquakes. I will do so using three case studies from the margins of two continental plateaux: the Turkish Iranian Plateau in West Asia, and the Pamir Plateau in Central Asia.

The rapid growth in urban populations across Central Asia means increasing exposure to earthquake hazard (Tucker 2004). Settlements across the arid parts of Central and West Asia were often sited near faults due to the proximity to topography, and the access to water it provided. These settlements then grew into cities, an Iranian example being Tehran (Berberian and Yeats 2017; Jackson 2006; Talebian et al. 2016). Examples within Central Asia would include Bishkek in Kyrgyzstan and Almaty in Kazakhstan, home to 3 million people between them (Amey et al. 2021; Amey et al. 2022; Watson et al. 2022b)

The wide zones of deformation combined with a plethora of pre-existing weaknesses in old continental crust result in a network of thousands of tectonic faults across the deformation zone, often breaking at orientations that differ from the Andersonian Fault Model (Anderson 1905), where the crust is taken to be intact and faults are created along the

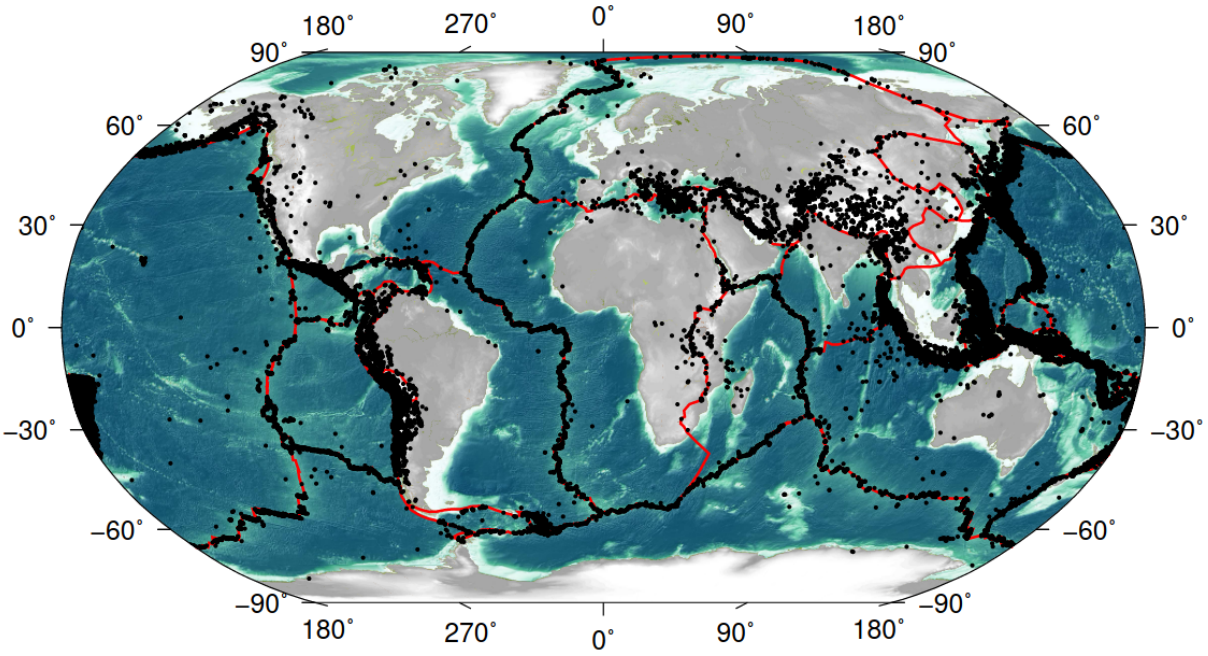

Figure 1.1: Map of plate boundaries (Bird 2003) and earthquakes M_w>5 from the gCMT catalog (Dziewonski et al. 1981; Ekström et al. 2012). Oceanic plate boundaries host earthquakes tightly clustered to the plate boundary line, whereas continental "plate boundaries" host earthquakes distributed across a wide zone. Figure taken from Ainscoe (2018).

planes of greatest shear stress. This results in faults that do not rupture in earthquakes often, with paleoseismology studies frequently finding earthquake repeat times of more than 1000 years .

A pulse of M>7 earthquakes in the Tian Shan over the past ∼ 200 years (Abdrakhmatov et al. 2016; Krüger et al. 2018; Kulikova and Krüger 2015) have lead to suggestions of network effects between faults over long distances: where the rupture of a large earthquake can precipitate a sequence of large earthquakes over a large area. Paleoseismic and geodetic studies of the faults within the Tian Shan show very slow slip rates consistent with earthquake repeat times on the scale of thousands of years (Landgraf et al. 2016; Liu and Stein 2016; Thompson et al. 2002). Similar behaviour has been observed in China (Liu et al. 2011); Mongolia, where four M ∼ 8 earthquakes were observed in the 20th Century (Baljinnyam 1993; Molnar and Qidong 1984); and the United States (Holbrook et al. 2006). In all these cases the earthquake repeat times for the faults were on the order of thousands of years. This potential connectivity provides a pressing reason for understanding large earthquakes across Central Asia, not just in populated zones.

Mechanisms for far field interaction between faults remain poorly understood (Liu and Stein 2016). Static Coulomb stress transfer is a well known mechanism where motion on a fault changes the normal stress state on nearby faults (within a few 10s km) which can bring the fault closer or future from failure, in theory affecting the chance of future earthquakes on that fault (King et al. 1994). However, this is a near field effect which we would not expect to influence faults separated by hundreds of kilometers, as in the Tian Shan. Another mechanism is the viscous relaxation after earthquakes which can impose time-delayed changes on fault normal stresses due to changes in the ductile crust following an earthquake (Freed and Lin 2001). Again, it is not clear whether this mechanism can transfer stress over hundreds of kilometers. Motion of fluids along faults has been another mechanism proposed for time-delayed, far-field interactions between faults, although this is an area that requires further research (Bloch et al. 2023).

In addition, there appears to be no link between rate of seismic moment acculumation and maximum earthquake magnitude. Therefore a fault that has very slowly accumulated strain over several thousand years can produce an earthquake of M 8 or more, with very little warning (Abdrakhmatov et al. 2016; Ou et al. 2020; Rizza et al. 2015). In slowly deforming zones, fault scarps may be produced at a slower rate than the geomorphic processes that erode them, making faults difficult to observe using remote sensing. Even where deformation is rapid fault scarps may not be preserved. In High Mountain Asia, examined in Chapter 2, the rate of erosion can be so rapid that fault scarps are difficult to preserve (Schurr et al. 2014; Strom and Abkhmatov 2018). In basins at the edge of high mountains, such as the north-west Tarim Basin in Chapter 4 the rate of sedimentation can be so high that slowly growing scarps are likely to be covered. In the Kura Basin, examined in Chapter 3, sea level changes within the Caspian Basin may have eroded many scarps, and the present tectonic configuration is relatively new (Marshall 2023).

Because of this long earthquake repeat time, there are many faults which have not ruptured during the instrumental record (Campbell et al. 2015; Grützner et al. 2017; Landgraf et al. 2016; Mikhailova et al. 2015; Walker et al. 2008). Where historical records are good, it is possible to construct earthquake catalogs thousands of years in duration (Ambraseys and Melville 2005; Cheng et al. 2017). However, these kinds of records are not available

everywhere, where they do exist they may be incomplete (Dodds et al. 2022b), and they do not help us understand the causative structures which are necessary for modelling earthquake hazard in the present (Amey et al. 2022).

Given the inadequacies with earthquake catalogs, it is necessary to understand how earthquakes relate to tectonic motion on faults, and how that motion is preserved in the landscape as topography. We can gain insights into this from modern earthquakes which can be observed through a variety of methods. Those insights can then be taken and applied to faults which have hosted earthquakes centuries ago, before the instrumental record, where we only have the historical record of the shaking and the traces the fault motion has left in the landscape. In the next section, I will outline the simple models for how earthquakes generate topography through motion on faults and then describe observations which complicate these models.

1.2 Links between topography and earthquakes

A starting model for the relationship between topography and earthquakes is that topographic growth occurs incrementally as faults release accumulated interseismic strain in earthquakes, and over the course of many earthquake cycles larger topography grows (Argand 1924; Reid 1910; Thatcher 1993). While true to a first order, many observations require us to move beyond this model.

The first is that some faults produce offsets aseismically. This has been observed along the San Andreas Fault in the US (Jolivet et al. 2015), the Ilyak Fault near Dushanbe in Tajikistan (Metzger et al. 2021), and we illustrate other examples of this in Azerbaijan in Chapter 3. Aseismic fault motion also occurs on several megathrust faults, with different zones of the fault being "coupled" to different degrees, inferred from GNSS (Scholz and Campos 2012) measurements and comparing accumulated geodetic strain to seismic moment tensor summation (Kostrov 1974), although this has limitations due to the length of the instrumented period relative to the repeat time of large earthquakes that dominate the moment release (McCaffrey 1997). The Hellenic Trench is an example where a high proportion of slip is apparently aseismic (Jackson and McKenzie 1988; Shaw et al. 2008).

Variations in coupling have been linked to rheological properties of fault zones (Birren and Reber 2019), but coupling has been shown to vary temporally as well as spatially, complicating the picture significantly (Konca et al. 2008; Loveless and Meade 2016). Friction models may help resolve this, as the degree of coupling depends on both on the friction coefficient (a rheological property) and the normal stress which can be variable (Scholz and Campos 2012). The relatability of subduction zone faults to faults within continental interiors is not clear, but creeping faults have been observed far from oceanic plate boundaries (Mackenzie et al. 2018; Metzger et al. 2021).

Furthermore, faults may creep within an earthquake cycle. Postseismic afterslip has been shown to contribute significantly to overall slip within an earthquake cycle. For example, after the Tabas e Golshan earthquake several metres of postseismic slip has been observed geodetically in the decades following the earthquake (Copley 2014; Zhou et al. 2016; Zhou et al. 2018).

Further observations of creeping faults are needed in different contexts to isolate the key variables that determine whether and when faults creep or slip in earthquakes. In Chapter 3 we use InSAR time series to observe creeping faults in Azerbaijan.

Chapters 2 and 4 are dedicated to understanding the tectonic circumstances of two M $\sim$ 7 earthquakes: the 1949 Khait Earthquake in Tajikistan, and the 1985 Wuqia Earthquake in northwest China. It is worth dedicating significant work to understanding the relatively few large earthquakes that occur, as these make up the largest part of seismic deformation, and their mechanisms often correlate much better with tectonic strain visible in the landscape than small earthquakes, although not always (England and Jackson 1989; Molnar 1979). They also present the biggest seismic hazard in the continents (England and Jackson 2011).

In Chapter 2 we use tectonic geomorphology, the impressions individual earthquakes leave in the landscape, in combination with seismology. Tectonic scarps are best preserved in flat, arid places where they are eroded slowly (Campbell et al. 2015; Rizza et al. 2015;

Walker et al. 2017). We can often find scarps from range bounding faults such as those bounding the Tian Shan and the Kazakh Steppe (Grützner et al. 2017; Wilkinson 2023). While major sources of hazard, particularly for the cities of Bishkek and Almaty, there are many active faults within the high mountains which have proven capable of generating very large earthquakes, such as the 1889 M_w 8.0–8.3 Chilik Earthquake (Abdrakhmatov et al. 2016) and the 1911 M_w Chon Kemin Earthquake (Kulikova and Krüger 2015). An understanding of faults in the high mountains is therefore essential.

These areas are subject to rapid erosion and redeposition of sediments, by flooding (Fan et al. 2020), glaciaion (Stübner et al. 2021) and landsliding (Strom and Abkhmatov 2018), making it difficult for subtle fault scarps to survive. These regions are also much less amenable to InSAR technquies to measure ground deformation due to snow cover in the winter making coherent interferograms difficult to obtain. Sparse GNSS points are the only geodetic data available.

Devastating earthquakes can also happen in landscapes where the tectonic geomorphology is subtle. For example the 2003 Bam Earthquake in Iran (Jackson et al. 2006) which killed between 26,000 and 40,000 people (Berberian 2005). The earthquake occurred at the end of a subtle fold, which was not obvious until subsequent analysis.

1.3 The Arabia-Eurasia Collision

In Chapter 3 we investigate the tectonic motions within the Kura Basin of Azerbaijan, an low-lying area between the Greater and Lesser Caucasus, using InSAR. We will now provide some wider context to this region.

Arabia is moving towards Eurasia at a rate of $\sim$ 18 mm/yr on an azimuth of $\sim$ 340 north (Altamimi et al. 2023) (Figure 1.2). It behaves as a rigid plate and is moving in a similar style to India, but at a slower rate (Viltres et al. 2022). The Turkish Iranian Plateau (Şengör and Kidd 1979) and the Zagros Mountains of Iran (Nissen et al. 2011) are being created by this collision. The Turkish Iranian Plateau (Figure 1.2) is composed

of several tarranes accreted in multiple stages, similar to the Pamir and Tibet (Allégre et al. 1984; Burtman and Molnar 1993; Şengör and Kidd 1979).

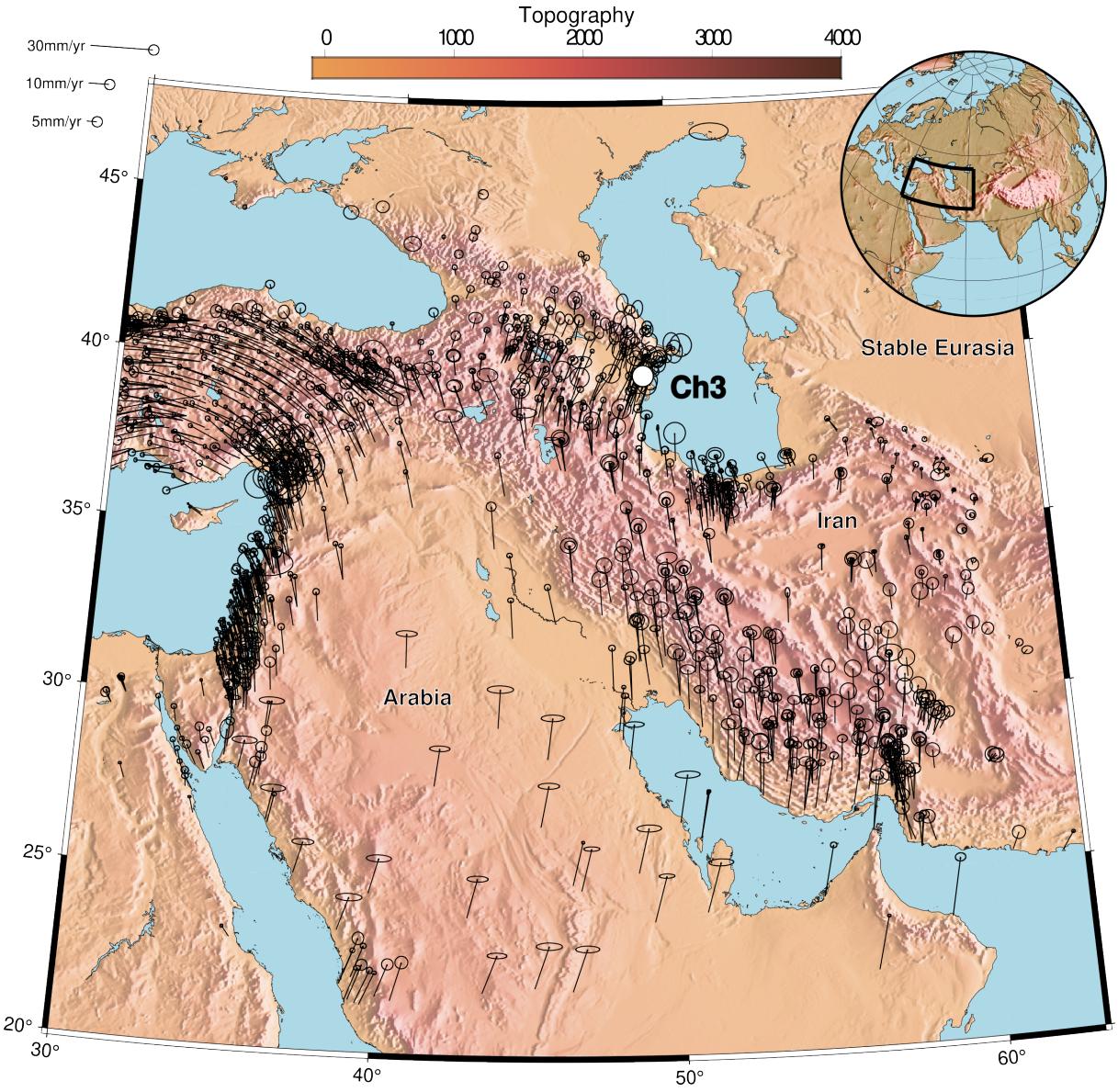

Figure 1.2: Convergence between Arabia and Eurasia shown with GNSS (Kreemer et al. 2014). The Arabian Peninsula is moving as a rigid plate towards Eurasia at around 18 mm/yr, driving up the Zagros Mountains in western Iran, and the Turkish Iranian Plateau and Caucasus. Anatolia is moving as a rigid plate via conjugate motion of the North- and East- Anatolian Faults. Chapter 2 examines the Kura Basin, a low lying area closing between the Greater- and Lesser- Caucasus.

Arabia began moving toward Eurasia at $\sim$ 56 Ma (McQuarrie et al. 2003). The exact time the Arabian indentor first contacted Eurasia is debated. In the Caucasus, ophiolite obduction appears to have ended $\sim$ 65 Ma (Allen et al. 2004; Berberian and King 1981), however large clastic sedimentary deposits associated with proximity to topography only

show up ∼6 Ma. Marine sedimentation at the northern margin of Arabia appears to have ceased ∼ 12 Ma (Dewey et al. 1986) Syntectonic deposition on the northern Arabian Margin is first observed at ∼ 16–23 Ma (Allen et al. 2004; Robertson et al. 2000). McQuarrie et al. (2003) state closure occurred no later the 10Ma based on analysis of seafloor magnetic anomalies.

The Turkish-Iranian Plateau is being sheared in a right lateral sense, reflected in the GNSS vectors which swing round to the east in the north-eastern section of the Plateau so that convergence is more or less perpendicular to the Caucasus. Greater north-eastward velocities in the east of the Plateau than the west are accommodated by anticlockwise vertical axis rotations (Copley and Jackson 2006). It is this north-eastward motion that drives the building of the Caucasus, discussed more in Chapter 2.

1.4 The India-Eurasia Collision

The collision began at around 50 Ma and today India is moving toward Eurasia at ∼35 mm/yr (Kreemer et al. 2014). It is driving up the Tibetan Plateau (Molnar and Tapponnier 1975), the Tian Shan (Thompson et al. 2002), and the Pamir. The Tibetan Plateau is isostatically compensated (Fielding et al. 1994) and is extruding eastward towards China (Copley 2008). North of Tibet, the Tarim Basin behaves as rigid plate within the weaker continental material of Tibet, the Tian Shan and the Pamir, showing little internal deformation (Neil and Houseman 1997). The Pamir lie at the western edge of the India-Eurasia collision and form a plateau similar to Tibet, but much smaller (Schwab et al. 2004). The Pamir are further discussed in Chapters 2 and 4.

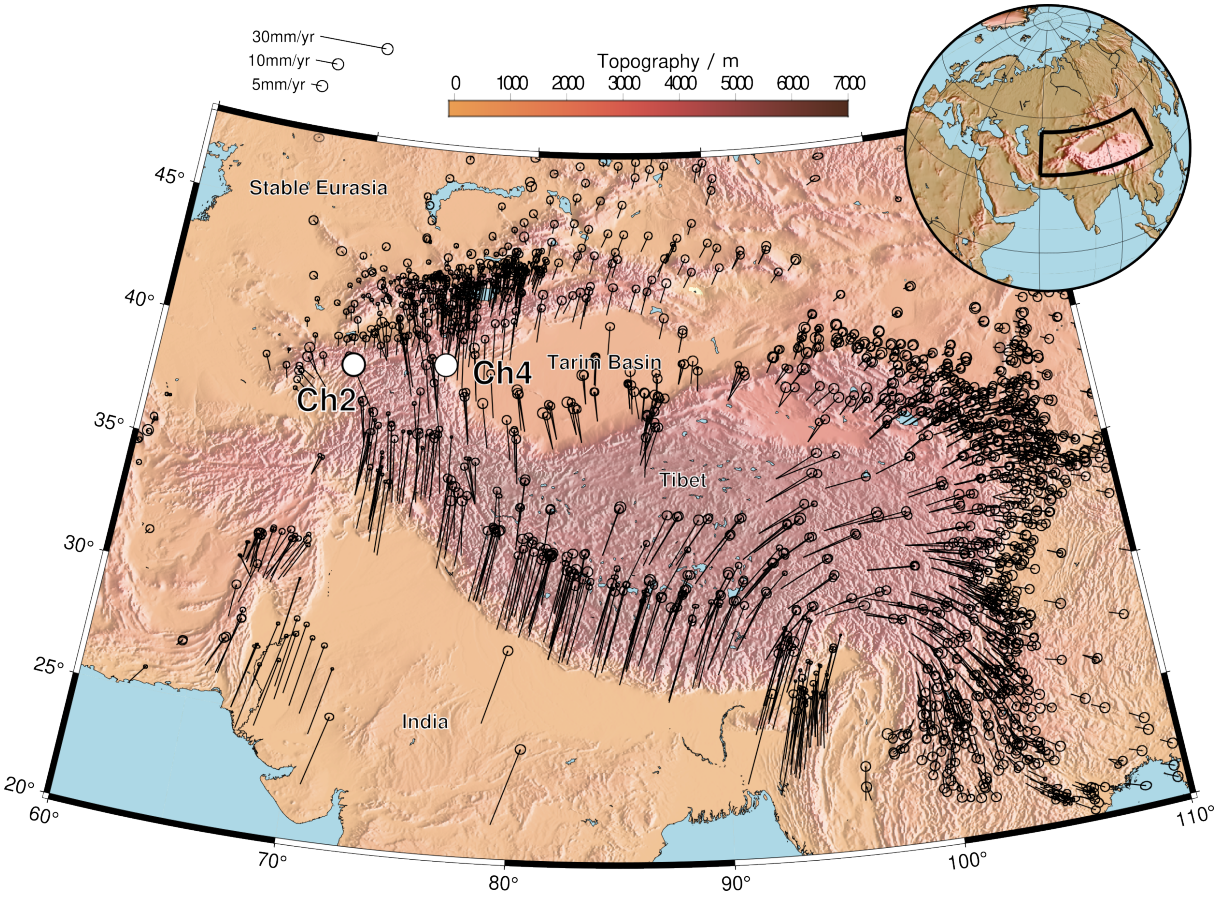

Figure 1.3: The India - Eurasia collision visualised with GNSS from Kreemer et al. (2014). The total convergence between India and Eurasia is ~35 mm/yr. This is strain is responsible for the building of the Tibetan Plateau, the Pamir, the Tian Shan and other ranges further east. Lateral escape of the Tibetan Plateau towards China can be seen in the GNSS. The relatively few GNSS stations in the Tarim Basin show it to be rotating clockwise as a rigid plate surrounded by weaker continental material. The Pamir, at the western end of the collision, are where the case studies in Chapters 2 and 4 are located.

1.5 Barriers to earthquake hazard mitigation

There is a large body of theory that states there is no such thing as a "Natural Disaster" (Hartman and Squires 2006; Smith 2006; Wescoat 2015). The physical processes which happen within the geosphere, biosphere, and atmosphere need to interact in certain ways with human beings and the systems they create to produce disasters.

As Horowitz (2020) puts it regarding Hurricane Katrina:

> *"Somebody had to build the levees before they could break"*

Like any natural hazard, earthquake hazard can be engineered against. The vast majority of fatalities in earthquakes are due to building collapse (Coburn et al. 1992). Examples of earthquake engineering exist across rich countries from the famous Taipei 101 in Taiwan (Li et al. 2011) to the Tokyo Skytree in Japan (Bock 2011). Beyond the flagship buildings, building codes to ensure earthquake resilience in countries like Japan and New Zealand are enforced (Zhang et al. 2022). Although, even in rich countries, older buildings constructed before the introduction of building codes need to be retrofitted (Georgescu et al. 2018).

Traditional earthen architecture is often cited as an exaggerating factor of earthquake hazard, for example the 2003 Bam Earthquake was an earthquake only M_w 6.5, but claimed over 26,000 lives, in part due to the inability of adobe structures to withstand ground shaking. However, un-reinforced masonry buildings also failed (Mostafaei and Kabeyasawa 2004; Nadim et al. 2004). While it is true that without reinforcement traditional structures can be as bad as any building without reinforcement, there are indications reinforcement as well as retrofitting can be done at low cost with appropriate materials (Cárdenas-Gómez et al. 2021; Islam and Iwashita 2010; Varum et al. 2014). It is not necessarily the case that more "modern" styles of architecture are safer. Many examples exist of more western styles of building collapsing in earthquakes (Ozkula et al. 2023). The issue is the political will to design building codes and enforce compliance.

Once a disaster has happened, the path of humanitarian aid to those who need it is a political one. The 2023 Kahramanmaraş Earthquake affected both Turkey and Syria, but areas in the north west under control of groups disliked by the Syrian government received too little too late (Alkhalil et al. 2023; Jalabi 2023). The USA has been documented using humanitarian aid for political ends (Cole 2015; James and Kulwin n.d.; McManus 1987; Prados 2017; Shah 2012). Th weaponisation of humanitarian aid leads to countries to be suspicious of it, even if in most cases the aid is genuine (Walsh 2011).

Finally, whether a country is able to put resources into earthquake hazard mitigation is a political choice. Cuba remains subject to a sanctions regime first imposed at the

height of the Cold War, and these remain a hindrance to its economic development and its ability to assign resources to earthquake hazard mitigation (Gordon 2016). Haiti is another example (Oliver-Smith 2010). Even if countries have the resources they need to tackle earthquake hazard, and the building codes in place, corruption between the state and private companies can lead to devastating consequences (Işık et al. 2024; Oliver-Smith 2010).

1.6 Overview of the text

The chapters of this thesis represent three case studies from different areas of the India/Arabia - Eurasia collision zone. Each study is in research paper form and contains contributions from other authors, outlined at the end of each chapter. The locations of these are given in Figure 1.4.

In Chapter 2, we examine the tectonic circumstances of the 1949 Khait Earthquake, which occurred at the boundary between the converging Tian Shan and Pamir, using a combination of tectonic geomorphology via remote sensing, calibrated earthquake relocations, and earthquake source modelling using scanned historic seismograms, the latter method done by Galina Kulikova (Kulikova 2016). We find evidence that the 1949 Khait earthquake did not rupture the geomorphically well expressed Vakhsh Fault, but a previously unknown fault within the Tian Shan Basement. From out geomorphic mapping and alignments of calibrated earthquake epicentres and mechanisms, we infer an incipitent tectonic rearrangement in the area, with north-west striking right-lateral strike-slip faults accommodating the convergence between the Pamir and Tian Shan via vertical axis rotations. The observation that convergence can be accommodated within the mountain range itself, not just on mature boundary faults, has implications for tectonic models of how mountain ranges converge. The fact that unmapped, geomorphically poorly expressed, faults may produce large earthquakes means seismic hazard assessors cannot assume the largest earthquakes will happen on the most geomorphically well developed faults.

In Chapter 3, we use InSAR time series velocity maps of the Kura Basin to visualise how present day tectonic strain is accommodated on the faults. We find evidence for

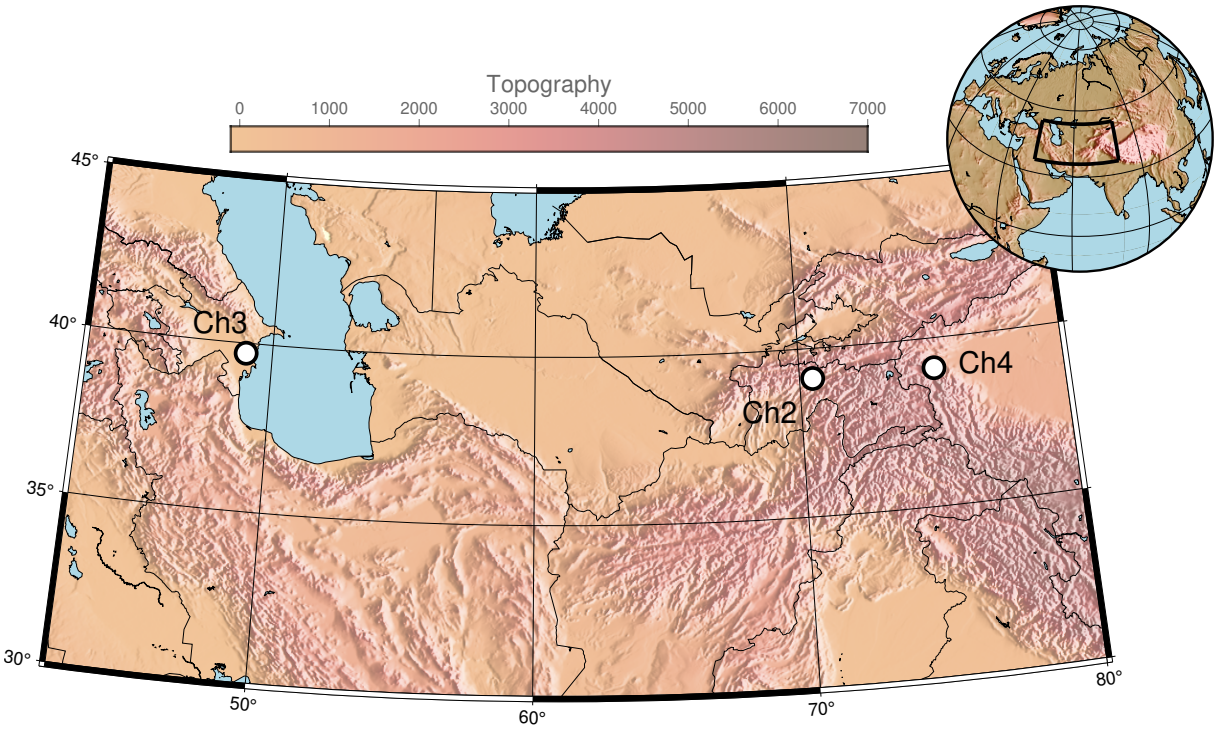

Figure 1.4: Locations across West and Central Asia studied in these thesis. The locations are marked with white dots, annotated with the relevant chapter number.

rapid creep on several of these faults, inspite of paleoseismological evidence for earthquakes on at least one of these faults (Marshall and College n.d.). In addition, we find evidence of a ∼50 km wide wedge of material collapsing into the South Caspian Basin, bounded by creeping faults. We speculate this is slumping due to graviational potential energy contrasts above a detachment of highly fluidised mud.

In chapter 4 we turn again to the Pamir, examining the tectonic circumstances around the 1985 Wuqia Earthquake using calibrated earthquake relocations. We find evidence suggesting the earthquake occurred on a north-west dipping fault well below the sedimentary cover. The seismology data is not congruent with either the surface geology or the surface ruptures associated with this earthquake. We suggest the 1985 earthquake occurred on a transpressive structure in the Tarim Basin basement, relict from previous rapid strike slip motion between the Pamir and Tarim Basin. Like Chapter 2, this has implications for how we assess seismic hazard, when previously unknown faults cause some of the largest earthquakes observed in an area.

1.7 Publications arising from this thesis

Chapter 2 Publication: B. W. W. Johnson, G. Kulikova, E.A. Bergman,F. Krueger, I. K. Pierce, J. Hollingsworth, R. T. Walker. *Rupture of the 1949 Khait earthquake on a cryptic fault: implications for earthquake hazard* (AGU Tectonics; in revision)

Chapter 3 Publication: B.W.W Johnson; J. Elliott; G. Yetirmishli; R. Javanshir; S. Kazimova; N. Marshall; J. Payne; R. T. Walker *Rapid fault creep in the fluid-rich Kura Basin, Azerbaijan, imaged with InSAR* (Geophysical Journal International (in review))

Chapter 4 has not yet been submitted for publication.

2 | Rupture of the 1949 Khait earthquake on a cryptic fault: implications for earthquake hazard

B. W. W. Johnson[1], G. Kulikova[2], E. A. Bergman[3], F. Krueger[4], I. K. Pierce[1], J. Hollingsworth[5], R. T. Walker[1]

[1] Department of Earth Sciences, University of Oxford, South Parks Road, OX13AN, United Kingdom.

[2] UP Transfer GmbH at the University of Potsdam, House 29, Room 5, Karl-Liebknecht-Str. 24 - 25, 14476, Potsdam.

[3] Global Seismological Services, 1900 19th St. Golden, Colorado 80401 U.S.A.

[4] Institute for Geosciences, University of Potsdam, Karl-Liebknecht-Str. 24 - 25, 14476, Potsdam

[5] ISTerre, Université Grenoble Alpes, Grenoble, France

Corresponding author: Ben Johnson (benedict.johnson@st-annes.ox.ac.uk)

Key Points:

- We examine the source parameters of the 1949 Khait earthquake, Tajikistan
- We conclude it was predominantly strike-slip on a previously unmapped fault at the Pamir-Tien Shan boundary
- The Khait earthquake shows the hazard posed by 'cryptic' faults in the continental interiors.

Abstract

The 1949 M_w 7.6 Khait earthquake, Tajikistan, was one of the most destructive of the Pamir – Tien Shan region, killing over 7000 people by building collapse and landsliding. It occurred at the transition between the Pamir and Tien Shan mountain ranges, which converge along the narrow Vashkh river valley. Therefore, it is important in understanding the tectonic and structural development at the junction of these two major

mountain ranges, as well as yielding important information regarding hazard and risk to local populations and infrastructure. Although widespread landsliding and intensities of shaking were recorded, no surface ruptures were mapped, and the earthquake epicentre and source are poorly known. To determine the location and focal mechanism of the 1949 earthquake we combine calibrated earthquake relocations with body-wave amplitude ratios from digitized paper seismograms. Our analysis shows that the earthquake nucleated within the Tien Shan basement with strike slip kinematics. Using high-resolution digital elevation models and orthophotos derived from high-resolution satellite imagery, we identify earthquake ruptures within the epicentral zone consistent with NW-SE right-lateral faulting. Relocated aftershocks and later seismicity also follows a NW-SE trend through the Tien Shan north of the Vakhsh river. Mapping tectonically offset moraines dated in previous literature, we find a Vakhsh Fault slip rate of only half the present day strain accumulation rate derived from GNSS. Our results suggest a significant proportion of the regional deformation may occur away from the geomorphologically well expressed Vakhsh and Darvaz faults, and on faults with little prior expression of activity.

2.1 Introduction

The 10 July 1949 Khait, Tajikistan earthquake (M_w 7.6) occurred at 09:45 local time (03:53∼UTC) and was particularly destructive, leading to over 7000 deaths predominantly as a result of widespread landsliding (Evans et al. 2009; Yablokov 2001). From Kondorskaya and Shebalin (1982): *"in an instant all the buildings in Khait were destroyed...; dust rose from the mountain slides; the entire area became cloudy and instantly grew dark... The ground shook so much that the trees bent to the ground. A car on the road... was tossed and the passengers were flung from the vehicle...."*. A shallow foreshock from 1941 of M∼6.4 is reported by Kondorskaya and Shebalin (1982)) west of Khait (70.5°E, 39.2°N), which caused some damage in the Yasman Valley, but it is unclear if anyone was killed. The 1949 earthquake played an important historical role, triggering the establishment of the Garm Research Station nearby, which became a centre of Soviet earthquake research, including into earthquake prediction (Rautian et al. 2007; Sadovsky and Nersesov 1974).

Table 2.1: Previous estimes of the 1949 Khait earthquake source parameters

Longitude / deg	Latitude / deg	Depth / km	Strike / deg	Dip / deg	Rake / deg	Magnitude	Reference
70.8706	39.3364	13±5	50	80	-20	M_S 7.8 / m_b 7.6 / M_w 7.6	This Study
70.8915	39.1739	20 (fixed)	-	-	-	M_S 7.3	ISC - Storchak et al. (2017)
70.8	39.2	16	-	-	-	MLH 7.4	Kondorskaya and Shebalin (1982)
-	-	-	-	-	-	M_w 7.5	Chen and Molnar (1977)

The Khait earthquake occurred near the Northern margin of the Pamir continental plateau, which is rapidly converging with the Tian Shan to the north at ∼13-19 mm/yr: half the north-south India-Eurasia shortening rate at this longitude (Altamimi et al. 2017; Ischuk et al. 2013; Metzger et al. 2020; Zubovich et al. 2010). The faulting accommodating this shortening appears to change along the margin, with relatively simple overthrusting of the Pamir into the Alai Valley, between 72°E and 74°E, contrasting with an increased right-lateral strike-slip component across the Vakhsh river valley of Tajikistan (between 70°E to 72°E). Whether the motion is localised on the geomorphologically well-expressed Vakhsh Fault, or whether strain is accommodated within basement rocks of adjacent parts of the Pamir and Tian Shan is not resolved.

Despite the high number of earthquakes in the Pamir region, the Khait earthquake is one of only five $M_w > 7$ instrumentally-recorded earthquakes within the Pamir (Figure 2.1). Another is the 1974 Markansu Earthquake, which also occurred within the Pamir Margin (Jackson et al. 1979). The 1911 and 2015 Sarez earthquakes both occurred within the Pamir interior (Elliott et al. 2020), along with the 1902 Karatag earthquake (Kulikova 2016). Understanding the source parameters and causative faulting of the 1949 earthquake thus offers a rare insight into the kinematics and earthquake potential of the Pamir margin. The 1949 earthquake occurred before the establishment of a global standardized seismic network, so the location, magnitude, and focal mechanism are not well resolved. Previous estimates for source parameters and locations are shown in Table 2.1 and Figure 2.1. Contemporary scientists were unable to locate surface rupturing from this event but mapped a suite of coseismic landslides including the 4 km long Khait Landslide, which buried the towns of Khait and Khisorak (Figure 2.6B) (Gubin 1960; Leonov 1960).

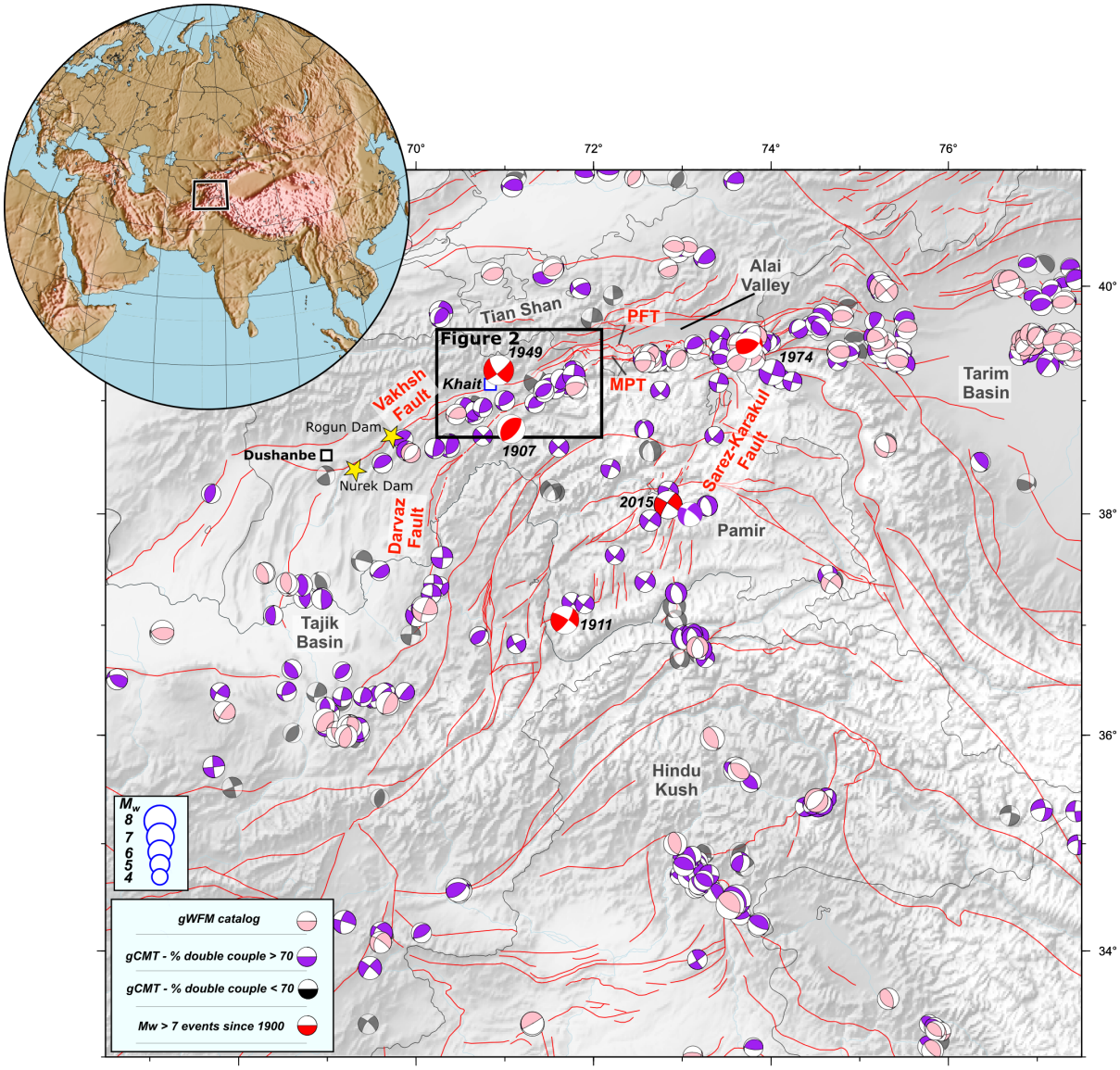

Figure 2.1: (Caption next page)

Figure 2.1: Earthquake mechanisms of the Pamir and surroundings from the gWFM (Wimpenny and Watson 2020), and gCMT (Dziewonski et al. 1981; Ekström et al. 2012) catalogs, with locations from the ISC-EHB catalog where available (Engdahl et al. 2020; Engdahl et al. 1998; Weston et al. 2018). gCMT mechanisms are split into those above and below 70% double couple. Earthquakes of M_w >7 since 1900 are shown in red, with mechanisms and locations from (Elliott 2020; Jackson et al. 1979; Kulikova et al. 2016; Mikhailova et al. 2015). Faults are from the Central Asia Fault Database (Mohadjer et al. 2016). Mechanisms along the Northern Pamir Margin show shortening in this region. This is consistent with GNSS studies which show 13–19 mm/yr convergence between the Pamir and Tian Shan. In the Pamir interior, crustal earthquakes are focused along the strike-slip Sarez-Karakul Fault Zone and in a normal earthquake zone in the southern Pamir. These accommodate east-west extension across the Pamir Plateau observed in GNSS studies. This east-west extension of the Pamir causes folding in the Tajik Basin as the eastwards-moving Pamir pushes up basin sediments into north-south folds. The strike slip Darvaz Fault is picked out by left lateral strike slip mechanisms, but the right lateral Vakhsh Fault appears to be a mixture of right-lateral strike-slip and thrusting. Along the Northern Pamir Margin, the Pamir overthrust the Alai Valley along the Pamir Frontal Thrust. Near Khait, this shortening is accommodated across several faults, including the Vakhsh Fault. MPT = Main Pamir Thrust; PFT = Pamir Frontal Thrust

To address the existing gaps in knowledge relating to the 1949 earthquake source, we determine an epicentre and focal mechanism from analysis of digitized analogue teleseismic records. We use modern regional networks deployed by GFZ Potsdam (Kufner et al. 2018b; Schurr et al. 2014) and use multi-event relocation software *mloc* to provide an updated epicentre of the 1949 earthquake, along with a catalog of well-located moderate magnitude earthquakes spanning 1949 to 2017. The 1941 earthquake mentioned above could not be located using *mloc* due to a paucity of arrival times. To map evidence of active faulting and potential earthquake rupturing we acquired 0.3 m resolution Worldview 3, and 0.7 m Pleiades, stereo optical imagery of the northern Yasman Valley and along the major Vakhsh fault. We conclude that the 1949 Earthquake was likely hosted in the Tian Shan basement rock and is unlikely to have activated the major Vakhsh Fault. This shows that while simple overthrusting occurs in the Alai Valley, in the Vakhsh Valley, where the previous sedimentary basin has completely closed, the zone of deformation has expanded to include the Tian Shan basement.

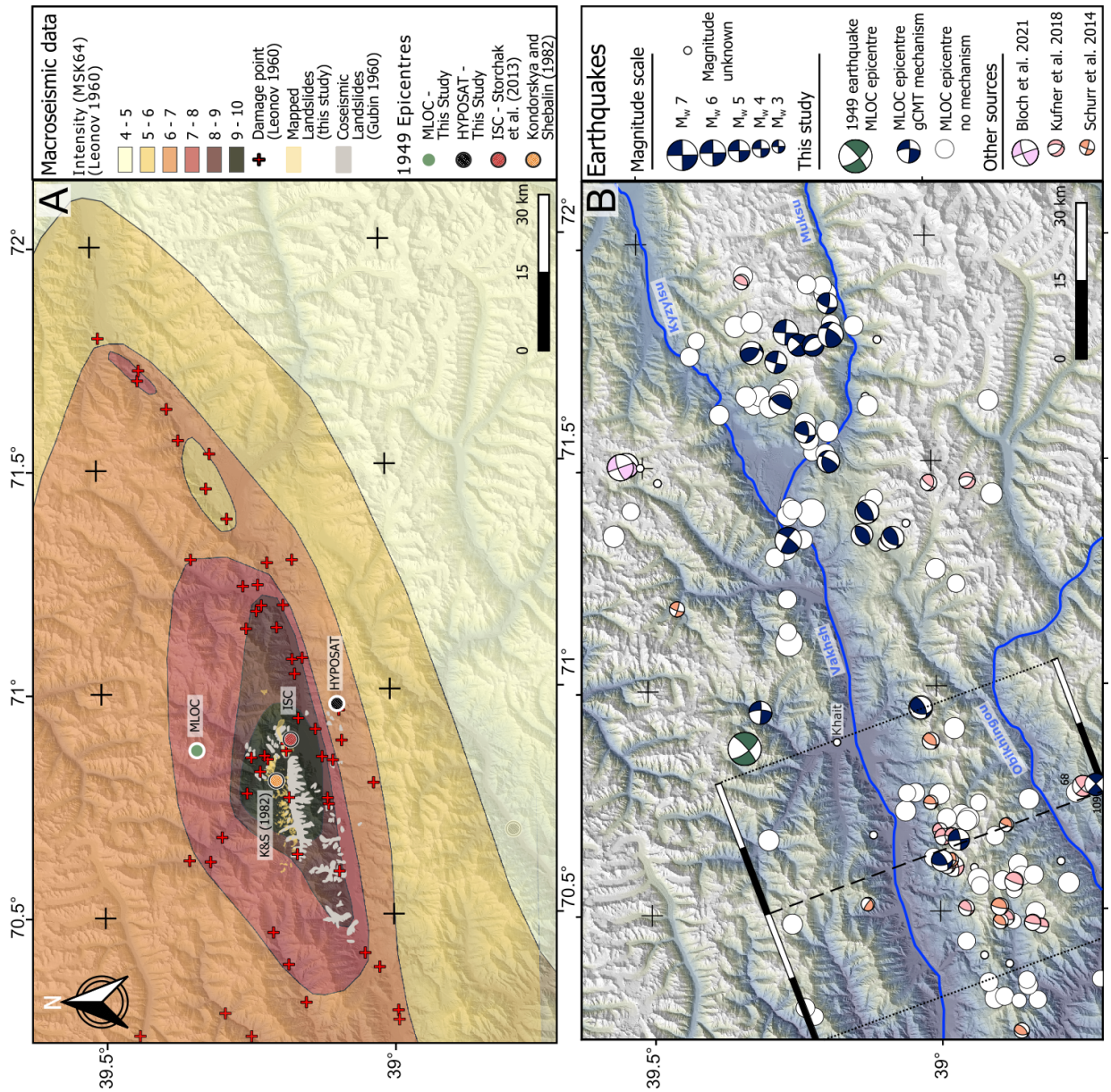

Figure 2.2: (Caption two pages on)

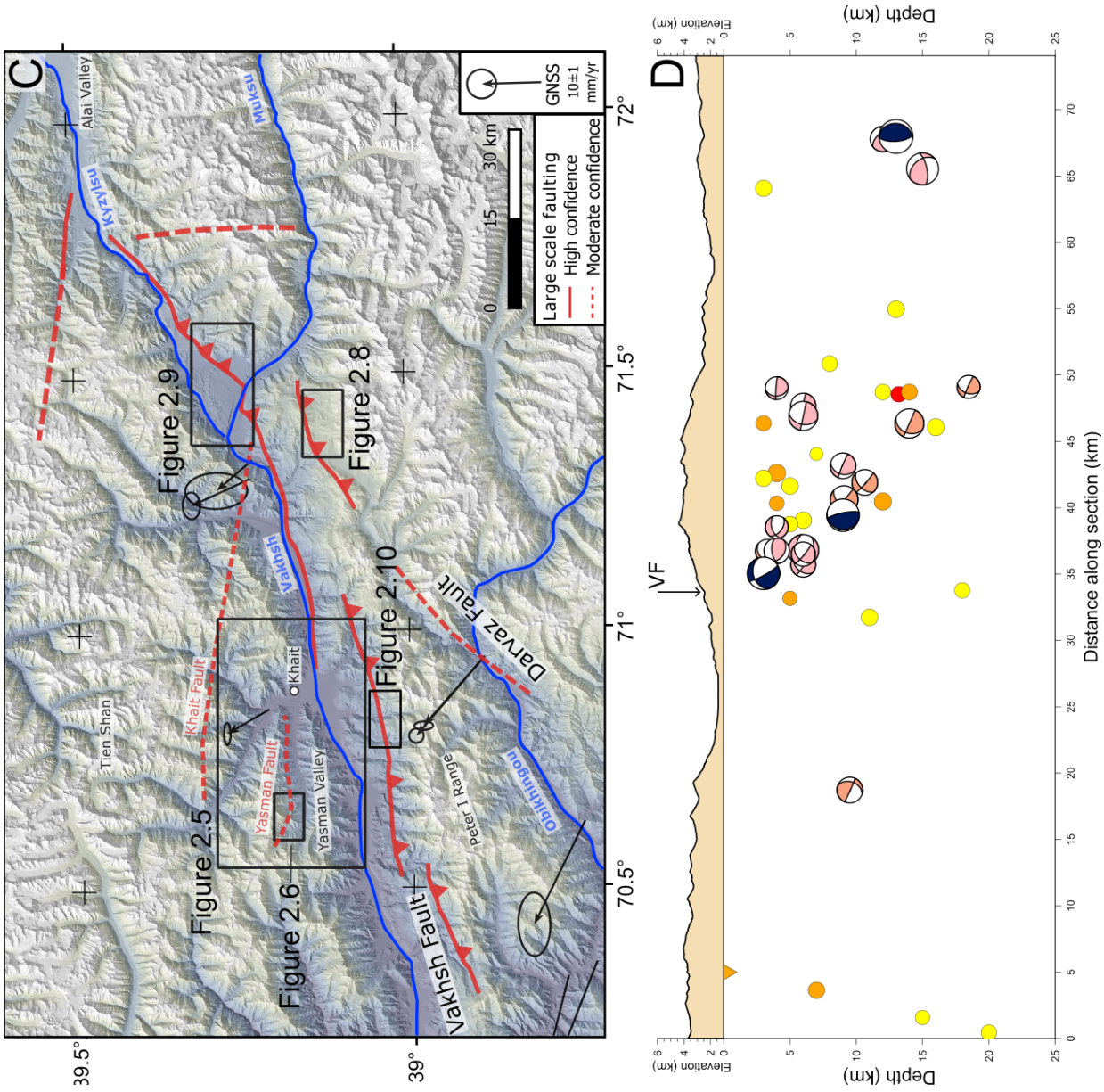

Figure 2.2: (Caption next page)

Figure 2.2: (Previous page) (A) Isoseismals from the earthquake based on data (red crosses) from Gubin (1960) and Leonov (1960) using the MSK64 scale (Medvedev et al. 1965). Previous location estimates for the 1949 earthquake epicentre are shown along with the location from this study (labelled MLOC). The elliptical damage contours are consistent with a crustal depth earthquake, and the long axis is roughly parallel to the Vakhsh Valley suggesting a source roughly parallel to this valley. The contour shapes may be biased by the lack of data to the north-east of Khait, and by the landslide susceptibility of the Yasman Valley, further discussed in the text. (B) Earthquake focal mechanisms and epicentres relocated using *mloc*. Our relocation puts the 1949 M_w 7.6 Khait Earthquake (dark green) ~30 km north of the Vakhsh Valley and waveform modelled mechanism indicates right lateral strike-slip on a NW or left-lateral motion on a SW-striking fault. The Vakhsh Fault is defined by a cluster of right-lateral strike-slip/thrust mechanisms in a diffuse alignment with the Valley. In cross section (D) these thrusts lie on a ~50° dip angle, roughly parallel to the focal planes. A gap in the earthquakes is present at around (71.2°E, 39.0°N), around where the Darvaz and Vakhsh Faults would be projected to intersect. (C) Solid red lines show high confidence fault mapping based on long term geomorphic offsets, and dashed lines show lower confidence mapping based on earthquake mechanism alignments. GNSS vectors from Metzger et al. (2020) show both right-lateral motion along the Vakhsh valley, and contraction across it. The station spacing is such that this motion cannot be allocated onto discrete faults.

2.2 Seismotectonic Setting

The Pamir Mountains form an extensive high-altitude continental plateau within the ongoing India-Eurasia collision, west of the larger Tibetan plateau (Burtman and Molnar 1993). They are bounded to the east by the low-lying and relatively undeformed Tarim basin (Neil and Houseman 1997); to the north by a series of narrow and partially consumed sedimentary basins that separate the Pamir from the Tien Shan mountain ranges (Leith and Alvarez 1985; Sobel et al. 2013); and to the northwest and west by the Afghan-Tajik depression, which is a large sedimentary basin that is deforming internally (Gągała et al. 2020; Kufner et al. 2018b; Sobel et al. 2013) (Figure 2.1).

The Pamir are composed of accreted terranes from the Paleozoic to Cenozoic with arcuate sutures. Terrane sutures of Paleozoic and Mesozoic ages are offset northward within the Pamir relative to Tibet and the Hindu Kush by 300-700 km, suggesting over 300 km of motion since the start of the Cenozoic (Burtman and Molnar 1993; Schwab et al. 2004).

The Pamir Frontal Thrust (PFT) and Main Pamir Thrust (MPT) accommodate around 10 mm/yr north-south convergence (Arrowsmith and Strecker 1999; Coutand et al. 2002;

Patyniak et al. 2021; Zubovich et al. 2016) (Figure 2.1). Westward, the north-south compression is taken up by the Vakhsh Thrust System and Darvaz Fault (Figure 2.1 and 2.1). Subduction beneath the southern and northern margins of the Pamir to depths of ∼300-350 km is well established by earthquake locations (Sippl et al. 2013a) seismic tomography (Kufner et al. 2016; Sippl et al. 2013c), receiver functions (Schneider et al. 2013; Schneider et al. 2019) and guided wave observations (Mechie et al. 2019). The crust of the Alai Valley is thought to be subducting beneath the Pamir, but along strike near Khait, the valley is closed and subduction has terminated.

The Vakhsh Thrust is the leading thrust of the Peter I Range: a fold and thrust belt formed by compression of Tajik Basin sediments between the Tian Shan and Pamir (Gągała et al. 2020; Leith and Alvarez 1985). Thrust earthquake focal mechanisms strike parallel to the surface trace of the Vashkh fault (Hamburger et al. 1993; Kufner et al. 2018a; Schurr et al. 2014). The fault is exposed as a plane of evaporite, with quaternary scarps, near to the Obikhingou River (70.111°E, 38.853°N) (Gągała et al. 2020). GNSS velocity profiles perpendicular to the Vakhsh valley near Garm (45 km WSW of Khait) show both 17 mm/yr shortening and 13 mm/yr right-lateral shear, and it has been suggested that the Vakhsh fault accommodates the strike-slip motion aseismically while accommodating the thrusting seismically (Metzger et al. 2020). Closer to Khait, however, the shortening across the Vakhsh Fault appears to be ∼5 mm/yr. Aseismic creep has been observed in InSAR data along the westward continuation of the Vakhsh fault (Metzger et al. 2021). It is currently unknown whether the Vakhsh Thrust has hosted a large historical earthquake.

Near Khait, PT axes from earthquake focal mechanisms indicate WNW-ESE compression (Kufner et al. 2018b; Lukk et al. 1995; Schurr et al. 2014)(Figure 2.1B). This deformation is thought to be concentrated onto the Vakhsh and Darvaz Faults (Hamburger et al. 1993; Metzger et al. 2020; Schurr et al. 2014; Trifonov 1978). However, earthquake location uncertainty and the prevalence of landslides and mass movement scarps make it difficult to positively identify earthquake surface ruptures and fault scarps (Strom and Abkhmatov 2018). Where fault scarps are present, they are discontinuous along strike.

The Darvaz fault runs down the western side of the Pamir, with earthquake focal mechanisms indicating it to be a vertically dipping left-lateral strike-slip fault (Kufner et al. 2018b; Lukk et al. 1995; Schurr et al. 2014). GNSS profiles perpendicular to the fault in the western Pamir show 10-15 mm/yr left lateral shear with ∼10 mm/yr extension. Soviet-era paleoseismic studies of the Darvaz Fault near Saghirdasht (70.66 °E, 38.64 °N) suggested strike-slip rates of 12-14 mm/yr, but their dating is uncertain (Trifonov 1978). It is suggested the Darvaz fault continues to the northern margin of the Pamir and links up with the MPT (Schurr et al. 2014; Sobel et al. 2013) although this is difficult to follow in the landscape. Our own mapping and earthquake locations suggests a more complicated junction between these faults where NS shear zones act to accommodate differential longitudinal convergence rates (Section 2.4.1, Figure 2.7).

The northern Pamir margin has very high relief and is glaciated. Lying at the convergence between the Indian Summer Monsoon and the Mid-Latitude Westerlies, Pamir glaciation is modulated through time by the relative strength of these weather systems (Benn and Owen 1998). This leads to incomplete and asynchronous preservation of glacial stages within the Pamir (Dortch et al. 2013). There is evidence of glacial advances in the Pamir at 16-12 ka, 24-28 ka, ∼65–40 ka, ∼80–60 ka, ∼200–100 ka, and >200 ka (Abramowski et al. 2006; Röhringer et al. 2012; Seong et al. 2009; Stübner et al. 2021; Wang et al. 2011; Zech et al. 2005).

Closer to Khait, the Fedchenko Glacier is the largest in the region, lying at the northwestern edge of the Pamir. It feeds into the Muksu Valley which joins the Vakhsh near Sary Tala (Figure 2.9). This has deposited lateral and recessional moraines in the Vakhsh Valley at ∼18 kyr which are tectonically offset (Grin et al. 2016) (Figure 2.9). South of Sary Tala, in the Peter I Range, there is a small complex of moraines within a region ∼10 km x 8 km showing evidence of up to 9 advances, which are also cut by a tectonic scarp (Figure 2.1c and 2.8). We suspect these smaller moraines postdate 18 ka, just because they are not as extensive as we might expect (although their catchment is quite small), and there is evidence for at least one Little Ice Age advance in the nearby Abramov Glacier over the past thousand years (Saks et al. 2024).

This glacial history has produced steep sided valleys throughout the region prone to landsliding and has concentrated human activity into comparatively little space on terraces. These factors present challenges in finding and assessing evidence of active faulting in the geomorphology, but also allow some age constraint on the tectonic geomorphology.

For these reasons, geomorphic evidence for the 1949 Khait Earthquake has so far been limited to damage and landsliding. These were mapped in the decades following the earthquake (Gubin 1960; Leonov 1960) (Figure 2.1A). When contoured, these data show a WSW-ENE elongation, consistent with both a shallow (i.e. crustal) earthquake source and a fault striking sub-parallel with the Vakhsh Fault, although these contours lack data in the north-east, making their shape uncertain. Coseismic landslides are concentrated north of the Vakhsh river valley, concurring with damage to settlements in the region (Figure 2.1A). In the remote mountainous regions north-east of Khait mapping and damage data are lacking, so the intensity contours are unconstrained. Taken together, the available macroseismic evidence suggests the 1949 earthquake ruptured a fault north of the Vakhsh Fault. The maximum intensity close to Khait was 10 on the MSK scale (a Soviet seismic intensity scale) representing "general destruction of buildings" (Medvedev et al. 1965). Dushanbe, ~200 km away, suffered "light damage to brick buildings" and cities as far away as Samarkand, ~350 km, felt enough shaking to "awaken people".

2.3 Materials and Methods

2.3.1 1949 Source Parameters Determination using analogue seismic data

The 1949 Khait earthquake was recorded by many seismic stations worldwide providing a wide azimuthal coverage (Figure 2.3) for seismic data. The old seismic bulletins (e.g., Storchak et al. (2015)) offer arrival times for various phases, which significantly contributes to the data required for determining epicentre location. However, many of the original analogue seismic records (the original paper seismograms) have not been available to us. Altogether we have collected the records from 42 seismic stations (grey triangles Figure

2.3A). But only records from 12 stations were suitable for digitization due to the poor quality of the scanned paper records.

The nearest stations, within the former USSR located closer than 3000 km to the epicentre had to be excluded for waveform modelling as their amplitudes exceeded the amplitude range of the seismometer, clipping the data. The remaining stations were mainly located in Europe, with three in Japan and the United States. Among the 12 stations used, 8 were situated in Europe, with 7 of them being in close proximity to each other. Therefore, the seismic network in Europe served as a large aperture seismic array. This allows the alignment and stacking of records, thereby enabling the identification of coherent wavelets generated by the source. For P-waves, this process is relatively straightforward (see Figure 2.3B), allowing us to generate a summation trace (SUM Z, Figure 3B) which tells us the rupture duration. We use this in Section 2.5.1 to estimate the length of the 1949 rupture. While the azimuthal coverage is not ideal, and greater coverage would reduce source parameter uncertainties (Table 2.1), we have stations that sample at least two quadrants of the focal sphere. In addition, one focal plane should pass through Europe and the other focal plane should pass between the Japanese and American stations, providing additional constraints, although having one nodal plane constrained by two stations is not ideal.

The majority of available analogue seismograms were recorded by the instruments consisted of mechanical pendula hinged to a stylus writing onto a slowly rotating drum. Minute marks tracked time on the records, and different stations were synchronized to a universal clock. The paper records were scanned at high resolution, and manually digitized using vector graphics software (we have used GIMP, (The GIMP Development Team., 2025)). The lines were smoothed with Bezier Curves, resampled at a 0.1s interval and converted to ASCII text format. Curvature of the trace due to the cylindrical drum was corrected using the method of Cadek (1987) and Grabovec and Allegretti (1994).

We derived a preliminary epicentre location for the 1949 using HYPOSAT (Schweitzer 2001; Schweitzer 2018). This software can use absolute arrivals as well as arrival times (e.g

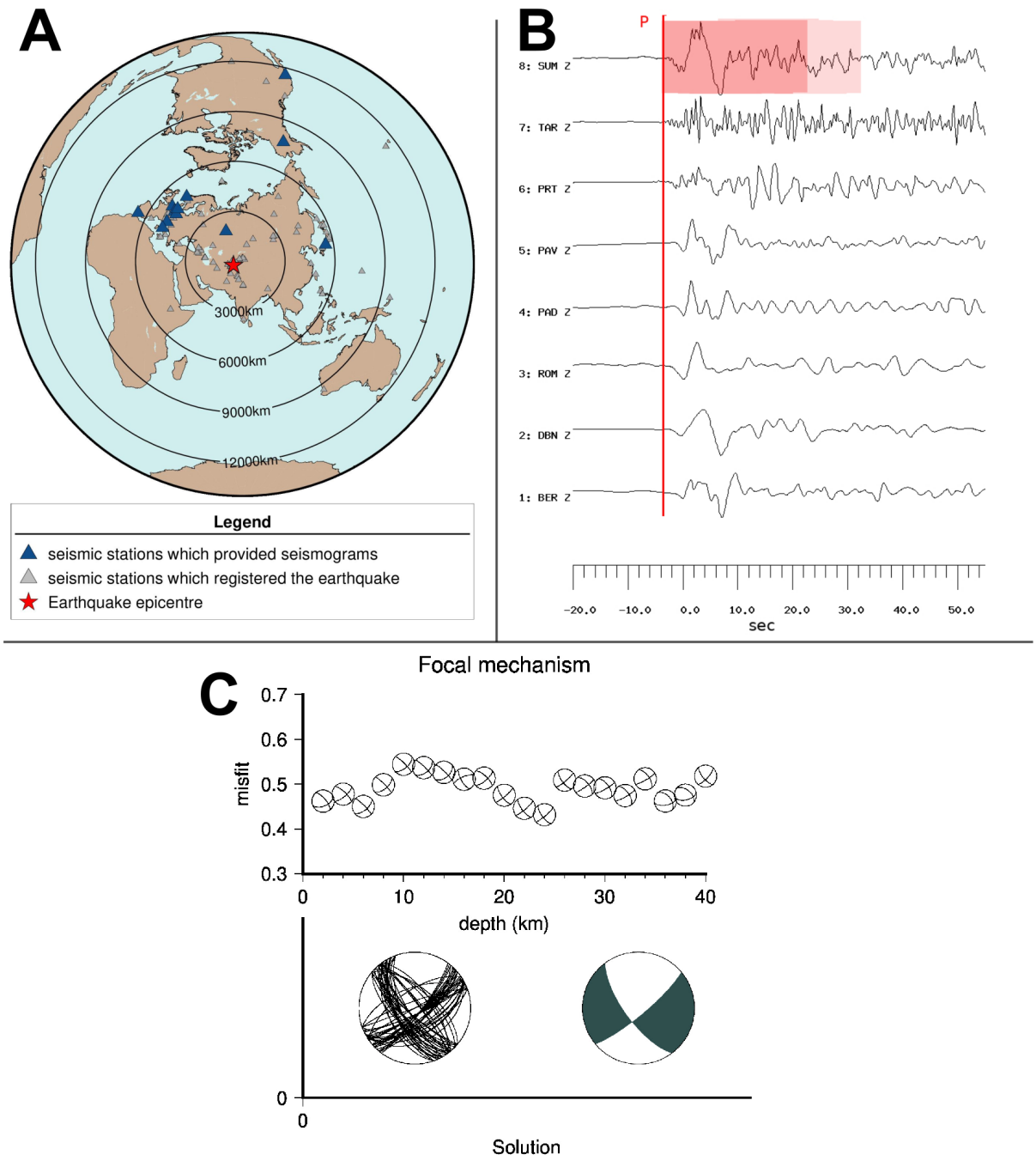

Figure 2.3: (A) Azimuthal distribution of all (according to the information provided in seismic bulletins) seismic stations (grey triangles), which recorded the 1949 Khait earthquake (red star); dark blue triangles show seismic stations whose records were digitized for focal mechanism determination. The azimuthal coverage is good enough to cover three of the four focal sphere quadrants, however a lack of data in Africa, Oceania and South America mean there is a greater than 180°azimuthal gap. (B) Digitized Z components from European stations show a mixture of strong and weak P wave arrivals, consistent with Europe's location near the nodal plane of the focal sphere. The duration of these arrivals, by inspection, is around 20 seconds (e.g. station GTT) which suggests a similar rupture duration. (C) The 5% lowest misfit focal mechanism solutions with the lowest misfit solution plotted (green). The lowest misfit solution is plotted at a range of fixed depths. Misfit is constant with depth, showing depth is not well constrained with the focal mechanism determination method, and that the focal mechanism itself is largely independent of depth.

S-P) differences. By using both, we determined the epicentre location and origin time of the earthquake. We observed timing errors on the order of up to 5 seconds between different stations, which may be attributed to uncertainties in phase picking, errors in minute marks on the digitized seismograms, or time misalignment across various stations. This resulted in a considerable location error ellipse of up to 20 km in latitude and 40 km in longitude. Consequently, the calibrated earthquake relocations (Section 2.3.2) was necessary.

A number of issues preclude using routine moment tensor inversion techniques (Dahm and Krüger, 2014, 1999) for focal mechanism and seismic moment determination of the earthquake in our case. Firstly, the bandwidth of the analogue seismic instruments at that time was not always sufficient to record the lower frequencies of large earthquakes (Mw $>$ 7). Teleseismic moment tensor inversion is often performed using 15-100 second bandwidths (Talebian and Jackson 2004) but instruments in 1949 had bandwidth between 4 and 10 seconds (Wiechert inverted pendulum), sometimes going up to maximum 20 seconds (Bosch-Omori instruments) (McComb and West 1931; Wood 1921). Secondly, frequency artefacts caused by the writing needles dislocating during strong shaking, and steps introduced when interpolating the trace across paper records affected the moment tensor solution. Thirdly, different components of motion could be misaligned in time or absent. For example, we were able to acquire only the Z component for station BER, and only the E-W component for station DBN. This is problematic, as moment tensor inversion often requires recordings from all perfectly aligned in time three components (NS, EW and Z) in order to derive radial and transverse components of motion. Finally, instrument calibration information was not always available or certain for every station and sometimes needed to be extracted from the literature (Wood 1921) where only reference values are given – not those for a specific day and time. This information is necessary to deconvolve the instrument response from the trace and extract the actual displacement (Scherbaum 2006).

Given the problems in using conventional moment tensor inversion to determine the focal mechanism, we instead used a comparison of amplitude ratios between observed and synthetic seismograms in order to determine the focal mechanism. Synthetic waveforms

were produced using synthetic Greens function database calculated with the FOMOSTO tool in the PYROCKO framework (Heimann et al. 2017; Heimann et al. 2019). In a grid search the synthetic records were simulated for different strike, dip and rake and their amplitude ratios (for P, PP, S, SS phases) were compared to corresponding amplitude ratios of the observed seismograms and misfit was calculated. These calculations were repeated for different test depths using a depth increment of 2 km. The minimum misfit between observed and modelled amplitude ratios determines the strike, dip and rake angle (focal mechanism, Figure 2.3C Bottom) and the most probable depth (Figure 2.3C Top) of the earthquake. For a more detailed account of this method see (Kulikova and Krüger 2015; Ou et al. 2020). It is frequently observed that paper records lacked distinct polarity indicators; consequently, the first motion polarity on the Z-component, which serves as a definitive marker for the compressional and dilational quadrants, could not be ascertained. In such instances, we must depend on alternative data, such as geological observations, to accurately identify the true fault plane. Regarding the 1949 Khait earthquake, there was one station (ROM, Italy) that provided a clear indication of the polarity, which was subsequently used. The focal mechanism is constrained to be a double-couple, although our geomorphic analysis indicates the source was probably more complex (section 4.4.1).

For the 1949 Khait earthquake, we computed three distinct types of magnitude: mB, MS and MW. The broadband body wave magnitude mB (Bormann and Saul 2009; Bormann et al. 2013) and the surface wave magnitude MS (using the Prague-Moscow Formula (Karnik et al. 1962)) were derived from the amplitude and period values obtained from the digitized waveforms (see Appendix A2). While the measurement of amplitude and period for body waves is relatively straightforward and yields reliable values, the amplitude measurement for surface waves presents complexities. The Prague-Moscow Formula (Karnik et al. 1962) for MS necessitates measurements at longer periods, approximately 20 seconds. However, this poses challenges for analogue instruments, as previously noted, since most instruments of that era had bandwidths ranging from 4 to 10 seconds. Consequently, the recorded surface wave signals experience amplitude saturation and insufficient amplitude measurement at lower frequencies. Mw was calculated by fixing the focal mechanism (as determined with amplitude ratios comparison) and generating synthetic seismograms

at different magnitudes to find the closest match to the observed amplitude. (Appendix A3). For a more detailed account of this method see (Kulikova and Krüger 2015; Ou et al. 2020).

2.3.2 Calibrated Earthquake Relocations

Overview

There is significant uncertainty and variance in reported epicentral location of the 1949 earthquake (Kondorskaya and Shebalin 1982; Storchak et al. 2015). The preliminary location determined using HYPOSAT in the previous section still has a 40 km uncertainty, and this is not sufficient to assign the earthquake to a fault in this region, and so elucidate the tectonic role of this earthquake.

Previously reported estimates of epicentral location were based on macroseismic evidence (Kondorskaya and Shebalin 1982; Storchak et al. 2015). These are sited close to Khait town, though this may be due to a lack of regionally extensive data. Damage report coverage (Figure 2.1a, red crosses) is unevenly distributed, with a particular gap to the north-east of Khait, so the exact shape of the damage contours is uncertain, and additionally the damage data do not always distinguish between damage caused by shaking and landsliding. Kondorskaya and Shebalin (1982) report that *"The village of Khait and 20 kishlaks [settlements] were buried by the slides in the Yasman River valley"*. Evans et al. (2009) have argued that sediments in the Yasman Valley would have had a particularly high susceptibility to shaking-induced landsliding, being composed of loess and saturated from rain during the night of 9-10 July 1949 (Stanyukovich 1997). Therefore, there is reason to believe the very high amounts of landsliding may not correlate well with the region of greatest ground motion, so do not help us pinpoint the earthquake epicentre.

Previous seismotectonic studies are unclear whether the Khait earthquake nucleated and was hosted on the large-scale Vakhsh Fault or on faults in the Tian Shan (Hamburger et al. 1993; Schurr et al. 2014). We were unable to find extensive surface ruptures on the southern side of the Vakhsh Valley, and recent GNSS and satellite radar measurements

further west imply the Vakhsh Fault may be creeping (Metzger et al. 2020; Metzger et al. 2021), possibly due to evaporites within the fault core, as observed in surface outcrops of the fault plane near the Obikhingou river (Gągała et al. 2020).

We refine the location of the 1949 earthquake by including it in a calibrated cluster of earthquakes analyzed with the program *mloc* (Version 10.5.3). *mloc* is based on the Hypocentroidal Decomposition (HDC) algorithm introduced by Jordan and Sverdrup (1981) but it incorporates additional procedures to produce (if appropriate data are available) hypocenters that are minimally biased by unknown Earth structure and that have realistic parameter uncertainties based on the variability of the data used. Relocations with these properties are referred to as "calibrated". The use of *mloc* in this study exactly parallels the relocation studies contributing to the Global Catalog of Calibrated Earthquake Locations (GCCEL), as described in Bergman et al. (2022).

Like all multiple event relocation algorithms *mloc* uses differences in observed arrival times of seismic phases to improve the relative locations of a set of earthquakes within a limited area (termed a 'cluster'). Uniquely among such algorithms, however, the hypocentroidal decomposition method uses projection operators to split the relocation problem into two parts. At each iteration, improvements to the relative locations, or "cluster vectors", of the events in the cluster (relative to a reference point called the hypocentroid) are determined. Next, improvements to the absolute location of the hypocentroid are determined in close analogy to a single event location, but using data selected from all the events in the cluster. After each iteration the cluster vectors are added to the hypocentroid to obtain absolute locations for the individual events. The choice of data used for the hypocentroid determines whether a converged relocation can be considered calibrated or not. For example, to relocate clusters in oceanic or remote continental areas lacking nearby seismograph stations, the hypocentroid might be located with teleseismic P arrivals. Such a cluster would not be considered calibrated, as the arrival time data would be biased by unknown Earth structure.

For this study, the hypocentroid was determined from direct-arriving local phases (Pg

and Sg) within 1.0° of each event in the cluster. Since the relative locations (cluster vectors) of all events have been determined in the first step of the relocation, these arrival times can be utilized to locate the hypocentroid as if it were an earthquake. Since the ray paths of the arrival time data used to establish the absolute location of the cluster (i.e., all the included events) are short, the biasing influence of unknown Earth structure is minimized. There is an obvious tradeoff between the limiting distance for data used to estimate the hypocentroid and the number of data used (and thus statistical power). The epicentral distance limit used here, 1.0°, is very typical for the calibrated clusters in GCCEL. To the extent that this distance range still encompasses significant lateral heterogeneity, the scatter introduced in the arrival time data will be reflected in the so-called empirical reading errors used for inverse weighting, and the parameter uncertainties will reflect that heterogeneity. Figure 2.4 illustrates this application of *mloc*.

The relocation process is iterative, both in a single run of *mloc*, but also in the sense that many runs are needed to properly deal with outlier readings and other sources of bias.

Treatment of Errors

Multiple event relocation allows for error treatment using the statistics of the arrival time data, which is not possible for single-event relocation. Errors in reported phase arrival times arise from multiple sources, including varying signal-to-noise levels, variations in analyst (or automatic) picking strategies, interference from multiple phases arriving close together, timing errors and differences in the precision to which arrival times are reported. At each run *mloc* produces an output file of the spread and mean of arrival times for each distinct station-phase pair ("empirical reading error"), using a robust estimator of spread. After the first run the empirical reading errors from the previous run are used for inverse weighting of the arrival time data. Empirical reading errors have a minimum value of 0.1 s so they cannot become unrealistically low.

It is essential to use a robust estimator of spread, meaning one that is insensitive to gross outliers, in this process so that outlier readings are exposed. *mloc* employs the "Sn"

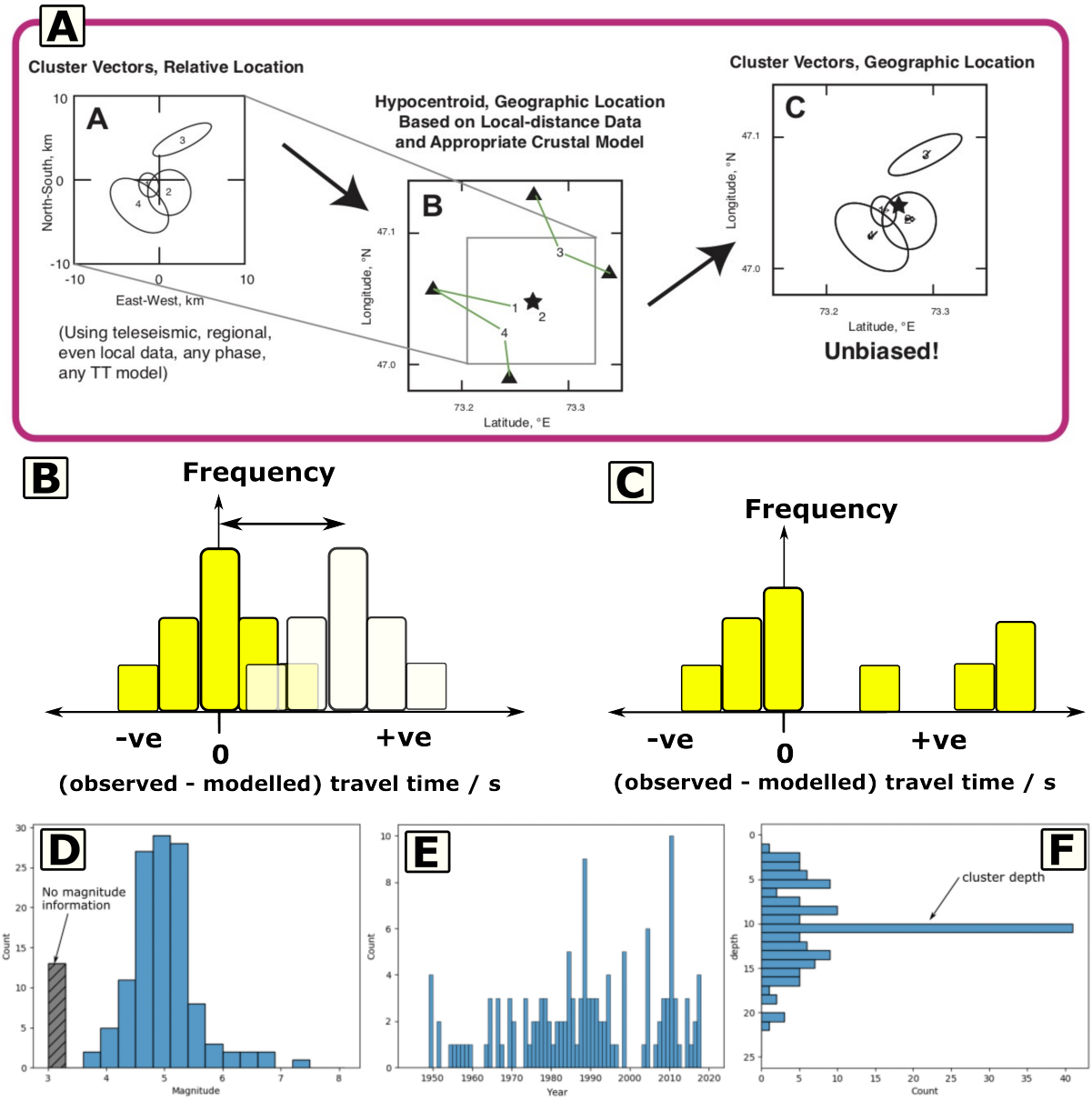

Figure 2.4: (A) Flowchart for the Hypocentroidal Decomposition Algorithm that *mloc* uses to determine calibrated locations. Calibration events are those with regional station data from the TIPAGE (2008-2012) seismometer deployment (Schurr et al. 2014). The calibration is then used to determine an unbiased location for the 1949 Khait Earthquake, despite there being limited contemporaneous seismometer coverage. (B&C) Sketch histograms of P phase arrivals for a station where many earthquakes in the cluster were recorded. (B) shows the case where there is a random error introduced by picking mistakes, and a systematic error introduced by a combination of picking strategies, consistent misidentification of a phase, and station timing error. These errors are automatically dealt with by the algorithm. In (C) we see the case where there is a systematic error affecting the phase arrivals, but it only affects some of the data. This is not dealt with by the algorithm and requires manual data cleaning using tools in *mloc*. Histograms for magnitude (D), year (E), and depth (F) are also shown. "Cluster depth" is the default depth.

algorithm (Croux and Rousseeuw 1992). Outlier readings are flagged in the event data files by the user between runs, either manually or with a utility program. This needs to be done gradually, taking only the greatest outliers each time, until the set of residuals for each station-phase approximates a normal distribution when normalized by the empirical reading error and mean residual (Fig 2.4b,c; Appendix A9). The mean residual is interpreted as the correction for whatever velocity model has been used to calculate the theoretical travel time for that station-phase, but this information is not relevant in *mloc*, except for the local-distance readings used for the hypocentroid, because all other arrival time data are utilized only as differenced travel times.

For the 1949 earthquake timing synchonisation errors to a world clock may have been an issue for some stations. We don't have a good idea of the magnitude of this uncertainty, but the HYPOSAT single event location analysis indicates that all residuals between observed and modelled travel times are of the order of 5 seconds (section 2.3.1). This suggests the timing errors arising from synchronisation problems are less than this. Assuming synchronisation errors between different stations that recorded the 1949 earthquake are independent, these would contribute to a larger location uncertainty, and not a systematic bias in the location. Therefore *mloc* likely deals with these synchronisation errors as well as any other random error described above.

2.3.3 Depth Control and Velocity Model

We use the ak135 global 1-D velocity model (Kennett et al. 1995) with a modified crust such that the travel time residuals in the distance range used for the hypocentroid are minimized (see Appendix A3). The crustal velocity model and event depths were refined during the initial runs with a set of events having especially good local data, with near-source arrivals (less than about 1.5-2.0 focal depths) to constrain focal depth. Once the crustal part of the model is established the crustal thickness is adjusted to fit the observed Pn arrivals. Once the velocity model is set, the depths of other events lacking near-source arrivals can often be usefully estimated. If events only have one or two direct arrival times $\sim$1 degree epicentral distance, and their depth can't be found using direct arrivals alone, another approach for depth constraint can be used. The 'Local Distance Method'

exploits the dominance of Pn arrivals in most event data sets. With epicenters stabilized by the abundance of data at all distances and azimuths, the Pn data tend to dominate the estimate of origin time, for a given assumed depth. If there are any direct crustal arrivals in the range beyond near-source but closer than the Pg/Pn crossover distance, their travel times are mainly influenced by the origin time, not focal depth, since for shallow events the raypath is nearly horizontal. Therefore shifting the focal depth causes changes in the residuals of those far-local arrivals in the same sense (but less precision) as for near-source arrivals, and thus gives a way to estimate focal depth. Focal depths determined in this way are vulnerable to the arrival time errors for the direct arrivals, as usually there are only one or two of these (Karasözen et al. 2016; Karasözen et al. 2019).
Depths can also be usefully estimated from teleseismic depth phases, various types of waveform modeling and fault models derived from InSAR data.

Event Selection

The cluster for this study includes 133 earthquakes that were large enough to have arrival time data at teleseismic distances from the ISC Bulletin (Storchak et al. 2017; Storchak et al. 2020) (Table 2.1). The bulk of arrival time data used for calibration came from the TIPAGE and TIPTIMON seismic deployments (Kufner et al. 2018a; Schurr et al. 2014). The TIPAGE deployment consisted of 40 stations in the Tajik Pamir and lasted 2008-2010; the TIPTIMON deployment consisted of 25 stations deployed within the Tajik Basin and southern Pamir from 2012-2014. In both deployments the station spacing ranged from *sim* 20-60 km. For the 1949 Khait Earthquake, historical seismogram digitisation described in Section 2.3.1 provided the bulk of the arrival times. Arrival time data for early aftershocks of the 1949 event was hand digitized from the ISS bulletin (Villaseñor and Engdahl 2005).

We prioritized an even time distribution of events in order to strongly link the locally-recorded events of 2008–2010 to the 1949 earthquake (Figure 2.5B). We chose events on the basis of having >100 phase arrivals rather than magnitude, as some of the pre-1960 events lacked magnitude information. This cluster included all events with a gCMT focal mechanism (Dziewonski et al. 1981; Ekström et al. 2012) and provided a magnitude range

of M_w 3.8–6.9 (Figure 2.5A). We also prioritized events close to a regional seismometer as this gave us better depth control (see Section 2.3.3). Where no depth control was possible, we assigned a default cluster depth of 10 km (Figure 2.5C). This does not affect the epicentral estimate when there is good azimuthal coverage, as any bias in depth is compensated in the origin time(Shearer 2019, p. 127).

Relocation Strategy

Because of the large changes in the constellation of observing stations across this cluster, we adopted a gradualist strategy for the relocation, beginning with a set of seven events, ranging in magnitude from 3.7–5.1, that were closely observed by the TIPAGE deployment between October 2009 and May 2010; they were also recorded by regional and teleseismic stations. In the process of relocating these events, which have good depth control from near-source stations, the crustal velocity model was also refined.

Starting from this kernel of well-located events, the cluster was gradually expanded by adding the events nearby in time. At each increment in building the cluster, several runs are used to refine the hypocentral parameters and arrival time datasets, flagging outliers and estimating empirical reading errors. The final calibrated hypocenters of the cluster are listed in Table 2.2.

2.3.4 Geomorphic Analysis

We acquired high-resolution stereo optical satellite imagery and DEMs of the Vashkh fault and the 1949 epicentral region, in order to identify evidence of recent fault slip, to measure scarp heights, slip vectors, and to map out geomorphic units displaced by faulting. We used 0.3 m Worldview 3 stereo and 0.5 m Pleiades tri-stereo imagery. Point clouds for the satellite DEMs are available for download on OpenTopography.

The DEM construction approach uses the disparity between satellite images taken from different positions of the same point, disparity being the vector required to map a pixel from one image onto the equivalent pixel in the other image. Position, orientation and camera model are read from the Rational Polynomial Coefficients (RPC)s supplied with the imagery. Once the RPC model is accounted for, the remaining disparity in the images

is assumed to be stereoscopic distortion from topography and can be used to construct a 3D point cloud. This can be gridded based on the average point height inside a cell to produce a DEM. The hillshaded DEM is then used for mapping and profiling possible fault scarps. The Pleiades imagery was processed using Agisoft Metashape Professional version 1.6. The Worldview 3 was processed with the NASA Ames Stereo Pipeline version 2.6.2 (Beyer et al. 2021; Beyer et al. 2018; Shean et al. 2016). Gridding at a higher resolution allows us to resolve small scale features in the point cloud, but also increases the noise in the DEM, so care is required when interpreting features.

For Ames Stereo Pipeline, we first orthorectify the raw stereo images using the JAXA AWd30 Digital Elevation model (Tadono et al. 2014; Takaku et al. 2014). This removes most of the disparity from the image pair, and allows us to use a smaller search area when correlating features between images, increasing reliability and reducing computing time. We then use ASP's MGM algorithm with a 7x7 correlation kernel and subpixel refinement to determine the remaining distortion in the images. The result is then gridded to 0.5 m resolution and smoothed using a 9x9 pixel median filter, and outlier point removal based on triangulation error (see Appendix A3 for processing parameters). For regions of particular interest, we rerun the above at 0.3 m resolution. We project the DEMs and orthoimages into the WGS84 / UTM zone 42N coordinate reference system (EPSG:32642) to allow us to make accurate meter-scale measurements.

For analysis of faulting we use the orthorectified optical imagery to identify surface ruptures and measure any offsets observable in the DEM. For measuring offsets we use the Measure Line tool in QGIS 3.28.3 using EPSG:32642 UTM Zone 42N. We manually measure lateral offsets due to the high gradients on the surfaces and DEM noise which preclude use of automatic tools such as LaDiCaoz (Zielke and Arrowsmith 2012). We estimate uncertainty by manually fitting the maximum and minimum possible offsets on streams using the orthoimagery (e.g. Figure2.10). For vertical displacements we fit footwall and hangingwall surfaces using linear regression and use the difference in intercepts at the fault trace (Tsai et al. 2022).

Mapped active faults are assigned a confidence level (1=high,2=moderate,3=low). High level confidence refers to linear traces that are clearly visible and are either associated

with offset landforms, are nearby along strike of offset landforms, and may also be associated with springs. Moderate confidence indicates a linear feature which aligns with high confidence features. Low confidence features appear visually similar to faults, but may also align with bedrock geological structures and so scarps may relate to differential erosion of bedrock, rather than active faulting.

Table 2.2: *mloc* relocated events. Depth constraint codes: c: fixed at arbitrary depth; d: depth fixed with teleseismic depth phases; m: mloc solution with free depth; n: depth fixed using near source direct arrivals; l: depth fixed using local distance method (described in Section 2.3.3); Calibration code (how constrained is the location): CH01-best; CH05-worst

Event number	Date	Time	Long	Lat	Depth	Strike	Dip	Rake	Magnitude	Depth constraint	Calibration code
1	10/07/1949	03:53:37	70.87061	39.3366	22	50	80	-20	7.6M_w	l	CH04
2	10/07/1949	14:13:21	71.26403	38.9969	10				5.0ml	c	CT04
3	10/07/1949	15:49:13	71.39584	39.21076	20				6.7MS	l	CH04
4	10/07/1949	16:24:01	71.10634	39.25517	20				6.5Ms	l	CH05
5	14/04/1951	04:10:06	71.65266	39.11131	15				-	n	CH04
6	12/05/1951	22:07:52	71.35382	39.55589	15				5.3MS	l	CH06
7	18/08/1954	23:32:11	70.67238	39.11505	15				-	l	CH05
8	15/06/1955	01:03:56	71.57675	39.17804	15				5.2MS	n	CH05
9	11/04/1956	01:45:12	70.38085	38.88154	15				-	n	CH05
10	13/01/1957	11:38:17	70.60721	38.789	10				-	n	CH03
11	07/01/1958	06:05:09	70.40051	38.92502	10				-	n	CH02
12	31/07/1959	19:53:03	70.48573	38.89856	10				-	n	CH02
13	16/03/1963	22:28:50	71.77883	39.08796	54				-	l	CH03
14	24/10/1964	06:50:56	70.76353	38.68794	15				-	l	CH04
15	25/10/1964	22:56:05	70.77611	38.69069	28.7				-	n	CH04
16	02/12/1964	12:31:40	70.66577	38.90327	33				4.7mb	n	CH07
17	11/04/1966	16:42:50	70.61553	39.00357	10				-	n	CH04
18	14/04/1966	21:06:14	70.59585	38.94022	10.3				-	n	CH03
19	06/07/1966	11:57:22	71.3672	39.04672	15				-	l	CH05
20	08/09/1967	05:23:40	70.48121	38.45464	12				4.9mb	l	CH05
21	22/03/1969	04:52:33	70.56975	38.93353	10				5.3mb	n	CH03
22	27/03/1969	11:19:25	71.81149	39.1282	20				4.9mb	l	CH04
23	27/03/1969	19:37:41	71.81734	39.16763	20				4.6MS	l	CH04
24	09/10/1970	13:48:47	71.53075	39.19212	10				-	l	CH03
25	08/12/1970	11:53:14	70.29964	38.8334	10				4.5mb	n	CH06
26	03/01/1973	14:31:02	71.8851	39.17562	27.4				5.5mb	n	CH02
27	03/01/1973	15:05:12	71.90237	39.1811	20				4.8mb	l	CH06
28	13/09/1973	06:40:33	70.55489	38.93078	9.2				4.5mb	n	CH04
29	29/12/1974	04:59:01	71.67186	39.24657	15				5.2MB	l	CH03
30	09/06/1975	18:36:46	70.30393	38.90781	3.6				5.1mb	n	CH03
31	02/10/1975	19:33:44	71.53063	39.20663	15				4.3mb	l	CH04
32	10/07/1976	10:21:21	70.66452	39.29765	32				5.2mb	c	CT03
33	03/09/1976	21:52:41	70.71432	38.9613	9.9				5.1mb	l	CH03
34	01/06/1977	20:07:26	70.24838	38.67493	0				4.5MB	l	CH05
35	20/06/1977	03:07:38	71.22997	38.96185	0				4.5MB	l	CH06
36	25/12/1977	16:18:50	70.70458	38.94938	2.9				5.4MB	n	CH04
37	15/06/1978	17:00:06	71.64034	39.30632	33				4.9MB	c	CT04
38	26/09/1978	19:21:46	70.76115	38.99837	10				5.1MB	l	CH03
39	30/12/1978	05:06:54	70.58215	38.50185	10				4.9mb	l	CH03
40	16/04/1979	04:56:17	70.58546	38.86304	11.9				4.8MB	c	CT05
41	20/10/1979	19:40:39	70.61967	39.01075	13.4				4.7mb	l	CH03

Event number	Date	Time	Long	Lat	Depth	Strike	Dip	Rake	Magnitude	Depth constraint	Calibration code
42	17/01/1980	22:47:13	71.6597	39.29582	3				5.0MB	c	CT05
43	19/03/1981	09:59:44	70.33974	38.9182	3				4.7Mb	l	CH03
44	14/04/1981	03:03:00	71.63194	39.10764	20				5.1Mb	c	CT05
45	23/02/1982	21:09:49	71.92982	39.31759	33				4.8MS	d	CH04
46	15/04/1982	16:15:35	71.75262	39.41529	20				4.7Mb	c	CT05
47	06/04/1983	22:18:44	71.42824	38.896	5				5.3Mb	l	CH02
48	01/10/1983	07:15:16	70.49506	38.83492	3				4.9Mb	n	CH03
49	19/02/1984	13:57:50	70.43224	38.95599	3				4.5Mb	c	CT05
50	26/10/1984	20:22:18	71.33522	39.25227	3	37	77	9	6.1M_w	l	CH02
51	26/10/1984	21:33:34	71.3146	39.25652	3				5.1Mb	l	CH03
52	27/10/1984	00:47:30	71.4117	39.24921	34				4.3Mb	c	CT04
53	30/10/1984	22:55:24	71.29742	39.27645	43				4.8Mb	c	CT05
54	06/01/1985	01:06:10	71.33633	39.22615	10				4.7Mb	n	CH02
55	16/03/1985	09:12:45	71.39088	39.25253	3				5.1Mb	n	CH02
56	01/10/1985	17:17:55	70.47604	39.25897	3				5.0Mb	n	CH03
57	31/10/1986	11:24:37	71.40377	39.24342	15.4				4.8Mb	n	CH03
58	23/02/1987	00:21:17	70.61222	38.99633	3	173	55	36	4.9M_w	l	CH03
59	17/07/1987	17:23:23	70.70097	38.95215	3				5.0Mb	l	CH04
60	21/12/1987	04:28:23	70.74636	38.84312	3				5.1Mb	l	CH02
61	09/01/1988	03:55:01	71.50925	39.17878	3	275	41	148	5.1M_w	l	CH02
62	10/01/1988	02:34:35	71.52753	39.18367	10				4.8Mb	c	CT03
63	28/01/1988	18:05:56	71.90644	39.20758	3				4.7Mb	l	CH02
64	16/05/1988	06:05:41	71.20319	39.25649	29.6				4.7Mb	c	CT04
65	30/05/1988	20:48:51	71.13059	39.25717	3				4.5Mb	c	CT05
66	10/06/1988	21:11:13	71.66122	39.26106	3				5.1Mb	c	CT03
67	20/09/1988	14:41:39	71.37408	38.54937	3				4.8Mb	l	CH03
68	03/10/1988	00:24:46	70.75941	38.75999	3				5.0Mb	l	CH02
69	14/12/1988	11:45:55	71.75731	39.30695	3	3	51	127	5.3M_w	l	CH02
70	03/05/1989	19:59:16	70.72493	39.05821	3				5.1Mb	l	CH02
71	01/07/1989	18:27:09	71.55833	39.21179	10				4.9Mb	c	CT03
72	06/11/1989	19:42:31	71.65889	39.31899	3				5.1Mb	l	CH04
73	30/09/1990	21:22:58	70.90736	38.9707	3				5.2Mb	l	CH02
74	03/11/1990	16:39:51	71.39521	39.11377	3	215	33	67	5.4M_w	l	CH02
75	11/11/1990	03:19:41	71.8169	39.33453	3				5.3Mb	c	CT03
76	26/02/1991	07:28:42	71.62002	39.36655	10				4.9Mb	c	CT04
77	03/03/1991	18:08:59	71.63497	39.2776	3				5.3Mb	c	CT02
78	26/04/1991	22:24:00	70.95485	39.02845	10	193	43	46	5.2M_w	l	CH02
79	11/01/1992	20:09:18	70.60247	38.86383	16.6				4.8mb	l	CH03
80	27/12/1992	21:09:35	71.74422	39.63576	33				5.0Mb	c	CT04
81	08/08/1993	22:41:42	70.4263	38.68899	3				4.9mb	c	CT04
82	02/10/1993	01:17:29	70.00493	39.06828	14.2				5.0mb	c	CT04
83	10/02/1994	02:24:34	71.59596	39.2171	10				5.1mb	c	CT04
84	01/05/1994	21:17:17	71.6433	39.25938	16	1	24	60	5.2M_w	c	CT03
85	04/05/1994	10:40:12	70.30777	38.89116	9.6				4.6mb	c	CT04
86	10/06/1994	03:00:42	70.55871	38.77624	16				5.2mb	c	CT03
87	20/02/1995	04:12:23	70.95072	39.30802	20.2	1	71	-6	5.3M_w	d	CH03
88	23/11/1996	01:56:53	70.76528	39.04081	15				4.7mb	c	CT04
89	05/03/1998	23:58:40	71.63692	38.89764	17.6				5.1mb	c	CT03
90	23/03/1998	10:11:49	70.74047	38.93106	15				4.3mb	c	CT05
91	14/06/1998	14:12:04	70.20366	38.67724	10.6				4.5mb	d	CH05
92	11/09/1998	05:53:49	70.33167	38.84949	35				4.7mb	c	CT03
93	22/09/1998	01:08:21	71.41234	39.11301	15				4.6mb	c	CT04
94	13/07/2003	14:36:15	70.56624	38.8916	32				4.7mb	c	CT04
95	20/10/2004	11:57:49	70.47137	38.55699	0				5.2mp	c	CT02
96	17/11/2004	07:34:25	71.73488	39.26509	33	195	83	4	5.1M_w	c	CT03
97	17/11/2004	20:58:19	71.80075	39.24652	14	185	88	-1	5.8M_w	c	CT02
98	18/11/2004	02:30:35	71.77162	39.22501	10	49	75	-5	5M_w	c	CT02
99	18/11/2004	21:18:52	71.8633	39.17276	0	201	63	18	4.8M_w	c	CT02
100	21/11/2004	20:45:20	71.77027	39.19962	0	322	42	-105	5M_w	c	CT02
101	06/07/2006	03:57:50	71.79269	39.16844	0	283	59	146	5.8M_w	d	CH02
102	02/02/2007	22:02:42	71.33539	39.07028	0	213	45	58	5.2M_w	c	CT02

Event number	Date	Time	Long	Lat	Depth	Strike	Dip	Rake	Magnitude	Depth constraint	Calibration code
103	31/07/2007	02:47:05	71.34367	39.1237	16	50	41	83	5M_w	d	CH03
104	29/09/2008	13:15:13	70.29797	38.86585	7.4				3.8mb	n	CH02
105	13/10/2008	17:16:09	70.35134	38.69936	10.4	47	28	128	5.3M_w	l	CH02
106	13/10/2008	17:35:44	70.34377	38.72358	10.4				4.2mb	l	CH02
107	25/05/2009	15:18:52	70.57591	38.85828	12.6				4.8mb	m	CH02
108	26/08/2009	07:26:37	70.65869	38.96666	12.3	83	79	178	4.9M_w	m	CH02
109	13/10/2009	12:47:15	70.7757	38.72603	14.8	47	86	3	5.1M_w	m	CH02
110	02/01/2010	02:15:04	71.45055	38.28074	7.3	232	58	-24	5.5M_w	m	CH02
111	14/02/2010	20:32:43	71.73	39.70472	13.7				4.0mb	m	CH02
112	21/02/2010	02:05:18	71.44749	38.24696	8.6				3.9mb	m	CH02
113	28/02/2010	01:01:31	71.43404	38.29802	6.4				4.3mb	m	CH02
114	25/04/2010	01:13:54	71.45145	38.24351	7.2				3.7mb	m	CH02
115	14/05/2010	07:02:08	71.42536	38.31184	5.7				4.0mb	m	CH02
116	04/07/2010	01:56:47	70.34364	38.85169	0				4.4mb	l	CH02
117	20/08/2010	16:57:13	71.82544	39.30531	0				5.3mb	l	CH02
118	07/10/2010	01:40:03	70.26825	39.22232	5				4.4MS	l	CH02
119	09/10/2010	10:15:14	70.288	39.23854	10				4.7mb	l	CH02
120	11/10/2011	01:17:14	70.57779	38.83686	0				4.8mb	l	CH03
121	05/11/2011	03:22:26	71.78772	39.4027	12.8				4.3MS	l	CH03
122	29/12/2011	15:27:17	70.72045	38.67907	42.4				4.3mb	c	CT03
123	12/05/2012	23:28:41	70.35395	38.66795	0				6.8mb	c	CT02
124	01/02/2014	08:31:17	70.5445	38.87171	10.1				4.1mb	n	CH02
125	29/08/2014	01:03:59	71.5763	39.21823	15	92	61	156	4.9M_w	l	CH02
126	01/10/2014	03:12:51	70.4751	38.87388	0				4.0mb	l	CH03
127	20/05/2015	03:31:40	70.19637	38.64161	0	78	26	155	5.2M_w	n	CH02
128	17/02/2016	23:58:01	71.42539	39.10115	24.3				4.4mb	n	CH02
129	24/03/2016	08:37:34	70.70731	38.98664	17.3				4.8mb	l	CH02
130	15/01/2017	13:18:09	70.76455	39.05527	12				4.4mb	n	CH03
131	03/05/2017	04:46:53	71.40902	39.52523	0				4.5mb	n	CH03
132	03/05/2017	04:47:11	71.47045	39.47744	5				6.4MS	n	CH02
133	03/05/2017	20:03:10	71.50573	39.50698	5				4.6MS	n	CH02

2.4 Results

2.4.1 Regional seismicity and source parameters of the 10th July 1949 Khait earthquake

We used digitized analogue seismograms to model the focal mechanism for the 1949 mainshock, as described in Section 2.3.1. We find that the earthquake had a strike slip mechanism of strike 50 ± 20, dip 80 ± 10 and rake -20 ± 10 (Figure 2.5). The mechanism's PT axes show north-south compression: consistent with the pattern represented by other moderate magnitude earthquakes in the region, and agreeing with geological and geodetic observations of N-S compression (Leith and Alvarez 1985; Metzger et al. 2020). We calculated surface wave, body wave and moment magnitudes of Surface Wave Magnitude (M_S) 7 8 ± 0.4, m_B 7.6 ± 0.2, and M_w 7.5 ± 0.2. These are slightly higher than previous

magnitude estimates (see Table 2.2).

We improved the 1949 epicentral location, producing a catalog of 133 well located events within 1 degree distance of Khait, spanning 1949 to 2020, as described in Section 2.3.2 (Figure 2.1b, 2.5). These events are presented in Table 2.1. We find the 1949 mainshock occurred further north than previously reported, north of the Obi-Khabud valley (Figure 2.5A) at 39.336 °N, 70.870 °E. The formal uncertainties from *mloc* are around ∼5 km, but this represents a lower bound. The depth of the 1949 earthquake hypocentre is 22 ± 4 km and is derived using the local distance method in *mloc*, described inSection2.3.3. This is backed up by a weak depth constraint from the focal mechanism inversion of ∼24 km (seeSection2.3.1 and Figure 2.3). It is around the base of the seismogenic layer, as understood from microseismicity studies (Schurr et al. 2014).

The initial estimate of the source time duration for the Khait earthquake was derived from the P-wave duration observed in teleseismic records from European stations. The P-wave records for the Z components of these European stations (refer to Figure 2.3B) were aligned and stacked to create a normalised summation trace (SUM_Z, as shown in Figure 2.3B, top). This stacked trace indicates that the source duration is between 25 and 35 seconds (highlighted in red). A visual inspection of the trace does not reveal a definitive single value for the source time duration; therefore, we refer to it as a range.

We were not able to accurately locate the 1941 M∼6.4 earthquake discussed inSection2.1 using *mloc*. We will now describe the key patterns visible in the 133 well located earthquakes and discuss their significance.

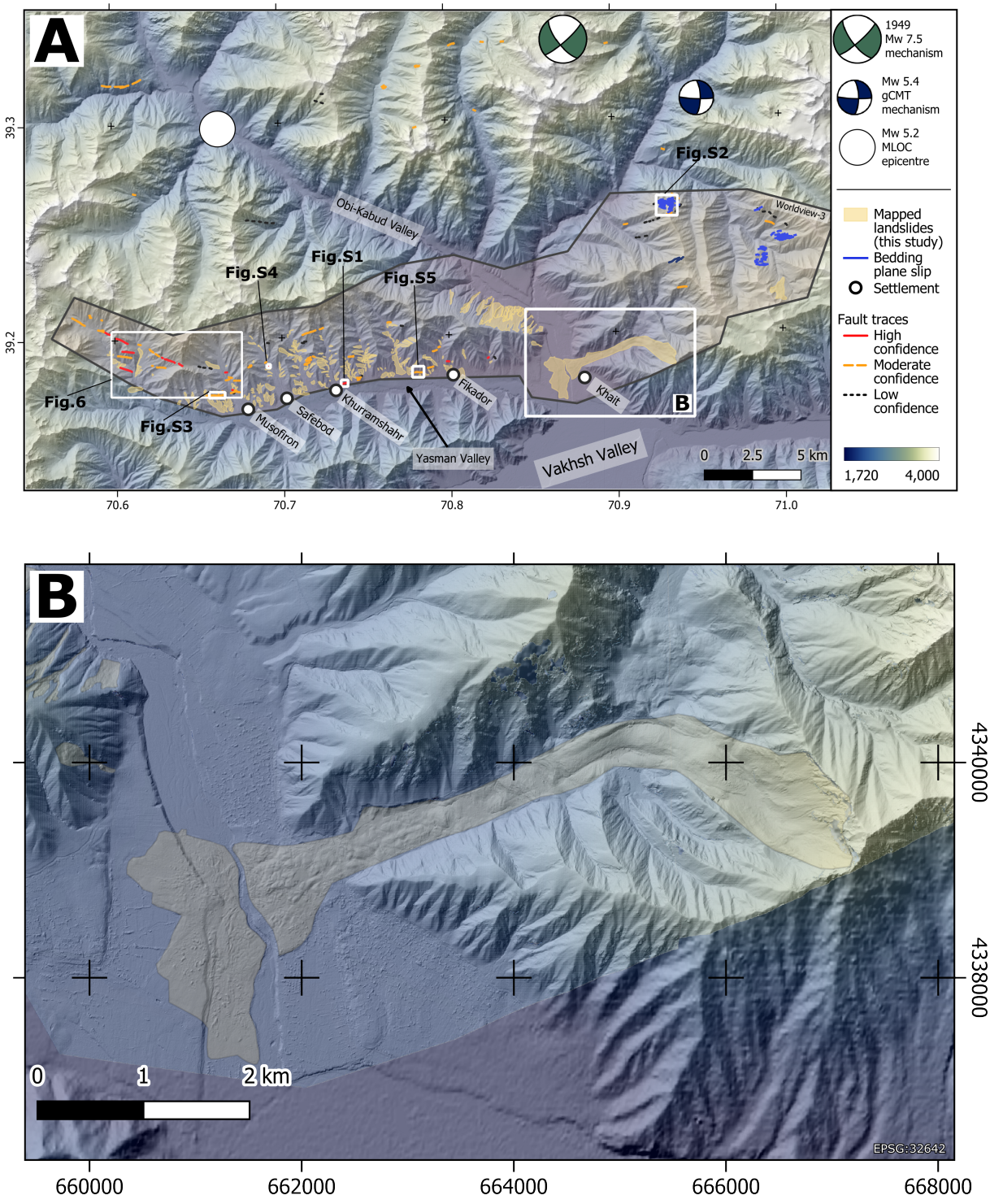

Figure 2.5: Mapped surface ruptures in the Vakhsh Valley. *mloc* relocated earthquakes are shown, including the M_w7.4 1949 Earthquake, these indicate the site of rupture initiation. The focal mechanism provides an average radiation pattern for the duration of the earthquake. The Worldview 3 0.3 m satellite imagery and DEM is shown by the pink polygon. Mapped surface ruptures are categorised into confidence levels and recent landslidesare mapped. We observe clear surface ruptures in the western end of the Vakhsh valley and can trace these east along the northern side of the valley to the town of Khait. East of Kahit, we find parallel scarps which may be bedding plane slip or sackungen (Appendix A5). (B) Close up of the Khait landslide, triggered by the 1949 Earthquake, which covered large parts of the towns of Khait.

In the western part of the cluster, the seismicity forms an ellipse with long axis roughly parallel to the Vakhsh valley (Figure 2.7A-1). In cross section, the earthquake hypocentres align along a plane dipping south at $\sim 50^{\circ}$ which intersects with the Vakhsh Fault surface trace. This alignment appears robust, as our depth errors are less than ∼5 km and the focal mechanism planes align with this 50° dipping plane. We interpret the 50° plane as a thick-skinned component of thrusting. Focal mechanisms show right lateral oblique thrusting on planes striking WSW-ENE, sub-parallel to the Vakhsh Thrust surface trace. This sense of motion agrees with GNSS and InSAR data (Metzger et al. 2020; Metzger et al. 2021).

Between (71°E, 39°N) and (71.3°E, 39°N) (Figure 2.7), where the Darvaz and Vakhsh faults converge, there is a ∼30 km long region where we do not observe earthquakes (Figure 2.1B). This behaviour may be due to lateral variability in the properties of the Vakhsh Thrust décollement, with varying proportions of seismic to aseismic slip. It may also be due to our catalog being incomplete and so not capturing the full earthquake cycle on all parts of the fault.

East of this, at (71.4°E, 39.1°N) (Figure 2.7-II) there are three thrust mechanisms, striking northeast-southwest, one of which occurred in 1990 (M_w 5.9) and two in 2007 (M_w5.5 and M_w 4.9). These are collocated with a linear east-west earthquake rupture visible in open-source imagery. Given the similarity in strike we believe these surface ruptures are either related to these earthquakes, or previous earthquakes on the same faults. We acquired a polygon of Pleiades imagery to investigate these ruptures (Figure 2.8, Section 2.4.2).

Further east, there are two distinct groups of earthquakes. One group (centre 71.6°E, 39.2°N) (Figure 2.7A-2) trends northeast, and appears to be the continuation of the three thrusts discussed above. The mechanisms are oblique left-lateral thrusts. The other group (centre 71.7°E, 39.2 °N; Figure 2.7A-3) trends north-south and is predominantly composed of right-lateral strike slip earthquakes, but also contains both a reverse and

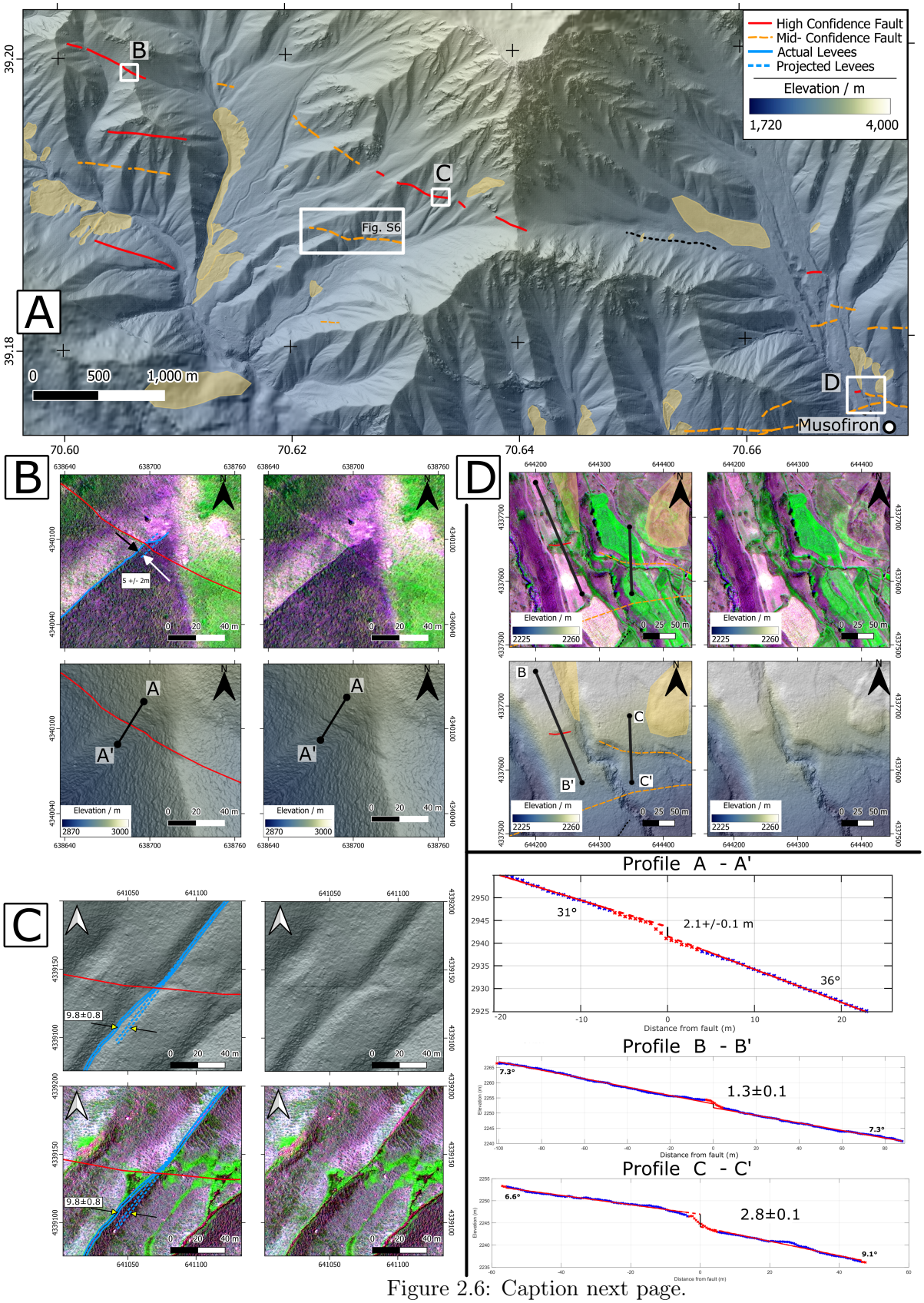

Figure 2.6: Caption next page.

Figure 2.6: (Previous page) (See Figure 2.5 for location) (A) Dip-slip and right-lateral strike-slip ruptures in the upper western end of the Yasman Valley. We observe a scarp crossing a wine-glass shaped drainage at (39.1991°N,70.6059°E), which is not deflected by topography, implying a steep fault dip. This crosses a smaller drainage showing a 5 m right-lateral stream deflection (B). In the hill-shaded DEM we measure a 2.1 m dip-slip offset in the western wall of the drainage consistent with a right-lateral fault (profile A-A'). Further east, at (39.18999°N,70.63390°E) we observe a scarp in the hillside, picked out by the areas of high Near-Infrared (green) in the false colour images (C). We interpret this to mark vegetation along springs associated with the fault. By projecting stream levees downhill we measure a right-lateral stream deflection of 9.8 m. Finally, at (39.17609°N,70.67037°E) north of the village of Musofiron, observe a scarp running across two different surfaces (D). Along profile B-B' we measure 1.3 m dip slip offset and along C-C' we measure 2.8 m dip-slip displacement. The disparity between these offsets may be due to B-B' scarp being modified to make the field boundary and canal, or could represent multiple earthquakes.

normal earthquake. Taken together with the wide range of geologically-derived PT axis orientations in this area (Kufner et al. 2018a), these mechanisms indicate a complex zone of faulting likely due to the intersection of the Vakhsh, Darvaz and Pamir Frontal Thrust Faults.

At the confluence of the Kyzyl-su and Muksu rivers (71.4°E, 39.2°N; Figure 2.7A-4) there is an alignment of epicentres trending WNW for ∼50 km from the Vashkh river valley in the east, to the 1949 mainshock at its western end. The three largest earthquakes in the group are the 1949 M_w 7.6 earthquake, and the two largest aftershocks which occurred on the same day M_S 6.7 and M_S 6.5. These are followed by a sequence which unfolded over the period 1984-88, culminating with an earthquake in 1995 that is SE of the 1949 event. This alignment in seismicity may represent activation of a tectonic structure, the full length of which was activated in 1949. We were not able to find surface ruptures in the open-source imagery, though this was either low resolution or obscured by snow.

2.4.2 Geomorphology of the 1949 Khait epicentral zone

In this section we assess geomorphic evidence for active faulting, both along the Vashkh fault itself, and also in the regions surrounding our relocated epicenter and in the regions of highest seismic intensity (Figure 2.1A). We analyse DEMs derived from 70 cm Pleiades optical satellite data along the Vashkh fault (region shown in Figure 2.8) and 30 cm Worldview 3 optical imagery on the north-side of the Yasman valley, where the largest

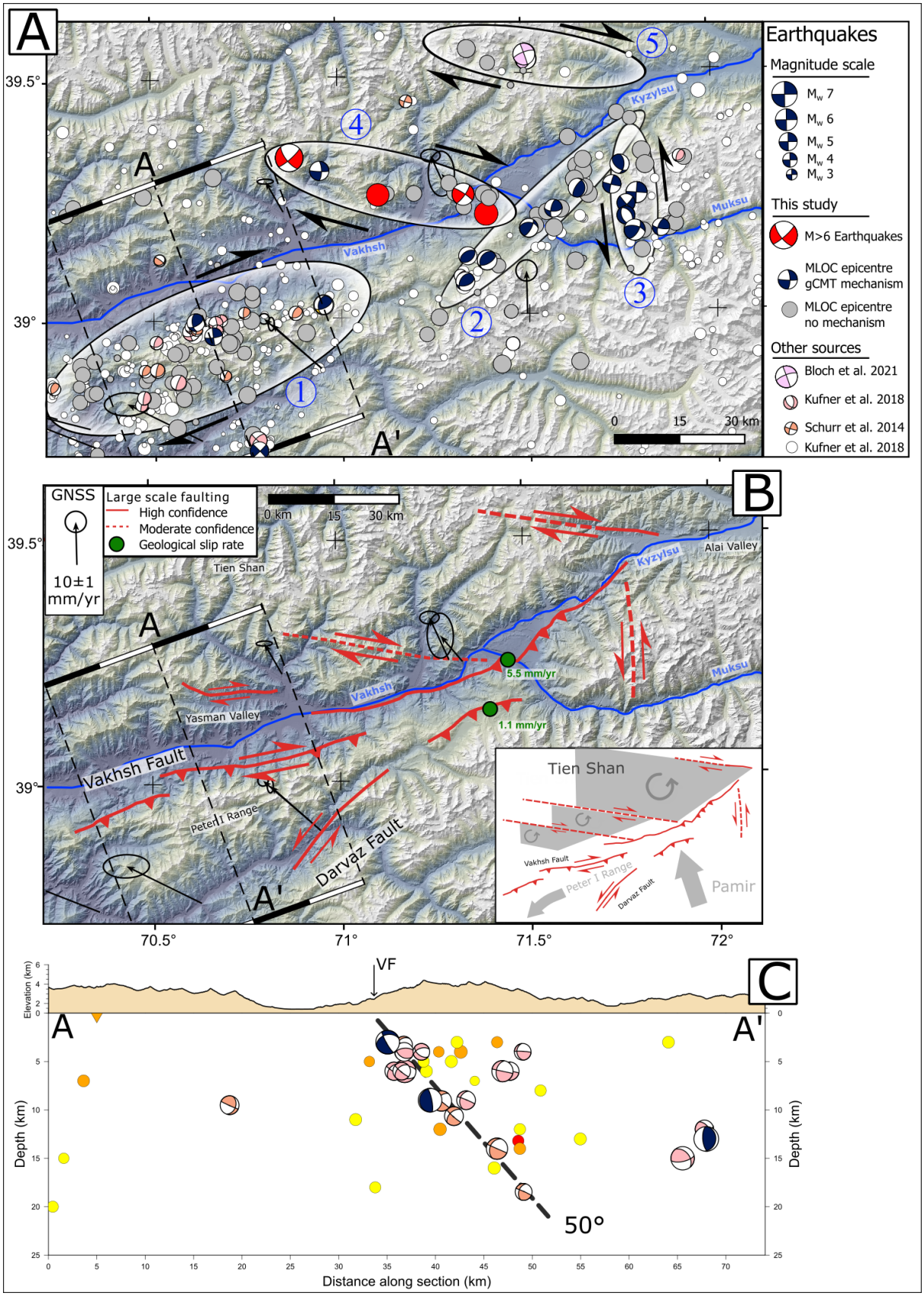

Figure 2.7: (Caption next page.)

Figure 2.7: (Previous page) Interpreted version of Figure 2.1. (A) MLOC-relocated epicentres and mechanisms grouped into clusters discussed inSection2.5.1. (B) Interpretation of tectonic regime based on our relocated earthquakes and geomorphic mapping. High confidence faults are those for which we have geomorphic evidence, moderate confidence faults are those we have inferred based on epicentre and mechanism alignments. Geologic slip rate sites (green circles) suggest only half the geodetic slip rate is accommodated by the Vakhsh Fault. We suggest that in addition to the already known Vakhsh and Darvaz Faults, there exist a set of NW-SE trending right-lateral faults within the Tian Shan accommodating part of the convergence between the Pamir and Tian Shan. This is in contrast to previous tectonic models which localise this motion on the Vakhsh Fault. (C) Cross section showing MLOC-relocated events. Epicentres with the better depth control are shown in hotter colours. We interpret the shallow plane to be the decollement between the Peter I Fold and Thrust Belt and the basement, with the steeper plane accommodating thick-skinned deformation.

macroseismic intensity was observed (Figure 2.6).

Vakhsh Valley

The Vakhsh Fault runs along the southern side of the Vakhsh Valley and is left-stepping. Large scale dip-slip offsets are visible, likely accumulated over many earthquake cycles (Figure 2.1C). Past literature has proposed the 1949 Khait Earthquake was hosted on the Vakhsh Fault. We examined the region between the Muksu River and the Obikhingou River (Figure 2.1C) using Open-Source imagery for signs of single-event earthquake ruptures consistent with this. We identified two possible sites and acquired high-resolution satellite imagery over the most promising of these. This was then used for 0.5 m DEM construction. For the other sites we rely on freely available 30 m DEMs and Open Source Imagery.

Firstly, we identify two scarps that displace lateral moraines near Sary Tala (71.429°E, 39.246°N) and alluvial fans near the Karakendzha (71.494°E, 39.250°N) (Figure 2.9). The heights of these scarps are very similar: 76 ± 4 m at Sary Tala and 74 ± 1 m near Karakendzha, implying the two displacements formed by a fault which bends/steps east as it crosses the Musku River. The moraines at Sary Tala are aged ∼18 kyr according to cosmogenic exposure dating of boulders (Grin et al. 2016). The alluvial fans near Karakendzha have not been dated, but must be younger than the Sary Tala moraines assuming the scarp began growing after the glacier retreated. The Karakendzha alluvial fan offsets peter out north-westwards, possibly due to sedimentation from the Dara River. However

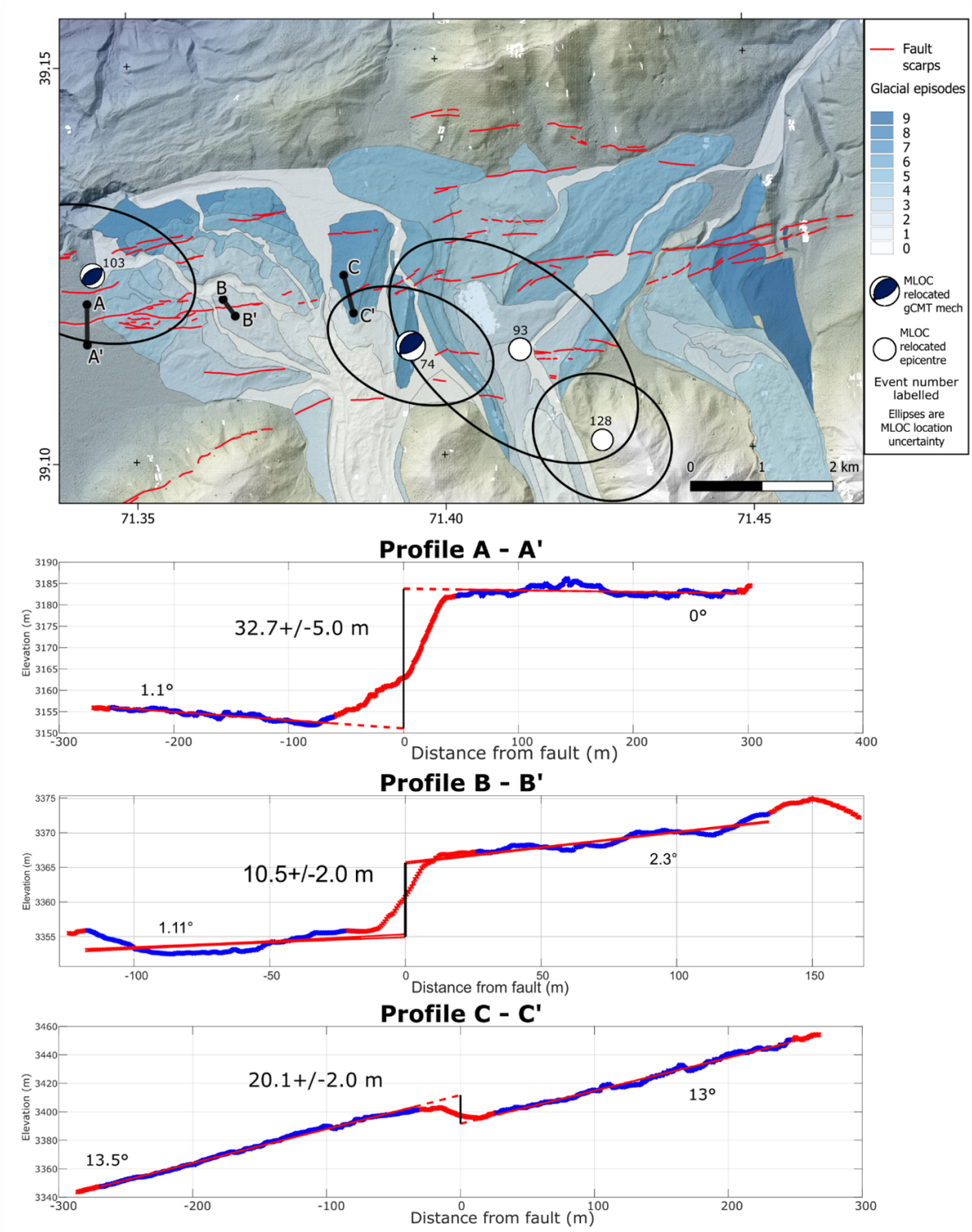

Figure 2.8: Pleiades-derived DEM showing glacial moraine complex on the south side of the Vakhsh Valley cut by linear, right-stepping scarps. There are progressive offsets in the older moraine sediments, implying multiple events on the fault. These scarps sit south of kilometre scale folding which is likely tectonic, and so we suggest are near-vertical splays whose motions no not reflect the underlying tectonic stresses. This is backed up by the mechanisms which are relocated using *mloc* to beneath the scarps.

a scarp becomes clear again near the town of Dzhaligan where it bounds the mountains from the Kyzyl-Suu river valley. This continues eastwards and presumably joins the Pamir Frontal Thrust.

We also identify active fault traces within a glacial moraine complex on the south side of the Vakhsh valley. The moraines are cut by scarps younger than the Last Glacial Maximum (LGM) (∼17 ka). We acquired 0.5m Pleiades imagery and DEMs over this area (Figure 2.8). It is within a high valley ∼1000 m above the Vakhsh Valley floor and divides the Peter I Range and the wider Pamir mountains. This site contains the divides between three major catchments, with rivers flowing into the Muksu River (east) the Vakhsh River (north) and into the Obikhingou River (west). At the base of the valley are a complex of glacial moraines, fed in the past by three small glaciers to the south. During the LGM, these glaciers likely filled this small valley and flowed into the Obikhingou catchment. Evidence for this is a WSW-oriented lateral moraine pair perched in the Obikhingou Catchment at (71.199°E, 39.033°N). Today, we observe a complex set of glacial moraines in the flat valley, representing about nine advances. These glacial deposits are cut by linear scarps which are co-located with thrust earthquake mechanisms described in Section 2.4.1 (Figure 2.7A-2).

Within the field of discontinuous scarps, we identify a prominent east-west scarp traversing undulating but overall low-relief glacial terrain, and make three profiles through this scarp in different surfaces (Figure 2.9). It is near-continuous for ∼10 km and has a straight trace even across highly undulating ground, suggesting a steeply-dipping (near vertical) planar slip surface. It contains both up- and downhill facing scarps, and a right-stepping en-echelon arrangement of scarps suggestive of a near-vertical strike-slip fault (McCalpin et al. 2009). However, direct lateral offsets of gullies and ridge crests are not clear. The scarps traverse multiple generations of moraine deposits. They are clearly expressed in the youngest geomorphic surfaces and are higher in older moraines (Figure 2.8). Two possible interpretations for these scarps exist. One is that they are backthrusts of the Vakhsh Thrust, as in Schultz (2000), where overburden of the fold and thrust belt forces a gravitational collapse in the back of the fold. This could be aided by the steeply dipping bedding of the geology in the area. Another possibility is that they are a thrust-termination of the Darvaz Fault. As the left-lateral Darvaz fault bends from a NE-SW

orientation to an E-W orientation, an unchanged slip vector would result in a change from strike-slip to thrust motion.

The final example of recent scarps is further west at (70.8125°E, 39.0256°N) (Figure 2.10). The hillslopes here are dissected by numerous short but prominent scarps. The scarps are short, linear and present in subparallel sets of ∼20. They frequently appear at the base of steep triangular facets, whose aspect appears approximately parallel to bedding planes. We interpret most of the scarps as landslip scarps. There are, however, some more laterally continuous scarps, that may have a tectonic origin, and these are mapped in red in Figure 2.10.

To conclude, although we find abundant evidence for post-glacial fault slip along the south side of the Vashkh fault, we find limited evidence of recent earthquake scarps developed on the fault. It is possible, at least along some sections, that the steep topography and extensive landsliding has erased all traces of the 1949 earthquake. However, considering the geodetic evidence for creep, the presence of evaporites in the fault core, and the lack of mapped coseismic landsliding, we believe it unlikely that the Vakhsh Fault ruptured in the 1949 earthquake.

Yasman valley

The Yasman Valley is a tributary leading into the Vakhsh Valley, west of Khait (Figure 2.1). It is the site of highest reported damage and landsliding in the 1949 earthquake. We find compelling evidence for recent active faulting and potential single-event surface rupturing along its northern side, over a distance of ∼25 km. We term this the Yasman Fault (Figures 2.5 & 2.7). We also mapped landsliding which likely occurred post-1949 based on visual comparison of vegetation growth to the Khait landslide. We acquired 0.3 m Worldview-3 imagery with a Near-Infrared (NIR) band for observing vegetation which we used to map surface ruptures and generate a DEM for scarp height measurement.

The clearest evidence of surface rupturing is observed along a 3 km-long section at the westernmost end of the valley (Figure 2.6A), where stream channels and ridge crests show ∼2–5 m of right-lateral displacement, and alignments of vegetation suggest a line of springs as potentially caused by faulting (Figure 2.6C).

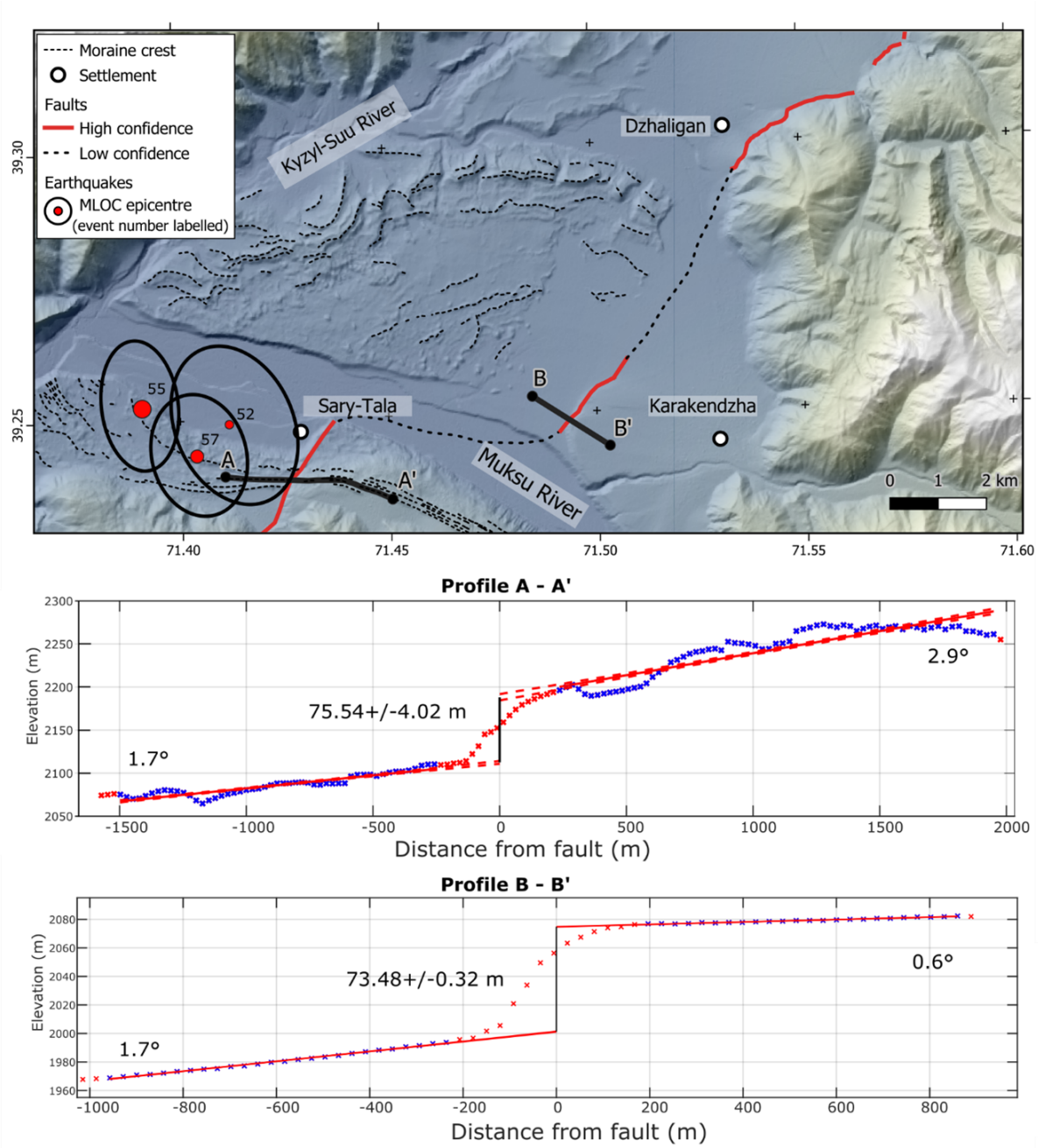

Figure 2.9: LGM moraine complex near Dzhaligan with dip slip offsets on both sides of the Muksu River. Lateral moraines dated to ∼18 kyr by Grin et al. (2016) are offset ∼75 m on sides of the north side of the river. North of the river, a similar magnitude offset is observed in a fan deposit which postdates the LGM. This indicates a slip rate on this fault of ∼5.5 mm/yr assuming a 50°dip suggested by earthquake depths. We interpret this to be a continuation of the Vakhsh/Darvaz Faults which joins up to the Pamir Frontal Thrust near Dzhaligan. Three earthquakes m_B 4.3–5.1 close to the offset further imply a tectonic origin. Topography is from the ALOS AWD 30m Global DEM (*JAXA ALOS World 3D 30 Meter DEM* 2019; Tadono et al. 2014; Takaku et al. 2014).

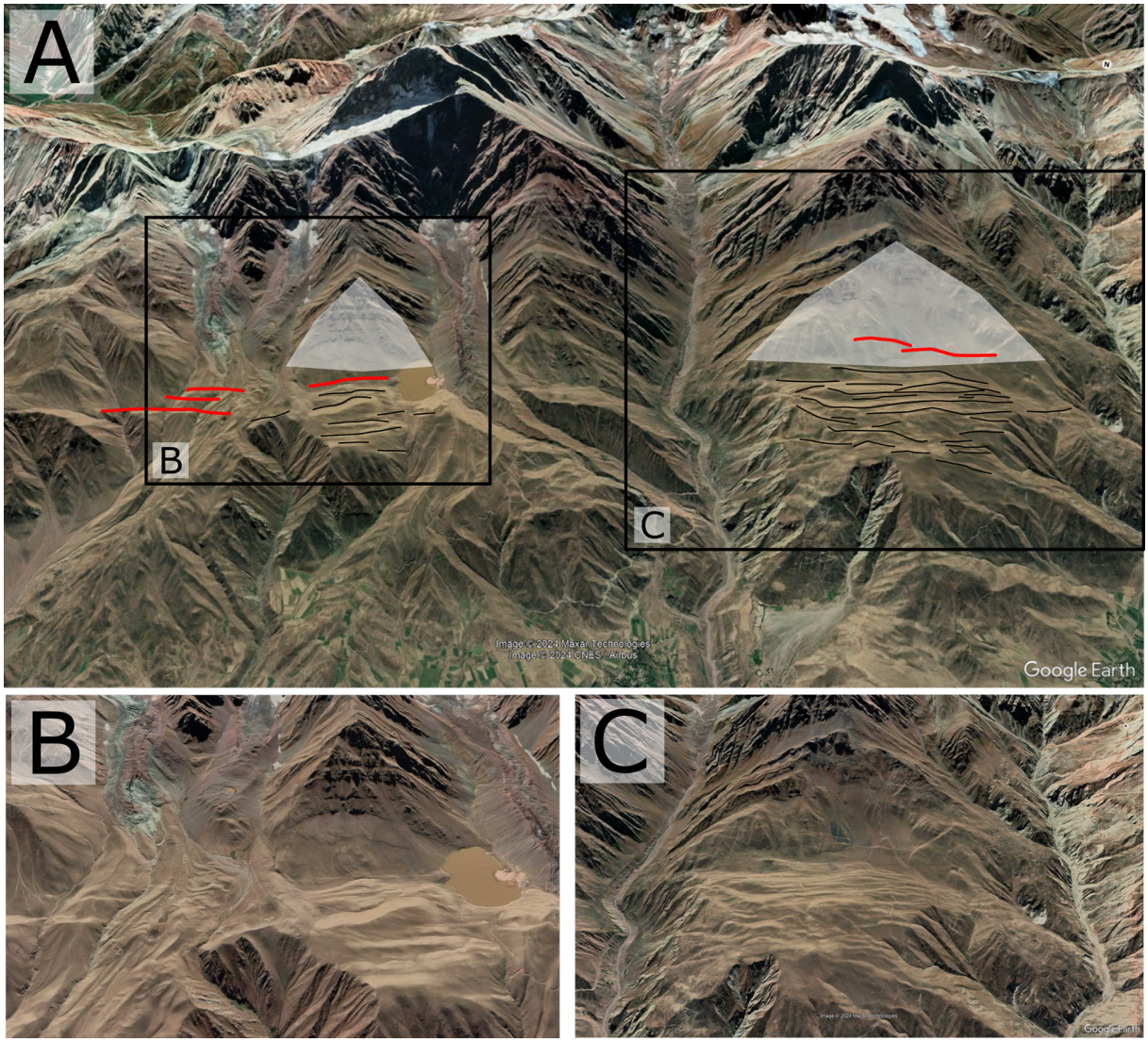

Figure 2.10: South-facing perspective Google Earth Imagery of a section of the Vakhsh Valley showing surface ruptures likely not from the 1949 Earthquake. Interpreted tectonic surface ruptures are in red. Scarps associated with landsliding are in black. Triangular facets in white are interpreted as exposed planes along which slumping has occurred.

In Figure 2.6B we observe right lateral stream offsets of between 5 ± 2 m and 2.1 ± 0.1 m. The fault trace continues north-west, beyond the limits of Figure 2.6B to the next catchment (Figure 2.6A), cutting across topographic contours. This implies a steeply dipping fault. We map two more high confidence potential ruptures about 600 m and 1300 m further south (Figure 2.6A). Further east, we identify a scarp crossing a hill slope, and measure a 9.8 ± 0.8 m right-lateral stream deflection (Figure 2.6C). We measure this displacement by projecting the stream levees above the fault to below the fault, and measure the offset between the present and projected stream.

Areas of high NIR (bright green) along the fault scarp represent vegetation, likely associated with a line of small springs. Further south, we observe a parallel alignment of springs, implying a parallel fault, but cannot identify any associated offset (Appendix A8).

Near Musofiron, we observe a south-facing scarp modified along a field boundary (Figure 2.6D). The fields under cultivation show up as areas of high NIR (bright green), with a fallow field showing as pale purple near the bottom-centre of the figure. A small landslide is visible in the top right of the figure. We measure a 2.8 ± 0.1 m dip-slip offset (profile C-C') where the scarp is part of the field boundary. To the west, across a stream, we observe a smaller 1.3 ± 0.1 m dip-slip offset (profile B-B'). It is possible that these two dip-slip measurements represent single and double event scarps, as the offset on profile C-C' is approximately double that of profile B-B', though it is possible that the scarp height has been modified where it runs along the field boundary, and we have assigned only moderate confidence to this part of the fault. The stream which runs to Musofiron appears deflected ∼25 m in a left-lateral sense, but we interpret this to result from the stream flowing around the raised field-boundary scarp, rather than a tectonic offset. On the hillside west of these examples, we observe fault traces of moderate confidence, as it is also possible that these are geological bedding planes (Appendix A6).

Further east, near Safebod, we find a scarp with apparent dip-slip offsets of around 1.4 ± 0.2 m. This is sharp in the orthophoto but not visible in the hillshaded DEM. A small stream cuts the scarp at a ∼90° angle, after which it spreads out into several smaller

channels. (Appendix A7). Near Khurramshahr, we observe a linear surface trace visible both in the elevation model and in the orthophoto. This scarp appears to offset a drainage ∼26–12 m in a left-lateral sense, in the opposite sense to the examples described earlier. Here the site interpretation is complicated by the presence of a recent landslide along-strike of the trace, and also by human modification, and we interpret the apparent left-lateral displacement as non-tectonic.

East of Khait the evidence for active faulting is less clear. We observe parallel scarps that follow topographic contours. These imply a moderate to shallow dip and align with bedding plane strikes in Soviet geological maps (Berezyuk n.d.). We therefore interpret them as slope failure scarps (Sackungen). It is possible that they are simply scarps formed due to differential erosion of layers of variable resistance, though we would expect purely lithological scarps to be more laterally continuous.

2.5 Discussion

2.5.1 Causative fault of the 1949 Earthquake

Our relocated 1949 epicentre is based on arrival time data, and thus locates the nucleation point of the earthquake. Together with macroseismic and landsliding data, our epicentre indicates the earthquake did not occur on the well-known Vakhsh fault, south of the Vashkh river, but on an unmapped fault within the Tian Shan basement north of the river. Surface rupturing has previously been difficult to map in the area due to inaccessibility and the steep, rapidly eroding landscape. The potential ruptures that we have identified from high-resolution optical satellite data are ∼15 km from the 1949 epicentre, are relatively recent and have metre-scale lateral offsets along the Yasman Valley. These metre-scale surface ruptures are consistent with a M_w 7.6 earthquake, and the right lateral sense is consistent with the focal mechanism of the 1949 earthquake, therefore we propose these ruptures were formed during the 1949 earthquake.

The 1949 Earthquake had a magnitude of M_w 7.6 (Table 2.1), equivalent to a scalar

moment of ∼3.2 x 10^{20} Nm. We have determined the hypocenter depth of 22-24 km using amplitude ratio comparison method. This is similar to the mloc derived depth of 22 km (Table 2.1). However, the misfit function has demonstrated limited dynamics, suggesting that the method is not as responsive to the centroid depth as we would prefer. As a result, the issue of the certainty regarding centroid depth and the dependency of the scalar moment estimate emerges. Therefore, we conducted tests on the bias related to M_O and magnitude using full-wavefield synthetics that were filtered with a standard Wiechert response for hypocenter depths between 10 and 30 km. Our findings revealed relative amplitude discrepancies of 1.1 for P waves on Z components and 1.3 for S waves on horizontal components. Consequently, we deduce that the uncertainties arising from the bias of the hypocenter and M_O fall within a range of 0.1 for M_w, which lies within our M_w error estimate of ±0.2.

Seismic moment is the product of the modulus of rigidity (∼3 x 10^{10} Pa·s), the area of the rupture plane, and the average amount of slip (Aki and Richards 2002). For the down-dip width we assume a vertical fault and rupture of the entire seismogenic thickness of ∼20 km based on the maximum depths from this study which is consistent with the base of crustal seismicity recorded by previous studies (Kufner et al. 2018b; Schurr et al. 2014). Taking the slip measurement from satellite imagery of ∼5+/-2 m (Figure 2.6B), we can then calculate a fault rupture length of 105 (+70/-30) km assuming vertical geometry. Another method to estimate fault length uses the duration of the P wave arrival duration and assumes this is the rupture duration. The ∼25-35 seconds P-wave arrival duration at stations in Europe (Figure 2.3) suggests a 75-105 km end-to-end rupture length, assuming a typical rupture propagation speed of ∼<3 km/s (Bouchon et al. 2001), and up to ∼150-210 km if the rupture propagated bilaterally from the centre of the fault. Super-shear rupture velocities > 3 km/s are possible, but tend to occur only on straight, simple, well developed faults (Ansal 2015), unlike the area where the 1949 earthquake occurred. Therefore, a total rupture length for the 1949 earthquake of ∼75–120 km is consistent with both estimation methods.

To the west of Khait we map ∼25 km of surface ruptures in the Yasman Valley, terming this the Yasman Fault. East of Khait, we also map another ∼10 km length of recent surface deformation, in addition to either bedding plane slip or sackung (Appendix A5). We therefore assume that most of the fault rupture remains unidentified, either because it failed to break the surface, or has been removed from the landscape by landsliding.

Regional seismicity may help to determine the missing parts of the potential earthquake source. We observe a NW-SE alignment of epicentres and mechanisms, from the relocated 1949 epicentre in the NW to the confluence of the Musku and Kyzyl-Suu Rivers in the SE (71.35°E, 39.25°N) (Figure 2.7A-4), as discussed in Section 2.4.1. This alignment includes two major aftershocks which occurred on the day of the 1949 earthquake, and the focal planes of subsequent earthquakes align well with this epicentre alignment. This suggests part of the 1949 rupture occurred on a WNW-trend delineated by these earthquakes (Figure 2.7A-4). We are unable to see ruptures in this area, however it is covered only by relatively coarse Open-Source imagery, and the terrain is extremely steep and prone to landsliding (Figure 2.1A) making it difficult to preserve ruptures.

Combining the observations, we infer that the 1949 Khait earthquake involved ∼85 km length of predominantly right-lateral rupture within the Tian Shan. This included ∼35 km length of rupture along the Yasman Fault, along which we see discontinuous surface rupture in satellite imagery, and ∼50 km rupture on a separate WNW-trending fault from the confluence of the Muksu and Kyzyl-Suu rivers which we term the Khait Fault (Figure 2.7). The relocated 1949 epicentre is sited at the NW end of this second fault, and roughly mid-way along the total combined fault. Nucleation at the relocated epicentre implies a westward rupture propagation along the Yasman Valley and a ESE-ward propagation towards the river confluence. If we assume ∼3 km/s rupture velocity, that implies a ∼16 s source time function, which is similar to the ∼20 s we estimate from P wave records in Europe (Figure 2.3).

These two parallel WNW ruptures match up with a set of ruptures and earthquakes that follow the same trend. The ruptures are at (71.8047°E, 39.5045°N) and the earthquake

alignment is highlighted in Figure 2.7A-5. These faults bound blocks which accommodate NS shortening by rotation on a vertical axis, playing a similar role to the much larger Dzhungarian and Talas-Fergana faults (Figure 2.7B) (Campbell et al. 2013; Rizza et al. 2019).

2.5.2 Seismicity of the Vakhsh Fault

Our study finds little evidence for the Vakhsh Fault rupturing in the 1949 earthquake, with faults in the Tian Shan interior likely being responsible. This result then prompts the question of whether the Vashk fault has potential for producing significant earthquakes.

GNSS and InSAR (Metzger et al. 2020; Metzger et al. 2021) velocity profiles across the Vakhsh Fault near Gharm show a steep gradient in fault-parallel velocity, implying shallow creep on the fault. However, fault perpendicular displacements have a much shallower gradient, and implies that thrusting is locked at depth. This is could be due to partitioning of strike-slip and thrust kinematics across different structures, analogous to the Main Recent Fault and the High Zagros Fault in Iran (Nissen et al. 2011).

The Vakhsh Fault itself evidently hosts moderate earthquakes up to M_w 5.9 (Figure 2.1b, Table 2.1). However, aside from the 1949 Earthquake we have no record of a M_w>7 earthquake within ~200 km of Khait (Mikhailova et al. 2015). Either the historical catalogue is incomplete, or the Vakhsh fault is incapable of hosting earthquakes this large. To better understand the behaviour of the Vakhsh Fault further geodetic analysis is required. The terrain and snow cover makes small-baseline time series InSAR difficult (Metzger et al. 2021), so deploying dense arrays of GNSS stations or corner-reflectors for PS InSAR may be required to better understand the earthquake potential of the Vakhsh Fault.

On a regional scale, we propose a two-stage model of intramontane convergence between the Pamir and Tian Shan. In the first stage, the convergence is accommodated by simple underthrusting and subduction, as in the Alai Valley (Patyniak et al. 2021; Sobel et al. 2013; Zubovich et al. 2016). In the second stage, once all of the low-lying basin has been subducted (as it has near Khait), the kinematics change and shortening is accommodated

by NW-SE striking right lateral faults, similar to the Dzungarian and Talas-Fergana Faults north of the Tian Shan (Rizza et al. 2019; Tsai et al. 2022) and the Kopeh Dagh Fault System in NE Iran (Hollingsworth et al. 2006). The Vakhsh Fault was likely site of this subduction in the past, analogous to the Pamir Frontal Thrust today. The relative convergence taken up by thrusting on the Vakhsh Fault and vertical axis rotations is unclear, and a question for future research.

2.5.3 Slip rate of the Vakhsh Fault

We can estimate long term slip rate on the Vakhsh Fault by examining how glacial moraines are tectonically offset. In Section 2.4.2 we identified two areas where moraines are offset.

One site is on the banks of the Muksu River (Figure 2.9) where lateral moraines of ∼18 kyr age (Grin et al. 2016) are offset by 75.5 m. The alluvial fan on the north side of the river (deposited after glacial retreat) has a similar 73.5 m offset. Both surfaces are near-horizontal, so we can take the vertical separations observed in Figure 2.9 to be approximately equal to the vertical component of a tectonic offset on a dipping fault (Mackenzie and Elliott 2017). This gives a vertical uplift rate of ∼4.2 mm/yr, which projected onto a 50° dipping fault, as indicated by earthquake cross sections (Figure 2.7), would give a slip rate of 5.5 mm/yr.

The other site is situated in the Peter I Range (Figure 2.8) where we observe sub-vertical backthrust faults cutting a moraine complex we suggest is younger than the LGM (18 kyr) but for which we have no firm dating. If we assume the oldest mapped moraine coincides with the LGM, the offset since the LGM would be 20.1 m (Figure 2.8 profile C-C'), giving a vertical uplift rate of 1.1 mm/yr. Given the fault is near-vertical, we can again assume that vertical separation observed in topographic profiles is equivalent to the vertical component of the tectonic offset (Mackenzie and Elliott 2017). If we assume instead the surface below the mapped moraines is coincident with the LGM, the LGM offset would be 32.7 m (Figure 2.8 profile A-A'), giving a vertical uplift rate of 1.8 mm/yr. This would give a fault slip rate of ∼1.1-1.8 mm/yr.

To synthesise these results, we suggest that the Musku River site represents an estimate of the Vakhsh Fault and the Peter I site either represents movement on a backthrust (Schultz 2000), or else a thrust-termination of the Darvaz fault. We therefore suggest the long term slip rate on the Vakhsh Fault is ~5.5 mm/yr. This is less than half the rate derived from geodetic estimates, which suggest >13 mm/yr present-day dip-slip strain accumulation on the fault (Metzger et al. 2020). This adds to the evidence the Vakhsh Fault, rather than being the dominant structure taking up convergence between the Pamir and Tian Shan, is one of several structures around the Vakhsh Valley accommodating this convergence since the LGM.

2.5.4 Implications for hazard in the region

Determining the source of the 1949 Khait Earthquake and characterizing the earthquake potential of active faults in the region have a particular present-day relevance for earthquake hazard.

Hydroelectricity is the main source of electricity for Tajikistan, and the country exports this to its neighbours (IEA 2022). Several hydroelectric dams have been built along the Vakhsh River, including at Nurek and Rogun, which are 150 km and 110 km from Khait respectively (Figure 2.1). Further expansion of hydroelectricity requires an understanding of the distribution of tectonic deformation through the region and knowledge of earthquake-hosting faults. In the worst case, earthquake shaking and fault movement may present risks to downstream communities from flooding and disruptions to power supplies across Central Asia if dams are damaged.

Earthquake shaking could impact flood risk within the Pamir by destabilising existing natural dams, such as the Usoi landslide dam, built by a 2 km^3 landslide mobilised by shaking from the 1911 M_w7.3 Sarez Earthquake (Emmer et al. 2020; Hanisch 2002; Kulikova et al. 2016). At a smaller scale, hundreds of glacial lakes have been identified across the Pamir, many of which are growing as glaciers retreat (Mergili et al. 2013). These represent both a source of water, and a hazard if the dams holding them fail. In 2002 the

village of Dasht in the southern Pamir was inundated in such an event, killing tens of people and destroying many houses (Mergili and Schneider 2011). Large earthquakes in the Vakhsh Valley may, therefore, pose risks outside the immediate epicentral region.

2.5.5 Do observations of small earthquakes elucidate sources of large earthquakes?

A common method of understanding the seismo-tectonics of a region is to deploy a dense network of seismometers for periods ranging from months to years, and use the small, very frequent earthquakes of M<∼4 to find active faults, and to understand whether visible geological faults are active and whether they have the potential to produce large earthquakes (Duverger et al. 2018; Frepoli et al. 2011; Kufner et al. 2018a; Schurr et al. 2014). This can be very valuable for highlighting the subterranean geometry of the faults (e.g. Kufner et al. (2018a), as well as observing crustal thicknesses (Schneider et al. 2019), and may illuminate areas of locking or creeping on certain faults, essential for understanding their mechanics and hazard (e.g. Lin and Lapusta (2018)). Finally, it makes calibrated earthquake relocation studies, like this one, possible.

In our study the earthquakes >M6 highlight a trend that is not evident from microseismicity, namely the WNW alignment identified in Figure 2.7A-4 which we hypothesised in the Section 2.5.1 consituted the greater part of the 1949 earthquake rupture. This fault is not highlighted by microseismicity in the same way as the Vakhsh Fault (Figure 2.7A-1), possibly because the 1949 released all stress on this fault and it is now locked and accumulating strain.

This has implications for hazard, because 1949 earthquake is part of a wider pattern of deadly continental earthquakes which have occurred on "cryptic" faults – faults which remain unknown until a major earthquake happens on them within instrumental records. This risk has been highlighted for oceanic convergent margins above megathrusts (Jara-Muñoz et al. 2022), but is present within convergent continental interior settings as well.

One example is the 2020 Mw6.4 Koryak Earthquake, in eastern Siberia (Salomon et al. 2025). This earthquake bears many similarities to the 1949 Khait Earthquake. Firstly, it nucleated on a previously unknown fault, which was not well expressed in the surface geomorphology prior to the earthquake. Secondly, it occurred in a convergent continental setting of the Pacific Cordillera in high mountains, far from the plate boundary. Thirdly, the causative fault has a strike inclined 45° to the nearby geological suture, which we might expect to be the line of weakness likely to break in an earthquake.

A further example is the 2017 earthquake doublet that occurred near the Eastern Denali Fault (EDF) in Southern Alaska (Choi et al. 2021). These Mw6.2 and Mw6.3 earthquakes both ruptured more than 10 km from the EDF, with fault plane strikes at 30°-45° inclination to the EDF. Choi et al. (2021) suggest the EDF is now a geological suture, with the active deformation now occurring over a 50 km wide zone further south. The Vakhsh Fault appears to be presently only taking up around half the deformation between the Pamir and Tian Shan, so it may be on its way to becoming a geological suture, with all strain distributed across the Pamir and Tian Shan.

2.6 Conclusions

We combine seismology and geomorphic analysis to shed light on the tectonic circumstances of the 1949 M_w7.6 Khait Earthquake and how it relates to the large Vakhsh Fault. Using historical seismograms, we determined a focal mechanism with strike, dip and rake of 50 ± 20, 80 ± 10 and -20 ± 10 respectively. We used multiple event relocation algorithm *mloc* to perform a relative relocation of 133 earthquakes of M_w>4, including the 1949 earthquake. We used regional seismometer deployments from the 2000s to 'calibrate' these locations and remove biases introduced by an assumed global seismic velocity model, resulting in locations with ∼5 km formal uncertainty. We located the 1949 earthquake hypocentre at (70.870°E, 39.336°N) at a depth of 22–24 km – significantly refining previous estimates of the 1949 earthquake location.

By analysing high resolution Worldview-3, Pleiades, and Open-Source imagery we mapped ∼35 km of earthquake surface rupture. We found evidence for faulting in the Yasman

Valley, north of the Vakhsh River, and discovered right-lateral strike slip offsets of 5–9 m. We believe these surface ruptures to be from the 1949 earthquake. We term this new fault the Yasman Fault. In addition, we found smaller dip slip offsets of ∼1–2 m. From alignments of 1949 earthquake aftershocks, we suggested that a further 50 km fault rupture occurred between the 1949 epicentre and the confluence of the Muksu and Kyzyl-Suu Rivers. We term this new fault the Khait Fault. We term this the Khait Fault. In addition we estimate the slip rate of the Vakhsh Fault to be ∼5.5 mm/yr since 18 kyr, about half the geodetic convergence rate between the Pamir and Tian Shan. We conclude that the 1949 earthquake probably did not occur on the Vakhsh Fault, instead rupturing a previously unknown fault within the Tian Shan basement. The 1949 Earthquake demonstrates a change in tectonic regime caused by the recent closure of the intramontane Vakhsh basin. Compared to the simple overthrusting of the Alai Valley further east, in the Vakhsh Valley shortening is accommodated by a mixture of slip on the Vakhsh Fault, extrusion of the Peter I Range, and vertical axis rotations in the Tian Shan. The 1949 earthquake demonstrates the hazards posed by "cryptic" faults, and shows how studying early-instrumental earthquakes may elucidate them.

Statement of Authorship for joint/multi-authored papers for PGR thesis

To appear at the end of each thesis chapter submitted as an article/paper

The statement shall describe the candidate's and co-authors' independent research contributions in the thesis publications. For each publication there should exist a complete statement that is to be filled out and signed by the candidate and supervisor **(only required where there isn't already a statement of contribution within the paper itself).**

Title of Paper	Rupture of the 1949 Khait earthquake on a cryptic fault: implications for earthquake hazard
Publication Status	□Published □ Accepted for Publication X Submitted for Publication □Unpublished and unsubmitted work written in a manuscript style
Publication Details	B. W. W. Johnson, G. Kulikova, E.A. Bergman,F. Krueger, I. K. Pierce, J. Hollingsworth, R. T. Walker. (AGU Tectonics; in revision)

Student Confirmation

Student Name:	Benedict Johnson		
Contribution to the Paper	Performed: calibrated earthquake relocations in *mloc*, processing of satellite imagery to produce orthophotos and digital elevation models, geomorphic and tectonic mapping of orthophotos and digital elevation models, interpretation, and wrote manuscript Collection and digitisation of historic seimsograms, single event location in HYPOSAT, and determination of focal mechanism for the 1949 Khait Earthquake was done by Galina Kulikova		
Signature Ben Johnson		Date	26-April-2026

Supervisor Confirmation

By signing the Statement of Authorship, you are certifying that the candidate made a substantial contribution to the publication, and that the description described above is accurate.

Supervisor name and title: Prof. Richard T. Walker		
Supervisor comments The above statement is accurate. The candidate led this work and made a substantial contribution.		
Signature 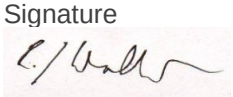	Date	26/04/2025

This completed form should be included in the thesis, at the end of the relevant chapter.

3| Rapid fault creep in the fluid-rich Kura Basin, Azerbaijan, imaged with InSAR

B. Johnson[1], J. R. Elliott[2], G. Yetirmishli[3], R. Javanshir[1,3], S. Kazimova[3], N. Marshall[1], J. Payne[2], R.T. Walker[1]

[1] COMET Department of Earth Sciences, University of Oxford, South Parks Road, OX1 3AN, United Kingdom.

[2] COMET, School of Earth & Environment, University of Leeds, LS2 9JT, UK.

[3] Republican Seismic Survey Center of Azerbaijan National Academy of Science, Baku, Azerbaijan.

Corresponding author: Ben Johnson (benedict.johnson@st-annes.ox.ac.uk)

Key points:

- We image widespread surface fault creep on faults of the Kura basin, Azerbaijan, likely resulting from the thick, fluid-rich, sediments.
- The observations potentially explain the relative lack of large earthquakes in recent decades and further back in time.
- A question remains on whether the structures are still capable of producing occasional large earthquakes, for instance the 1902 Shemakhi event.

Abstract

Current geodetic velocities show that over half (up to 10 mm/yr) of Arabia-Eurasia shortening in the west is accommodated within a relatively narrow zone across the Kura basin of Azerbaijan, in which the most prominent active structure is the Kura Fold and Thrust Belt, bordering the southern margin of the Greater Caucasus. GNSS velocities furthermore suggest equivalent amounts of north-south right-lateral shear across the eastern Kura

basin along the West Caspian fault zone that is accommodating relative motion between the Kura basin and the South Caspian basin. Although destructive historical earthquakes are known to have occurred, their spread is restricted geographically and their moment release accounts for only half of the accumulated deformation. These observations can be explained by incompleteness of the historical record, that the faults fail in rare larger earthquakes, or that they slip aseismically. To distinguish between these hypotheses we produce an InSAR velocity field using Sentinel-1 SAR data to image active tectonic deformation within the Kura basin of Azerbaijan. Tectonic signals are superimposed on those relating to non-tectonic processes, including widespread mud volcano inflation that highlights the important role of fluid flow within the basin sediments. We show aseismic creep occurs on two parallel faults of the West Caspian fault zone, and infer this also on the Kura Fold and Thrust Belt from sharp gradients in velocity indicating active fold growth. Recent paleoseismic studies of the faults imaged here indicate discrete slip events, and we speculate that the creep may be episodic, perhaps triggered by deeper earthquake events or by periods of enhanced fluid mobilisation. Together, the right-lateral and left-lateral faults appear to accommodate a large-scale expulsion of the Absheron region towards the South Caspian Basin, perhaps driven by gravitational potential energy contrasts.

Plain Language Summary

Azerbaijan is a region with many active faults and growing mountain ranges, though the number and size of known earthquakes does not account for all the motion that is expected to have accumulated. It may be that earthquakes are missing from the historical record or that the faults fail in rare but very large earthquakes. Alternatively it may mean that many of the faults are constantly sliding, or creeping, such that no motion is being stored up to be released in seismic events. To discriminate between these ideas we use satellite radar images acquired on multiple different dates using the European Space Agency Sentinel 1A satellite, which allow motions of the ground to be imaged. First we had to overcome a number of technical challenges related to signals from agriculture and from water extraction before we are able to examine the active fault movements. From the final maps of ground motion we are able to show that major faults in the east and northern sides of the Kura basin are creeping. This behaviour is likely caused by the

large amounts of fluids circulating in the sediments of the Kura basin, which are visible at the surface as mud volcanism. Our results are important for assessing the earthquake potential of active faults in Azerbaijan, but there are remaining questions about whether the behaviour we image is a temporary or permanent behaviour. Our results also help to understand the role of the active faults, which appear to allow a large-scale movement of material from the highlands of the eastern Caucasus towards the interior of the South Caspian Basin.

3.1 Introduction

Active faulting in the Kura basin, Azerbaijan, results from tectonic shortening related to the Arabia-Eurasia continental collision, and also from motion of the South Caspian Basin (SCB), which is a deep water and oceanic-floored aseismic block that moves relative to the surrounding continental regions (e.g. (Ismail-Zadeh et al. 2020; Jackson et al. 2002), Figure 3.1). Approximately 10 mm/yr of northward-directed Eurasia-Arabia shortening (Ismail-Zadeh et al. 2020; Kadirov et al. 2014; Viltres et al. 2022) is accommodated between the Lesser Caucasus range, the Greater Caucasus, and the active structures of the Kura Fold and Thrust Belt (KFTB) (Figures 3.1 and 3.2). The KFTB is the most prominent structure geomorphically, and consists of south-verging fault-related folds and surface-breaching thrust faults, which likely connect at depth to deep reverse faults along the southern Caucasus margin (Mosar et al. 2010; Poblet and Lisle 2011), Figure 3.1). The proportion of the present-day shortening accommodated across the fold-and-thrust belt, and on structures to north and south, is not known. Displacement of a mid-Holocene terrace across the southernmost of several parallel folds and faults near Agsu yields an uplift rate of 2.9 $\pm$ 0.6 mm/yr (Pierce et al. 2024).

There is also relative motion between the continental-floored Kura basin and the Oceanic SCB to its east. Direct constraints on the relative motion are hard to estimate, as much of the SCB is underwater, and so measurements are restricted to its edges (e.g. Walker et al. (2021)). West-directed shortening and underthrusting of the South Caspian basement beneath the Kura basin is well-defined by deep seismicity (e.g. Jackson et al. (2002)). The extent and rate of lateral slip along the margin are harder to constrain. A velocity

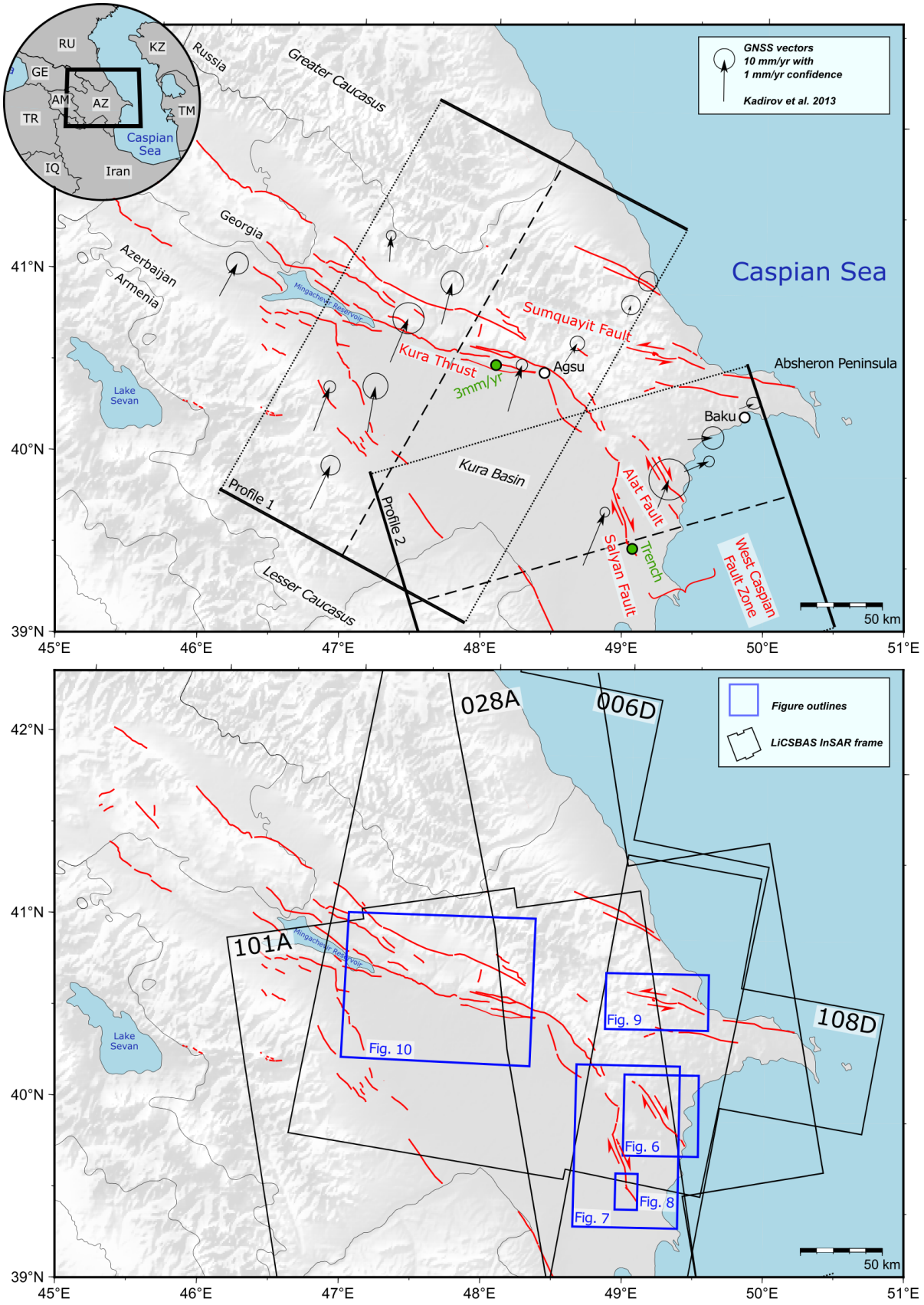

Figure 3.1: (Caption next page.)

Figure 3.1: (Previous page.) GNSS velocities relative to Eurasia from Kadirov et al. (2014), with 95% confidence ellipses, and active fault traces visible in the geomorphology (mapped by the authors). Swath profiles of GNSS velocities, as shown in Fig. 3.2, are represented by black rectangles. Profile 1 is orthogonal to the Salyan fault (West Caspian fault zone) and Profile 2 is orthogonal to the Kura fold-and-thrust belt. A geologic uplift rate from Pierce et al. (2024) is shown, as is the trench site from Marshall (2023). Bottom: footprints of ascending and descending Sentinal 1A radar images used in this study, labelled with the prefix of the Frame ID (Table 3.1)

triangle construction for the west Caspian region suggests lateral slip along the boundary is negligible (Copley and Jackson 2006), though recent GNSS measurements suggest up to 10 mm/yr of north-south right-lateral motion may be accommodated in the eastern part of the Kura basin (e.g. Kadirov et al. (2014); Figure 3.1). A paleoseismic investigation by Marshall (2023) identified two apparent right-lateral faults in the easternmost Kura basin (the Salyan and Alat faults, Figure 3.2), and provided an initial estimate of Holocene average slip-rate on the Salyan fault of ∼5 mm/yr.

The active faults of the Kura basin propagate through a sedimentary sequence up to ∼10 km in thickness (Inan et al. 1997). The major part of the sequence dates from the last 5 Ma, overlying older marine shales of Miocene age (e.g. Green et al. (2009)). The sediments are rich in fluids (e.g. Javanshir et al. (2015)), as expressed by abundant and widespread occurrence of mud volcanism where fluid-rich sediments are extruded from the ground (e.g. Antonielli et al. (2014) and Planke et al. (2003). Mud volcanoes are present worldwide, but particularly in fold and thrust belt settings, both onshore and offshore (Kioka and Ashi 2015; Kopf 2002).

The Caspian Sea currently sits at -28m above global mean sea level, but reached its highest Pleistocene level of 50m (termed the Early Khvalynian Transgression). The age of this transgression is poorly constrained between 70ka-20ka (Dolukhanov et al. 2010; Krijgsman et al. 2019) but it appears to have recently covered the Kura Basin and "reset" the landscape south of the Kura Fold and Thrust Belt, with Khvalynian deposits reaching up to 100m in the Kura Basin (Krijgsman et al. 2019). Another later transgression reached 0m at 10 ka (Krijgsman et al. 2019), but this does not extend as far into the

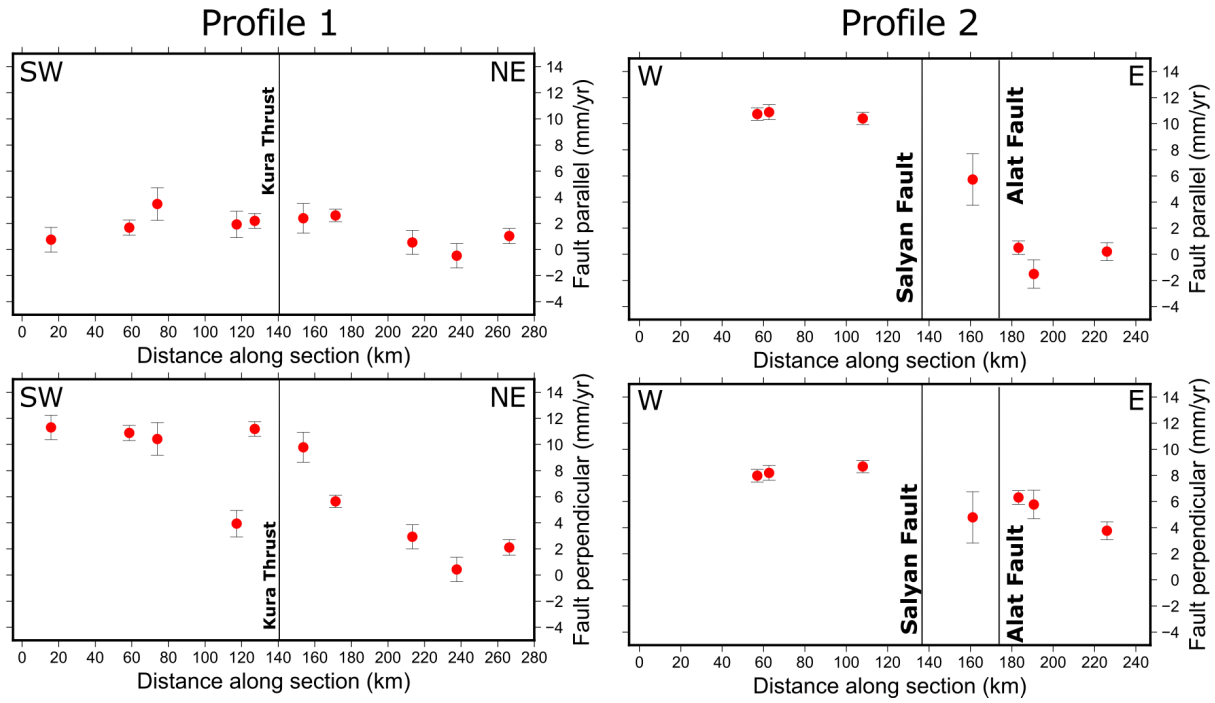

Figure 3.2: (a) Fault parallel and (b) fault perpendicular components of GNSS velocities for the Salyan and Alat faults in the West Caspian fault zone (Profile 1 in Figure 3.1). Approximately 10 mm/yr of right-lateral motion is accommodated across the overall zone. Shortening is less easy to constrain but appears to be 2–4 mm/yr. (c) Fault parallel and (d) fault perpendicular components of GNSS velocities for the Kura Thrust (Profile 2 in Figure 3.1). There is no discernible fault parallel (strike-slip) motion, but 10 mm/yr of N-S shortening (fault perpendicular motion).

Kura Basin as the Early Khvalynian transgression. Together, it seems likely any footwall subsidence has been "filled in" by marine sediments in the very recent geological past.

Comparing geodetic and seismic rates of motion across the Kura basin suggests that only ∼10-40% of geodetic strain in the Caucasus has been released in earthquakes recorded from 1908 to 1981 (Jackson and McKenzie 1988), and known historical seismicity over the past 400 years accounts for only 25% of the shortening (Ambraseys and Jackson 1997). This discrepancy in accumulation and release rates may indicate that many events are missing from the historical record, which has recently been demonstrated, for example, from the eastern side of the Caspian sea in Turkmenistan (Dodds et al. 2022a). Alternatively, it may mean that the strain is released in occasional very large earthquakes, and recent paleoseismic studies of both the fold and thrust belt, and of the Salyan right-lateral strike-slip fault in the eastern Kura basin, both appear to show multiple discrete

Table 3.1: Statistics for the LiCSAR frames used in this analysis (denoted by their track number). For the Salyan, Alat faults, and Sumquayit Faults we used 028A and 108D, and for the Kura Basin we used 101A and 006D. IFGs = interferograms, Epochs = SAR acquisitions. Line-of-sight velocity fields are shown in Figure 3.3 prior to masking.

Track	Start	End	Duration (yr)	Epochs	No. IFGs generated	No. IFGs Used
101A	Jan 2017	Apr 2023	6.25	226	993	679
028A (200m)	Oct 2014	Nov 2023	9.1	226	1493	1359
108D (200m)	Oct 2014	Nov 2023	9.1	221	1207	1006
006D	Jan 2017	Apr 2023	6.25	181	995	658

slip events over the last few thousand years (Marshall 2023; Pierce et al. 2024). However, the paucity of earthquakes may suggest that much of the strain is being released by aseismic creep, which might be suspected given the fluid-rich sedimentary basin through which the faults propagate. Determining the relative importance of each of these factors is necessary for understanding the seismic hazard of Azerbaijan and surrounding countries, as well as providing more general insight into the earthquake potential of deforming belts within thick sedimentary basins.

3.2 Materials and Methods

We use *Sentinel-1* satellite radar data to generate interferogram networks for time series analysis of surface displacements across the region. The Sentinel-1A satellite launched in 2014, generating near-global coverage every 12 days, and was supplemented by Sentinel-1B in 2017, increasing the frequency of acquisition of global coverage to every 6 days for many regions until it failed at the end of 2021. We use acquisitions from October 2014 to December 2023 to construct our time series of displacements from which we calculate the decadal average velocities (Table 3.1).

We make use of the LiCSAR and LiCSBAS processing chains to generate the unwrapped interferograms, and run the timeseries analysis respectively (Lazecký et al. 2020; Morishita et al. 2020). We use interferograms produced by the LiCSAR processing chain, in

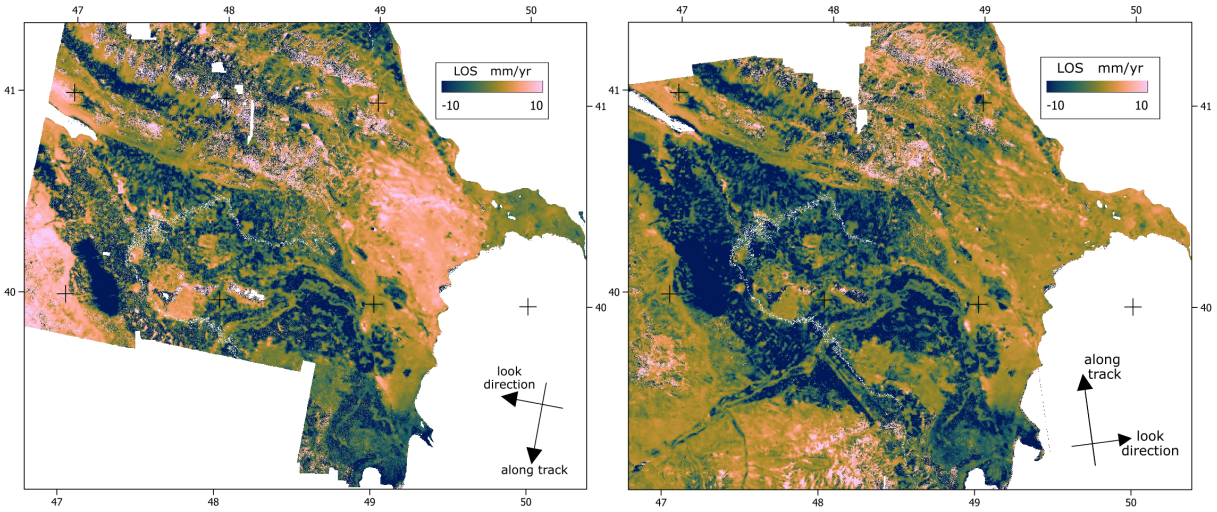

Figure 3.3: (a) Ascending and (b) Descending Sentinel 1A velocity fields.

ascending and descending geometries. For tracks 028A and 108D we downsample to 200 m to overcome an unwrapping error apparent in the 100 m velocity field which polluted the fault-perpendicular swath profiles, the other two tracks we leave at the 100 m resolution returned by LiCSAR. We form a redundant network of interferograms to detect unwrapping errors using phase-loop closure tests. We also check for interferograms where a high proportion of pixels have high residuals from the time-series deformation model, which we expect would be due to unwrapping errors across a large proportion of the interferogram.

For the time-series analysis, we clip the original LiCSAR frame to a set of regions of interest around the faults. This allows us both to reduce computation time and to keep interferograms that would otherwise be rejected due to unwrapping errors outside our regions of interest. We apply atmospheric corrections based on the Generic Atmospheric Correction Online Service (Yu et al. 2018a) (GACOS) for InSAR (Yu et al. 2017; Yu et al. 2018a; Yu et al. 2018b). This derives tropospheric delay maps based on weather models from the European Centre for Medium Range Weather forecasts. These are used to calculate a correction for the interferograms in LiCSBAS (see Morishita et al. (2020) for more details). Line-of-sight velocity fields prior to masking are shown in Figure 3.3.

Unwrapping errors are common around the KFTB due to isolated patches of high-coherence pixels within a set of low-coherence pixels. We check for such errors in two ways. First,

we perform tests for loop closure within a set of three interferograms. We take the phase ($\emptyset$) of each pixel in wrapped interferograms generated from Epoch 1, Epoch 2 and Epoch 3. If there are no unwrapping errors then equation 1 applies

$$\emptyset_{12} + \emptyset_{23} - \emptyset_{13} = 0 \tag{3.1}$$

If the residual is greater than 1.5 radians the interferogram containing the error can be isolated by looking at all loops it appears in (Morishita et al. 2020). Secondly, assuming approximately linear deformation in time, we examine the residual between interferograms and the least squares model prediction of deformation for that time period. Unwrapping errors show up as contiguous regions of high similarly valued residuals. If unwrapping errors are indicated, we remove the affected pixels for that interferogram using the LiCSBAS 'nullify' option.

Assuming that tectonic deformation is linear we can use the residuals relative to the model to check whether any missed unwrapping errors (potentially caused by variations in land use) are biasing the signal we observe across faults. We use a residual Root Mean Squared (RMS) mask (i.e. RMS residuals for a certain pixel in all interferograms). If we were to find agreement between the residual RMS mask and the potential tectonic signals this would suggest that the signals result from unwrapping errors used in the inversion. However, we do not find agreement, and are confident that unwrapping errors have not significantly affected our results.

Another challenge in interpreting tectonic signals is introduced by the intensive agriculture in the Kura basin, which can lead to phase bias being introduced at the boundaries of the vegetated regions due to interferograms with short timespans being used in the time series (6, 12 and 24 days) (Maghsoudi et al. 2022). This effect can lead to apparent changes in line-of-sight velocity, which can be misinterpreted as a tectonic signal (Figure A10 & A11). This effect is of particular concern at the KFTB, where the front of the fold coincides with a change between intensive agriculture in the basin, and lighter agriculture on the hanging-wall. To test the reliability of the observed signals in this region we first

removed 6, 12 and 24 day interferograms, and we still observe a velocity contrast across the thrust.

To further assess whether bias is introduced by abrupt changes in vegetation we used a velocity threshold to exclude pixels with velocities below -5 mm/yr, which retained pixels over towns and excluded areas over fields. We validated this approach using the Normalised Difference Vegetation Index (NDVI) derived by from *Sentinel-2* data. NDVI is derived by using a near-infrared band sensitive to vegetation and normalising using an optical band insensitive to vegetation (e.g. red) to correct for shadows or other variations in spectral reflectance. Negative values tend to characterise clouds or water; values near zero bare rock, small positive values grassland or cropland, and higher values temperate to tropical rainforest. In the case of *Sentinel-2* the NDVI is derived from the band combination (SentinelHub):

$$NDVI = \frac{B8 - B4}{B8 + B4} \quad -1 \leq NDVI \leq 1 \tag{3.2}$$

Applying a mask for NDVI >0.3 in springtime achieves a similar result on visual inspection to velocity thresholding at -5 mm/yr.

In addition, we used an upper velocity threshold of +10 mm/yr to remove uplift signals we interpret as linked to deposition in salt pans, e.g. at (40.541°N,47.325°E), about 30 km SE of the Mingacevir Reservoir (Figure A12) (Ruch et al. 2012).They show up as regions of high reflectivity in *Sentinel-2* L2A images (e.g. 2023-6-12, or 2023-12-29). Similarly high reflectivity is observed in *Sentinel-2* imagery around the edges of lakes north of Mingecevir Reservoir (e.g. 41.006°N, 46.938°E). The high-velocity areas are low-lying, and ridges have lower reflectivity. We believe these areas are uplifting due to evaporation of ponded brackish/saline water leaving salt crystals. This could be rainwater leaching evaporitic minerals from the surrounding sediments deposited during the last Caspian Highstand. This mechanism can cause uplift of up to ∼150 mm/yr in high-percentage halite deposits (Ruch et al. 2012), so it is a plausible source of the uplift we observe here.

We used the common area between ascending and descending geometries of the *Sentinel-*

1 orbit to decompose line-of-sight motion into East-West motion and Up-Down (UD) motion (Motagh et al. 2017; Watson et al. 2022a; Wright et al. 2004). To account for north-south motion, we fit quadratic polynomials to north and east components of GNSS velocity using Generic Mapping Tools Software (Wessel et al. 2019). Around the KFTB, the north-south component of the line-of-sight unit vector is around 0.1 so unaccounted for northward velocity will result in minimal changes to line-of-sight velocity. Prior to decomposition, we referenced the time series to the same point in space.

3.3 Results

The vertical and east-directed components of the final decomposed velocity field are presented in Figures 3.4 & 3.5. A number of large-scale features are visible at this scale, resulting both from tectonic and non-tectonic processes. Most of the Kura basin shows a negative vertical velocity (Figure 3.4). This is unlikely to represent basin-wide subsidence from sediment compaction and de-watering as it is restricted to those parts of the basin that are vegetated. Also, features such as river courses and settlements within the basin do not show the same negative velocity signals, and the subsidence rates within rivers are ∼80 mm/yr slower than in the surrounding fields (Figs. A10 & A11). We instead interpret the negative velocity as phase bias resulting from the widespread agricultural vegetation in the basin (Ansari et al. 2021; De Zan et al. 2015; Maghsoudi et al. 2022). Isolated regions of rapid negative velocity, particularly along the southern edges of the basin may represent subsidence due to groundwater extraction (e.g. Motagh et al. (2017)).

Another widespread non-tectonic signal in the eastern parts of the Kura basin and Absheron peninsula is caused by mud volcanoes (e.g. Hovland et al. (1997), which are widespread in eastern Azerbaijan, and also offshore in the Caspian sea. Inflation caused by injection of mud at very shallow depth produces short-wavelength peaks in positive vertical velocity, and in paired lobes of positive and negative eastward velocity due to radial outward motion of the ground during inflation (Segall 2010). Though individual mud volcanoes in Azerbaijan have been monitored previously using InSAR (Antonielli et al. 2014; Iio and Furuya 2018; Odonne et al. 2021), our region-wide analysis suggests that many of the mud volcanic systems are active, even in the absence of eruption.

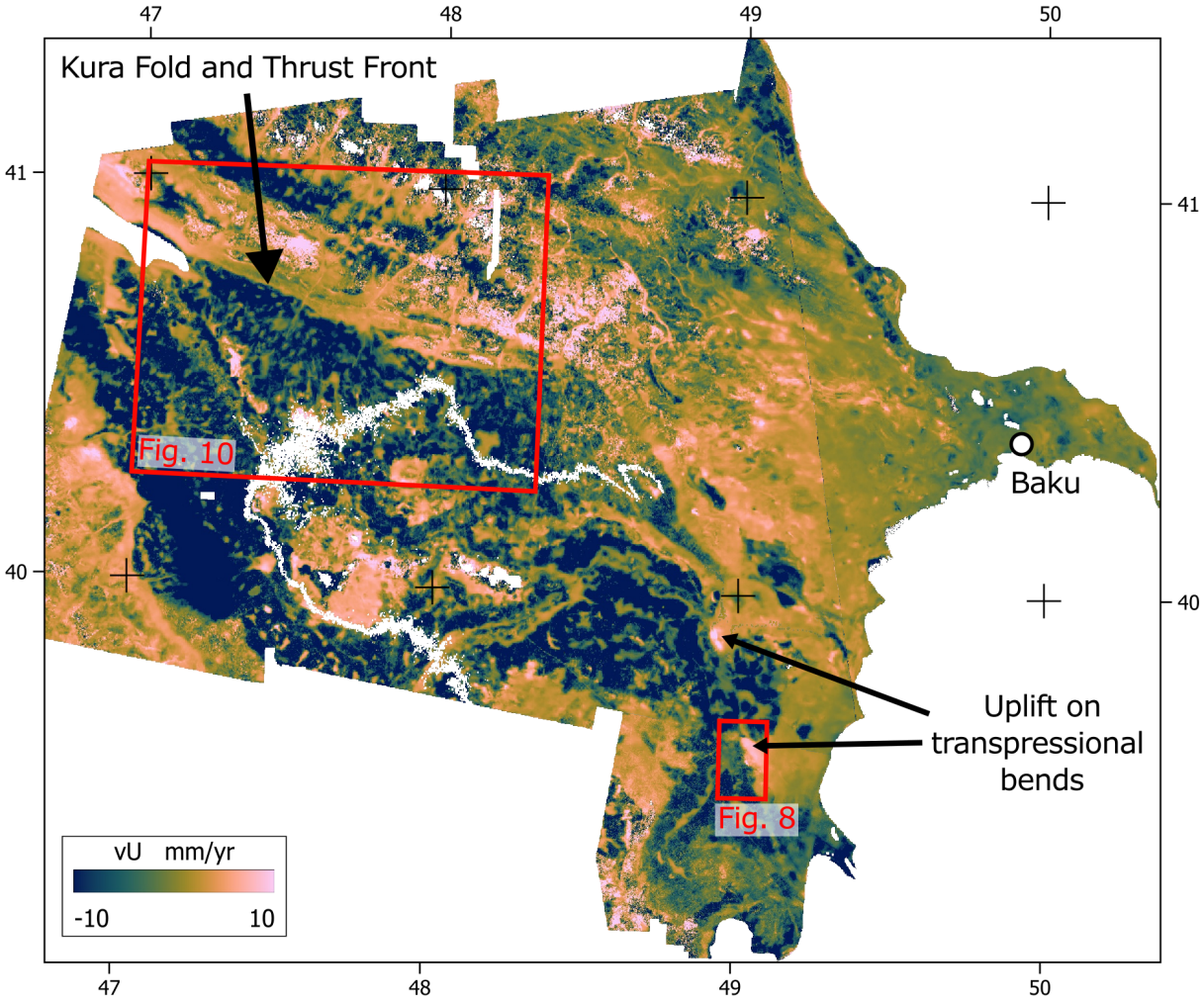

Figure 3.4: Decomposed vU (vertical) component of the velocity field. Arrows point to the sharp contrast in vU across the southern margin of the KFTB, and also at places along the Salyan fault, including localised uplift signals at transpressional bends along the fault trace. Various non-tectonic signals are identified, as described in the text. Boxes show the regions represented in later figures.

The significant phase bias from agriculture in the Kura basin presents a challenge in interpreting tectonic signals, but two prominent gradients in velocity are noted in proximity to the mapped active faults. The first of these is in the eastern margin of the Kura basin, where abrupt changes in east-directed velocity are noted across the mapped Alat fault, within the West Caspian fault zone (Figure 3.6), along with a more subtle signal across the parallel Salyan fault (Figure 3.7). Our velocity field is not sensitive to N-S shortening across the KFTB, and yet an abrupt change from subsidence to uplift across the southern margin of the fold belt is observed in the vertical component (Figure 3.4).

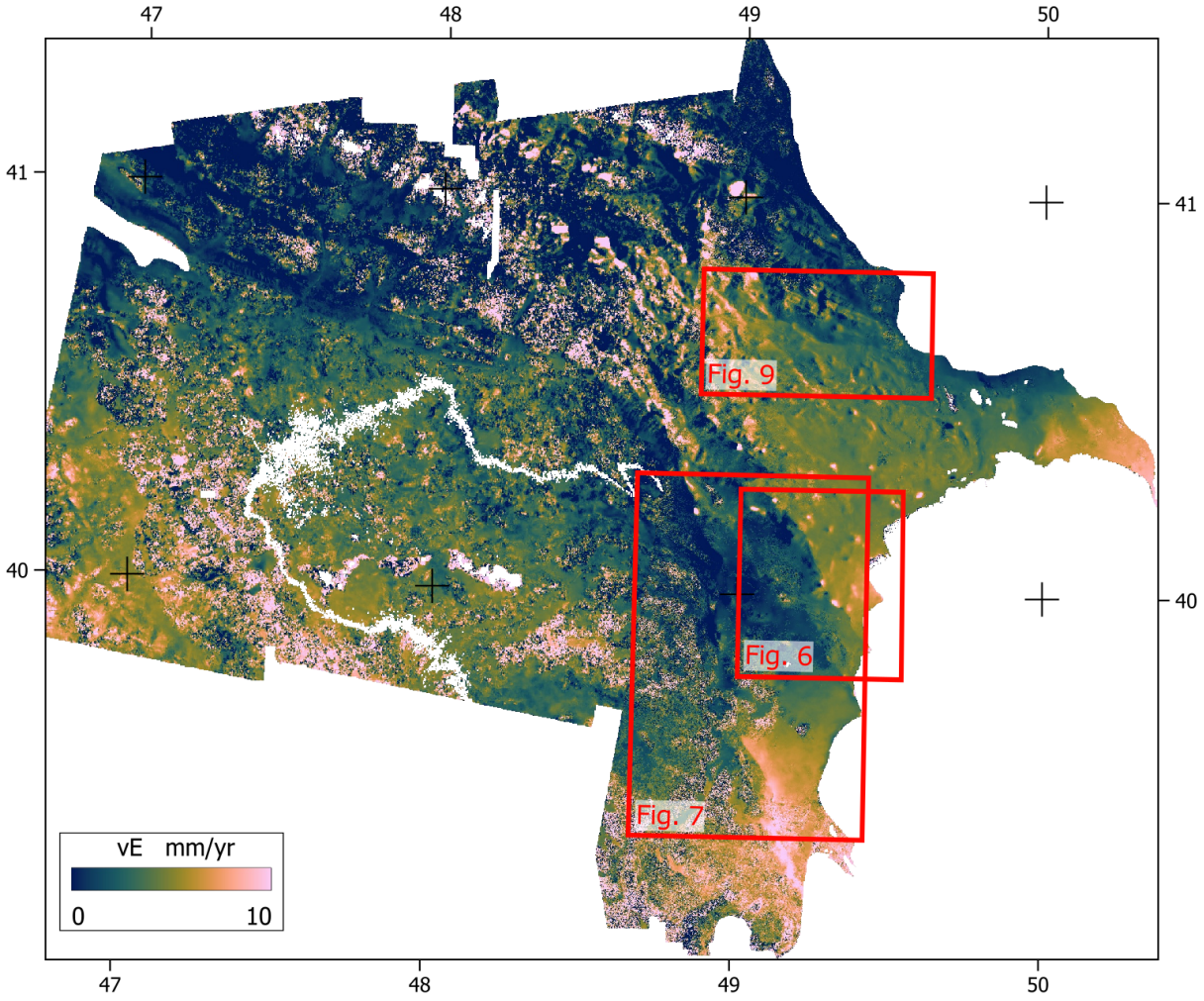

Figure 3.5: Decomposed vE (eastward) component of the velocity field. Probable fault-related signals consistent with right-lateral faulting are associated with the West Caspian fault zone, with white arrows pointing to the Salyan and Alat faults where they intersect with the coast, and a third possible fault, which is unmapped. Possible further fault-related signals are observed north of Baku. Boxes show the regions represented in later figures.

The extent to which this signal reflects tectonic motion is complicated by the change in agriculture across the margin, which might introduce phase bias. Below we discuss first the evidence in the velocity field for slip along the West Caspian fault zone (Alat and Salyan faults). We then discuss potential for tectonic signals in proximity to Baku in the Absheron peninsula, and along the KFTB.

3.3.1 West Caspian Fault zone

Two distinct steps in velocity are observed coincident with the Salyan and Alat faults of the West Caspian Fault Zone (Figure 3.2, e.g. Marshall (2023)). Both faults have an

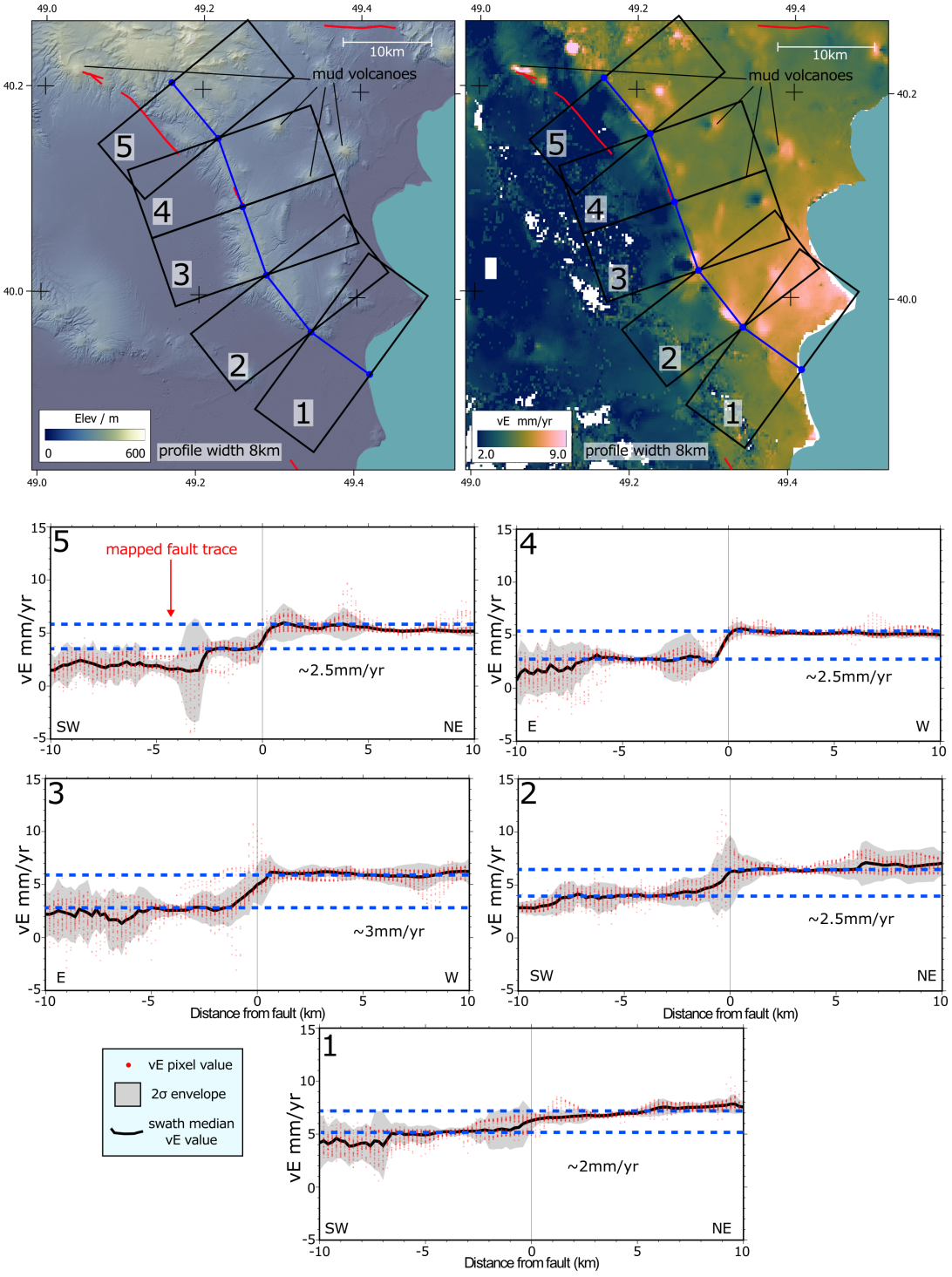

Figure 3.6: East velocity on the Alat Fault, with the blue line representing the sharp change in eastward velocity, and the red lines marking faults with geomorphic expression, as mapped by Marshall (2023). Multiple profiles (1-5) show an offset in velocity near the fault, indicating creep behaviour. The approximate rates of east-directed creep are indicated, based upon the offset between best-fit lines east and west of the fault (blue dashed lines). The velocity field is sampled to 500 m horizontal resolution to avoid unwrapping errors caused by noise. Panel 6 shows a detail of the fault mapped by Marshall (2023) with right-lateral stream offsets marked by black arrows.

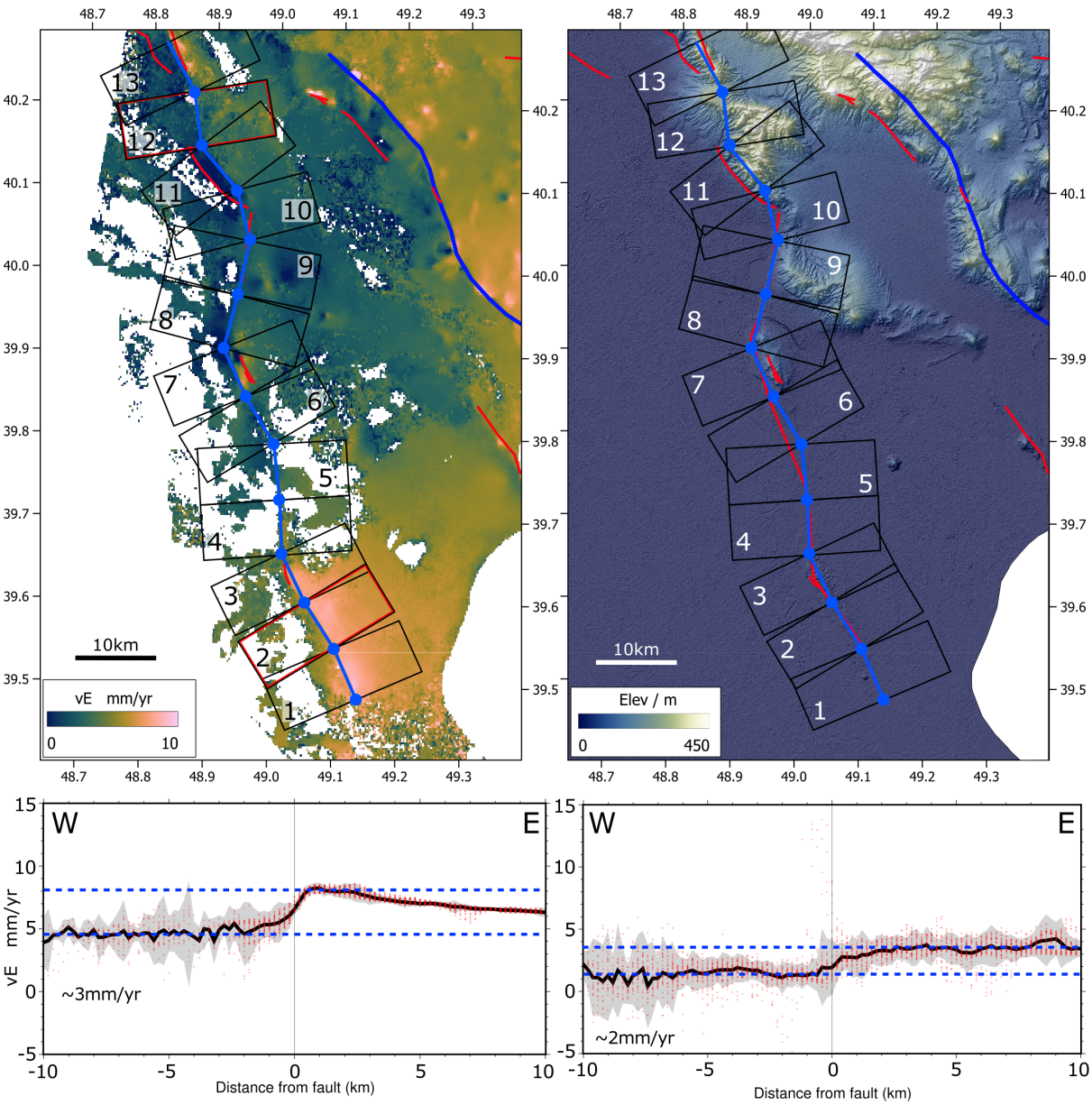

Figure 3.7: Decomposed eastward velocity for the Salyan Fault along with mapped active faults in red. Only two profiles (highlighted in red) show discernible steps in eastward velocity across the fault.

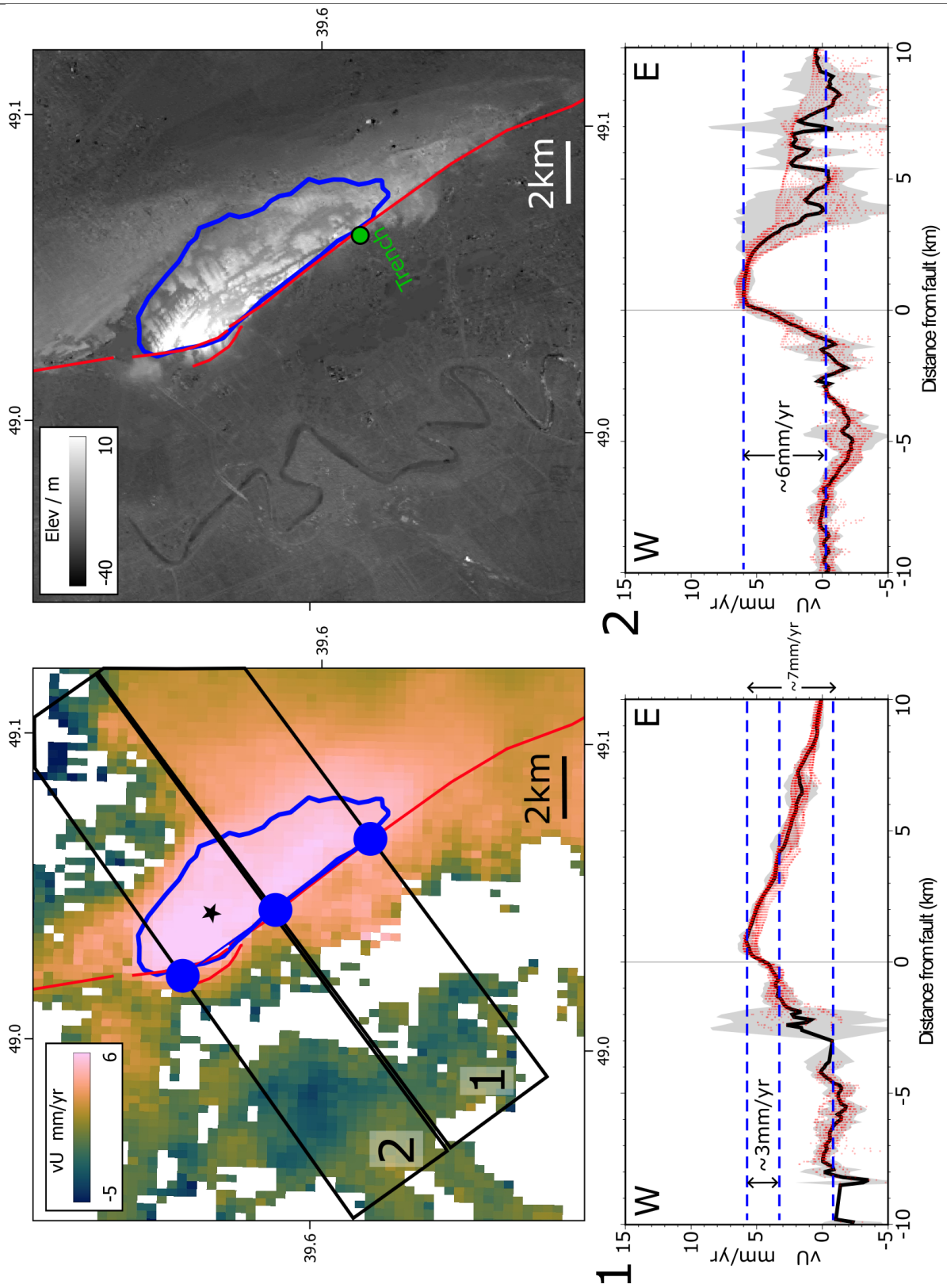

Figure 3.8: (a) Vertical velocity and (b) topography at a transpressional fault bend along the Salyan fault. At the fault bend the topography is elevated and folded stratigraphy is visible (bounded by blue polygon), implying anticlinal folding with the fault trace along its western side. The velocity field shows uplift of between 3 and 6 mm/yr across the fold, with a sharp step at the western margin and an uplift that gradually decreases over ~10 km eastwards from the fault. A line-of-sight displacement time series for the pixel at the black star is shown for track 108D in Figure A13.

overall trend of ∼340°, though they also have a number of distinct bends (Figures 3.1, 3.6, and 3.7). The Alat fault is clearly visible in the east-directed velocity map (Figure 3.5), but does not produce an identifiable signal in the vertical direction (Figure 3.4), suggestive of predominantly strike-slip motion. Though our InSAR velocity maps are insensitive to N-S motion, which should show up the major part of the strike-slip motion on a fault trending ∼340°, the increased east-directed velocity on the eastern side of the fault is consistent with an overall right-lateral slip.

The east-directed velocity map centred on the Alat fault is shown in Figure 3.6, along with profiles of east-directed velocity drawn perpendicular to the fault. The profiles show ∼2.5 mm/yr (maximum 3 mm/yr, minimum 2 mm/yr) of change in east-velocity across the fault. The change is abrupt, indicating surface or near-surface fault creep, but we are unable to distinguish between those two scenarios because of the limit of resolution of our dataset. Given that the fault trends ∼340°, the full slip rate could reach ∼7 mm/yr, substantially faster than the 2.5 mm/yr imaged in the east-velocity map. The creeping fault location obtained from the InSAR map is shown as a blue line in Figure 3.6. The fault trace in blue, obtained from the velocity map, is offset from a fault trace mapped from geomorphic expression, which is shown in red in Figure 3.6 (Marshall 2023). A close-up satellite view of the previously mapped fault trace is shown as panel '6' in Figure 3.7, with several right-lateral stream deflection highlighted. The presence of this fault trace, with clear late Quaternary right-lateral displacement, suggests the surface location of faulting may vary through time.

East-directed velocity map and profiles for the Salyan fault are shown in Figure 3.7. Only two of the profiles show discernible steps in velocity across the fault, with rates of ∼3 mm/yr (profiles 2 & 12). These measurements, combined with the local strike direction, suggest the strike-slip rate along the fault might reach ∼15 mm/yr locally, though the absence of discernible changes in east-directed velocity along much of the fault suggests the rate may be substantially lower overall.

The interpretation of creeping sections on the Salyan Fault of ∼10 km, surrounded by

locked sections of the fault, is difficult to understand physically. The locked sections would act as "pins" tying the fault at either end of the creeping section, so the origin of the stress that drives the creep is unclear. The creeping section of the San Andreas Fault is surrounded by locked sections (Titus et al. 2006) but is 175 km long, and so the effect of being "pinned" at both ends is reduced. One driver for ∼10 km creeping sections could be postseismic motion, where a large earthquake has ruptured the fault south of a creeping section, inducing stress on the creeping section of the fault. Marshall (2023) find evidence from paleoseismic trenching for several earthquakes in within profile 2 (Figure 3.7). One of these earthquakes could have ruptured the Salyan Fault to near profile 12, inducing stress on the creeping section at profile 12. More investigation is needed to verify creep on the Salyan Fault and map it in greater detail to test this hypothesis.

A question arising from our geodetic observations of creep is whether the paleoseismic trench observations by Marshall (2023) are discrete slip events (i.e. earthquakes) or the gradual accumulation of creep along the fault. Two points of evidence for the former hypothesis are the presence of filled fissures and the upward-termination of strands of fault at progressively shallower sedimentary horizons. Filled fissures suggest that the ground fissured during a discrete slip event (Lienkaemper and Williams 2007; McCalpin et al. 2009). Upward-termination of fault strands suggests multiple discrete slip events which each activate different strands of the fault when they occur; continuous creep might be expected to persist on the same strands, although acceleration during "creep events" may also explain this. Taken together, the evidence suggests multiple earthquakes have occurred on the Salyan Fault in addition to its creeping behaviour. An analogy could be the strike-slip Hayward Fault in California, where seven paleoearthquakes are inferred to have occurred on the creeping section of the fault (Lienkaemper and Williams 2007).

The vertical velocity adjacent to the Salyan fault (Figure 3.8), shows significant vertical displacements adjacent to bends in the fault, at places where geological folding is also recognised, and where the presence of an up-to-the-east active fault scarp suggests a component of long-term vertical displacement (e.g. Marshall (2023)).

The above observations, along with right-lateral displacements interpreted from GNSS

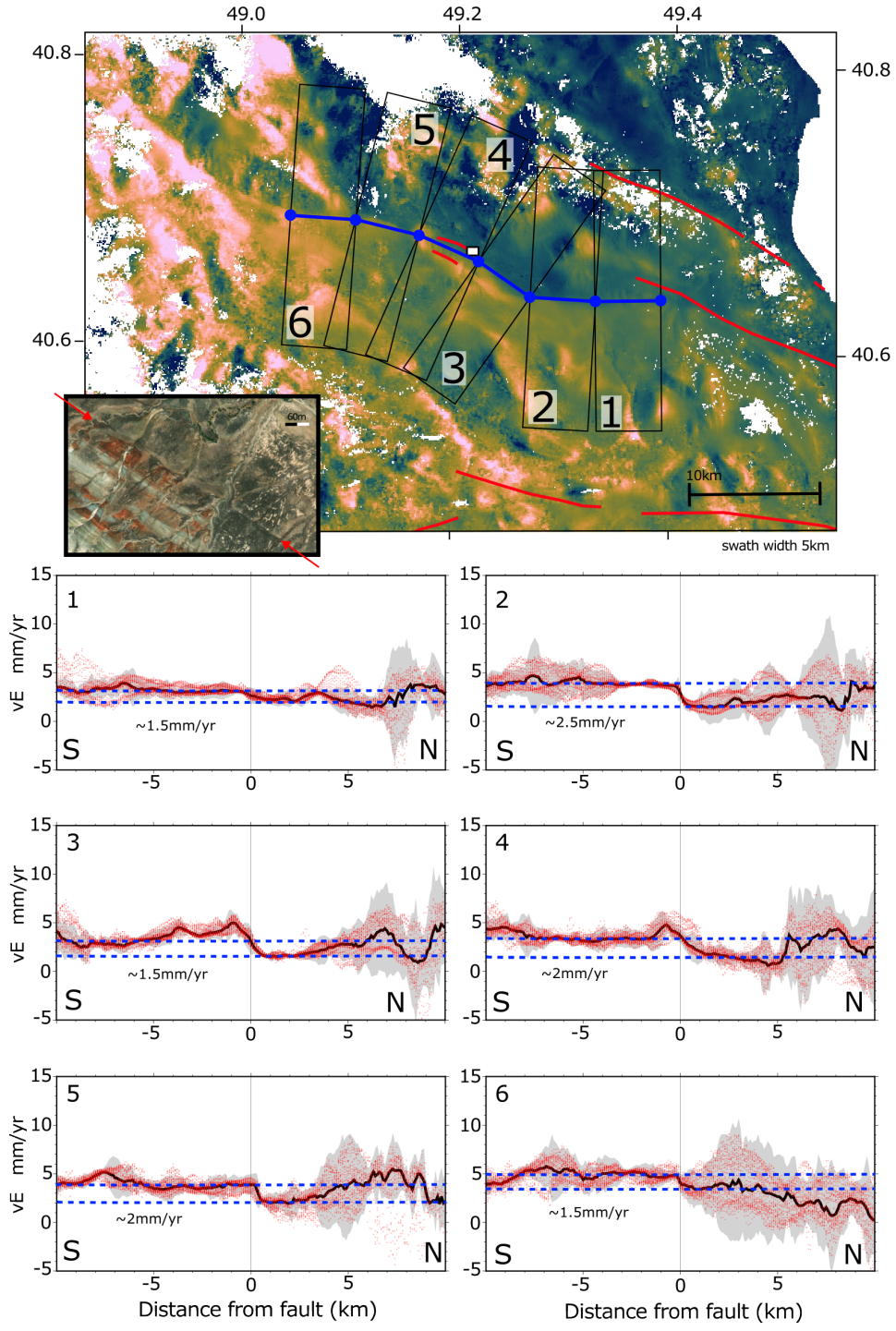

Figure 3.9: East velocity field showing apparent east-west left-lateral fault creep in the region west of the Absheron Peninsula (see Figure 3.5 for location), and coinciding with a fault visible in the geomorphology that runs along bedding and displaces alluvial fan surfaces (shown in red on figure, with an satellite view of the region in the yellow box shown as an inset). Six fault-perpendicular swath profiles show rate of east-west motion across the fault is between 1.5–2.5 mm/yr. The velocities either side of the fault are fit to a horizontal line to assess the contrast across the fault. "Bumps" in the velocity profile associated with mud diapirism and volcanism are excluded from the fitting. Profile 3 shows a decrease in motion relative to its surrounding profiles, likely due to the fault bend reducing the component of fault-parallel motion visible in the east-west direction.

measurements (Figure 3.2) and from geomorphological evidence of right-lateral displacement on both the Salyan and Alat faults (Marshall 2023) lead us to interpret both faults as predominantly right-lateral strike-slip, with localised vertical displacement occurring at transpressional bends along the Salyan fault. The Alat fault appears to have the greater rate of slip of the two faults, and might accommodate the major part of the ∼10 mm/yr of right-lateral shearing implied from GNSS velocities across the Kura basin (Figure 3.2). There is no long-term geological slip-rate measurement across the Alat fault. On the Salyan fault, Marshall (2023), estimate a minimum Holocene slip-rate of 3.9–4.8 mm/yr based upon a displaced terrace riser of assumed age.

3.3.2 West of the Absheron Peninsula (the Sumquayit Fault)

The Absheron Peninsula and adjacent inland areas have few mapped active structures, and yet the proximity to Baku gives it a particular importance in earthquake hazard. We observe a small step in east-west velocity across a previously unidentified fault to the west of the Absheron Peninsula, beginning ∼20 km west of the town of Sumquayit (Figure 3.9). We do not observe the step in the vertical velocity field, implying strike-slip motion. The sense of displacement implies left-lateral faulting. As on the Salyan and Alat faults, the sharp contrast implies shallow creep.

Several swath profiles through the eastward velocity field are presented in Figure 3.9. Each profile is 20km long and is centred on the Sumquayit Fault. We observe several short-wavelength 'bumps' in the grey 2sigma envelope, which we interpret as linked to shallow mud diapirism (e.g. Figure 3.9 profiles 3 & 4). We ignore these bumps when fitting a velocity step across the fault. The velocity contrast reaches a maximum of ∼2.5 mm/yr at profile 2, and is 2 mm/yr in profiles 4 and 5. Profile 3 shows a decrease in velocity to 1.5 mm/yr, which may be due to a bend in the fault, meaning a smaller amount of fault-parallel motion in accommodated in the east-west direction. At the eastern end the velocity contrast is 1.5 mm/yr (profile 1) and can no longer be imaged moving further east. Western swath profiles show a velocity contrast of 1.5 mm/yr (profile 6), but noise in the velocity map on the northern side of the fault causes difficulty in fitting the offset. An apparent velocity contrast continues to the north-west, beyond the limit of our profiles,

but the region is noisy so we do not attempt to calculate a velocity contrast. It is possible the fault follows this path north-west into the Greater Caucasus.

Digital elevation models show the area to be heavily folded, with axes parallel / sub-parallel to the step in velocity. The velocity step closely aligns to the foot of an anticline, expressed as an elongated hill with relief ∼350 m. Topographically correlated InSAR anomalies are unlikely to have caused the velocity change, as the sharpness of the velocity contrast does not correspond to the relatively smooth topography and a ∼350 m relief is unlikely to contribute significantly to the line-of-sight velocity. Fault traces visible in the geomorphology are marked in red on Figure 3.9. Optical satellite imagery (e.g. inset map in Figure 3.9) shows a prominent scarp parallel to bedding within the northern anticline limb, which displaces a series of alluvial fan surfaces.

The sharp step in velocity, consistency over several tens of kilometres, and coincidence with a fault visible in the geomorphology together make us confident that the signal represents surficial aseismic slip of ∼1.5-2.5 mm/yr on an east-west left-lateral tectonic fault. Left-lateral slip on an east-west fault is perhaps surprising, as faults with a similar orientation in the Caspian Sea and further east in the Kopetdag of Turkmenistan appear to have a major right-lateral component of slip (e.g. Walker et al. (2021)). We note that east-west left-lateral faulting onshore is in agreement with a single earthquake focal mechanism from the area (Figure 3.1).

3.3.3 Kura fold-and-thrust belt

As our InSAR velocity maps are insensitive to N-S motion, we cannot directly image N-S shortening across the E-W KFTB. However, the vertical velocity map does show a sharp change, with uplift of the northern side of the north-dipping frontal thrust (Figure 3.4). The interpretation of tectonic displacement across the KFTB is complicated by a sharp change in land usage across its southern, fault-bounded, margin. The southern, footwall, side of the fault is farmed, whereas the hanging-wall block to the north is not. We mitigate this by applying a threshold mask as outlined in Section 3.2 to retain only those pixels in the footwall that do not contain agriculture. After the threshold was applied a

sharp step in vertical velocity is still apparent, with rates of 5–10 mm/yr (Figure 3.10).

The step in vertical velocity is abrupt, and indicative of fault creep either at the surface or at shallow ($<$ 1 km) depths. We do not have a direct estimate on the near surface fault dip, though assuming that it dips in the range 30°–60°, the vertical rates across the southern margin of the fold and thrust belt are consistent with that fault accommodating the major part of the N-S shortening seen in GNSS velocities across the fault (Figure 3.2). A similar uplift is observed on 10kyr timescales with Pierce et al. (2024) obtaining a Holocene vertical rate of 2.9 mm/yr from a displaced alluvial terrace located within Figure 3.10 profile 4 (Figure 3.1.

3.4 Discussion

3.4.1 Observations of creeping faults

Our InSAR analysis demonstrates clear evidence of rapid creep on faults within the Kura basin of Azerbaijan, including the West Caspian fault zone (Marshall 2023) and the KFTB (Pierce et al. 2024). We also highlight a potential E-W left-lateral fault close to Baku, which is also creeping. We have shown that the West Caspian fault zone comprises at least two parallel right-lateral strike-slip faults slipping at rates of up to 7 mm/yr, with the most rapid slip on fault traces that are not clearly identified in the geomorphology. Determining the rate of surface slip across the KFTB is challenging, due to artefacts introduced by agricultural vegetation, but we are able to determine that creep occurs to the near surface.

It is perhaps not surprising that the faults of the Kura basin are creeping, as the thick and rapidly deposited basin sediment accumulations are fluid-rich and support high fluid pressures (Allen et al. 2002; İnan et al. 2024; Javanshir et al. 2015; Pierce et al. 2024). Mud volcanoes provide an insight into the dynamics of fluids at depth, which is often invoked to explain the timescales of earthquake and aftershock occurrence (Miller et al. 2004; Walters et al. 2018). The mud volcanoes are aligned along the major faults (Roberts et al. 2011), and widespread mud volcano inflation indicates focussed fluid flow in prox-

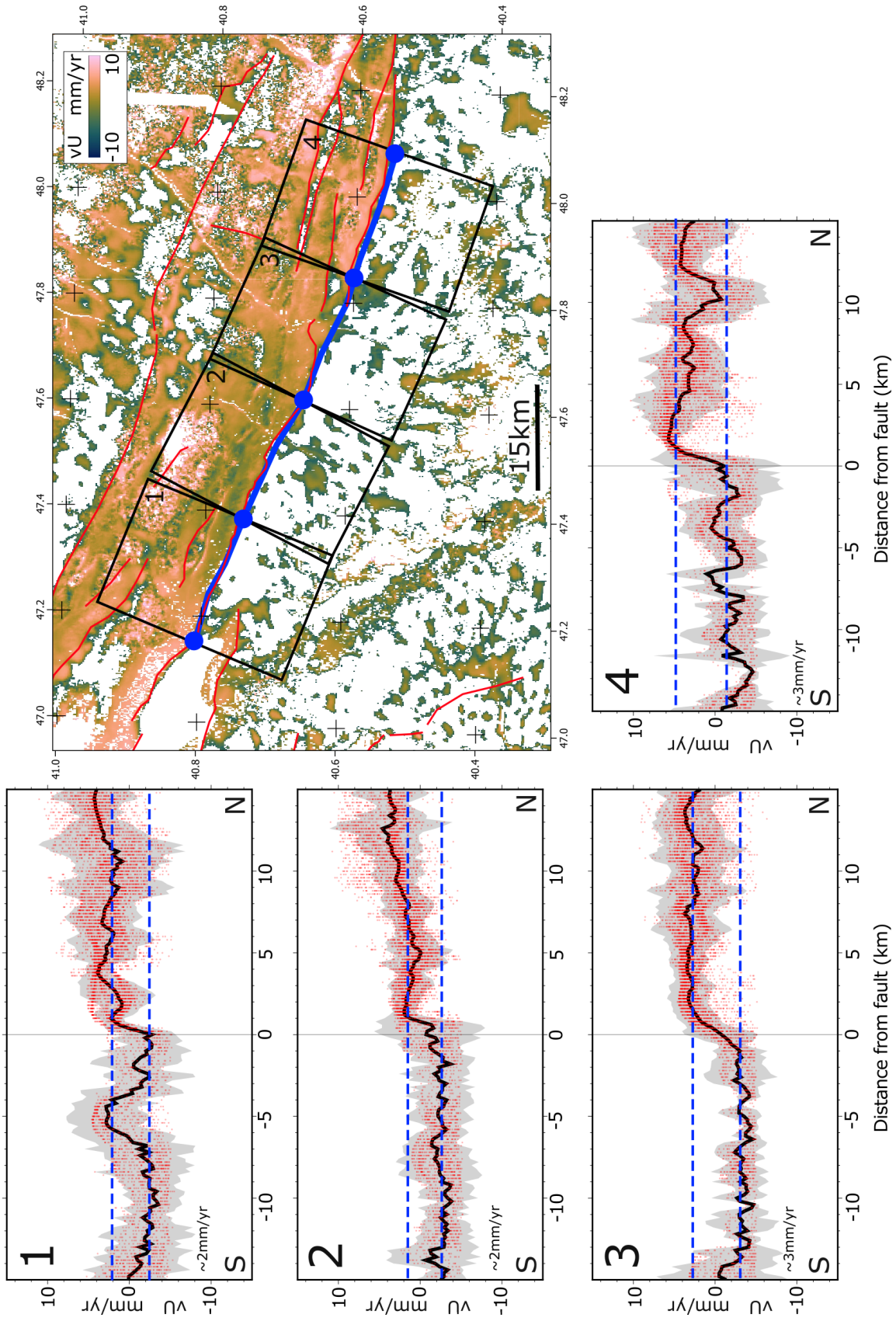

Figure 3.10: Vertical velocity field for the KFTB, filtered using a velocity threshold where pixels with vU > -5 mm/yr are retained, in order to exclude pixels in agricultural areas that may show apparent subsidence signals related to "phase bias". Parallel swath profiles along the fault show a consistent near-fault velocity jump of ∼2–3 mm/yr.

imity to the faults. The driving force behind them is thought to be overpressuring of fluidised sediment, often present in areas of extremely high sedimentation rate, such as accretionary wedges (Platt 1990). However there are many suggestions for the source of this fluid, including pore-fluid expulsion during compaction (Kopf 2002) and organic breakdown by methane-producing microbes (Niemann et al. 2006). Erupted material tends to be mud, fluid and gas, often methane, which can lead to explosive eruptions and even columns of fire (Kopf 2003). Mud volcanoes are associated with mud diapirs, which are large bodies of buoyant, viscous mud which rise through the crust in a similar manner to salt (Chen et al. 2014; Kopf 2002). They also represent a significant hazard to communities living around them and to offshore infrastructure where they are present, for example in the Caspian Sea. While beyond the scope of this work, we have shown it is feasible to monitor mud volcano deformation across Azerbaijan on day-week timescales.

Despite the clear imaging of surface creep there is evidence that both the West Caspian fault zone and the KFTB have ruptured in earthquakes in the past (Marshall 2023; Pierce et al. 2024). Eastern parts of the KFTB and adjacent parts of the range-front thrust fault may have hosted a part of the 1902 and 1667 Shamakhi earthquakes, as evidenced by the isoseismal distribution and paleoseismic evidence for recent surface rupturing on the range-front fault at Agsu (Pierce et al. 2024) (Fig. 3.1). More westerly parts of the fold belt show paleoseismic evidence for a discrete slip event, potentially in an earthquake, in the period 334–118 BCE (Pierce et al. 2024). The Salyan fault in the West Caspian fault zone, which we show to be creeping, appears to have hosted up to seven discrete surface-rupturing events over the last five thousand years (Marshall et al. 2023). In this latter case there are no substantial historical records of earthquakes in proximity.

Assuming that the paleoseismic interpretations are correct, we now examine why there is an apparent discrepancy between our observations of present-day creep and the paleoseismic records of discrete surface rupturing. Firstly, it is possible that either only a certain amount of strain within a fault zone is accommodated seismically, with a portion of strain being released as creep on a different fault. An analogy would be the Hellenic Arc, where only ∼20% of the strain observed via geodesy is released in earthquakes (Reilinger et al.

2006; Shaw and Jackson 2010). Secondly, we could be observing permanent spatial heterogeneity in locking: where short sections of an overall creeping fault are locked leading to earthquake rupture (e.g. along the Phillipine Fault (Dianala et al. 2020)), although this doesn't seem to be the case for the Salyan Fault, where we see creep around the site where Marshall (2023) identify paleoearthquake rupture. Thirdly, the discrepancy could be related to time-varying fault behaviour, with periods of fault creep interspersed with periods of locking and strain accumulation. This could be due to temporal variations in locking (Meltzner et al. 2015) on timescales longer than an earthquake cycle. Fourthly, earthquake ruptures nucleating on a deeper, locked, section of the fault could enable dynamic weakening in the shallow, creeping, section allowing an otherwise velocity-strengthening medium to host discrete ruptures (Harris 2017).

A final way to reconcile observations of earthquake rupture and creep is changes in fault behaviour within an earthquake cycle. There is a potential analogy between the behaviour of the KFTB and the Tabas Fold and Thrust Belt of Iran, which hosted the M_w 7.3 1978 Tabas-e-Golshan thrust-faulting earthquake which ruptured to the surface on steeply-dipping splays from a shallowly-dipping thrust plane at depth (Berberian 1979; Walker et al. 2015). Post-seismic slip at the surface is on-going over forty years after the earthquake, as imaged with both InSAR (Copley 2014; Zhou et al. 2018) and optical image correlation (Zhou et al. 2016), and it is possible that the signals we observe are part of a long postseismic response to earthquake slip. In this way, the 1902 Shemakhi earthquake may have ruptured deeper parts of a thrust system beneath the greater Caucasus, and prompted accelerated and localised aseismic slip in the upper parts of the fault system, which are then recognised as discrete 'earthquake' ruptures in paleoseismic trench exposures.

The faults of the Kura basin are potentially an outstanding natural laboratory for the study of fault creep and episodic slip behaviour, but to understand the time dependence of the creep behaviour that we have imaged requires further work, integrating geological, geodetic, and seismological methods. Better instrumentation of faults poorly oriented for InSAR measurement, such as the Salyan Fault, is also required. A combination of dense

GNSS and creepmeters would provide valueable ground-truth to the geodetic data, and would elucidate how localised to the faults creep is, giving insight into the depth of creeping sections (Özdemir et al. 2025). This would also provide better temporal resolution into creep behavior than can be achieved with InSAR. This work is essential to better understand the hazards that these faults pose.

3.4.2 Fault kinematics: extrusion towards the South Caspian Basin

Our InSAR measurements and previous GNSS observations, help us to identify zones of active faulting, and to understand how the population of active faults accommodate tectonic motions. The Kura Basin is converging with Eurasia, and this is accommodated in the KFTB and the Greater Caucasus (e.g. Figure 3.11). Eastwards, towards the Gobustan region and the Absheron Peninsula, the Kura Frontal Thrust bends southwards, joining with a series of parallel right-lateral faults of the west Caspian fault zone. Along the north of the Absheron Peninsula we observe slip on the newly identified Sumquayit left-lateral fault (Figure 3.11).

The West Caspian and Sumquayit faults together define the margins of a triangular wedge moving eastwards relative to the rest of the Kura Basin, which is clearly imaged in the insar velocity field (Figure 3.5), and also the GNSS measurements (Figure 3.1). The southern boundary of this wedge is much more sharply defined in the velocity field than the northern boundary (the Alat Fault could be moving at up to 10 mm/yr, while the Sumquayit Fault is likely only moving at 1.5–2 mm/yr), implying internal deformation of the wedge. The wedge encompasses much of the Gobustan National Park, which has an abundance of mud volcanoes, and pervasive folding of young (Pliocene and Quaternary) sediments evident in aerial imagery.

In Figure 3.11 we highlight a subset of folds within the SCB, which are NE-SW trending, and appear to be restricted to the region adjacent to the onshore Gobustan wedge, suggesting that they may be related to the lateral expulsion imaged onshore. We speculate that convergence of the Kura Basin with Eurasia, combined with the large contrast in

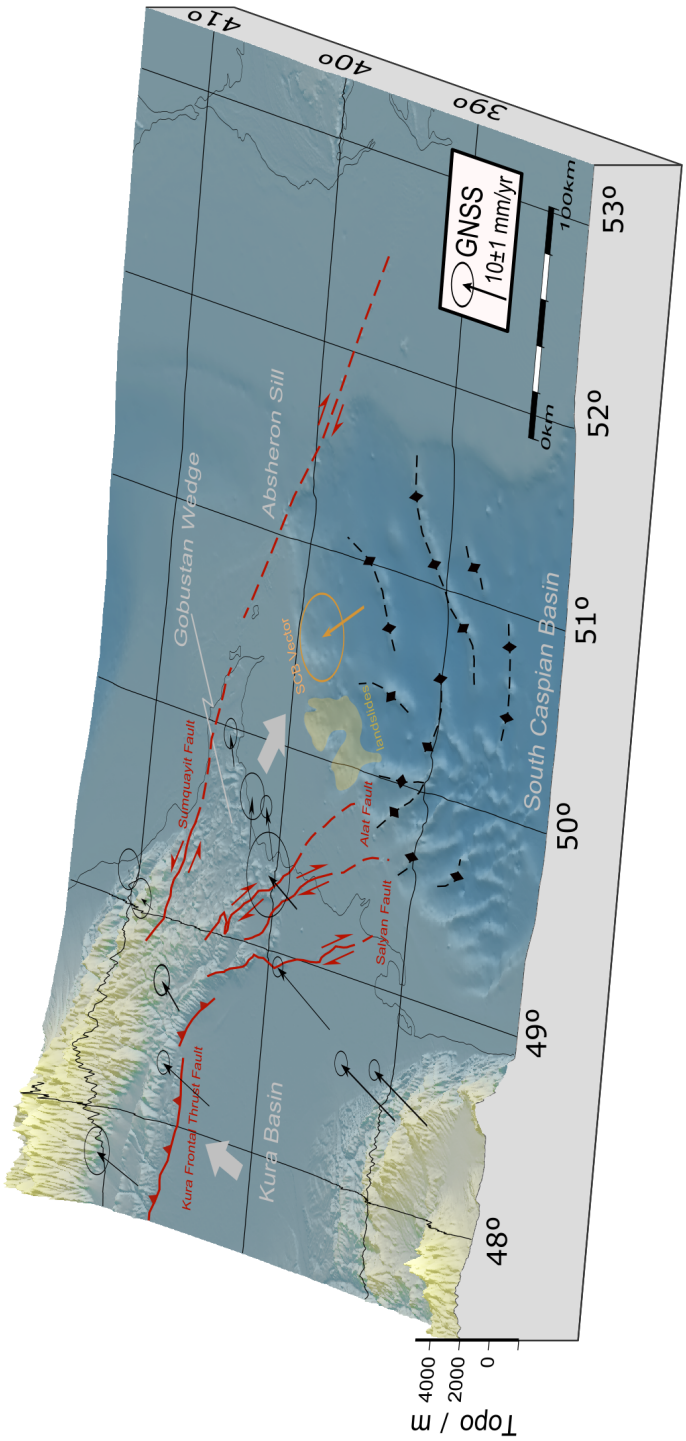

Figure 3.11: Perspective view showing merged topography and bathymetry for the South Caspian Basin and its surroundings, with the coastlines shown as thin black lines. Faults are mapped in red. NE-SW trending folds in the deeper parts of the basin are highlighted in black with diamond decorations. Large submarine landslides visible in the bathymetry are highlighted in yellow. GNSS data from Kadirov et al. (2014) shows the convergence of the Kura Basin with Eurasia taken up by the KFTB and the Caucasus. The triangular region bounded by the Alat Fault and the Sumquayit Fault is moving eastward relative to the Kura Basin, and appears to extrude into the SCB, possibly contributing the folding of offshore sediments. The SCB velocity vector in yellow is from Dodds et al. (2022a) who used the rates of the basin-bounding faults to infer the velocity of the basin.

elevation between the eastern Caucasus and the adjacent SCB, is driving a lateral extrusion of material within the Gobustan Wedge. Sedimentary thicknesses in the Caspian are thought to reach up to 28 km (Knapp et al. 2004), with over ten kilometres of Pliocene and Quaternary clastic sediment overlying thick Miocene muds of the Maykop formation, which are the source rocks for the extensive hydrocarbon deposits in the basin (Abrams and Narimanov 1997). Offshore folds are usually interpreted to detach within the Maykop mud formation (Allen et al. 2003; Devlin et al. 1999; Knapp et al. 2004). We suggest that material within the wedge is moving towards the deep Basin, detaching along the Maykop muds, and causing folding within the offshore basin sediments.

If our model is correct, it means that observations of surface motions and faulting seen within the onshore Kura basin may reflect deformation within the sedimentary cover rather than the underlying basement, and therefore may respond both to local gravitational forces as well as regional tectonic forces. The relative motions of the basement underlying the South Caspian and Kura basins are more likely to represent the regional tectonics. There is evidence of subduction of the SCB beneath the Talesh Mountains from earthquake focal mechanisms (Jackson et al. 2002), so the SCB may be subducting beneath the crust of the Gobustan Wedge, while the sediment is pushed into the basin by the converging Lesser and Greater Caucasus.

3.5 Conclusions

We have imaged rapid surface and near-surface creep along right-lateral strike-slip faults of the west Caspian fault zone, along the KFTB, at the northern margin of the basin, and near the Absheron Peninsula close to Baku. The conjugate right-lateral and left-lateral faults together appear to be accommodating a large-scale expulsion of crustal material towards the interior of the SCB. The existence of widespread near surface creep on faults of the Kura basin is perhaps not surprising, given the widespread evidence of fluid mobilisation within the underlying sediments. The behaviour of the faults, and whether they also have potential to slip in earthquakes, has implications for the seismic hazard that they pose, but also poses unanswered questions about the long-term behaviour of the

faults, and whether they undergo periods of slip accumulation and release in earthquakes.

Acknowledgments

This project was funded by the Leverhulme Trust, through the projects "EROICA" (RPG-2018-371) and "NEPTUNE" (RPG- 2018-243), by the NERC-ESRC Increasing Resilience to Natural Hazards program 'Earthquakes without Frontiers' (NE/J02001X/1), allocation 0009090 from the Research England GCRF Support Fund, and through the EPSRC Impact Accelerator project 0013867 'Multi-hazard risk assessment for infrastructure / ground engineering projects', and COMET (GA/13/M/031). COMET is the NERC Centre for the Observation and Modelling of Earthquakes, Volcanoes and Tectonics, a partnership between UK Universities and the British Geological Survey. Benedict Johnson is supported by the Oxford NERC-DTP (NE/S007474/1)

Data Availability

All *Sentinel-1* and *Sentinel-2* data used in this study was obtained at no cost through the European Space Agency Copernicus SciHub server or NASA's ASF DAAC, and is available for download at no cost. Interferograms generated by the LiCSAR processing chain were downloaded from the COMET LiCS Portal. The LiCSBAS time series analysis software used to generate velocity fields from interferograms is available at the Github repository. The velocity maps generated in this study will be made available at the Zenodo repository 10.5281/zenodo.14497284. Software to decompose line of sight velocities into east-west and up-down velocities is available at the Github repository.

Statement of Authorship for joint/multi-authored papers for PGR thesis

To appear at the end of each thesis chapter submitted as an article/paper

The statement shall describe the candidate's and co-authors' independent research contributions in the thesis publications. For each publication there should exist a complete statement that is to be filled out and signed by the candidate and supervisor **(only required where there isn't already a statement of contribution within the paper itself).**

Title of Paper	Rapid fault creep in the fluid-rich Kura Basin, Azerbaijan, imaged with InSAR
Publication Status	□Published □ Accepted for Publication X Submitted for Publication □Unpublished and unsubmitted work written in a manuscript style
Publication Details	Johnson, Benedict; Elliott, John; Yetirmishli, Gurban; Javanshir, Rashid; Kazimova, Sabina; Marshall, Neill; Payne, Jessica; Walker, Richard (Geophysical Journal International (in review))

Student Confirmation

Student Name:	Benedict Johnson		
Contribution to the Paper	Performed the time series InSAR analysis, valiation, mapping, interpretation of results, and wrote the manuscript.		
Signature Ben Johnson		Date	26-April-2026

Supervisor Confirmation

By signing the Statement of Authorship, you are certifying that the candidate made a substantial contribution to the publication, and that the description described above is accurate.

Supervisor name and title: Prof. Richard T. Walker		
Supervisor comments The above statement is accurate. The candidate led this work and made a substantial contribution.		
Signature 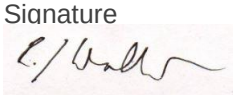	Date	26/04/2025

This completed form should be included in the thesis, at the end of the relevant chapter.

4 | The 1985 Wuqia Earthquake: rupture beneath the sedimentary cover on a strike-slip transpressive structure

4.1 Introduction

4.1.1 The 1985 Wuqia Earthquake

The M_w 6.9 Wuqia Earthquake ruptured on 23^{rd} August 1985 in north-west China, about 60 km west of the city of Kashgar. The earthquake caused "some deaths",~10,000 injuries (Feng et al. 1986) and around 2,000,000 yuan damage to the hydroelectic power station, equivalent to around 1,000,000 USD today. The population of the region has grown significantly since 1985, with the city of Kashgar having doubled in size since the year 2000 (*China: Xīnjiāng (Prefectures, Cities, Districts and Counties) - Population Statistics, Charts and Map* 2025). This means the exposure to earthquake hazard in the region has increased dramatically. In addition, hazards relating to water scarcity exist. China has been addressing the water scarcity, caused by a combination of agricultural expansion in Xinjiang and declining glacier volumes in the Tian Shan and Pamir due to climate change, by building more dams to provide energy and water storage. Displacement hazard from future earthquakes has the potential to damage dams in the future, particularly given one has been constructed very close to the 1985 surface ruptures (Figure 4.4).

The 1985 earthquake has been difficult to fit into a tectonic model for the region. The structural geology of the surface sediments does not correlate very well with the focal mechanism determined from seismology (Burtman and Molnar 1993; Fan et al. 1994; Wang et al. 1987). Some authors attribute this mismatch to inaccuracies with the seismologically-determined source parameters and epicentre (Li et al. 2019). Others attribute it to differential behaviour between the crystalline basement of the Tarim and the surface sediments (Ainscoe 2018). Distinguishing between these scenarios is important because it tells us whether we may miss seismic hazard by examining surface geology

alone. In Chapter 2 we demonstrated this was the case for the 1949 M_w7.4 Khait Earthquake.

In this chapter, we generate a catalogue of calibrated earthquake locations using the *mloc* software to build a better understanding of the location and potentially depth of the Wuqia mainshock and of other seismicity within its vicinity. Using our improved catalogue of earthquake locations, combined with published details of geological structure and of surface rupture, we build a source model for the 1985 Wuqia Earthquake.

4.1.2 Tectonic background

The Pamir Mountains form an extensive high-altitude continental plateau within the ongoing India-Eurasia collision, west of the larger Tibetan plateau (Burtman and Molnar 1993). The plateau is bounded to the east by the low-lying and relatively undeformed Tarim basin (Neil and Houseman 1997). Evidence from GNSS (Ischuk et al. 2013; Metzger et al. 2020; Zubovich et al. 2016), geology (Robinson et al. 2004; Rutte et al. 2017a; Rutte et al. 2017b), and geodynamic modelling (Jay et al. 2017) suggests ongoing east-west extension due to gravitational potential energy contrasts between the Pamir and their surroundings. In the Tajik Basin, to the west of the Pamir, this has driven the growth of parallel north-south striking folds since 12 Ma (Abdulhameed et al. 2020). Present-day fold growth via creep in the Tajik Basin has been imaged with InSAR (Metzger et al. 2021; Wilkinson 2023). On the eastern margin of the Pamir, this east west extension is thought to be the driving force behind the growth of the Tuomuluoan Thrust (Figure 4.2) and other parallel structures into the Tarim Basin sediments.

The Tarim Basin is a Proterozoic piece of continental crust pinned between the Tibetan Plateau, Pamir, and Tian Shan (Neil and Houseman 1997). It exhibits clockwise rotation about a vertical axis, potentially driven by underthrusting Indian lithosphere (Copley 2012), and behaves as a rigid plate, as testified by the lack of internal topography relative to the surrounding mountain ranges (Davies et al. 2016). There are a small number of faults within the Tarim (Tong et al. 2012) and seismicity studies show some internal deformation does occur within the basin (Sloan et al. 2011; Xu et al. 2006).

The boundary between the Pamir and Tarim, the Kashgar Yecheng Transfer System (KYTS) (Figure 4.1), today has very little strike-slip motion across it according to GNSS (Zubovich et al. 2010), but there is thermochronological (Sobel et al. 2011) and geological (Burtman and Molnar 1993) evidence that this was more rapid in the past. Cowgill et al. (2009) estimates ∼280 km of right lateral motion between the Pamir and Tarim has been accommodated by this system during the Late Cenozoic. Burtman and Molnar (1993) suggest ∼300 km northward motion of the Pamir based on deflection of a Paleozoic geological suture and the length of a south-dipping intermediate depth seismic zone which the authors suggest being continental subduction, and subsequent workers agree (Sippl et al. 2013b).

Strike-slip faulting occurs north of the Tarim basin and Wuqia region. In particular, the Talas Fergana Fault (TFF; Figure 4.1) terminates at the northern edge of the basin near to the site of the Wuqia Earthquake. This right lateral strike slip fault runs ∼400 km along a NW-SE trend dividing the West Tian Shan and Fergana Basin from the Central and Eastern Tian Shan. It has a geological slip rate of ∼2.2-6.3 mm/yr (Rizza et al. 2019), which is faster than the present-day geodetic slip rate (Abdrakhmatov et al. 1996; Reigber et al. 2001; Zubovich et al. 2010). Rizza et al. (2019) suggest this is due to the Talas Fergana Fault accommodating vertical axis rotations, which geodetic measurements of slip do not account for. This is backed up by paleomagnetic evidence for anticlockwise rotation of the Fergana Basin by 20 ± 10^{o}, relative to the Issyk Kul Basin, since the Paleogene (Thomas et al. 1993). The southern termination of the fault is not clear. Rizza et al. (2019) suggest termination with thrust splays in the Arpa Basin within the Tian Shan (Figure 4.1). Others suggest the fault continues well into the Tarim Basin, linking with the right lateral Shache-Yangdaman Fault (Shache-Yangdaman Fault (SYF)) (Figure 4.1) (Bande et al. 2017; Wei et al. 2013). This SYF is not expressed in Quaternary geomorphology but is visible in seismic reflection profiles and is thought to be active in the Pliocene (Wei et al. 2013). It is possible this fault still moves very slowly, but its geomorphic expression is obscured by the rapid sedimentation from Pamir erosion.

The northwestern corner of the Tarim Basin thus has complicated tectonics, as it is at the

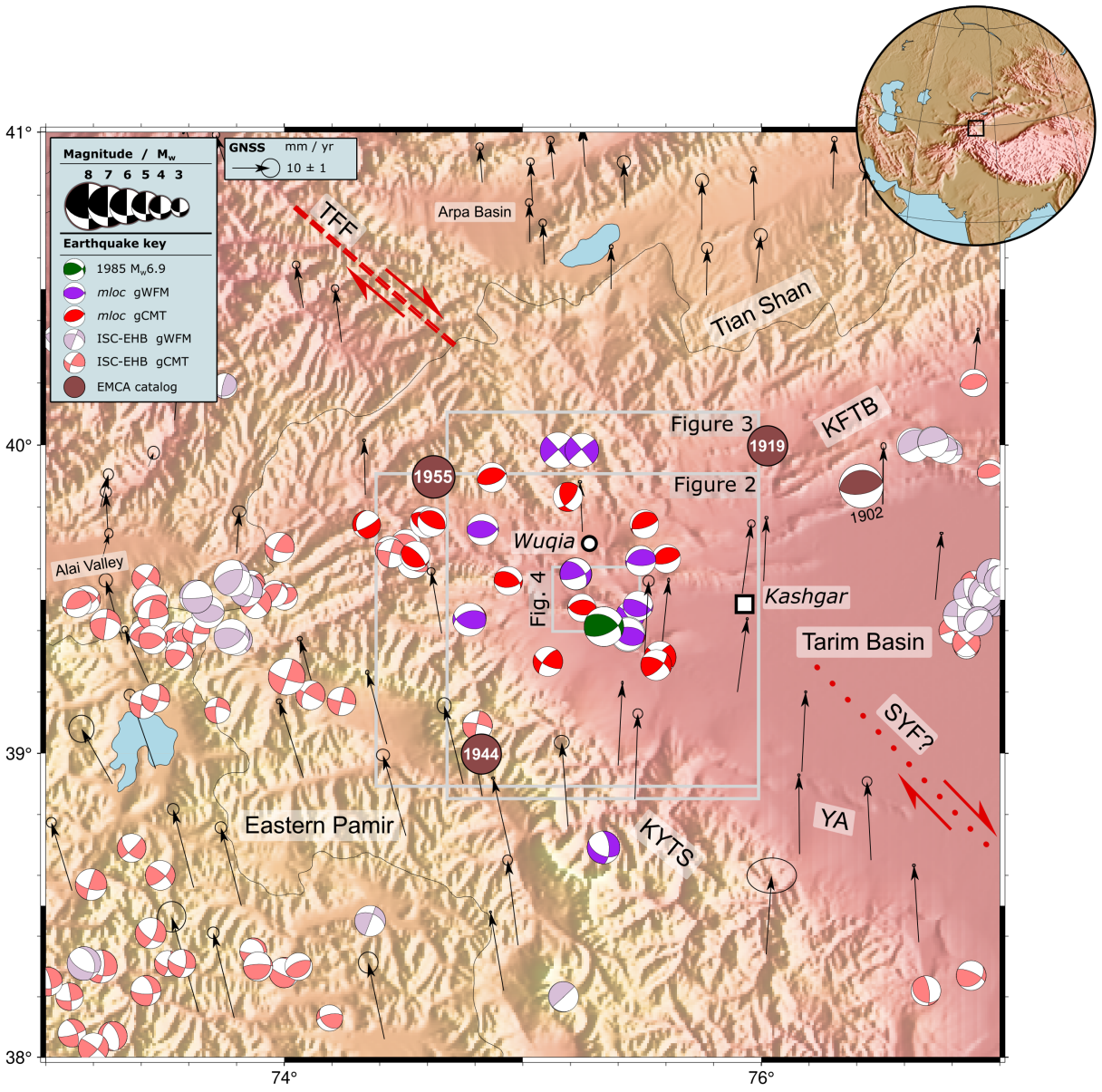

Figure 4.1: Focal mechanisms and GNSS vectors for the Pamir-Tian Shan-Tarim Basin intersection. The 1986 M_w 6.9 Wuqia Earthquake is in green. Mechanisms relocated with *mloc* are in bold colours. Mechanisms not relocated with *mloc* are in pale colours, and are placed at the ISC-EHB epicentre if available (Weston et al. 2018). Red mechanisms are from the gCMT catalog (Dziewonski et al. 1981; Ekström et al. 2012), purple mechanisms from the gWFM catalog of manually body-waveform modelled mechanisms (Wimpenny and Watson 2020). Earthquakes before 1976 are from the EMCA catalog (Mikhailova et al. 2015), apart from the 1902 earthquake which is from Kulikova and Krüger (2017). The active TFF is marked with a dashed line, and the relict SYF is marked with a dotted line. TFF = Talas Fergana Fault; SYF = Shache-Yangdaman Fault; KFTB = Kepingtage Fold and Thrust Belt; KYTS = Kashgar-Yecheng Transfer System ; YA = Yengisar Anticline

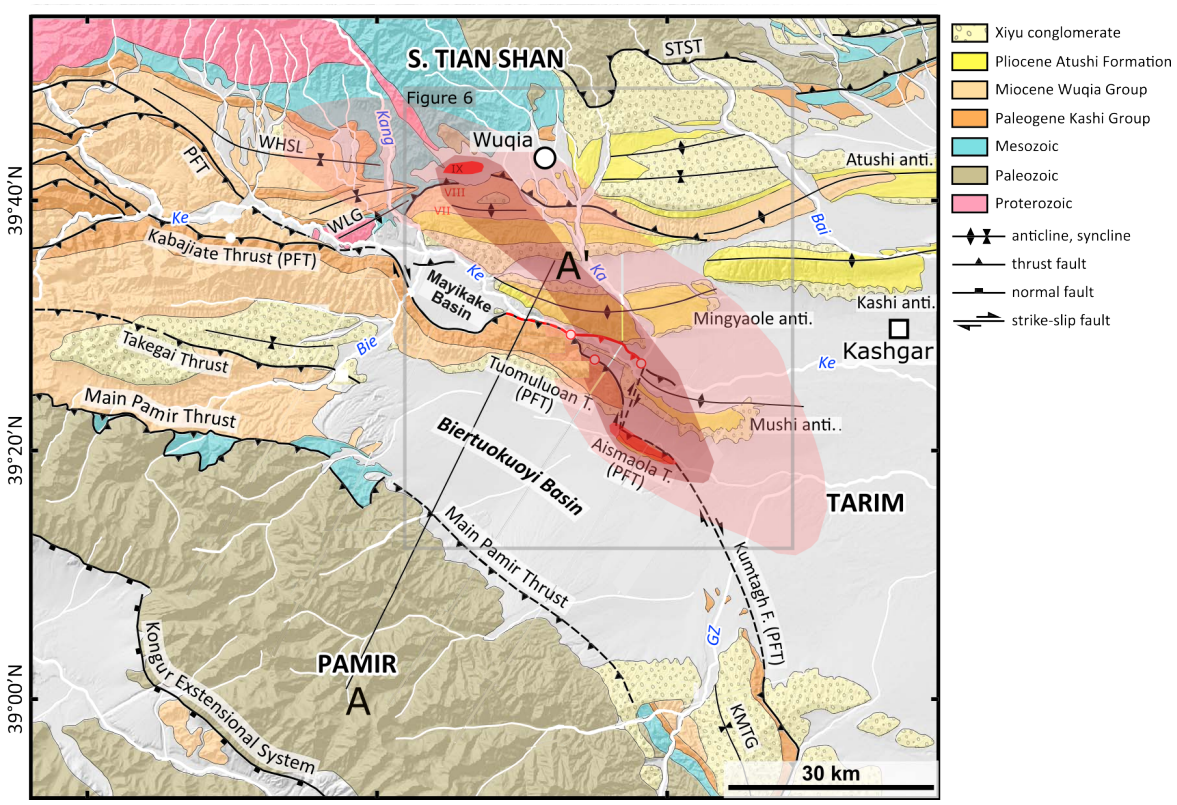

Figure 4.2: Geological map adapted from Li et al. (2019). The surface ruptures from the 1985 M_w 6.9 Wuqia earthquake are in red. These ruptures are at the point where the Kepingtage Fold and Thrust Belt meets the north-east verging thrusts associated with Pamir convergence. Profile A-A' from Li et al. (2019) is shown with *mloc* earthquakes overlain in Figure 4.3. The Biertuokuoyi Basin is a piggyback basin filled with ~10 km scale alluvial fans from the Quaternary. Intensity contours for the 1985 Wuqia earthquake are from Feng et al. (1986) and Feng et al. (1988). Ke = Kyzylsuu River

intersection of four different tectonic systems: the Pamir Frontal Thrust accommodating Pamir-Tian Shan convergence; the Kepingtage Fold and Thrust Belt accommodating Tarim - Tian Shan convergence; the Talas-Fergana Fault accommodating some amount of strike slip between these systems; and the SYF within the Tarim Basin. In addition, there are structures within the sedimentary cover accommodating convergence between the Pamir, Tarim and Tian shan.

The first of these structures in the sedimentary cover is the south-west-dipping Tuomuluoan Thrust, which exposes the Paleogene Kashi Group and thrusts it over the Pleistocene Xiyu Conglomerate, representing at least 18 km of slip along the fault ($\sim$ 16 km lateral motion) (Li et al. 2019). It is roughly contiguous with the Pamir Frontal Thrust: the fault which accommodates most of the convergence between the Pamir and Alai Valley (Figure 4.1) (Patyniak et al. 2021; Sobel et al. 2013; Zubovich et al. 2016). Using seismic reflection data, Li et al. (2019) map the thrust to a flat detachment between the sediments and basement at $\sim$7 km depth. This connects to a set of parallel ramps over which the Pamir are thrust. The thrust carries forward the Biertuokuoyi Piggyback Basin filled with relatively undeformed Pliocene-Quaternary sediments (Li et al. 2019; Ori and Friend 1984). The surface exposure of the thrust is at the Kyzylsuu River, which has eroded the northern limb of the associated fold significantly. The shortening rate across it is $\sim$6–7 mm/yr since 15 ka (Li et al. 2012). Bufe et al. (2017) use InSAR analysis to find a present day uplift rate of 0–2 mm/yr for the Tuomuluoan Fold, which is similar to the geological uplift rate of $>$1.7 mm/yr, derived from Li et al. (2012)'s shortening rate and the fault dip.

The Mingyaole Anticline is a fold growing above a horizontal detachment between Paleogene and Neogene sediments (Li et al. 2019). In the present, Bufe et al. (2017) find an uplift rate of $\sim$3 mm/yr for the Mingyaole Anticline using InSAR. The geological uplift rate for the Mingyaole Anticline is $\sim$1.5–3 mm/yr (Bufe et al. 2017; Li et al. 2015; Thompson 2013), so only slightly slower than the present day rate from InSAR. This anticline additionally shows signs of dextral shear, with en-echelon normal faults striking at $\sim$30°, consistent with shear on a plane striking $\sim$300°.

While the Tuomuluoan Thrust verges north-east, there are several structures close to the Pamir that verge south-west (dip north-east) as evidenced by seismic reflection profiles. These include the Yengisar Anticline (76.383°E, 38.860°N)(labelled YA in Figure 4.1) (Wang and Wang 2016).

Around 20 km east of the Mingyaole Anticline, seismic reflection profiling finds a sedimentary thickness of ∼10–15 km (Gao et al. 2013), thicker than the ∼8-10 km in the Biertuokuoyi Basin (Figure 4.3).

4.1.3 Seismicity in the north-west Tarim

The largest instrumentally recorded earthquake in the north-western Tarim is the 1902 M_w 7.7 Atushi (Kashgar) earthquake, a low angle thrust that likely ruptured one of the north-dipping range front thrusts of the Tian Shan (Kulikova and Krüger 2017). The epicentral uncertainty of this earthquake is ∼50–100 km (Figure 4.1). The 1902 earthquake magnitude was previously considered to be M8.6 (Gutenberg 1956) but was revised down by Kulikova and Krüger (2017). Three additional large earthquakes are the Soviet Surface Wave Magnitude (Bindi et al. 2013; Bormann 2002) (M_{LH}) 6.7 1919 earthquake, located within the Kepingtage Fold and Thrust Belt, the M_{LH} 6.7 1944 earthquake located on the eastern margin of the Pamir, and the 1955 M_{LH} 7 earthquake located at the intersection of the Pamir, Tian Shan and Tarim Basin (Figure 4.1) (Mikhailova et al. 2015). No mechanisms were available for these three earthquakes.

Earthquake focal mechanisms and hypocentres for the north-west Tarim Basin have been modelled by Sloan et al. (2011) and Xu et al. (2006) respectively. They find thrust earthquakes clustering at $<$ 20 km depth and other, smaller, events without mechanisms clustering ∼30–50 km depth. The thrust earthquakes are likely related to the Kepingtage Fold and Thrust Belt (Figure 4.1) as they lie along the northern margin of the Tarim Basin. They also observe strike slip earthquakes at ∼20–30 km depth with PT axes indicating north-south contraction further out into the basin (77.0°E, 39.5°N), showing some amounts of internal deformation exist within the Tarim Basin. Normal earthquakes striking north-south are also present in this area at ∼10–20 km depth. Sloan et al. (2011)

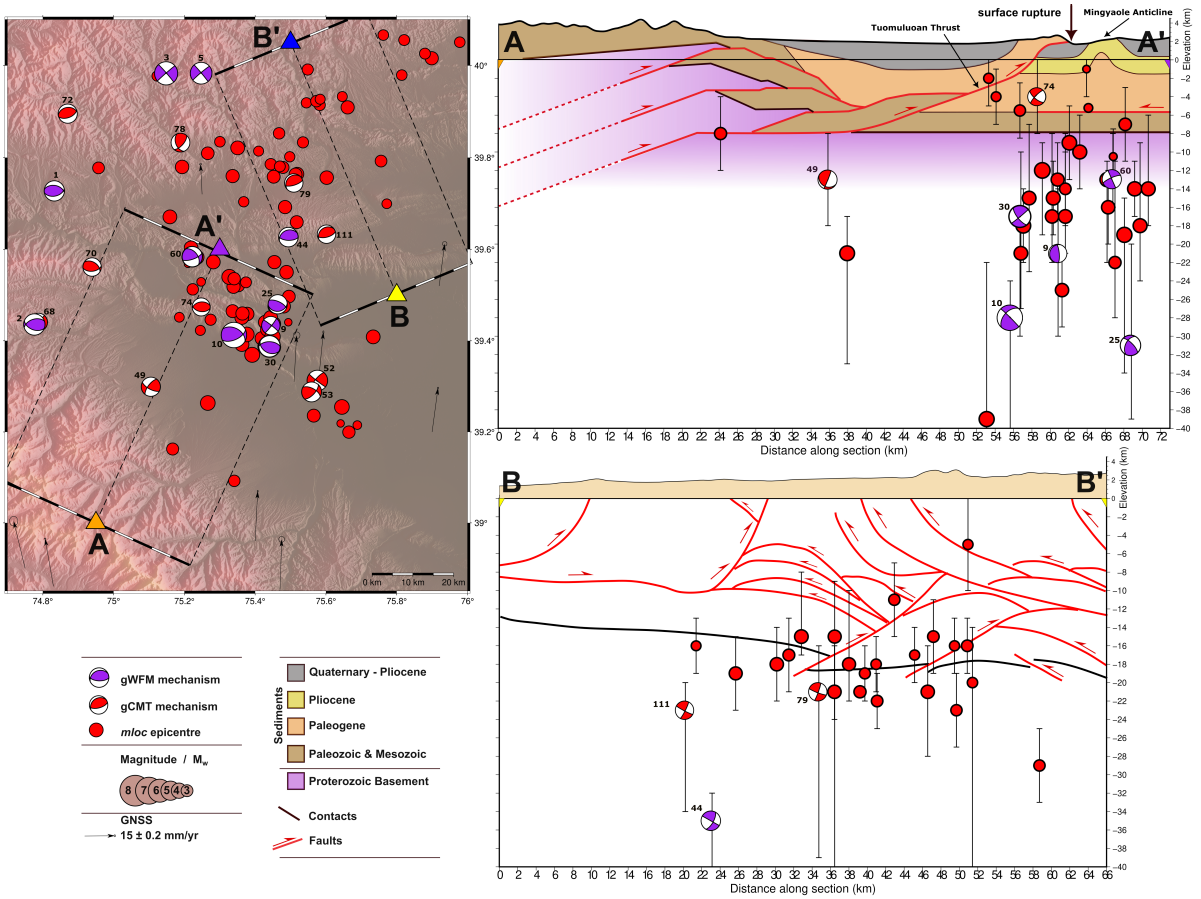

Figure 4.3: Relationship between relocated earthquakes and subsurface geology. More reliable gWFM mechanisms are purple (Wimpenny and Watson 2020), less reliable gCMT mechanisms are in red (Dziewonski et al. 1981; Ekström et al. 2012). Depths are those determined from the *mloc* model, and are hypocentre depths not centroid depths. Cross section A-A' has the geological cross section from Li et al. (2019) and shows that most of the earthquakes in the 1985 sequence occurred below the sedimentary cover, and that very few occurred near the thrust ramps. The mainshock itself initiated at 28 km depth, with the 11^{th} Sept aftershock initiating at 17 km depth. Profile B-B' has structures from Gao et al. (2013), and shows most earthquakes are happening at or below the contact between the sediments and crystalline basement. Given the backthrusting structures, it is unclear which plane the focal mechanisms ruptured on.

suggest these represent flexture from loading of the Pamir onto the Tarim basin.

4.2 The 1985 Wuqia Earthquake

Around the epicentre of the 1985 earthquake there are two surface structures which abut at the Kyzylsuu River (Figure 4.2). The southwest-dipping Tuomuluoan Thrust, and the south-verging Mingyaole Anticline, both of which started growing at around 0.5–1.6 Ma (Bufe et al. 2017) and are growing eastwards into the Tarim Basin at a rate of ∼12 km/Myr (Thompson Jobe et al. 2018).

4.2.1 Macroseismic data

Macroseismic data were collected by Feng et al. (1986) between 12^{th} September and 9^{th} November 1985. Intensity contours from Feng et al. (1986) are using the China Seismic Intensity scale, which is similar to the Modified Mercalli Scale (Hu et al. 1996; Li et al. 2021) and are displayed in Figure 4.6.

The Macroseismic contours form an ellipse with a NW-SE trend, with a ∼100 km long axis for the intensity VII contour. This lines up well with the location and strike of the surface ruptures (also surveyed by Feng et al. (1988)). Towns marked on the intensity map (Feng 1999) appear to constrain the contours well. In particular there seems to be evidence of intensity VI and below in the Biertuokuoyi Basin, and even less near the Pamir Front.

Two small sites of intensity IX occur at either end of the intensity VIII lobe. The northern one covers part of the town of Wuqia, and is near to a small fold (75.2024°E, 39.6737°N), which could be the growing above a fault that moved in the earthquake, although no ruptures were discovered here. The southern one is near the Aismaola Thrust (Figure 4.2). No surface ruptures were discovered at the front of this thrust, and the enhanced damage here may be due to the river sediments just north of this fold being more susceptible to liquefaction.

Table 4.1: Focal mechanism determinations compiled by Ainscoe (2018) for the 23^{rd} August M_w6.9 Wuqia Mainshock. SV Az. = Slip vector azimuth. B+M93 = (Burtman and Molnar 1993); F94 = (Fan et al. 1994); W87 = (Wang et al. 1987). Values in italics show the conjugate fault planes. Ranges for parameters are also shown.

Model	Method	M_o (N·m)	M_w	Strike (°)	Dip (°)	Rake (°)	SV Az. (°)	Centroid Depth (km)	Longitude (°E)	Latitude (°N)
B+M93	Single event with directivity	2.22×10^{19}	6.8	60 *(35–85)* *316*	76 *(58–78)* *46*	47 *(32–57)* *160*	45 *150*	18 <25	75.27	39.43
	Three sub-events	3.6×10^{18}	6.3	45	70	62	12	18	75.27	39.43
		7.9×10^{18}	6.6	68	71	34	56	19	75.27	39.43
		9.9×10^{18}	6.6	61 *282* *326* *309*	72 *34* *58* *41*	52 *142* *158* *152*	39 *135* *158* *151*	18	75.27	39.43
F94	–	2.79×10^{19}	6.9	66 *56–76* *299* *289–309*	59 *49–69* *45* *35–55*	56 *46–66* *133* *123–143*	29 *155*	16	75.27	39.49
W87	–	5.7×10^{19}	7.1	60 *310*	80 *40*	50 *160*	48 *146*	–	75.2	39.4
GCMT	–	3.29×10^{19}	6.9	63 *315*	80 *29*	62 *159*	45 *154*	15	75.09	39.54
ISC-EHB									75.43	39.36

4.2.2 Source parameters from seismology

Source parameters for the 1985 Wuqia M_w 6.9 mainshock and M_w 6.1 aftershock have been calculated by multiple workers (Table 4.1). Burtman and Molnar (1993) and Fan et al. (1994) use a body-waveform modelling approach (Taymaz et al. 1991; Wimpenny and Watson 2020) which is sensitive to focal mechanism and depth but not epicentral location. Earthquakes are modelled as a point source, so larger events (such as the M_w 6.9 mainshock) are difficult to model, as the fault plane length scale approaches the wavelength of the 15 s–100 s period seismic waves used in the inversion. Both Burtman and Molnar (1993) and Fan et al. (1994) run models where the M_w 6.9 event is split into multiple sub-events, but the introduction of more free parameters runs the risk of overfitting the data.

A common feature of all focal mechanism determinations (Burtman and Molnar 1993; Ekström et al. 2012; Fan et al. 1994; Wang et al. 1987) is a focal plane striking ~300°and dipping 30–50°to the northeast, with a mixture of thrusting and right-lateral motion on it.

Table 4.2: Focal mechanism determinations compiled by Ainscoe (2018) for the 11^{th} September M_w6.1 earthquake, the largest aftershock of the 1985 Wuqia earthquake. SV Az. = Slip vector azimuth. B+M93 = Burtman and Molnar (1993); F94 = Fan et al. (1994). Values in italics show the conjugate fault planes. Ranges for parameters are also shown.

Model	Method		M_o (N·m)	M_w	Strike (°)	Dip (°)	Rake (°)	SV Az. (°)	Centroid Depth (km)	Longitude (°E)	Latitude (°N)
B+M93	Single event		8.1×1010^{17}	5.9	108 (48–138) *272*	31 (21–38) *60*	104 (44–129) *82*	2 *198*	7 (4–10)	75.44	39.36
F94			1.19×10^{18}	6	118 (88–148) *271* *241–301*	39 (18–61) *54*	112 (82–142) *173* *178–238*	1 *208*	6	75.44	39.36
GCMT	–		1.82×10^{19}	6.1	90 *299*	44 *50*	68 *110*	29 *179*	10	75.32	39.5
ISC-EHB										75.24	39.46

Burtman and Molnar (1993) regard the alternative north-east striking plane as "probably the auxiliary plane" although it is unclear whether this is based on seismological evidence or the surface rupture mapping of Feng et al. (1986), which they were aware of (Appendix A16).

Wang et al. (1987) model the mechanism based on the azimuthal distribution of Rayleigh Wave amplitudes (Kanamori and Given 1981). They find very similar results for the M_w 6.9 mainshock as Burtman and Molnar (1993) and Fan et al. (1994) with a very different method, which greatly increases our confidence in the focal mechanism.

The largest aftershock of 11^{th} September 1985 presented problems for Burtman and Molnar (1993) who state that:

> "the source parameters are constrained largely by SH phases, and they fit two different classes of solution: largely strike-slip displacement on northwesterly or northeasterly trending planes, or largely thrust faulting on east-west trending planes. Ekström (1987) reported the latter type, which we favour, but not with much confidence."

Fan et al. (1994) model this event with 4 more P wave observations than Burtman and Molnar (1993) and achieve better fits with the thrust mechanism, so we believe this is probably more robust. They do model the event as two periods of rupture separated by 8 s resulting in a bimodal source-time function. This results in a shallow centroid depth

of ∼6 km. Using *mloc* we find a depth of at least ∼17 km for this event, based on depth phases and local distance method (Section 4.3.3) so we suggest they may be modelling the depth phases as one of their sub-events, resulting in the shallow centroid depth.

4.2.3 Surface ruptures

Feng et al. (1988) state that the mainshock did not produce surface ruptures, and that these only appeared after the 11^{th} September aftershock. However, they also say that the discovery of surface ruptures after this aftershock prompted them to look for more ruptures, which could mean the original survey in 1985 was not thorough. So it is unclear at what point during the earthquake sequence the ruptures occurred. The rupture set in the east of Figure 4.4 was completed during April, May and September 1986 (Ainscoe 2018; Feng et al. 1988).

Surface ruptures have been studied by both field studies and remote sensing (Figure 4.4) and can be found in Appendices A18 and A19. Ainscoe (2018) digitised the results of Feng et al. (1986) and Feng et al. (1988) who mapped the rupture section east of the Tuomuluoan Thrust and south of the Mingyaole Anticline, on the north bank of the Kyzylsuu River. They found both vertical and right-lateral offsets. The south-west-up vertical coseismic offsets were on average ∼0.7 ± 0.4 m based on 12 measurements of fresh scarp heights, and the right lateral coseismic offsets were on average 1.3 ± 0.4 m based on five measurements of offset geomorphic markers. These occurred on pre-existing scarps whose heights varied from 10 m to 4 m, likely produced over multiple earthquake cycles. He et al. (2024) trenched the surface ruptures in three places and measured fault dip at the surface. Typically, the ruptures had dips of ∼10–20°to the south-west, with strike-slip stepovers with dips of ∼80°. This is consistent with a thrust sheet shallowly dipping to the south-west, and likely represents the leading edge of the Tuomuluoan Thrust, imaged in seismic reflection data to dip ∼25°(Li et al. 2019). Additional ruptures were found on the south bank of the Kyzylsuu River, further west of those mapped by Feng et al. (1986) and Feng et al. (1988), (Figure 4.4) but were present in imagery from 1971 so were interpreted to have not been involved in the 1985 earthquake (Feng et al. 1988).

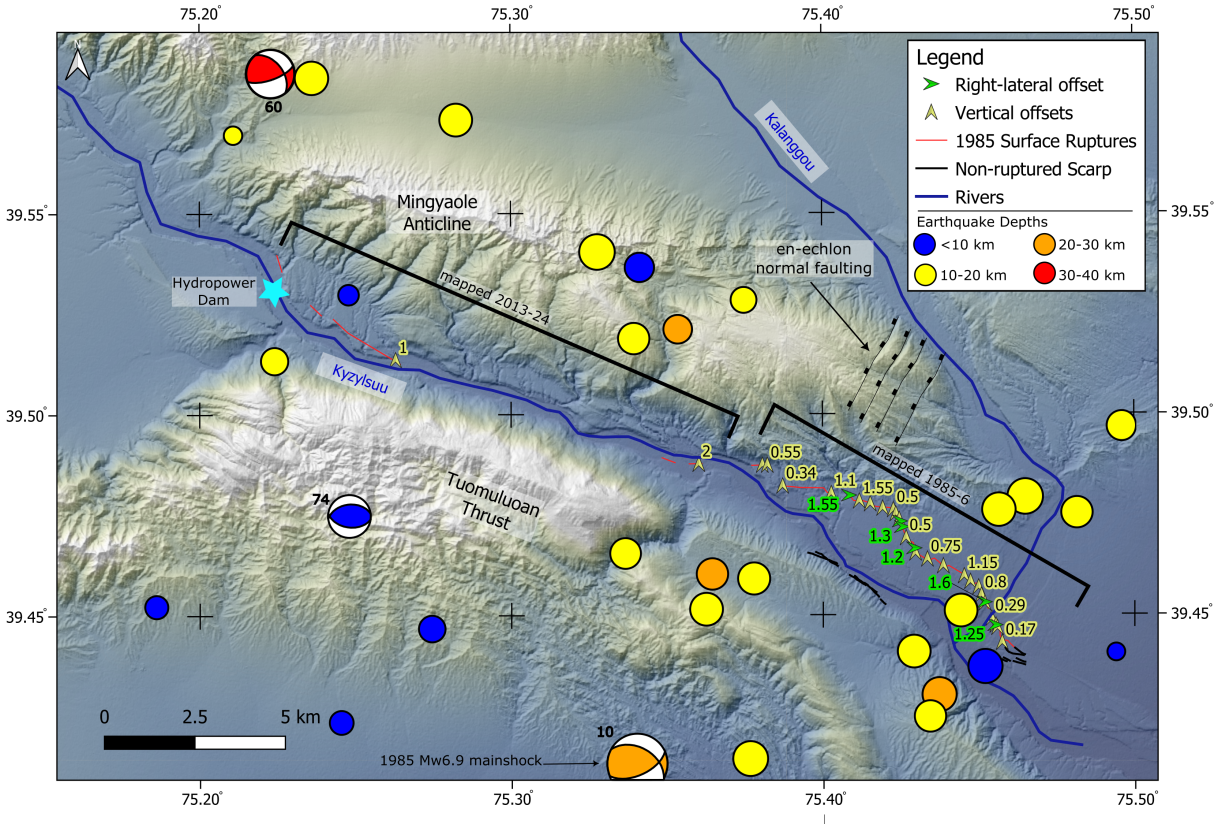

Figure 4.4: Map of surface ruptures for the 1985 Wuqia Earthquake, including field mapping from Feng et al. (1986), Feng et al. (1988), and He et al. (2024) and remote mapping from Ainscoe (2018). Yellow vertical arrows show south-west-up vertical offsets and green horizontal arrows show right-lateral offsets in metres from Feng et al. (1986) and He et al. (2024). The more continuous ruptures in the west (75.45°E, 39.46°N) ruptured a pre-existing scarp of ∼10 m, and the ruptures in the east (75.25°E, 39.60°N) ruptured a scarp ∼20 m height. Pre-existing scarps that did not move in the 1985 earthquake are on the South Bank of the Kyzylsuu River in black. *mloc* epicentres coloured by depths are also shown.

Ainscoe (2018) identified further ruptures to the west using pre- and post- earthquake imagery. They suggest these were not mapped by field expeditions in the 1980s, as they were ∼3 km distant from the mapped ruptures, and had no nearby residents or road access. Some of these were surveyed in the field by He et al. (2024). At 75.3584°E, 39.4877°N, they find two colinear ruptures on a set of two river terraces, the youngest and lowest elevation, on opposite sides of the river. He et al. (2024) find the larger of these are steeply dipping at ∼70°and find a ∼2 m south-west-up vertical offset. They do not survey the ruptures that Ainscoe (2018) identify as having appeared after the 1985 earthquake.

Further west, at 75.2628°E, 39.5135°N, He et al. (2024) survey a post-1985 scarp identified by Ainscoe (2018), again within the youngest river terrace, measuring a 1 m vertical offset. This new scarp is colinear with a larger scarp, dipping vertically, upthrown by about 20 m on the southern side. This indicates the fault has ruptured multiple times previously, again consistent with a north-east vergent Tuomuluoan Thrust. Between 2013 and 2019 a dam was constructed in the Kyzylsuu River, and it appears the 1985 surface ruptures pierce the eastern edge of this dam. This presents a displacement hazard, where movement on the fault may damage the integrity of the dam, leading to flooding or perhaps collapse, although we do not know what mitigation the engineers built in. Finally, the scarp bends to the north, following the eastern edge of the Mayikake Basin (Figure 4.2), although this scarp has been covered by the new reservoir since imaged by Ainscoe (2018) in 2013. He et al. (2024) suggest the contrasts between steeper dips at the western end of the ruptures, and shallower dips at the eastern end, are caused by bedding plane slip on the Tuomuluoan fold.

4.3 Methods – Calibratated Earthquake Relocations

4.3.1 Overview

We refine the location of the 1985 earthquake and its aftershocks by including it in a calibrated cluster of earthquakes analyzed with the program mloc;version 10.5.3 as in

Chapter **2** for the 1949 Khait Earthquake. *mloc* is based on the HDC algorithm introduced by Jordan and Sverdrup (1981) but it incorporates additional procedures to produce hypocenters that are minimally biased by unknown Earth structure and that have realistic parameter uncertainties based on the variability of the data used. Relocations with these properties are referred to as "calibrated". The use of *mloc* in this study exactly parallels the relocation studies contributing to GCCEL, as described in Bergman et al. (2022). A "ground truth" of these methods is provided by the relocation of the Mangyshlak nuclear explosion sequence, where calibrated *mloc* epicentres centred directly on collapse craters (Mackey and Bergman 2014).

Like all multiple event relocation algorithms *mloc* uses differences in observed arrival times of seismic phases to improve the relative locations of a set of earthquakes within a limited area (termed a 'cluster'). Uniquely among such algorithms, however, the hypocentroidal decomposition method uses projection operators to split the relocation problem into two parts. At each iteration, improvements to the relative locations, or "cluster vectors", of the events in the cluster (relative to a reference point called the hypocentroid) are determined. Next, improvements to the absolute location of the hypocentroid are determined in close analogy to a single event location, but using data selected from all the events in the cluster. After each iteration the cluster vectors are added to the hypocentroid to obtain absolute locations for the individual events. The choice of data used for the hypocentroid determines whether a converged relocation can be considered calibrated or not. For example, to relocate clusters in oceanic or remote continental areas lacking nearby seismograph stations, the hypocentroid might be located with teleseismic P arrivals. Such a cluster would not be considered calibrated, as the arrival time data would be biased by unknown Earth structure.

For this study, the hypocentroid was determined from direct-arriving local phases (Pg and Sg) within 1.0°of each event in the cluster. Most of this data came from the 8H seismic network, deployed over the period from August 2015 to May 2017 **(Appendix A20)** (Yuan et al. 2018). We used phase arrival time data from Bloch et al. (2021) who used a waveform-envelope-coherence-based approach (Comino et al. 2017) to detect events, and

automated picking algorithms from (Aldersons 2004; Diehl et al. 2009) to obtain P and S arrival times. Further arrival time data are from the ISC Bulletin (Storchak et al. 2017; Storchak et al. 2020)

Since the relative locations (cluster vectors) of all events have been determined in the first step of the relocation, these arrival times can be utilized to locate the hypocentroid as if it were an earthquake. Since the ray paths of the arrival time data used to establish the absolute location of the cluster (i.e., all the included events) are short, the biasing influence of unknown Earth structure is minimized. There is an obvious tradeoff between the limiting distance for data used to estimate the hypocentroid and the number of data used (and thus statistical power). The epicentral distance limit used here, 1.3°, is typical for the calibrated clusters in GCCEL. For this cluster, 473 phase readings contributed to the hypocentroid, the vast majority of these being events between September 2015 and March 2017 – the interval over which the 8H seismic network was deployed. To the extent that this distance range still encompasses significant lateral heterogeneity, the scatter introduced in the arrival time data will be reflected in the so-called empirical reading errors used for inverse weighting, and the parameter uncertainties will reflect that heterogeneity. Figure 2.4 in Chapter 2 illustrates this.

The relocation process is iterative, both in a single run of *mloc*, but also in the sense that many runs are needed to properly deal with outlier readings and other sources of bias.

4.3.2 Treatment of Errors

Multiple event relocation allows for error treatment using the statistics of the arrival time data, which is not possible for single-event relocation. Errors in reported phase arrival times arise from multiple sources, including varying signal-to-noise levels, variations in analyst (or automatic) picking strategies, interference from multiple phases arriving close together, timing errors and differences in the precision to which arrival times are reported. At each run *mloc* produces an output file of the spread and mean of arrival times for each distinct station-phase pair ("empirical reading error"), using a robust estimator of spread.

After the first run the empirical reading errors from the previous run are used for inverse weighting of the arrival time data. Empirical reading errors have a minimum value of 0.1 s so they cannot become unrealistically low.

It is essential to use a robust estimator of spread, meaning one that is insensitive to gross outliers, in this process so that outlier readings are exposed. *mloc* employs the "Sn" algorithm (Croux and Rousseeuw 1992). Outlier readings are flagged in the event data files by the user between runs, either manually or with a utility program. This needs to be done gradually, taking only the greatest outliers each time, until the set of residuals for each station-phase approximates a normal distribution when normalized by the empirical reading error and mean residual. The mean residual is interpreted as the correction for whatever velocity model has been used to calculate the theoretical travel time for that station-phase, but this information is not relevant in *mloc*, except for the local-distance readings used for the hypocentroid, because all other arrival time data are utilized only as differenced travel times.

4.3.3 Depth Control and Velocity Model

We use the ak135 global 1-D velocity model (Kennett et al. 1995) with a modified crust such that the travel time residuals in the distance range used for the hypocentroid are minimized. The crustal velocity model and event depths were refined during the initial runs with a set of events having especially good local data, with near-source arrivals (less than about 1.5–2.0 focal depths) to constrain focal depth. Once the crustal part of the model is established the crustal thickness is adjusted to fit the observed Pn arrivals.

Once the velocity model is set, the depths of other events lacking near-source arrivals can often be usefully estimated. If events only have one or two direct arrival times ∼1 degree epicentral distance, and their depth can't be found using direct arrivals alone, another approach for depth constraint can be used. The 'Local Distance Method' exploits the dominance of regional Pn arrivals in the dataset relative to near source. With epicenters stabilized by the abundance of data at all distances and azimuths, the Pn data tend to dominate the estimate of origin time, for a given assumed depth. If there are

any direct crustal arrivals in the range beyond near-source but closer than the Pg/Pn crossover distance, their travel times are mainly influenced by the origin time, not focal depth, since for shallow events the ray path is nearly horizontal. Therefore shifting the focal depth causes changes in the residuals of those far-local arrivals in the same sense (but less precision) as for near-source arrivals, and thus gives a way to estimate focal depth. Focal depths determined in this way are vulnerable to the arrival time errors for the direct arrivals, as usually there are only one or two of these, in this case only KSH, which was problematic (see Section 4.4.1) (Bergman et al. 2022; Karasözen et al. 2016; Karasözen et al. 2019).

Depths can also be usefully estimated from teleseismic depth phases (Walker et al. 2013), various types of waveform modelling (Maggi et al. 2000) and fault models derived from InSAR data (Nealy et al. 2017). In this study we rely on mostly on depth phases and the Local Distance Method for determining depths. Where both centroid depths from waveform modelling and *mloc*-derived depth phase depths are available, we prefer the *mloc* depth. This is because the *mloc* location is a hypocentre (or nucleation point of the earthquake) rather than a centroid (theoretical centre of seismic energy in a point source earthquake model).

4.3.4 Event Selection

We prioritized an even time distribution of events in order to strongly link the locally-recorded events of 2015 and 2017 to the 1985 earthquake, in order to have many station-phases common to many events across the cluster. We chose events on the basis of having >100 phase arrivals rather than by magnitude, as some events did not have magnitude data recorded, or had multiple different magnitudes. This cluster included all events with gCMT focal mechanisms within ∼1 degree of the 1985 earthquake epicentre (Dziewonski et al. 1981; Ekström et al. 2012) and provided a magnitude range of M_w 2.5–6.9 (Figure 4.5). We also prioritized events close to a regional seismometer as this gave us better depth control. Where no depth control was possible, we assigned a default cluster depth of 13 km. This does not affect the epicentral estimate when there is good azimuthal coverage, as any bias in depth is compensated in the origin time (Shearer 2019, p. 127).

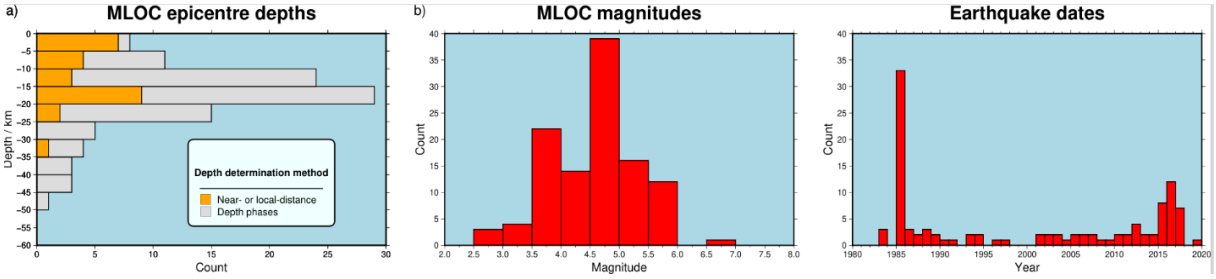

Figure 4.5: Statistics for the cluster of 111 earthquakes analysed with *mloc* (see also Table 4.3). (a) histogram of depths coloured by depth determination method. While the distributions are similar, there is a clear bias toward shallower depths for the near- and local distance method. this could be due to this method being used more on recent earthquakes, and so be a sampling issue, or could reflect limitations with depth phases getting mixed up with first arrivals for shallow earthquakes. (b) the encompassed small events with good near-souce data to calibrate the cluster, and included the all events greater than M_w 5 within ~1 degree of the 1985 earthquake epicentre. (c) The cluster was constructed from events in the 2015-2017 period with good near-source data, and was build backwards in time from there, incrementally adding events to get good connectivity with the 1985 mainshock and aftershocks, which make up the bulk of the cluster.

4.3.5 Relocation Strategy

Because of the large changes in the constellation of observing stations across this cluster (e.g. the fall of the Soviet Union in 1991 and the reconfiguration of the Chinese seismic network in 2008) we adopted a gradualist strategy for the relocation, beginning with a set of seven events, ranging in magnitude from 3.7–5.1, that were closely observed by the 8H deployment between 2015 and 2017; they were also recorded by regional and teleseismic stations. In the process of relocating these events, which have good depth control from near-source stations, the crustal velocity model was also refined.

Starting from this kernel of well-located events, the cluster was gradually expanded by adding the events nearby in time. At each increment in building the cluster, several runs are used to refine the hypocentral parameters and arrival time datasets, flagging outliers and estimating empirical reading errors.

4.4 Results

For this study we relocate a cluster of 111 earthquakes (Table 4.1) within ~ 100km distance of the previous seismological epicentres of the 1985 M_w 6.9 Wuqia Earthquake

(Table 4.1).

4.4.1 Location and depth of the 1985 mainshock

The *mloc* relocation shifts the 1985 mainshock 15 km to the north-north-east of the Catalog of well particularly well located earthquake hypocentres (Weston et al. 2018) (ISC-EHB) location and 25 km east of the gCMT centroid location. It reduces the formal epicentral location uncertainty to ∼2 km. This places the epicentre ∼7 km south-west of the mapped surface ruptures, but at a depth of ∼28 +13 –5 km. This is deeper than centroid depth determinations from Burtman and Molnar (1993) and Fan et al. (1994) of 18 km and 16 km respectively. This is consistent with other studies which find hypocentres tend to be deeper than centroids, possibly reflecting earthquake initiation at depth and propagation up the rupture plane (Elliott et al. 2015; Karasözen et al. 2019; Semmane et al. 2005; Takada et al. 2009).

We attempted to apply the *mloc* 'local distance' depth determination method for the mainshock hypocentre to corroborate the depth phases using station KSH (described in Section 4.3.3) but could not find a depth, origin time and location that reduced the absolute value of the KSH residual to less than 1 s, while satisfying the teleseismic and regional data. At the location most consistent with the teleseismic data, the KSH residual was ∼ -5 s. If we assume this residual is due to an incorrect modelled depth in a model where P Waves travel at 6 km/s, we need a modelled depth of −9 km to reduce this residual to zero:

$$-5 \text{ s} \times 6 \text{ km s}^{-1} = -30 \text{ km} \rightarrow -9 \text{ km depth} \tag{4.1}$$

This is non-physical, as the elevation in this area is only ∼1 km. Therefore this residual is not purely due to an incorrect modelled depth.

To test whether this anomaly between observed and modelled direct P wave arrival time at KSH was due to an incorrect epicentral location, we tried moving the mainshock epicentre to 75.66500°E, 39.46669°N ∼30 km closer to KSH, based on the rough distance needed to remove a 5 s anomaly within a model with a 6 km/s P wave velocity. We included all

teleseismic data for this event previously excluded as anomalous in case this had caused us to locate the event in a "local minimum" of misfit (Shearer 2019). We fixed longitude, latitude, and depth in the model and did several inversions for origin time only, manually adjusting depth over several model iterations. After several model iterations and data cleaning, the misfit for the mainshock epicentre was still ∼20% greater than the location most consistent with teleseismic data.

In addition to changing the epicentral location, we changed the origin time for the mainshock, but this did not resolve the conflict between the local distance and depth phase methods. Making the origin time earlier reduced the misfit at KSH, but made the depth phase estimate deeper, which increased the misfit at KSH.

We suggest that some complexity in the rupture could account for this highly negative KSH residual. Perhaps separate sub-events, or directivity, as suggested by (Burtman and Molnar 1993; Fan et al. 1994)(Table 4.1). Another possibility is a timing error at KSH relative to the world clock that seismic stations are synchronised with.

In addition to relocating the mainshock, we relocated many immediate aftershocks, as these have been shown to cluster around the edge of the rupture patch of large earthquakes (Nealy et al. 2017), giving us an indirect estimate of the mainshock source dimensions and depth range. Our aftershock cluster spans around 10–20 km depth, which is roughly the depth of the mainshock centroid (Burtman and Molnar 1993; Fan et al. 1994), but shallower than our hypocentre depth. It is also similar to depths of other strike slip earthquakes further east within the Tarim Basin, as determined by Sloan et al. (2011).

4.4.2 1985 Aftershock Distribtion

We find a strong alignment between immediate aftershocks and the macroseismic data (Figure 4.6) Aftershocks which occurred within 5 days of the mainshock create a line ∼60 km long on a NW-SE axis. They also lie within the macroseismic damage zone VIII (Figure 4.6 cross section A-A').

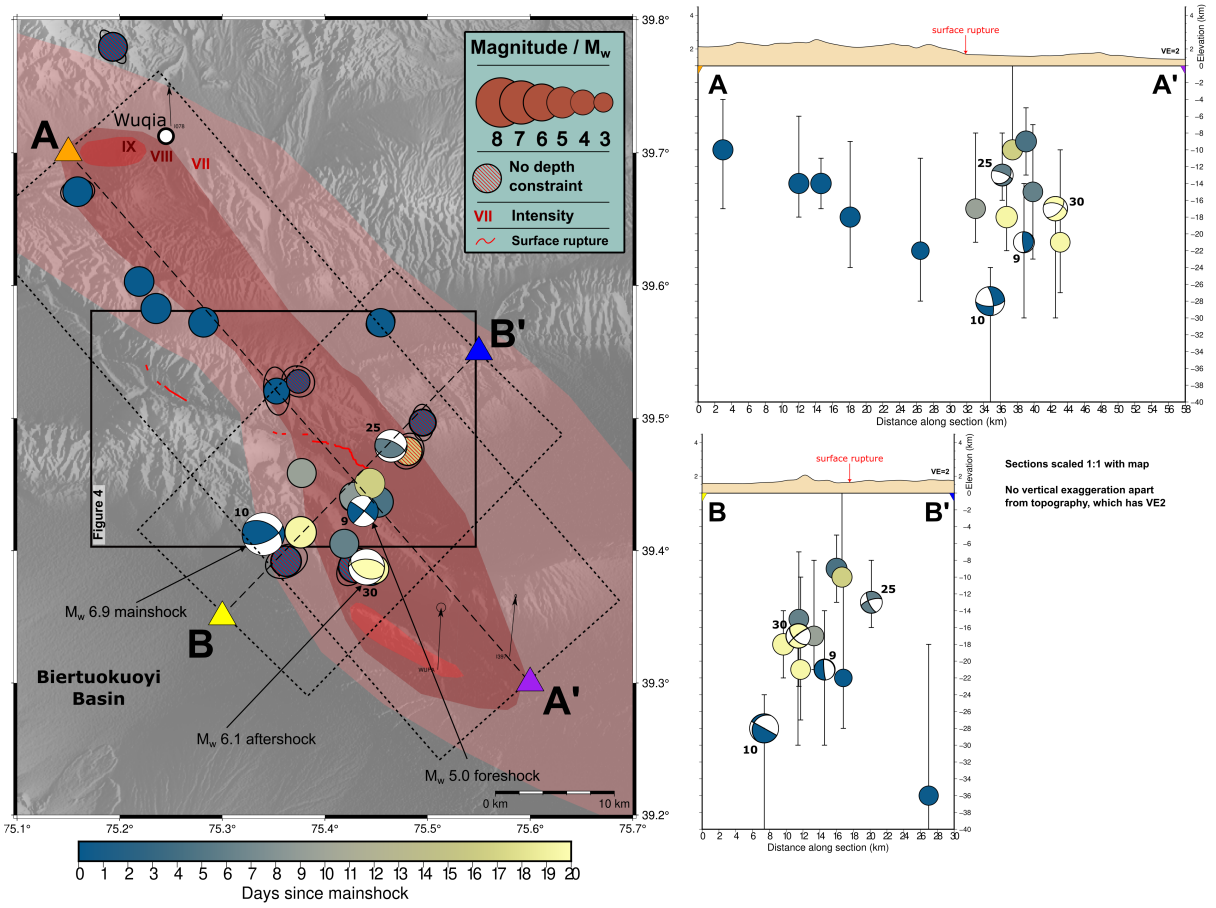

Figure 4.6: Aftershocks within 20 days of the 23^{rd} August 1985 M_w 6.9 Wuqia mainshock color coded by time since the mainshock, with formal uncertainty error ellipses from the *mloc* relocation. A M_w 5 foreshock, ~6 hours before the mainshock is labelled. Red-hashed epicentres are those with no depth constraint. and do not appear in cross sections. Intensity contours from Feng et al. (1986) are using the China Seismic Intensity scale, which is similar to the Modified Mercalli Scale (Hu et al. 1996; Li et al. 2019). Early aftershocks align well with the long axis of the intensity contours (Cross section A-A‘), as well as the strike of the focal mechanism for the mainshock, and other aligned focal mechanisms (Figure 4.4). Subsequent aftershocks align on a perpendicular axis, which appears to align with the south-dipping plane M_w 6.1 aftershock focal mechanism.

We suggest these aftershocks are rupturing along the 1985 mainshock fault plane or a parallel structure. This would be consistent with the strike of the north-east dipping nodal plane for the mainshock focal mechanism and mechanisms of subsequent earthquakes, for example Events 53 and 60 (Figure 4.3; Table 4.3), and the two mechanisms west of the Mingyaole Anticline. In cross section, the aftershocks appear to lie on a slope dipping ∼60°to the south-west. This is not consistent with them lying on the same plane as the mainshock, but could indicate rupture on conjugate structures. This is discussed further in Section 4.5.3.

Table 4.3: Earthquakes relocated with *mloc* with mechanisms where available. Where multiple mechanisms were available, we selected the gWFM over the gCMT due to these being manually modelled by an analyst, rather than automatically generated. For the 1985 mainshock and 11^{th} Sept aftershock, we add the mechanism used in plotting Figures 4.1, 4.4, and 4.6. See Tables 4.1 and 4.2 for all mechanisms for these events. The depth code refers to the method of depth determination used in *mloc* with d=depth phase, l=local distance method, n=near-source data, m=free depth inversion in *mloc*. The calibration code refers to the confidence in the location (reflected in the size of the epicentre uncertainty ellipse. 1 is the best constrained, 5 is the least constrained. Where M_w isn't available we give M_S or m_B

Ev Nb	Date	Time (UTC)	Latitude	Longitude	Depth	Strike	Dip	Rake	Mag.	Dep. Code	Calibration Code	Mechanism Source
1	14/09/1969	16:15:24	39.72743	74.8325	20	79	47	76	5.5M_w	d	CH02	F94
2	08/10/1978	14:20:05	39.43563	74.77603	40	252	49	62	5.8M_w	d	CH02	F94
3	13/02/1983	01:40:12	39.98314	75.14842	16	319	87	-178	6.3M_w	d	CH02	F94
4	05/06/1983	10:39:38	39.25489	75.645	15	-	-	-	5.1m_B	d	CH02	
5	05/04/1983	06:50:31	39.98346	75.24736	11	220	48	-13	5.9M_w	d	CH02	F94
6	25/01/1985	18:03:24	38.73706	75.07931	14	-	-	-	5.2m_B	d	CH02	
7	22/02/1985	08:26:30	39.55	75.48862	22	-	-	-	4.7m_B	d	CH02	
8	29/06/1985	13:32:27	39.26352	75.2661	21	-	-	-	5.1m_B	d	CH02	
9	23/08/1985	08:32:57	39.42989	75.43694	21	308	85	175	5.0M_w	d	CH02	F94
10	23/08/1985	0.529167	39.41255	75.34001	28	315	29	159	6.9M_w	d	CH02	F94
11	23/08/1985	13:45:29	39.7797	75.1935	13	-	-	-	4.7$\mathbf{m_S!}$ ($\mathbf{m_S!}$)	c	CT03	
12	23/08/1985	14:11:41	39.67074	75.15905	10	-	-	-	4.8m_B	d	CH03	
13	23/08/1985	15:38:27	39.57238	75.28171	18	-	-	-	4.8m_B	d	CH02	
14	23/08/1985	16:06:43	39.52051	75.35292	22	-	-	-	4.2m_B	d	CH04	
15	23/08/1985	16:25:30	39.60309	75.21893	14	-	-	-	4.8m_B	d	CH02	
16	23/08/1985	16:32:57	39.58273	75.23546	14	-	-	-	4.9m_B	d	CH02	
17	23/08/1985	18:41:27	39.5278	75.37403	13	-	-	-	3.8m_B	c	CT03	
18	23/08/1985	19:19:09	39.57205	75.45426	36	-	-	-	4.6m_B	d	CH02	
19	24/08/1985	04:17:55	39.3851	75.44471	13	-	-	-	4.9m_B	c	CT03	
20	24/08/1985	12:26:27	39.39204	75.36253	13	-	-	-	4.9m_B	c	CT04	
21	24/08/1985	15:33:02	39.49671	75.49531	13	-	-	-	4.4m_B	c	CT03	
22	24/08/1985	18:23:44	39.38766	75.42798	13	-	-	-	5.0m_B	c	CT03	
23	28/08/1985	00:09:59	39.43689	75.45164	9	-	-	-	5.0m_B	l	CH02	
24	29/08/1985	13:15:07	39.40522	75.41888	15	-	-	-	4.7m_B	d	CH02	
25	29/08/1985	23:39:50	39.47913	75.46439	13	294	66	103	5.2M_w	d	CH02	F94
26	01/09/1985	01:38:47	39.4406	75.42876	13	-	-	-	4.8m_B	c	CT03	
27	01/09/1985	23:34:07	39.45864	75.37743	17	-	-	-	4.7m_B	d	CH02	
28	08/09/1985	22:43:15	39.47522	75.48096	13	-	-	-	4.6m_B	c	CT03	
29	08/09/1985	23:04:15	39.45079	75.44382	10	-	-	-	4.8m_B	l	CH02	

Continued on next page

Ev Nb	Date	Time (UTC)	Latitude	Longitude	Depth	Strike	Dip	Rake	Mag.	Dep. Code	Calibration Code	Mechanism Source
30	11/09/1985	20:45:51	39.38775	75.44054	17	271	54	73	5.8M_w	d	CH02	F94
31	11/09/1985	21:08:50	39.41388	75.37634	18	-	-	-	5.1m_B	d	CH02	
32	11/09/1985	23:04:58	39.38604	75.4481	21	-	-	-	4.7m_B	d	CH02	
33	25/09/1985	01:47:07	39.42447	75.43401	17	-	-	-	4.6m_B	d	CH02	
34	03/10/1985	19:30:25	39.36917	75.39161	39	-	-	-	5.2m_B	d	CH03	
35	03/10/1985	23:53:51	39.40868	75.44907	12	-	-	-	5.4m_B	d	CH02	
36	19/12/1985	00:46:56	39.45099	75.36217	15	-	-	-	4.8m_B	l	CH02	
37	19/12/1985	01:50:28	39.46483	75.33619	13	-	-	-	4.5$\mathbf{m_S!}$	l	CH02	
38	20/12/1985	01:52:59	39.45975	75.36408	25	-	-	-	4.6m_B	l	CH02	
39	28/01/1986	09:28:24	39.69215	75.48445	18	-	-	-	4.6m_B	l	CH02	
40	13/02/1986	0.392361	39.65928	75.51756	19	-	-	-	4.5m_B	l	CH02	
41	03/10/1986	07:48:39	39.51818	75.3388	16	-	-	-	4.6m_B	l	CH02	
42	30/04/1987	05:17:39	39.75129	74.59388	15	113	44	86	5.6M_w	d	CH02	gCMT
43	08/06/1987	13:30:35	39.75182	74.61904	13	298	27	91	5.2m_B	d	CH02	gCMT
44	06/01/1988	15:31:15	39.62659	75.4939	35	248	30	69	5.3M_w	d	CH02	F94
45	12/08/1988	18:58:50	39.63745	74.576	44	-	-	-	5.6m_B	d	CH03	
46	23/09/1988	04:46:41	39.64237	74.54851	27	106	23	64	5.1M_w	d	CH02	gCMT
47	26/05/1989	01:08:47	39.53968	75.32702	19	-	-	-	5.2m_B	d	CH02	
48	26/06/1989	21:40:32	39.16254	75.16676	8	-	-	-	4.2m_B	l	CH02	
49	17/04/1990	01:59:30	39.29924	75.10521	13	118	68	156	5.2m_B	l	CH02	gCMT
50	06/03/1991	18:32:42	39.23582	75.56551	7	-	-	-	4.5m_B	l	CH02	
51	03/04/1993	05:02:54	39.90925	75.66129	21	-	-	-	4.6m_B	d	CH03	
52	30/11/1993	20:37:15	39.31282	75.57569	21	219	74	4	4.9m_B	d	CH02	gCMT
53	12/01/1994	10:22:53	39.28785	75.55936	28	298	60	151	4.9m_B	d	CH02	gCMT
54	16/12/1994	12:45:27	39.40855	75.73354	20	-	-	-	4.8m_B	d	CH03	
55	13/08/1996	06:15:18	39.53585	75.3406	7	-	-	-	4.3m_B	l	CH03	
56	09/09/1997	08:16:35	39.82119	75.35054	17	-	-	-	4.8m_B	l	Southern	
57	11/03/2001	18:04:10	39.76444	75.51878	21	-	-	-	4.6m_B	d	CH03	
58	18/09/2001	09:19:05	39.80942	75.26606	18	-	-	-	4.4m_B	d	CH02	
59	18/12/2002	21:50:13	39.75835	75.45226	18	-	-	-	4.5m_B	d	CH02	
60	25/12/2002	12:57:08	39.58381	75.22225	31	321	48	152	5.6M_w	d	CH02	F94
61	20/03/2003	17:43:19	39.99147	75.54865	29	-	-	-	3.9m_B	l	CH02	
62	01/09/2003	23:16:37	38.69165	75.33846	12	115	49	-141	5.5M_w	d	CH02	F94
63	12/10/2004	07:18:32	39.75628	75.6021	15	-	-	-	4.7m_B	d	CH02	
64	08/02/2005	02:42:13	39.47585	75.45591	13	-	-	-	4.9m_B	d	CH02	
65	22/05/2005	00:01:55	39.51245	75.22365	14	-	-	-	4.0m_B	l	CH02	
66	05/01/2006	23:14:29	39.97937	75.81435	45	-	-	-	3.7$\mathbf{m_S!}$	l	CH02	
67	24/05/2006	18:11:28	39.91431	75.58242	23	-	-	-	3.9m_B	l	CH02	
68	15/04/2007	22:20:12	39.44054	74.78773	26	131	71	-179	4.9M_w	d	CH02	gCMT
69	22/11/2007	00:18:30	40.01601	75.89893	47	-	-	-	4.6m_B	d	CH03	
70	10/04/2008	07:17:24	39.56132	74.93931	34	302	45	119	5.0M_w	d	CH02	gCMT
71	17/02/2009	04:42:52	39.85275	75.46752	15	-	-	-	4.0m_B	l	CH02	
72	10/06/2010	06:38:05	39.89557	74.87026	25	261	35	99	5.2M_w	d	CH01	gCMT
73	20/08/2010	23:19:52	39.97734	75.12299	11	-	-	-	3.6m_B	l	CH02	
74	01/01/2011	01:56:05	39.47403	75.24765	4	263	44	79	4.9M_w	l	CH01	gCMT
75	08/09/2011	00:15:52	39.83321	75.53515	11	-	-	-	3.9m_B	l	CH02	
76	02/03/2012	13:40:07	39.74361	74.34505	7	179	26	-150	4.9M_w	l	CH01	gCMT
77	20/03/2012	06:24:48	40.0554	75.82098	17	-	-	-	3.8m_B	l	CH02	
78	01/06/2012	12:32:27	39.83261	75.18893	45	158	48	36	5.1M_w	d	CH01	gCMT
79	01/08/2012	09:52:18	39.74476	75.50916	21	226	22	65	5.0M_w	d	CH01	gCMT
80	03/10/2013	06:59:25	39.94647	76.07192	16	-	-	-	3.7$\mathbf{m_S!}$	l	CH02	
81	04/11/2013	08:04:35	39.76312	75.51413	15	-	-	-	4.5m_B	l	CH01	
82	20/06/2014	19:35:56	40.05083	75.97821	15	-	-	-	3.7$\mathbf{m_S!}$	l	CH02	
83	08/07/2014	00:31:10	39.79245	75.75574	17	-	-	-	4.1m_B	l	CH03	
84	16/02/2015	18:58:36	39.91917	75.5448	20	-	-	-	3.6m_B	l	CH02	
85	11/09/2015	09:24:34	38.74018	75.03609	1	-	-	-	3.7m_B	n	CH02	
86	13/11/2015	08:50:07	39.4405	75.4936	1	-	-	-	2.6l	n	CH02	
87	19/11/2015	05:20:04	39.19968	75.66485	7	-	-	-	4.3m_B	n	CH02	
88	30/11/2015	09:23:37	39.92273	75.57294	16	-	-	-	4.0m_B	n	CH01	
89	16/12/2015	21:36:55	39.21503	75.68867	14	-	-	-	3.0l	n	CH02	

Continued on next page

Ev Nb	Date	Time (UTC)	Latitude	Longitude	Depth	Strike	Dip	Rake	Mag.	Dep. Code	Calibration Code	Mechanism Source
90	22/12/2015	15:01:38	39.77752	74.95745	3	-	-	-	4.1m_B	n	CH01	
91	24/12/2015	19:52:55	40.02607	75.87971	17	-	-	-	3.8$\mathbf{m_S!}$	n	CH02	
92	17/01/2016	18:59:47	39.44604	75.27419	5.5	-	-	-	3.9m_B	n	CH02	
93	28/02/2016	03:02:46	39.21874	75.64153	10	-	-	-	2.6l	n	CH03	
94	26/04/2016	09:33:56	39.7597	75.33629	17	-	-	-	4.6m_B	n	CH01	
95	15/05/2016	16:59:12	39.78556	75.44423	22	-	-	-	4.0$\mathbf{m_S!}$	n	CH01	
96	15/05/2016	17:02:29	39.77848	75.47852	21	-	-	-	4.2m_B	m	CH01	
97	17/05/2016	00:24:32	39.78082	75.46983	19	-	-	-	3.8$\mathbf{m_S!}$	n	CH01	
98	24/05/2016	11:08:04	39.80178	75.49775	18	-	-	-	3.6m_B	n	CH01	
99	31/05/2016	06:17:33	39.56851	75.21032	10.5	-	-	-	2.7l	n	CH02	
100	27/07/2016	01:51:57	39.70368	75.36771	1	-	-	-	3.6m_B	n	CH02	
101	27/09/2016	20:51:06	39.81408	75.40967	17	-	-	-	3.5m_B	n	CH01	
102	16/10/2016	02:55:25	39.42272	75.24516	2	-	-	-	3.5m_B	n	CH02	
103	04/12/2016	01:03:42	39.09249	75.34105	34	-	-	-	4.0m_B	m	CH02	
104	16/02/2017	09:25:15	39.69941	75.77193	16	-	-	-	3.4m_B	n	CH02	
105	03/03/2017	05:11:31	39.52893	75.24735	5.22	-	-	-	3.0l	m	CH02	
106	04/03/2017	07:14:53	39.45136	75.18587	4	-	-	-	3.4m_B	n	CH02	
107	19/03/2017	07:57:04	39.92694	75.58366	5	-	-	-	3.5m_B	n	CH02	
108	21/03/2017	14:46:38	39.93275	75.64613	16	-	-	-	3.5m_B	n	CH02	
109	27/03/2017	15:26:56	40.06626	75.76215	17	-	-	-	3.7m_B	n	CH01	
110	30/03/2017	11:10:04	39.83445	75.30047	13	-	-	-	3.7m_B	n	CH01	
111	12/01/2019	04:32:02	39.63307	75.60156	23	236	28	73	4.6m_B	d	CH01	gCMT

It is unlikely that the macroseismic contours are distorted by damage from these aftershocks, because all four in the northern lobe of the damage polygon were $M_w < 5.0$ and occurred at greater than 10 km depth. This means they probably weren't capable of causing intensity VII or VIII damage, which involves people "losing balance" and "finding it difficult to stand" respectively (Hu et al. 1996; Li et al. 2021).

We observe an additional NE-SW alignment of aftershocks, passing through the easternmost surface ruptures (Figure 4.6 cross section B-B'). These appear to lie on a plane dipping ∼45-60°southwards and include the 11^{th} September aftershock (Event 30), whose south-dipping planes roughly align with the aftershocks. It is likely these aftershocks are picking out the structure on which the 11^{th} September aftershock ruptured.

Li et al. (2019) propose that the true epicentre of the Wuqia mainshock might be ∼10–30 km south-west of the ISC-EHB epicentre, depending on the depth, so that it could rupture on the Tuomuluoan thrust or one of the thrusts from the Pamir basement. This would also require the mechanism to have a dip ∼40–60°shallower than modelled for the north-east-striking nodal plane. In addition the strike of this plane would need to be ∼60°greater to match the surface trace and seismically imaged section of the Tuomuluoan

thrust. Finally, to form right lateral surface ruptures (Feng et al. 1986; He et al. 2024) the rake of the mechanism would need to be the inverse of what was modelled, as the north-east-striking plane has a left-lateral sense.

We do not find significant aftershock activity in the Biertuokuoyi Basin nor in the Pamir foothills. This suggests that the ramp faults identified in (Li et al. 2019) did not play a significant role in the 1985 earthquake sequence, and in our view rules out their hypothesis that the 1985 earthquake occurred on these faults.

4.4.3 Depth distribution of the cluster

The modal depth is 15–20 km with an average depth error of $\sim \pm$ 5 km (Figures 4.4 and 4.6). We observe earthquake depths of up to 45–50 km (Figure 4.5), a trend identified by Sloan et al. (2011) in other areas of the Tarim Basin, and attributed to thickened lower crust granulite facies rocks, rendered metastable by low water content, so seismic to greater depths than younger areas of continental crust (Jackson et al. 2008). We observe 8 events at less than 5 km depth.

Given the issues with depth determination from depth phases, it is worth examining the depths derived from the local distance method (Section 4.3.3) to see if the distribution differs from the depth phase depths. Figure 4.5a shows a histogram of depths categorised by whether they were solved by near or local distance methods or depth phases. The distributions are different, with the local distance depths more likely to be shallower than the depth phase depths. This could be because of differences in time — the events within the 2015–2017 8H instrumental period were more likely to be constrained with local distance methods than the earlier earthquakes. Alternatively, this could reflect a bias, meaning that events with depths derived from depth phases are in fact shallower than modelled.

Ainscoe (2018) suggest that, given these mismatches between the geomorphology and the mechanism, it is possible instead that the Wuqia mainshock ruptured within the crystalline basement on an unmapped fault. Seismic reflection surveys penetrate only the first ~10 km of the surface, of which most is sediment (Li et al. 2019) so the geometry of base-

ment faulting is virtually unconstrained. To generate surface ruptures, Ainscoe (2018) argue that the M_w 6.1 11^{th} September 1985 aftershock generated the surface ruptures. The focal mechanism for this event is more consistent with the geomorphic expression of faulting in the area, and the centroid depth was reported to be shallow (Fan et al. 1994).

4.5 Discussion

4.5.1 Source of the surface ruptures

A discontinuous set of ruptures together extending for ∼30 km in length are likely to be associated with the 1985 earthquake (Section 4.2.3; Figure 4.4), though the timing of surface rupture formation is not well constrained, and could have occurred any time between August 1985 and mid 1986. Ainscoe (2018) discuss a number of possibilities for the surface rupture including 1) the majority are due to the 1985 earthquake mainshock; 2) the majority are due to the 11^{th} September aftershock; 3) the ruptures formed aseismically via postseismic afterslip.

It is unlikely that the 1985 mainshock caused the surface ruptures between the Mingyaole Anticline and the Tuomuluoan Thrust for several reasons. Firstly, it was a deep earthquake, as determined by our modelling which finds a hypocentre depth of 28 +13 -5 km, and body-waveform modelling which finds centroid depths of ∼15–20 km, and certainly within the crystalline basement. Secondly, the surface ruptures are inconsistent with both focal planes suggested by the 1985 focal mechanism. For the north-east dipping right-lateral plane, the ruptures are of the opposite sense (i.e. express an up-to-the-south-west sense). For the south-dipping plane, the ruptures (a) do not agree with the strike of this plane and (b) do not agree with the sense of motion, as right lateral ruptures cannot be produced by a left lateral focal mechanism.

The north-east dipping plane would project to the surface somewhere in the Biertuokuoyi Basin, where there do not appear to be surface ruptures. This is to be expected, given the depth of the earthquake and the young, unconsolidated sediments of the basin. The

M_w 6.4 2015 Pishan Earthquake, ∼250 km south of Wuqia at the south-western edge of the Tarim Basin, left no surface ruptures despite a centroid depth of only ∼7 km (Li et al. 2016). Furthermore, the 2020 Kalpan Earthquake, ∼100 km east of Wuqia within the Kepingtage Fold and Thrust Belt (FTB), also left no surface ruptures, rupturing on a shallow detachment (Wang et al. 2022; Zhang et al. 2023).

It is possible that the 11^{th} September aftershocks are responsible for the easternmost ruptures mapped 1985–6 (Figure 4.5). Our modelling finds the depth of this epicenter to be ∼17 km using both depth phases and the local distance method (Section 4.3.3). This is a lot deeper than the ∼7 km modelled by Fan et al. (1994) and Burtman and Molnar (1993). We believe this is due to Fan et al. (1994) fitting a double source to the depth phases, resulting in a shallow centroid estimate (Appendix A17).

At our depth and location, the south-west dipping focal plane from the 11^{th} Sept aftershock would project to the surface at the northern edge of the Mingyaoloe anticline -15 km distant from the nearest surface rupture. To make a rupture only ∼7 km from our *mloc* epicenter, the dip of the south dipping plane would need to be 65–70°, about 10–15°steeper than modelled by Fan et al. (1994), which is possible, as the P wave nodal planes are not well constrained by stations (Appendix A17). Assuming this is the case, we can examine whether the surface ruptures are consistent with the moment magnitude of this earthquake (5.9–6.1).

Assuming a fault width from the epicenter to the surface of ∼18 km, the ∼10 km length of the ruptures mapped 1985-6, a shear modulus of $3x10^{10}$ Pa·s and a slip of 0.5 m (based on displacement to length scaling relationships (e.g. Scholz et al. (1986)), this gives a seismic moment of $2.7x10^{18}$ Nm which is M_w 6.2. This result pushes the upper end of acceptable magnitudes, and the slip is smaller than the observed surface ruptures. One way to resolve the discrepancy would be to invoke an amount of afterslip, which given the ∼9–12 months before a survey of the ruptures is reasonable, as afterslip timescales are generally within a year or so of the earthquake (Savage et al. 2005). In addition, the afterslip moment can be up to three times the seismic moment (Churchill et al. 2022), so it

is plausible that the original ruptures were augmented by afterslip before being measured by Feng in mid-1986. It is likely that the afterslip occurred predominantly prior to the time of field measurement, as Ainscoe (2018) find less than 2 m fault movement via image correlation, and He et al. (2024) do not appear to find different scarp heights to Feng et al. (1988). Therefore it is possible the easternmost ruptures were caused by the 11^{th} September aftershock, and further augmented by afterslip over the ∼9 months before the full rupture survey by Feng et al. (1988).

The westernmost ruptures, mapped by Ainscoe (2018) and He et al. (2024) are more difficult to assign to an earthquake. The westernmost ruptures would be consistent with the shallow 2011 M_w 4.9 thrust mechanism at the western end of the Tuomuluoan Thrust (Event 11, Figure 4.5) but these ruptures are still visible in Google Earth imagery from 2006. It is possible the 2011 earthquake added to the scarp height since they were identified remotely, as the 1 m height was only measured very recently (He et al. 2024). A possibility is that they are caused by transient aseismic creep in response to the stress changes from the Wuqia earthquake (e.g. Ainscoe (2018). InSAR today shows the Tuomuluoan Fold is growing at less than 2 mm/yr (Bufe et al. 2017), so if creep was responsible for forming the 1–2 m scarps, it has now ceased. Metre scale postseismic displacements from creep are known, but they have not been known to form scarps (Copley et al. 2014; Zhou et al. 2016).

4.5.2 Structure involved in the 1985 Mainshock

We agree with Ainscoe (2018) that the Wuqia earthquake likely ruptured on a pre-existing structure related to the SYF (Figure 4.7). As described in Section 4.1.2 this structure is likely to have originally linked with the Talas Fergana Fault when rapid right-lateral motion was occurring between the Pamir and Tarim Basin. We have described in (Section 4.2.2) the evidence for the Wuqia Earthquake occurring on the north-east dipping plane, which is consistent with slip on a fault with similar orientation and sense to the SYF. Further points of evidence are described below.

Firstly, two body-waveform modelled gWFM mechnanisms of M_w 6 show strike slip fault-

ing coincident with the projection of the Talas Fergana Fault with the same orientation suggesting the right lateral kinematics continue past the Arpa Valley into the Tian Shan (Figure 4.1).

Secondly, there is evidence some of the anticlines near to the Pamir are growing above faults dipping north-east into the Tarim Basin, for example the Yengisar Anticline (Figure 4.1) (Wang and Wang 2016). This shows active structures with similar kinematics to the Wuqia Earthquake mechanism.

Thirdly, there is evidence of some amount of right lateral strike slip motion in the Mingyaole Anticline, with south-west-striking en-echelon normal faults visible within the fold (Figure 4.4).

4.5.3 An earthquake double-event?

The presence of surface ruptures with dip opposite to the seismologically derived focal mechanism, apparently without a corresponding earthquake, lead us to suspect an earthquake double event: where two earthquakes occur simultaneously so that they are difficult to distinguish in the seismology but nonetheless represent motion on two different faults. Burtman and Molnar (1993) comment that the waveforms for the 1985 Wuqia Earthquake are consistent with a multi-event rupture (Appendix A16)

InSAR studies have allowed the imaging of earthquake doublets with conjugate mechanisms (i.e. motion on faults with opposite dips). The 2008 M_w6.9 Iwate-Miyagi Island Earthquake, in northeast Japan, appears to have ruptured simulataneously on two conjugate faults at similar depths based on InSAR, GNSS and earthuqake aftershock data (Abe et al. 2013). This shows that despite the apparent space problem implied by faults of opposite dips both slipping, it does happen in nature. While the faults in this earthquake doublet were the same depth, the 2016 M_w6.4 MeiNong Earthquake in Taiwan shows there can be depth separation between the structures involved in the earthquake, as is the case for the 1985 Wuqia Earthquake. InSAR analysis shows motion during the MeiNong Earthquake on structures at 5-10 km depth and 15-20 km depth (Huang et al. 2016). The

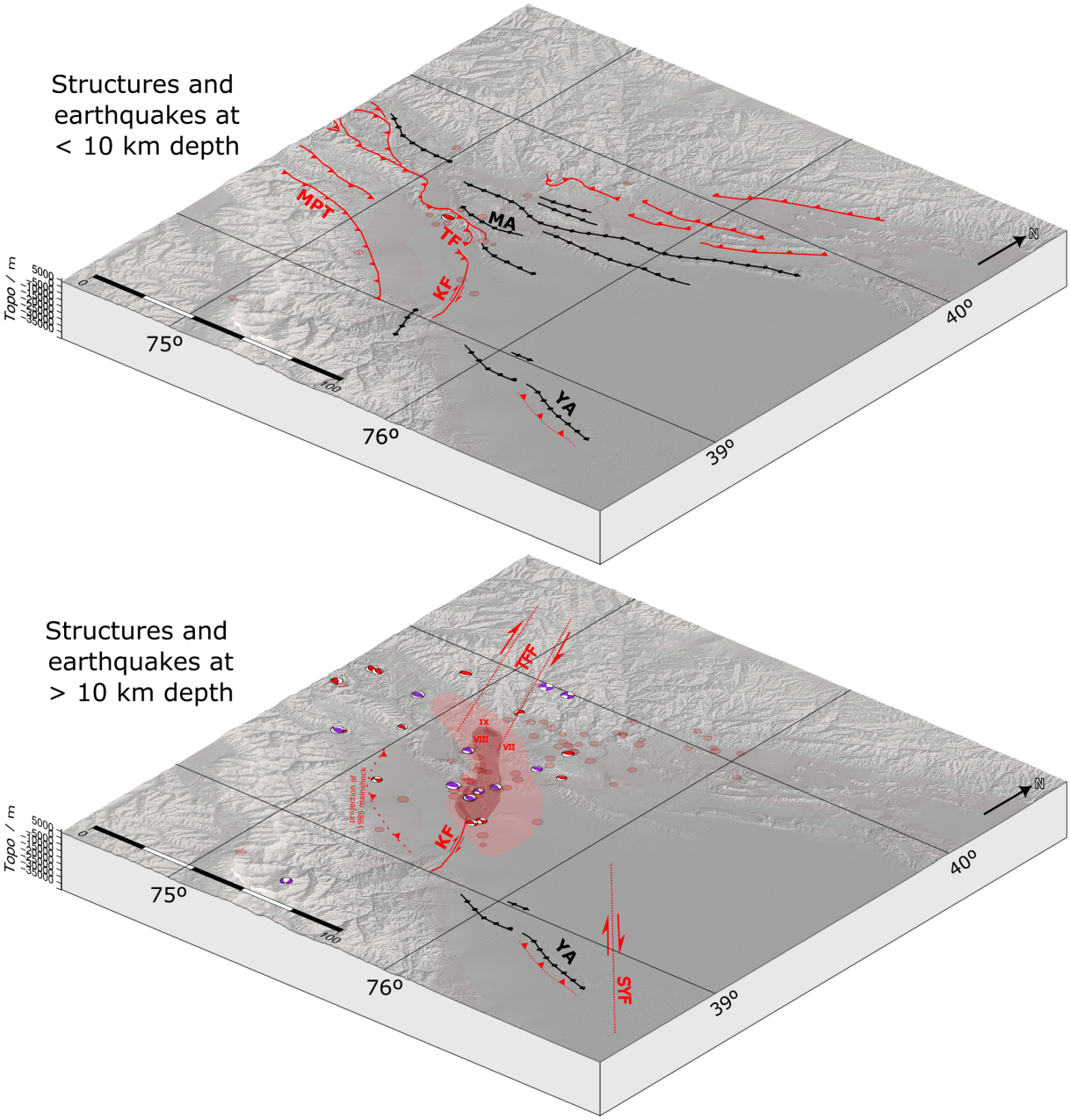

Figure 4.7: Tectonic model for the 23^{rd} August 1985 M_w 6.9 Wuqia mainshock. The top panel shows surface sedimentary structures and earthquakes shallower than 10 km depth within the sedimentary cover. The majority of shallow earthquakes are concentrated on the surface structures such as the TF, MA and KF. The bottom panel shows earthquakes deeper than 10km and structures that suggest a transpressional strike-slip system at depth. The SYF is visible in seismic reflection profiles but is not evident at the surface. The TFF is a projection of active mapping by (Rizza et al. 2019), and the two right lateral strike slip earthquakes nearby suggest it is active. The intensity contours of the 1985 mainshock line line up well with the TFF zone, and multiple earthquake mechanisms. Taken together, this suggests the 1985 mainshock occurred on a north-east dipping fault relating to the stepover between the TFF and SYF. TF=Tuomuluoan Thrust Fault; MA=Mingyaole Anticline; KF=Kumtagh Fault; SYF=Shache-Yangdaman Fault; TFF=Talas-Fergana Fault

seismologically derived hypocentre was on the deeper fault, similar to our finding of a relatively deep *mloc* hypocentre. Rupture initiation on the deeper fault is consistent with conceptualisations of the brittle-ductile transition depth as being the site where earthquakes nucleate (Doglioni et al. 2011). **ainscoeEarthquakesActiveFaults** conducted Coulomb stress modelling of the 1985 Wuqia Earthquake to understand whether motion on the deeper fault plane identified by Burtman and Molnar (1993) would push structures at shallower depths closer to failure. This showed that structures within $\sim$ 5 km of the surface, such as the Tuomuluoan Thrust, would not be pushed substantially closer to failure. Another possibility could be dynamic triggering: where a stressed fault is pushed to the point of failure by transient stresses from seismic waves emanating from another earthquake. This appears to be what happened during the 1997 Harnai Earthquake, Pakistan, where two fault planes over 50 km away ruptured within 20 seconds of eachother, despite Coulomb stress modelling indicating rupture on the first plane made rupture on the second plane less likely (Nissen et al. 2016). This provides a means by which rupture of the deeper fault could have caused rupture on the Tuomuluoan Thrust during the 1985 Wuqia Earthqake.

We believe the 1985 Wuqia earthquake was a double-event on conjugate faults. It first ruptured a deeper, previously unidentified structure linking the TFF with the SYF. This triggered slip in its conjugate: the shallower Tuomuluoan Thrust. This explains the existence of the surface ruptures with opposite dip to the focal mechanism – too long to be explained by the shallower 11th September aftershock – and the apparent complexity of the earthquake seismology (Burtman and Molnar 1993; Fan et al. 1994). The September 11th aftershock shows that conjugate faulting is present – albeit temporally separated from the mainshock – given the aftershock sequence indicates it was the south-dipping plane that ruptured in this earthquake (Figure 4.3 cross section B-B').

4.5.4 Is the sedimentary cover seismogenic?

We find in our study most earthquakes nucleate in the crystalline basement and not in the sedimentary cover, in contrast to other fold and thrust belts such as the Zagros where an equal distribution of basement and sedimentary faulting is observed (e.g. Karasözen

et al. (2019), Nissen et al. (2011), and Nissen et al. (2014)). One reason for this could be the relative youth of sediments in the north-west Tarim Basin compared to the Zagros. In the north-west Tarim, the top $\sim$ 80 % the sedimentary thickness is composed of sediments of Paleogene age or younger (Figure 4.3) (Gao et al. 2013; Li et al. 2019). In the Zagros, only $\sim$ 40–50 % of the sedimentary thickness Paleogene or younger (Casciello et al. 2009; Molinaro et al. 2005; Nissen et al. 2011; Sherkati et al. 2005). This could mean that the sediments in the north-west Tarim are relatively weak and generally not capable of nucleating earthquakes.

It is possible that given our selection bias towards immediate aftershocks of the 1985 earthquake we have a non-representative sample of seismicity, but we do have all the moderate magnitude events within $\sim$ 100 km from 1985 to the present, and of those only event 74 appears to be within the sedimentary cover (Figure 4.3).

Caution should be given to our depth estimates. For one, there is evidence that depth determinations with *mloc* represent an upper limit, and that the centroid is generally shallower (e.g. Karasözen et al. (2019)).

4.5.5 Implications for seismic hazard

We find the Wuqia earthquake likely occurred on a structure not obvious from the structures visible at the surface, which are dominated by the convergence between the Pamir and Tian Shan. Despite the dominance of these structures, we find several of the moderate magnitude earthquakes of the past 40 years are not related to them, with most of our hypocentres occurring below the sedimentary cover.

This is in contrast to other areas of the Tarim Basin margin, where the larger earthquakes correlate well with the observed surface structures, for example the 1902 M_w 7.7 Atushi earthquake (Figure 4.1) (Kulikova and Krüger 2017); the 2015 M_w 6.3 Pishan earthquake (Ainscoe et al. 2017); and the 2020 M_w 6.0 Kalpin earthquake (Zhang et al. 2023).

The difference here is likely due to the north-west Tarim being the junction between several faults (Figure 4.1). This highlights that structures that might be considered "inactive" by examining surface geomorphology, such as the SYF (Figure 4.1), could still present seismic hazards.

4.6 Conclusions

Using calibrated earthquake relocation software, *mloc*, we generate a cluster of 111 earthquakes, including the 1985 M_w 6.9 Wuqia earthquake, its immediate aftershocks, and subsequent moderate magnitude events with focal mechanisms. We suggest a tectonic model where the 1985 earthquake ruptured a previously unmapped transpressional flower structure within the basement of the Tarim Basin, connecting the Shache-Yangdaman fault with the active Talas Fergana Fault. We suggest that strike-slip motion across this fault is now very slow, and so it does not generate a clear imprint in the geomorphology, which is dominated by the far more rapid Pamir-Tian Shan convergence.

While the 1985 earthquake source parameters appear incompatible with the observed surface ruptures, we suggest a double event on conjugate faults explains the surface rupture pattern and the complexities in the seismic source described by those who modelled the source parameters. We suggest the 1985 earthquake nucleated at 18km depth and propagated towards the surface, with

The 11^{th} September aftershock appears to have been too deep to cause any surface ruptures, as there are none observed around where the fault plane projects to the surface.

We find much of the seismic activity is concentrated in the basement of the Tarim Basin, in contrast to other fold and thrust belts, such as the Simply Folded Belt in Iran. This shows the value of examining historical large earthquakes within continental interiors, rather than relying exclusively on surface geomorphology for evidence of seismic hazard.

Statement of Authorship for joint/multi-authored papers for PGR thesis

To appear at the end of each thesis chapter submitted as an article/paper

The statement shall describe the candidate's and co-authors' independent research contributions in the thesis publications. For each publication there should exist a complete statement that is to be filled out and signed by the candidate and supervisor **(only required where there isn't already a statement of contribution within the paper itself).**

Title of Paper	Rupture of the 1985 Wuqia Earthquake on a transpressional strike slip basement structure: implications for seismic hazard in sedimentary basins
Publication Status	□Published □ Accepted for Publication □Submitted for Publication xUnpublished and unsubmitted work written in a manuscript style
Publication Details	Johnson, Benedict; E.A. Bergman; R.T. Walker

Student Confirmation

Student Name:	Benedict Johnson		
Contribution to the Paper	Performed calibrated earthquake relocations, interpretation and analysis, wrote the manuscript		
Signature Ben Johnson		Date	26-April-2026

Supervisor Confirmation

By signing the Statement of Authorship, you are certifying that the candidate made a substantial contribution to the publication, and that the description described above is accurate.

Supervisor name and title:	Prof. Richard T. Walker	
Supervisor comments The above statement is accurate. The candidate led this work and made a substantial contribution.		
Signature 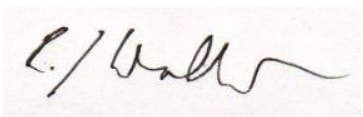	Date	26/04/2025

This completed form should be included in the thesis, at the end of the relevant chapter.

5 | Concluding Remarks

This thesis has examined convergent continental margins using a series of case studies. Chapters 2 and 4 focussed on the Pamir-Tian Shan convergence zone, being driven by India's northward motion towards Asia. Chapter 3 looked at the closure of the Kura Basin between the Greater and Lesser Caucasus driven by the motion of Arabia into Eurasia.

The Kura Basin case study has shown that aseismic creep is likely a widespread phonomenon outside the United States, where most research into creep has occurred. Adding to the database of creeping faults gives others the ability to study how variations in geology, slip rate, kinematics and other factors influence whether creep occurs.

5.1 Thesis conclusions

The tectonics of the Pamir and the Turkish-Iranian Plateau share many similarities (Şengör and Kidd 1979). The Turkish-Iranian Plateau is analogous to the Pamir Plateau; the Kura Basin is analogous to the Alai Valley; the Greater Caucasus analogous to the Tian Shan; and the Arabian plate to the Indian plate.

The most interesting insight of this thesis is the possibility, raised in Chapter 3, that gravitational potential energy drives motions that could be interpreted as arising from tectonics. We find evidence of rapid creep on two conjugate faults in the Kura Basin, Azerbaijan, with up to ∼7 mm/yr creep on right-lateral the Alat Fault, and ∼1.5–2.5 mm/yr creep on the left-lateral Sumquayit Fault. Together these faults form pincers pushing out a wedge of material we term the Gobustan wedge into the South Caspian Basin. The eastward motion of the Gobustan Wedge is a combination of the convergence between the Lesser and Greater Caucasus and the gravitational potential energy contrasts between the Gobustan Wedge and the South Caspian Basin, with apparent folding of sediments within the Basin in response to motion of the Gobustan Wedge.

As outlined in Chapter 1, we generally interpret movement along faults to be driven by far-field tectonic forces, driven by gravity in the form of ridge-push or slab pull at the edges of tectonic plates. If this is true, it means that strain imposed by these tectonic

forces needs to be accommodated through the entire crust, with deformation occurring in a brittle manner in the upper crust, and in a ductile manner in the lower crust and mantle. What this means is simply: we expect surface deformation to be similar to deformation at depth. For example, where we see the development of folding in the Kura Basin in Azerbaijan, we believe this is showing motion on faults at depth which over time build the topography.

The case of the Gobustan Wedge shows that gravitationally driven motion of surface sediments can act to obscure the role of tectonic forces in a region. If tectonic forces are wholely responsible for the eastwards motion of the Gobustan Wedge, then we must infer that the surface motion on the bounding Salyan and Sumquayit faults is representative of motion at depth on those faults. If, however, the surface sediments have been mobilised by gravity, surface motion on these faults may not be representative of motion at depth. This could mean a fault that appears to be creeping at the surface could in fact be accumulating strain.

In Chapter 2 and Chapter 3 we saw examples of how large gravitational potential energy contrasts combined with tectonic convergence can mobilise sediments. In Chapter 3 we used InSAR time series analysis to show how the convergence observed in GNSS is accommodated on individual faults. In Chapter 2 we see this in the right-lateral motion of the Peter I Range relative to the Tian Shan, which appears to also be happening via creep. Here the gravitational potential energy contrasts are between the Peter I Range and the Tajik Basin, and the tectonic convergence is between the Pamir and Tian Shan.

Through this thesis we see the role of fluids in these motions is very important. Throughout the Kura Basin in Chapter 3 the faults are moving via creep. In addition to the Alat and Sumquayit Faults discussed above, we find evidence of at least ∼5 mm/yr uplift on the creeping frontal thrust the Kura Fold and Thrust Belt, and find about 3–6 mm/yr uplift at a transpressional bend in the Salyan Fault. We know there are fluidised sediments at depth in the Kura Basin from geological studies and the many mud volcanoes of Azerbaijan which follow fault lineaments. This shows pressurised fluids migrate to the surface along lines of weakness presented by faults.

In Chapter 4 we see a case where sediments are deposited in a flat basin with no graviational potential energy contrasts — they are at the lowest point in the landscape. Here, the motion of the sediments is more strongly controlled by the tectonic motion between the converging Pamir and Tian Shan compared to the Peter I Range or the Kura Basin. The 1985 Wuqia earthquake here represents motion on a long lived, localised tectonic boundary along the Pamir margin which has now been concealed beneath young sediments in the basement of the Tarim Basin.

A unifying theme of this thesis is the danger presented by slow-moving faults which are not well expressed in geomorphology. This may be because they are buried beneath rapidly accumulating sedimentary covers, as in the case of the Wuqia Earthquake, or because in high mountains rapidly shaped by erosion any traces the faults leave are rapidly removed, as in the case of the 1949 Khait Earthquake. Even with the earth observation capabilities we have now, these faults are not obvious. The occurrence of large earthquakes on unmapped faults also shows the limitations of the relatively short earthquake catalogues we have, which does not capture the full earthquake cycle on all, or even most, of the faults within the continents. The 1949 Khait earthquake and the 1985 Wuqia earthquake represent a warning for Azerbaijan, where rapid motions in the sediments driven by gravitational forces and accommodated aseismically by creep could be obscuring the accumulation of tectonic forces within the basement which may one day release a large earthquake.

5.2 Further work

This thesis presents several lines of inquiry it would be worth pursuing further.

The most urgent is that more paleoseismic work should be done in and around the Kura Basin, Azerbaijan. Results so far suggest that the Salyan Fault has broken in several earthquakes during the Holocene. Developing an understanding of how creep on faults looks in the paleoseismological record is essential. Are all the "ruptures" in a paleoseismic

trench seismogenic, or could they be recording creep events which we observe geodetically on other faults? Reconciling the rapid creep observed with InSAR in the present day with the paleoseismology is essential for understanding the seismic hazard posed to Azerbaijan and its surroundings.

Determining the relative contribution of tectonic forces and gravitational forces to the motion observed in the Kura Basin is necessary to understand how much strain may be accumulating in the basement to be released in an earthquake. It may be possible to model the expected velocities on these faults, if adequate constitutive relations can be determined for the weakest sediments which control the rate of deformation. Similarly, for the Peter I Range in Tajikistan this modelling would be useful.

The phenomenon of gravitationally driven motion in sedimentary basins should be explored further, in particular the physical conditions of the sediments which allow it to occur. In the Kura Basin, the presence of fluids is well known, and it may be that the water content of sedimentary basins is a key factor in whether the sediments can be mobilised by gravity. Accretionary wedges around subduction zones are another site where this process may be happening. Building our knowledge of the places where this graviational collapse is occuring will allow us to understand the geological conditions necessary for it to happen.

Finally, many of the insights of this thesis came from close examination of large historical earthquakes which happened when instrumentation was much poorer. Because of the paucity of large continental earthquakes since a standardised world-wide seismic network was completed in the 1960s, it is necessary to continue delving into the past to learn about earthquakes, rather than waiting for them to happen in the present.

Bibliography

Abdrakhmatov, KE et al. (2016). "Multisegment Rupture in the 11 July 1889 Chilik Earthquake (M 8.0–8.3), Kazakh Tien Shan, Interpreted from Remote Sensing, Field Survey, and Paleoseismic Trenching". In: *Journal of Geophysical Research: Solid Earth* 121.6, pp. 4615–4640. ISSN: 2169-9356. DOI: 10.1002/2015JB012763.

Abdrakhmatov, KY et al. (Dec. 1996). "Relatively Recent Construction of the Tien Shan Inferred from GPS Measurements of Present-Day Crustal Deformation Rates". In: *Nature* 384.6608, pp. 450–453. ISSN: 1476-4687. DOI: 10.1038/384450a0.

Abdulhameed, S et al. (May 2020). "Tajik Basin and Southwestern Tian Shan, Northwestern India-Asia Collision Zone: 2. Timing of Basin Inversion, Tian Shan Mountain Building, and Relation to Pamir-Plateau Advance and Deep India-Asia Indentation". In: *Tectonics* 39.5. ISSN: 0278-7407, 1944-9194. DOI: 10.1029/2019TC005873.

Abe, T et al. (Feb. 2013). "Nonplanar Fault Source Modeling of the 2008 Mw 6.9 Iwate–Miyagi Inland Earthquake in Northeast Japan". In: *Bulletin of the Seismological Society of America* 103.1, pp. 507–518. ISSN: 0037-1106. DOI: 10.1785/0120120133.

Abramowski, U et al. (May 2006). "Pleistocene Glaciations of Central Asia: Results from 10Be Surface Exposure Ages of Erratic Boulders from the Pamir (Tajikistan), and the Alay–Turkestan Range (Kyrgyzstan)". In: *Quaternary Science Reviews* 25.9, pp. 1080–1096. ISSN: 0277-3791. DOI: 10.1016/j.quascirev.2005.10.003.

Abrams, MA and AA Narimanov (1997). "Geochemical Evaluation of Hydrocarbons and Their Potential Sources in the Western. South Caspian Depression, Republic of Azerbaijan". In: *Marine and Petroleum Geology* 14.4, pp. 451–468.

Ainscoe, EA et al. (2017). "Blind Thrusting, Surface Folding, and the Development of Geological Structure in the M 6.3 2015 Pishan (China) Earthquake". In: *Journal of Geophysical Research: Solid Earth* 122.11, pp. 9359–9382. ISSN: 2169-9356. DOI: 10.1002/2017JB014268.

Ainscoe, E (2018). "Earthquakes and Active Faults in Central Asia". DPhil. University of Oxford.

Aki, K and PG Richards (2002). "Quantitative Seismology, 2nd Ed." In: *Quantitative Seismology*.

Aldersons, F (2004). "Toward a Three-Dimensional Crustal Structure of the Dead Sea Region from Local Earthquake Tomography". PhD thesis. Tel-Aviv Israel: Tel-Aviv University.

Alkhalil, M et al. (May 2023). "Inequitable Access to Aid after the Devastating Earthquake in Syria". In: *The Lancet Global Health* 11.5, e653–e654. ISSN: 2214-109X. DOI: 10.1016/S2214-109X(23)00132-8.

Allégre, CJ et al. (Jan. 1984). "Structure and Evolution of the Himalaya–Tibet Orogenic Belt". In: *Nature* 307.5946, pp. 17–22. ISSN: 1476-4687. DOI: 10.1038/307017a0.

Allen, M et al. (2004). "Late Cenozoic Reorganization of the Arabia-Eurasia Collision and the Comparison of Short-Term and Long-Term Deformation Rates". In: *Tectonics* 23.2. ISSN: 1944-9194. DOI: 10.1029/2003TC001530.

Allen, MB et al. (May 2003). "Late Cenozoic Deformation in the South Caspian Region: Effects of a Rigid Basement Block within a Collision Zone". In: *Tectonophysics* 366.3, pp. 223–239. ISSN: 0040-1951. DOI: 10.1016/S0040-1951(03)00098-2.

Allen, MB et al. (Sept. 2002). "Onset of Subduction as the Cause of Rapid Pliocene-Quaternary Subsidence in the South Caspian Basin". In: *Geology* 30.9, pp. 775–778. ISSN: 0091-7613. DOI: 10.1130/0091-7613(2002)030<0775:OOSATC>2.0.CO;2.

Altamimi, Z et al. (2023). "ITRF2020 Plate Motion Model". In: *Geophysical Research Letters* 50.24, e2023GL106373. ISSN: 1944-8007. DOI: 10.1029/2023GL106373.

Altamimi, Z et al. (June 2017). "ITRF2014 Plate Motion Model". In: *Geophysical Journal International* 209.3, pp. 1906–1912. ISSN: 0956-540X. DOI: 10.1093/gji/ggx136.

Ambraseys, NN and JA Jackson (July 1997). "Seismicity and Strain in the Gulf of Corinth (Greece) Since 1694". In: *Journal of Earthquake Engineering* 01.03, pp. 433–474. ISSN: 1363-2469. DOI: 10.1142/S1363246997000179.

Ambraseys, NN and CP Melville (Nov. 2005). *A History of Persian Earthquakes*. Cambridge University Press. ISBN: 978-0-521-02187-6.

Amey, RMJ et al. (Sept. 2021). "Significant Seismic Risk Potential From Buried Faults Beneath Almaty City, Kazakhstan, Revealed From High-Resolution Satellite DEMs". In: *Earth and Space Science* 8.9. DOI: http://dx.doi.org/10.1029/2021EA001664.

Amey, RMJ et al. (Nov. 2022). "Improving Urban Seismic Risk Estimates for Bishkek, Kyrgyzstan, through Incorporating Recently Gained Geological Knowledge of Hazards". In: *Natural Hazards*. ISSN: 1573-0840. DOI: 10.1007/s11069-022-05678-0.

Anderson, E (Jan. 1905). "The Dynamics of Faulting". In: *Transactions of the Edinburgh Geological Society* 8.3, pp. 387–402. DOI: 10.1144/transed.8.3.387.

Ansal, A, ed. (2015). *Perspectives on European Earthquake Engineering and Seismology: Volume 2*. Vol. 39. Geotechnical, Geological and Earthquake Engineering. Cham: Springer International Publishing. ISBN: 978-3-319-16963-7 978-3-319-16964-4. DOI: 10.1007/978-3-319-16964-4.

Ansari, H et al. (Feb. 2021). "Study of Systematic Bias in Measuring Surface Deformation With SAR Interferometry". In: *IEEE Transactions on Geoscience and Remote Sensing* 59.2, pp. 1285–1301. ISSN: 1558-0644. DOI: 10.1109/TGRS.2020.3003421.

Antonielli, B et al. (Dec. 2014). "Pre-Eruptive Ground Deformation of Azerbaijan Mud Volcanoes Detected through Satellite Radar Interferometry (DInSAR)". In: *Tectonophysics* 637, pp. 163–177. ISSN: 0040-1951. DOI: 10.1016/j.tecto.2014.10.005.

Argand, E (1924). "La tectonique de l'Asie. Conférence faite á Bruxelles, le 10 août 1922". In: *Congrès géologique international (XIIIe session)- Belgique 1922*, p. 171.

Arrowsmith, JR and MR Strecker (Nov. 1999). "Seismotectonic Range-Front Segmentation and Mountain-Belt Growth in the Pamir-Alai Region, Kyrgyzstan (India-Eurasia Collision Zone)". In: *GSA Bulletin* 111.11, pp. 1665–1683. ISSN: 0016-7606. DOI: 10.1130/0016-7606(1999)111<1665:SRFSAM>2.3.CO;2.

Avouac, JP and P Tapponnier (1993). "Kinematic Model of Active Deformation in Central Asia". In: *Geophysical Research Letters* 20.10, pp. 895–898. ISSN: 1944-8007. DOI: 10.1029/93GL00128.

Baljinnyam, I (1993). *Ruptures of Major Earthquakes and Active Deformation in Mongolia and Its Surroundings*. Geological Society of America. ISBN: 978-0-8137-1181-2.

Bande, A et al. (Jan. 2017). "Talas–Fergana Fault Cenozoic Timing of Deformation and Its Relation to Pamir Indentation". In: *Geological Society, London, Special Publications* 427.1, pp. 295–311. ISSN: 0305-8719, 2041-4927. DOI: 10.1144/SP427.1.

Benn, DI and LA Owen (Apr. 1998). "The Role of the Indian Summer Monsoon and the Mid-Latitude Westerlies in Himalayan Glaciation: Review and Speculative Discussion". In: *Journal of the Geological Society* 155.2, pp. 353–363. ISSN: 0016-7649. DOI: 10.1144/gsjgs.155.2.0353.

Berberian, M (Dec. 1979). "Earthquake Faulting and Bedding Thrust Associated with the Tabas-e-Golshan (Iran) Earthquake of September 16, 1978". In: *Bulletin of the Seismological Society of America* 69.6, pp. 1861–1887. ISSN: 0037-1106. DOI: 10.1785/BSSA0690061861.

Berberian, M (Dec. 2005). "The 2003 Bam Urban Earthquake: A Predictable Seismotectonic Pattern along the Western Margin of the Rigid Lut Block, Southeast Iran". In: *Earthquake Spectra* 21.1_suppl, pp. 35–99. ISSN: 8755-2930. DOI: 10.1193/1.2127909.

Berberian, M and GCP King (Feb. 1981). "Towards a Paleogeography and Tectonic Evolution of Iran". In: *Canadian Journal of Earth Sciences* 18.2, pp. 210–265. ISSN: 0008-4077. DOI: 10.1139/e81-019.

Berberian, M and RS Yeats (Dec. 2017). "Tehran: An Earthquake Time Bomb". In: *Tectonic Evolution, Collision, and Seismicity of Southwest Asia: In Honor of Manuel Berberian's Forty-Five Years of Research Contributions*. Ed. by R Sorkhabi. Vol. 525. Geological Society of America, p. 0. ISBN: 978-0-8137-2525-3. DOI: 10.1130/2016.2525(04).

Berezyuk, N (n.d.). *OneGeology VSEGEI Maps*.

Bergman, EA et al. (Oct. 2022). "A Global Catalog of Calibrated Earthquake Locations". In: *Seismological Research Letters* 94.1, pp. 485–495. ISSN: 0895-0695. DOI: 10.1785/0220220217.

Beyer, R et al. (July 2021). *NeoGeographyToolkit/StereoPipeline 3.0.0*. Zenodo. DOI: 10.5281/ZENODO.5140581.

Beyer, RA et al. (Sept. 2018). "The Ames Stereo Pipeline: NASA's Open Source Software for Deriving and Processing Terrain Data". In: *Earth and Space Science* 5.9, pp. 537–548. ISSN: 23335084. DOI: 10.1029/2018EA000409.

Bindi, D et al. (Feb. 2013). "Location and Magnitudes of Earthquakes in Central Asia from Seismic Intensity Data: Model Calibration and Validation". In: *Geophysical Journal International* 192.2, pp. 710–724. ISSN: 0956-540X. DOI: 10.1093/gji/ggs039.

Bird, P (2003). "An Updated Digital Model of Plate Boundaries". In: *Geochemistry, Geophysics, Geosystems* 4.3. ISSN: 1525-2027. DOI: 10.1029/2001GC000252.

Birren, T and JE Reber (2019). "The Impact of Rheology on the Transition From Stick-Slip to Creep in a Semibrittle Analog". In: *Journal of Geophysical Research: Solid Earth* 124.3, pp. 3144–3154. ISSN: 2169-9356. DOI: 10.1029/2018JB016914.

Bloch, W et al. (2021). "Structure and Stress Field of the Lithosphere Between Pamir and Tarim". In: *Geophysical Research Letters* 48.22, e2021GL095413. ISSN: 1944-8007. DOI: 10.1029/2021GL095413.

Bloch, W et al. (Apr. 2023). "The 2015–2017 Pamir Earthquake Sequence: Foreshocks, Main Shocks and Aftershocks, Seismotectonics, Fault Interaction and Fluid Processes". In: *Geophysical Journal International* 233.1, pp. 641–662. ISSN: 0956-540X. DOI: 10.1093/gji/ggac473.

Bock, T (2011). "Robotic High-Rise Construction of Pagoda Concept: Innovative Earthquake-Proof Design for the Tokyo Sky Tree". In: *Proceedings of CTBUH 2011 World Conference*.

Bormann, P (2002). "Magnitude of Seismic Events, IASPEI". In: *New Manual of Seismological Observatory Practice*. Vol. 1. PotsdamGeoForschungsZentrum, pp. 16–50.

Bormann, P and J Saul (2009). "Earthquake Magnitude". In: *Encyclopedia of Complexity and Systems Science*. Springer, New York, NY, pp. 2473–2496. ISBN: 978-0-387-30440-3. DOI: 10.1007/978-0-387-30440-3_151.

Bormann, P et al. (2013). "Data Analysis and Seismogram Interpretation (Draft, under Review)". In: *New Manual of Seismological Observatory Practice 2 (NMSOP-2);* 14 mb, 152 pages. DOI: 10.2312/GFZ.NMSOP-2_CH11.

Bouchon, M et al. (2001). "How Fast Is Rupture during an Earthquake? New Insights from the 1999 Turkey Earthquakes". In: *Geophysical Research Letters* 28.14, pp. 2723–2726. ISSN: 1944-8007. DOI: 10.1029/2001GL013112.

Bufe, A et al. (2017). "Temporal Changes in Rock Uplift Rates of Folds in the Foreland of the Tian Shan and the Pamir from Geodetic and Geologic Data". In: *Geophysical Research Letters* 44.21, pp. 10, 977–10, 987. ISSN: 1944-8007. DOI: 10.1002/2017GL073627.

Burtman and Molnar (1993). "Geological and Geophysical Evidence for Deep Subduction of Continental Crust beneath the Pamir". In.

Cadek, O (1987). "Studying Earthquake Ground Motion in Prague from Wiechert Seismograph Records". In: *Studying earthquake ground motion in Prague from Wiechert seismograph records* 96.5, pp. 438–447. ISSN: 0016-8696.

Campbell, GE et al. (2013). "The Dzhungarian Fault: Late Quaternary Tectonics and Slip Rate of a Major Right-Lateral Strike-Slip Fault in the Northern Tien Shan Region". In: *Journal of Geophysical Research: Solid Earth* 118.10, pp. 5681–5698. ISSN: 2169-9356. DOI: 10.1002/jgrb.50367.

Campbell, GE et al. (Aug. 2015). "Great Earthquakes in Low Strain Rate Continental Interiors: An Example from SE Kazakhstan". In: *Journal of Geophysical Research: Solid Earth* 120.8, pp. 5507–5534. ISSN: 2169-9356. DOI: 10.1002/2015JB011925.

Cárdenas-Gómez, JC et al. (Jan. 2021). "Evaluation of Reinforced Adobe Techniques for Sustainable Reconstruction in Andean Seismic Zones". In: *Sustainability* 13.9, p. 4955. ISSN: 2071-1050. DOI: 10.3390/su13094955.

Casciello, E et al. (Sept. 2009). "Fold Patterns and Multilayer Rheology of the Lurestan Province, Zagros Simply Folded Belt (Iran)". In: *Journal of the Geological Society* 166.5, pp. 947–959. ISSN: 0016-7649. DOI: 10.1144/0016-76492008-138.

Cawood, PA et al. (Jan. 2013). "The Continental Record and the Generation of Continental Crust". In: *GSA Bulletin* 125.1-2, pp. 14–32. ISSN: 0016-7606. DOI: 10.1130/B30722.1.

Chen, SC et al. (Oct. 2014). "Distribution and Characters of the Mud Diapirs and Mud Volcanoes off Southwest Taiwan". In: *Journal of Asian Earth Sciences* 92, pp. 201–214. ISSN: 1367-9120. DOI: 10.1016/j.jseaes.2013.10.009.

Chen, WP and P Molnar (1977). "Seismic Moments of Major Earthquakes and the Average Rate of Slip in Central Asia". In: *Journal of Geophysical Research (1896-1977)* 82.20, pp. 2945–2969. ISSN: 2156-2202. DOI: 10.1029/JB082i020p02945.

Cheng, J et al. (Oct. 2017). "An Mw-Based Historical Earthquake Catalog for Mainland China". In: *Bulletin of the Seismological Society of America* 107.5, pp. 2490–2500. ISSN: 0037-1106, 1943-3573. DOI: 10.1785/0120170102.

China: Xīnjiāng (Prefectures, Cities, Districts and Counties) - Population Statistics, Charts and Map (2025). https://www.citypopulation.de/en/china/xinjiang/admin/.

Choi, M et al. (Feb. 2021). "Is the Eastern Denali Fault Still Active?" In: *Geology* 49.6, pp. 662–666. ISSN: 0091-7613. DOI: 10.1130/G48461.1.

Churchill, RM et al. (2022). "Afterslip Moment Scaling and Variability From a Global Compilation of Estimates". In: *Journal of Geophysical Research: Solid Earth* 127.4, e2021JB023897. ISSN: 2169-9356. DOI: 10.1029/2021JB023897.

Coburn, A et al. (1992). "Factors Determining Human Casualty Levels in Earthquakes: Mortality Prediction in Building Collapse." In: *Proceedings of the tenth world conference on earthquake engineering* 10, pp. 5989–5994.

Cole, M (Oct. 2015). *U.S. Military Used Christian NGO as Front for North Korea Espionage*. https://theintercept.com/2015/10/26/pentagon-missionary-spies-christian-ngo-front-for-north-korea-espionage/.

Comino, JÁL et al. (2017). "Automated Full Waveform Detection and Location Algorithm of Acoustic Emissions from Hydraulic Fracturing Experiment". In: *Procedia Engineering* 191, pp. 697–702. ISSN: 18777058. DOI: 10.1016/j.proeng.2017.05.234.

Copley, A (Sept. 2008). "Kinematics and Dynamics of the Southeastern Margin of the Tibetan Plateau". In: *Geophysical Journal International* 174.3, pp. 1081–1100. ISSN: 0956-540X. DOI: 10.1111/j.1365-246X.2008.03853.x.

— (Oct. 2012). "The Formation of Mountain Range Curvature by Gravitational Spreading". In: *Earth and Planetary Science Letters* 351–352, pp. 208–214. ISSN: 0012-821X. DOI: 10.1016/j.epsl.2012.07.036.

— (May 2014). "Postseismic Afterslip 30 Years after the 1978 Tabas-e-Golshan (Iran) Earthquake: Observations and Implications for the Geological Evolution of Thrust Belts". In: *Geophysical Journal International* 197.2, pp. 665–679. ISSN: 0956-540X. DOI: 10.1093/gji/ggu023.

Copley, A and J Jackson (2006). "Active Tectonics of the Turkish-Iranian Plateau". In: *Tectonics* 25.6. ISSN: 1944-9194. DOI: 10.1029/2005TC001906.

Copley, A et al. (Aug. 2014). "Active Faulting in Apparently Stable Peninsular India: Rift Inversion and a Holocene-age Great Earthquake on the Tapti Fault". In: *Journal of Geophysical Research: Solid Earth* 119.8, pp. 6650–6666. ISSN: 2169-9313. DOI: 10.1002/2014JB011294.

Coutand, I et al. (2002). "Late Cenozoic Tectonic Development of the Intramontane Alai Valley, (Pamir-Tien Shan Region, Central Asia): An Example of Intracontinental Deformation Due to the Indo-Eurasia Collision". In: *Tectonics* 21.6, pp. 3-1-3–19. ISSN: 1944-9194. DOI: 10.1029/2002TC001358.

Cowgill, E et al. (July 2009). "Low Quaternary Slip Rate Reconciles Geodetic and Geologic Rates along the Altyn Tagh Fault, Northwestern Tibet". In: *Geology* 37.7, pp. 647–650. ISSN: 0091-7613. DOI: 10.1130/G25623A.1.

Croux, C and PJ Rousseeuw (1992). "Time-Efficient Algorithms for Two Highly Robust Estimators of Scale". In: *Computational Statistics*. Ed. by Y Dodge and J Whittaker. Heidelberg: Physica-Verlag HD, pp. 411–428. ISBN: 978-3-662-26811-7. DOI: 10.1007/978-3-662-26811-7_58.

Davies, NS et al. (Mar. 2016). "Resolving MISS Conceptions and Misconceptions: A Geological Approach to Sedimentary Surface Textures Generated by Microbial and Abiotic Processes". In: *Earth-Science Reviews* 154, pp. 210–246. ISSN: 0012-8252. DOI: 10.1016/j.earscirev.2016.01.005.

De Zan, F et al. (Dec. 2015). "Phase Inconsistencies and Multiple Scattering in SAR Interferometry". In: *IEEE Transactions on Geoscience and Remote Sensing* 53.12, pp. 6608–6616. ISSN: 1558-0644. DOI: 10.1109/TGRS.2015.2444431.

Devlin, WJ et al. (Dec. 1999). "The South Caspian Basin – Young, Cool, and Full of Promise 1". In: *AAPG Bulletin* 83.12. ISSN: 0149-1423.

Dewey, J et al. (Jan. 1986). "Shortening of Continental Lithosphere: The Neotectonics of Eastern Anatolia — a Young Collision Zone". In: *Geological Society, London, Special Publications* 19.1, pp. 1–36. DOI: 10.1144/GSL.SP.1986.019.01.01.

Dianala, JDB et al. (2020). "The Relationship Between Seismic and Aseismic Slip on the Philippine Fault on Leyte Island: Bayesian Modeling of Fault Slip and Geothermal Subsidence". In: *Journal of Geophysical Research: Solid Earth* 125.12, e2020JB020052. ISSN: 2169-9356. DOI: 10.1029/2020JB020052.

Diehl, T et al. (June 2009). "Automatic S-Wave Picker for Local Earthquake Tomography". In: *Bulletin of the Seismological Society of America* 99.3, pp. 1906–1920. ISSN: 0037-1106. DOI: 10.1785/0120080019.

Dodds, N et al. (Sept. 2022a). "Interseismic Deformation and Strain-Partitioning along the Main Köpetdag Fault, Turkmenistan, with Sentinel-1 InSAR Time-Series". In: *Geophysical Journal International* 230.3, pp. 1612–1629. ISSN: 0956-540X. DOI: 10.1093/gji/ggac139.

Dodds, N et al. (May 2022b). "A Major Medieval Earthquake on the Main Köpetdag (Kopeh Dagh) Fault, Turkmenistan". In: *Bulletin of the Seismological Society of America* 112.4, pp. 2189–2215. ISSN: 0037-1106. DOI: 10.1785/0120210195.

Doglioni, C et al. (Feb. 2011). "Role of the Brittle–Ductile Transition on Fault Activation". In: *Physics of the Earth and Planetary Interiors* 184.3, pp. 160–171. ISSN: 0031-9201. DOI: 10.1016/j.pepi.2010.11.005.

Dolukhanov, PM et al. (Oct. 2010). "The Khvalynian Transgressions and Early Human Settlement in the Caspian Basin". In: *Quaternary International*. Caspian–Black Sea–Mediterranean Corridors during the Last 30 Ka: Sea Level Change and Human Adaptive Strategies 225.2, pp. 152–159. ISSN: 1040-6182. DOI: 10.1016/j.quaint.2009.10.039.

Dortch, JM et al. (Oct. 2013). "Timing and Climatic Drivers for Glaciation across Semi-Arid Western Himalayan–Tibetan Orogen". In: *Quaternary Science Reviews* 78, pp. 188–208. ISSN: 0277-3791. DOI: 10.1016/j.quascirev.2013.07.025.

Duverger, C et al. (Oct. 2018). "Dynamics of Microseismicity and Its Relationship with the Active Structures in the Western Corinth Rift (Greece)". In: *Geophysical Journal International* 215.1, pp. 196–221. ISSN: 0956-540X. DOI: 10.1093/gji/ggy264.

Dziewonski, AM et al. (1981). "Determination of Earthquake Source Parameters from Waveform Data for Studies of Global and Regional Seismicity". In: *Journal of Geophysical Research: Solid Earth* 86.B4, pp. 2825–2852. ISSN: 2156-2202. DOI: 10.1029/JB086iB04p02825.

Ekström, G et al. (June 2012). "The Global CMT Project 2004–2010: Centroid-moment Tensors for 13,017 Earthquakes". In: *Physics of the Earth and Planetary Interiors* 200–201, pp. 1–9. ISSN: 0031-9201. DOI: 10.1016/j.pepi.2012.04.002.

Ekström, G (1987). "A Broad Band Method of Earthquake Analysis". PhD thesis. Cambridge: Harvard University.

Elliott, A et al. (June 2020). "Satellite Imaging of the 2015 M7.2 Earthquake in the Central Pamir, Tajikistan, Elucidates a Sequence of Shallow Strike-Slip Ruptures of the Sarez-Karakul Fault".

In: *Geophysical Journal International* 221.3, pp. 1696–1718. ISSN: 0956-540X. DOI: 10.1093/gji/ggaa090.

Elliott, JR (Nov. 2020). "Earth Observation for the Assessment of Earthquake Hazard, Risk and Disaster Management". In: *Surveys in Geophysics* 41.6, pp. 1323–1354. ISSN: 1573-0956. DOI: 10.1007/s10712-020-09606-4.

Elliott, JR et al. (2008). "InSAR Slip Rate Determination on the Altyn Tagh Fault, Northern Tibet, in the Presence of Topographically Correlated Atmospheric Delays". In: *Geophysical Research Letters* 35.12. ISSN: 1944-8007. DOI: 10.1029/2008GL033659.

Elliott, JR et al. (2015). "The 2013 M 6.2 Khaki-Shonbe (Iran) Earthquake: Insights into Seismic and Aseismic Shortening of the Zagros Sedimentary Cover". In: *Earth and Space Science* 2.11, pp. 435–471. ISSN: 2333-5084. DOI: 10.1002/2015EA000098.

Emmer, A et al. (Sept. 2020). "70 years of Lake Evolution and Glacial Lake Outburst Floods in the Cordillera Blanca (Peru) and Implications for the Future". In: *Geomorphology* 365, p. 107178. ISSN: 0169-555X. DOI: 10.1016/j.geomorph.2020.107178.

Engdahl, ER et al. (2020). "ISC-EHB 1964–2016, an Improved Data Set for Studies of Earth Structure and Global Seismicity". In: *Earth and Space Science* 7.1. ISSN: 2333-5084. DOI: 10.1029/2019EA000897.

Engdahl, ER et al. (June 1998). "Global Teleseismic Earthquake Relocation with Improved Travel Times and Procedures for Depth Determination". In: *Bulletin of the Seismological Society of America* 88.3, pp. 722–743. ISSN: 0037-1106.

England, P and G Houseman (1986). "Finite Strain Calculations of Continental Deformation: 2. Comparison with the India-Asia Collision Zone". In: *Journal of Geophysical Research: Solid Earth* 91.B3, pp. 3664–3676. ISSN: 2156-2202. DOI: 10.1029/JB091iB03p03664.

England, P and J Jackson (1989). "Active Deformation of the Continents". In: *Annual Review of Earth and Planetary Sciences* 17.1, pp. 197–226. DOI: 10.1146/annurev.ea.17.050189.001213.

— (May 2011). "Uncharted Seismic Risk". In: *Nature Geoscience* 4, pp. 348–349. ISSN: 1752-0908. DOI: 10.1038/ngeo1168.

England, P and P Molnar (2005). "Late Quaternary to Decadal Velocity Fields in Asia". In: *Journal of Geophysical Research: Solid Earth* 110.B12. ISSN: 2156-2202. DOI: 10.1029/2004JB003541.

Evans, SG et al. (Nov. 2009). "Landslides Triggered by the 1949 Khait Earthquake, Tajikistan, and Associated Loss of Life". In: *Engineering Geology* 109.3, pp. 195–212. ISSN: 0013-7952. DOI: 10.1016/j.enggeo.2009.08.007.

Fan, G et al. (1994). "Active Tectonics of the Pamirs and Karakorum". In: *Journal of Geophysical Research: Solid Earth* 99.B4, pp. 7131–7160. ISSN: 2156-2202. DOI: 10.1029/93JB02970.

Fan, X et al. (Apr. 2020). "The Formation and Impact of Landslide Dams – State of the Art". In: *Earth-Science Reviews* 203, p. 103116. ISSN: 0012-8252. DOI: 10.1016/j.earscirev.2020.103116.

Farr, TG and M Kobrick (2000). "Shuttle Radar Topography Mission Produces a Wealth of Data". In: *Eos, Transactions American Geophysical Union* 81.48, pp. 583–585. ISSN: 2324-9250. DOI: 10.1029/EO081i048p00583.

Feng, X et al. (1986). "The Wuqia earthquake of Xinjiang [in Chinese]". In: *Earthquake Research in China* 2.1, pp. 56–60.

Feng, X (1999). "The intensity and causative tectonics of the 1985 Wuqia, Xinjiang, earthquake". In: *Inland Earthquake* 13.2, pp. 169–178.

Feng, Z et al. (1988). "The deformation zone of Wuqia earthquake of M = 7.4 in 1985". In: *Seismology & Geology* 10.2, pp. 39–45.

Fielding, E et al. (Feb. 1994). "How Flat Is Tibet?" In: *Geology* 22.2, pp. 163–167. ISSN: 0091-7613. DOI: 10.1130/0091-7613(1994)022<0163:HFIT>2.3.CO;2.

Forsyth, D and S Uyeda (Oct. 1975). "On the Relative Importance of the Driving Forces of Plate Motion*". In: *Geophysical Journal International* 43.1, pp. 163–200. ISSN: 0956-540X. DOI: 10.1111/j.1365-246X.1975.tb00631.x.

Freed, AM and J Lin (May 2001). "Delayed Triggering of the 1999 Hector Mine Earthquake by Viscoelastic Stress Transfer". In: *Nature* 411.6834, pp. 180–183. ISSN: 1476-4687. DOI: 10.1038/35075548.

Frepoli, A et al. (Mar. 2011). "Seismotectonic of Southern Apennines from Recent Passive Seismic Experiments". In: *Journal of Geodynamics*. Active Tectonics of the Circum-Adriatic Region 51.2, pp. 110–124. ISSN: 0264-3707. DOI: 10.1016/j.jog.2010.02.007.

Gągała, Ł et al. (2020). "Tajik Basin and Southwestern Tian Shan, Northwestern India-Asia Collision Zone: 1. Structure, Kinematics, and Salt Tectonics in the Tajik Fold-and-Thrust Belt of the Western Foreland of the Pamir". In: *Tectonics* 39.5, e2019TC005871. ISSN: 1944-9194. DOI: 10.1029/2019TC005871.

Gao, R et al. (Aug. 2013). "Fine Crustal Structure beneath the Junction of the Southwest Tian Shan and Tarim Basin, NW China". In: *Lithosphere* 5.4, pp. 382–392. ISSN: 1941-8264. DOI: 10.1130/L248.1.

Georgescu, ES et al. (May 2018). "Seismic and Energy Renovation: A Review of the Code Requirements and Solutions in Italy and Romania". In: *Sustainability* 10.5, p. 1561. ISSN: 2071-1050. DOI: 10.3390/su10051561.

Goes, S et al. (Feb. 2008). "Evidence of Lower-Mantle Slab Penetration Phases in Plate Motions". In: *Nature* 451.7181, pp. 981–984. ISSN: 1476-4687. DOI: 10.1038/nature06691.

Gordon, J (2016). "Economic Sanctions as 'Negative Development': The Case of Cuba". In: *Journal of International Development* 28.4, pp. 473–484. ISSN: 1099-1328. DOI: 10.1002/jid.3061.

Grabovec, D and I Allegretti (Dec. 1994). "On the Digitizing of Historical Seismograms". In: *Geofizika* 11.1, pp. 27–31. ISSN: 0352-3659, 1846-6346.

Green, T et al. (Jan. 2009). "Sedimentation and Subsidence in the South Caspian Basin, Azerbaijan". In: *Geological Society, London, Special Publications* 312.1, pp. 241–260. DOI: 10.1144/SP312.12.

Grin, E et al. (Aug. 2016). "10Be Surface-Exposure Age Dating of the Last Glacial Maximum in the Northern Pamir (Tajikistan)". In: *Quaternary Geochronology* 34, pp. 47–57. ISSN: 1871-1014. DOI: 10.1016/j.quageo.2016.03.007.

Grützner, C et al. (2017). "Active Tectonics Around Almaty and along the Zailisky Alatau Rangefront". In: *Tectonics* 36.10, pp. 2192–2226. ISSN: 1944-9194. DOI: 10.1002/2017TC004657.

Gubin, I (1960). "Zakonomernosti Seismicheskikh Proyavlenii na Territorii Tadshikis- tana". In: *Akademii nauk SSR, Moscow*, pp. 279–294.

Gutenberg, B (1956). "Great Earthquakes 1896–1903". In: *Eos, Transactions American Geophysical Union* 37.5, pp. 608–614. ISSN: 2324-9250. DOI: 10.1029/TR037i005p00608.

Hamburger, MW et al. (Nov. 1993). "Velocity Structure and Seismicity of the Garm Region, Central Asia". In: *Geophysical Journal International* 115.2, pp. 497–511. ISSN: 0956-540X. DOI: 10.1111/j.1365-246X.1993.tb01202.x.

Hanisch, J (2002). "Usoi Landslide Dam in Tajikistan – the World's Highest Dam. First Stability Assessment of the Rock Slopes at Lake Sarez". In: *Landslides*. Routledge. ISBN: 978-0-203-74919-7.

Harris, RA (2017). "Large Earthquakes and Creeping Faults". In: *Reviews of Geophysics* 55.1, pp. 169–198. ISSN: 1944-9208. DOI: 10.1002/2016RG000539.

Hartman, CW and GD Squires (2006). *There Is No Such Thing as a Natural Disaster: Race, Class, and Hurricane Katrina*. Taylor & Francis. ISBN: 978-0-415-95487-7.

He et al. (2024). "Deformation pattern of the 23 August 1985 Wuqia Mw6.9 Earthquake surface rupture (Xinjiang Province) - Control from inherited folding - related structures". In: *Earth Science* 49.2, pp. 511–521. DOI: 10.3799/dqkx.2023.176.

Heimann, S et al. (2017). *Pyrocko - An Open-Source Seismology Toolbox and Library*. DOI: 10.5880/GFZ.2.1.2017.001.

Heimann, S et al. (Nov. 2019). "A Python Framework for Efficient Use of Pre-Computed Green's Functions in Seismological and Other Physical Forward and Inverse Source Problems". In: *Solid Earth* 10.6, pp. 1921–1935. ISSN: 1869-9510. DOI: 10.5194/se-10-1921-2019.

Holbrook, J et al. (July 2006). "Stratigraphic Evidence for Millennial-Scale Temporal Clustering of Earthquakes on a Continental-Interior Fault: Holocene Mississippi River Floodplain Deposits, New Madrid Seismic Zone, USA". In: *Tectonophysics* 420.3, pp. 431–454. ISSN: 0040-1951. DOI: 10.1016/j.tecto.2006.04.002.

Hollingsworth, J et al. (Sept. 2006). "Strike-Slip Faulting, Rotation, and along-Strike Elongation in the Kopeh Dagh Mountains, NE Iran". In: *Geophysical Journal International* 166.3, pp. 1161–1177. ISSN: 0956-540X. DOI: 10.1111/j.1365-246X.2006.02983.x.

Horowitz, A (July 2020). "Katrina: A History, 1915–2015". In: *Katrina*. Harvard University Press. ISBN: 978-0-674-24678-2.

Hovland, M et al. (Nov. 1997). "The Structure and Geomorphology of the Dashgil Mud Volcano, Azerbaijan". In: *Geomorphology* 21.1, pp. 1–15. ISSN: 0169-555X. DOI: 10.1016/S0169-555X(97)00034-2.

Hu, YX et al. (July 1996). *Earthquake Engineering*. London: CRC Press. ISBN: 978-0-429-07861-3. DOI: 10.1201/9781482271645.

Huang, MH et al. (2016). "Multiple Fault Slip Triggered above the 2016 Mw 6.4 MeiNong Earthquake in Taiwan". In: *Geophysical Research Letters* 43.14, pp. 7459–7467. ISSN: 1944-8007. DOI: 10.1002/2016GL069351.

IEA (2022). *Tajikistan 2022 Energy Sector Review*. Tech. rep.

Iio, K and M Furuya (Oct. 2018). "Surface Deformation and Source Modeling of Ayaz-Akhtarma Mud Volcano, Azerbaijan, as Detected by ALOS/ALOS-2 InSAR". In: *Progress in Earth and Planetary Science* 5.1, p. 61. ISSN: 2197-4284. DOI: 10.1186/s40645-018-0220-7.

Inan, S et al. (Nov. 1997). "Deep Petroleum Occurrences in the Lower Kura Depression, South Caspian Basin, Azerbaijan: An Organic Geochemical and Basin Modeling Study". In: *Marine*

and Petroleum Geology 14.7, pp. 731–762. ISSN: 0264-8172. DOI: 10.1016/S0264-8172(97)00058-5.

İnan, S et al. (July 2024). "Mudrock Overpressure, Fracturing, and Mud Volcanism in the Lower Kura Depression, Azerbaijan". In: *International Journal of Earth Sciences*. ISSN: 1437-3262. DOI: 10.1007/s00531-024-02442-6.

Isacks, B et al. (1968). "Seismology and the New Global Tectonics". In: *Journal of Geophysical Research (1896-1977)* 73.18, pp. 5855–5899. ISSN: 2156-2202. DOI: 10.1029/JB073i018p05855.

Ischuk, A et al. (2013). "Kinematics of the Pamir and Hindu Kush Regions from GPS Geodesy". In: *Journal of Geophysical Research: Solid Earth* 118.5, pp. 2408–2416. ISSN: 2169-9356. DOI: 10.1002/jgrb.50185.

Işık, E et al. (Jan. 2024). "Seismic Performance and Failure Mechanisms of Reinforced Concrete Structures Subject to the Earthquakes in Türkiye". In: *Sustainability* 16.15, p. 6473. ISSN: 2071-1050. DOI: 10.3390/su16156473.

Islam, MS and K Iwashita (2010). "Earthquake Resistance of Adobe Reinforced by Low Cost Traditional Materials". In: *Journal of Natural Disaster Science* 32.1, pp. 1–21. DOI: 10.2328/jnds.32.1.

Ismail-Zadeh, A et al. (Aug. 2020). "Geodynamics, Seismicity, and Seismic Hazards of the Caucasus". In: *Earth-Science Reviews* 207, p. 103222. ISSN: 0012-8252. DOI: 10.1016/j.earscirev.2020.103222.

Jackson, J et al. (Sept. 2006). "Seismotectonic, Rupture Process, and Earthquake-Hazard Aspects of the 2003 December 26 Bam, Iran, Earthquake". In: *Geophysical Journal International* 166.3, pp. 1270–1292. ISSN: 0956-540X. DOI: 10.1111/j.1365-246X.2006.03056.x.

Jackson, J (June 2006). "Fatal Attraction: Living with Earthquakes, the Growth of Villages into Megacities, and Earthquake Vulnerability in the Modern World". In: *Philosophical Transactions of the Royal Society A: Mathematical, Physical and Engineering Sciences* 364.1845, pp. 1911–1925. DOI: 10.1098/rsta.2006.1805.

Jackson, J and D McKenzie (Apr. 1988). "The Relationship between Plate Motions and Seismic Moment Tensors, and the Rates of Active Deformation in the Mediterranean and Middle East". In: *Geophysical Journal International* 93.1, pp. 45–73. ISSN: 0956-540X. DOI: 10.1111/j.1365-246X.1988.tb01387.x.

Jackson, J et al. (1979). "Seismotectonic Aspects of the Markansu Valley, Tadjikstan, Earthquake of August 11, 1974". In: *Journal of Geophysical Research: Solid Earth* 84.B11, pp. 6157–6167. ISSN: 2156-2202. DOI: 10.1029/JB084iB11p06157.

Jackson, J et al. (Feb. 2002). "Active Tectonics of the South Caspian Basin". In: *Geophysical Journal International* 148.2, pp. 214–245. ISSN: 0956-540X. DOI: 10.1046/j.1365-246X.2002.01588.x.

Jackson, J et al. (Mar. 2008). "New Views on the Structure and Rheology of the Lithosphere". In: *Journal of the Geological Society* 165.2, pp. 453–465. ISSN: 0016-7649, 2041-479X. DOI: 10.1144/0016-76492007-109.

Jalabi, R (Feb. 2023). "Syrians Left to Fend for Themselves as Earthquake Relief Fails to Materialise". In: *Financial Times*.

James, B and N Kulwin (n.d.). *Blowback*.

Jara-Muñoz, J et al. (June 2022). "The Cryptic Seismic Potential of the Pichilemu Blind Fault in Chile Revealed by Off-Fault Geomorphology". In: *Nature Communications* 13.1, p. 3371. ISSN: 2041-1723. DOI: 10.1038/s41467-022-30754-1.

Javanshir, RJ et al. (Jan. 2015). "Validation of Lateral Fluid Flow in an Overpressured Sand-Shale Sequence during Development of Azeri-Chirag-Gunashli Oil Field and Shah Deniz Gas Field: South Caspian Basin, Azerbaijan". In: *Marine and Petroleum Geology* 59, pp. 593–610. ISSN: 0264-8172. DOI: 10.1016/j.marpetgeo.2014.07.019.

JAXA ALOS World 3D 30 Meter DEM (Apr. 2019). DEM.

Jay, CN et al. (2017). "Kinematics and Dynamics of the Pamir, Central Asia: Quantifying Surface Deformation and Force Balance in an Intracontinental Subduction Zone". In: *Journal of Geophysical Research: Solid Earth* 122.6, pp. 4741–4762. ISSN: 2169-9356. DOI: 10.1002/2017JB014177.

Jolivet, R et al. (2015). "Aseismic Slip and Seismogenic Coupling along the Central San Andreas Fault". In: *Geophysical Research Letters* 42.2, pp. 297–306. ISSN: 1944-8007. DOI: 10.1002/2014GL062222.

Jordan, TH and KA Sverdrup (Aug. 1981). "Teleseismic Location Techniques and Their Application to Earthquake Clusters in the South-Central Pacific". In: *Bulletin of the Seismological Society of America* 71.4, pp. 1105–1130. ISSN: 0037-1106.

Kadirov, FA et al. (Nov. 2014). "GPS-based Crustal Deformations in Azerbaijan and Their Influence on Seismicity and Mud Volcanism". In: *Izvestiya, Physics of the Solid Earth* 50.6, pp. 814–823. ISSN: 1555-6506. DOI: 10.1134/S1069351314060020.

Kanamori, H and JW Given (Oct. 1981). "Use of Long-Period Surface Waves for Rapid Determination of Earthquake-Source Parameters". In: *Physics of the Earth and Planetary Interiors* 27.1, pp. 8–31. ISSN: 0031-9201. DOI: 10.1016/0031-9201(81)90083-2.

Karasözen, E et al. (June 2016). "Normal Faulting in the Simav Graben of Western Turkey Reassessed with Calibrated Earthquake Relocations". In: *Journal of Geophysical Research: Solid Earth* 121.6, pp. 4553–4574. ISSN: 2169-9313, 2169-9356. DOI: 10.1002/2016JB012828.

Karasözen, E et al. (2019). "Seismotectonics of the Zagros (Iran) From Orogen-Wide, Calibrated Earthquake Relocations". In: *Journal of Geophysical Research: Solid Earth* 124.8, pp. 9109–9129. ISSN: 2169-9356. DOI: 10.1029/2019JB017336.

Karnik, V et al. (1962). "Standardization of the Earthquake Magnitude Scale". In: *Studia Geophysica et Geodaetica* 6, pp. 41–48.

Kennett, BLN et al. (July 1995). "Constraints on Seismic Velocities in the Earth from Traveltimes". In: *Geophysical Journal International* 122.1, pp. 108–124. ISSN: 0956-540X. DOI: 10.1111/j.1365-246X.1995.tb03540.x.

King, GCP et al. (June 1994). "Static Stress Changes and the Triggering of Earthquakes". In: *Bulletin of the Seismological Society of America* 84.3, pp. 935–953. ISSN: 0037-1106. DOI: 10.1785/BSSA0840030935.

Kioka, A and J Ashi (2015). "Episodic Massive Mud Eruptions from Submarine Mud Volcanoes Examined through Topographical Signatures". In: *Geophysical Research Letters* 42.20, pp. 8406–8414. ISSN: 1944-8007. DOI: 10.1002/2015GL065713.

Knapp, CC et al. (Sept. 2004). "Crustal-Scale Structure of the South Caspian Basin Revealed by Deep Seismic Reflection Profiling". In: *Marine and Petroleum Geology* 21.8, pp. 1073–1081. ISSN: 0264-8172. DOI: 10.1016/j.marpetgeo.2003.04.002.

Konca, AO et al. (Dec. 2008). "Partial Rupture of a Locked Patch of the Sumatra Megathrust during the 2007 Earthquake Sequence". In: *Nature* 456.7222, pp. 631–635. ISSN: 1476-4687. DOI: 10.1038/nature07572.

Kondorskaya, N and N Shebalin (1982). *New Catalog of Strong Earthquakes in the U.S.S.R. from Ancient Times Through 1977*. Tech. rep., p. 609.

Kopf, AJ (2002). "Significance of Mud Volcanism". In: *Reviews of Geophysics* 40.2, pp. 2-1-2–52. ISSN: 1944-9208. DOI: 10.1029/2000RG000093.

— (Oct. 2003). "Global Methane Emission through Mud Volcanoes and Its Past and Present Impact on the Earth's Climate". In: *International Journal of Earth Sciences* 92.5, pp. 806–816. ISSN: 1437-3262. DOI: 10.1007/s00531-003-0341-z.

Kostrov, B (1974). "Seismic Moment and Energy of Earthquakes, and Seismic Flow of Rock". In: *Izv. Acad. Sci. USSR Phys. Solid Earth* 1, pp. 23–40.

Kreemer, C et al. (2014). "A Geodetic Plate Motion and Global Strain Rate Model". In: *Geochemistry, Geophysics, Geosystems* 15.10, pp. 3849–3889. ISSN: 1525-2027. DOI: 10.1002/2014GC005407.

Krijgsman, W et al. (Jan. 2019). "Quaternary Time Scales for the Pontocaspian Domain: Interbasinal Connectivity and Faunal Evolution". In: *Earth-Science Reviews* 188, pp. 1–40. ISSN: 0012-8252. DOI: 10.1016/j.earscirev.2018.10.013.

Krüger, F et al. (Dec. 2018). "Magnitudes for the Historical 1885 (Belovodskoe), the 1887 (Verny) and the 1889 (Chilik) Earthquakes in Central Asia Determined from Magnetogram Recordings". In: *Geophysical Journal International* 215.3, pp. 1824–1840. ISSN: 0956-540X. DOI: 10.1093/gji/ggy377.

Kufner, SK et al. (Feb. 2016). "Deep India Meets Deep Asia: Lithospheric Indentation, Delamination and Break-off under Pamir and Hindu Kush (Central Asia)". In: *Earth and Planetary Science Letters* 435, pp. 171–184. ISSN: 0012-821X. DOI: 10.1016/j.epsl.2015.11.046.

Kufner, SK et al. (2018a). "Seismic Anisotropy Beneath the Pamir and the Hindu Kush: Evidence for Contributions From Crust, Mantle Lithosphere, and Asthenosphere". In: *Journal of Geophysical Research: Solid Earth* 123.12, pp. 10, 727–10, 748. ISSN: 2169-9356. DOI: 10.1029/2018JB015926.

Kufner, SK et al. (2018b). "Seismotectonics of the Tajik Basin and Surrounding Mountain Ranges". In: *Tectonics* 37.8, pp. 2404–2424. ISSN: 1944-9194. DOI: 10.1029/2017TC004812.

Kulikova, G (2016). "Source Parameters of the Major Historical Earthquakes in the Tien-Shan Region from the Late 19th to the Early 20th Century". PhD thesis.

Kulikova, G and F Krüger (June 2015). "Source Process of the 1911 M8.0 Chon-Kemin Earthquake: Investigation Results by Analogue Seismic Records". In: *Geophysical Journal International* 201.3, pp. 1891–1911. ISSN: 0956-540X. DOI: 10.1093/gji/ggv091.

— (Nov. 2017). "Historical Seismogram Reproductions for the Source Parameters Determination of the 1902, Atushi (Kashgar) Earthquake". In: *Journal of Seismology* 21.6, pp. 1577–1597. ISSN: 1573-157X. DOI: 10.1007/s10950-017-9683-z.

Kulikova, G et al. (May 2016). "Source Parameters of the Sarez-Pamir Earthquake of 1911 February 18". In: *Geophysical Journal International* 205.2, pp. 1086–1098. ISSN: 0956-540X. DOI: 10.1093/gji/ggw069.

Landgraf, A et al. (2016). "Repeated Large-Magnitude Earthquakes in a Tectonically Active, Low-Strain Continental Interior: The Northern Tien Shan, Kyrgyzstan". In: *Journal of Geophysical Research: Solid Earth* 121.5, pp. 3888–3910. ISSN: 2169-9356. DOI: 10.1002/2015JB012714.

Lazecký, M et al. (Jan. 2020). "LiCSAR: An Automatic InSAR Tool for Measuring and Monitoring Tectonic and Volcanic Activity". In: *Remote Sensing* 12.15, p. 2430. ISSN: 2072-4292. DOI: 10.3390/rs12152430.

Leith, and *Alvarez* (July 1985). "Structure of the Vakhsh Fold-and-Thrust Belt, Tadjik SSR: Geologic Mapping on a Landsat Image Base". In: *GSA Bulletin* 96.7, pp. 875–885. ISSN: 0016-7606. DOI: 10.1130/0016-7606(1985)96<875:SOTVFB>2.0.CO;2.

Leonov, N (1960). "The Khait, 1949 earthquake and geological conditions of its occurrence". In: *Izvestia of the Academy of Sciences of the USSR, Geophysical Series 3*, pp. 409–424.

Li, QS et al. (Jan. 2011). "Dynamic Behavior of Taipei 101 Tower: Field Measurement and Numerical Analysis". In: *Journal of Structural Engineering* 137.1, pp. 143–155. ISSN: 0733-9445. DOI: 10.1061/(ASCE)ST.1943-541X.0000264.

Li, S et al. (Feb. 2021). "Comparison of Macroseismic-Intensity Scales by Considering Empirical Observations of Structural Seismic Damage". In: *Earthquake Spectra* 37.1, pp. 449–485. ISSN: 8755-2930. DOI: 10.1177/8755293020944174.

Li, T et al. (2012). "Equivalency of Geologic and Geodetic Rates in Contractional Orogens: New Insights from the Pamir Frontal Thrust". In: *Geophysical Research Letters* 39.15. ISSN: 1944-8007. DOI: 10.1029/2012GL051782.

Li, T et al. (2015). "Hinge-Migrated Fold-Scarp Model Based on an Analysis of Bed Geometry: A Study from the Mingyaole Anticline, Southern Foreland of Chinese Tian Shan". In: *Journal of Geophysical Research: Solid Earth* 120.9, pp. 6592–6613. ISSN: 2169-9356. DOI: 10.1002/2015JB012102.

Li, T et al. (Mar. 2016). "The 2015 Mw 6.4 Pishan Earthquake: Seismic Hazards of an Active Blind Wedge Thrust System at the Western Kunlun Range Front, Northwest Tibetan Plateau". In: *Seismological Research Letters* 87.3, pp. 601–608. ISSN: 0895-0695. DOI: 10.1785/0220150205.

Li, T et al. (2019). "Along-Strike and Downdip Segmentation of the Pamir Frontal Thrust and Its Association With the 1985 Mw 6.9 Wuqia Earthquake". In: *Journal of Geophysical Research: Solid Earth* 124.9, pp. 9890–9919. ISSN: 2169-9356. DOI: 10.1029/2019JB017319.

Lienkaemper, JJ and PL Williams (Dec. 2007). "A Record of Large Earthquakes on the Southern Hayward Fault for the Past 1800 Years". In: *Bulletin of the Seismological Society of America* 97.6, pp. 1803–1819. ISSN: 0037-1106. DOI: 10.1785/0120060258.

Lin, YY and N Lapusta (2018). "Microseismicity Simulated on Asperity-Like Fault Patches: On Scaling of Seismic Moment With Duration and Seismological Estimates of Stress Drops".

In: *Geophysical Research Letters* 45.16, pp. 8145–8155. ISSN: 1944-8007. DOI: 10.1029/2018GL078650.

Liu, M and S Stein (Nov. 2016). "Mid-Continental Earthquakes: Spatiotemporal Occurrences, Causes, and Hazards". In: *Earth-Science Reviews* 162, pp. 364–386. ISSN: 0012-8252. DOI: 10.1016/j.earscirev.2016.09.016.

Liu, M et al. (Apr. 2011). "2000 Years of Migrating Earthquakes in North China: How Earthquakes in Midcontinents Differ from Those at Plate Boundaries". In: *Lithosphere* 3.2, pp. 128–132. ISSN: 1941-8264. DOI: 10.1130/L129.1.

Loveless, JP and BJ Meade (Feb. 2016). "Two Decades of Spatiotemporal Variations in Subduction Zone Coupling Offshore Japan". In: *Earth and Planetary Science Letters* 436, pp. 19–30. ISSN: 0012-821X. DOI: 10.1016/j.epsl.2015.12.033.

Lukk, AA et al. (1995). "Earthquake Focal Mechanisms, Deformation State, and Seismotectonics of the Pamir-Tien Shan Region, Central Asia". In: *Journal of Geophysical Research: Solid Earth* 100.B10, pp. 20321–20343. ISSN: 2156-2202. DOI: 10.1029/95JB02158.

Mackenzie, D et al. (Nov. 2018). "A Creeping Intracontinental Thrust Fault: Past and Present Slip-Rates on the Northern Edge of the Tien Shan, Kazakhstan". In: *Geophysical Journal International* 215.2, pp. 1148–1170. ISSN: 0956-540X. DOI: 10.1093/gji/ggy339.

Mackenzie, D and A Elliott (June 2017). "Untangling Tectonic Slip from the Potentially Misleading Effects of Landform Geometry". In: *Geosphere* 13.4, pp. 1310–1328. ISSN: 1553-040X. DOI: 10.1130/GES01386.1.

Mackey, KG and E Bergman (Aug. 2014). "Ground-Truth Locations for the Mangyshlak Peaceful Nuclear Explosion Sequence, Western Kazakhstan". In: *Bulletin of the Seismological Society of America* 104.4, pp. 2116–2119. ISSN: 0037-1106. DOI: 10.1785/0120130330.

Maggi, A et al. (June 2000). "Earthquake Focal Depths, Effective Elastic Thickness, and the Strength of the Continental Lithosphere". In: *Geology* 28.6, pp. 495–498. ISSN: 0091-7613. DOI: 10.1130/0091-7613(2000)28<495:EFDEET>2.0.CO;2.

Maghsoudi, Y et al. (June 2022). "Characterizing and Correcting Phase Biases in Short-Term, Multilooked Interferograms". In: *Remote Sensing of Environment* 275, p. 113022. ISSN: 0034-4257. DOI: 10.1016/j.rse.2022.113022.

Marshall, N et al. (Dec. 2023). "Seismotectonic Aspects of the Ms 7.3 1948 October 5th Aşgabat (Ashgabat) Earthquake, Türkmenistan: Right-Lateral Rupture across Multiple Fault Segments, and Continuing Urban Hazard". In: *Geophysical Journal International*, ggad488. ISSN: 0956-540X, 1365-246X. DOI: 10.1093/gji/ggad488.

Marshall, NR (2023). "Earthquakes and Active Tectonics of the South Caspian Region, Central Asia". DPhil. Oxford: University of Oxford.

Marshall, NR and W College (n.d.). "Earthquakes and Active Tectonics of the South Caspian Region, Central Asia". In: ().

McCaffrey, R (Aug. 1997). "Statistical Significance of the Seismic Coupling Coefficient". In: *Bulletin of the Seismological Society of America* 87.4, pp. 1069–1073. ISSN: 0037-1106. DOI: 10.1785/BSSA0870041069.

McCalpin, JP et al. (2009). "Chapter 6 Paleoseismology of Strike-Slip Tectonic Environments". In: *International Geophysics*. Vol. 95. Elsevier, pp. 421–496. ISBN: 978-0-12-373576-8. DOI: 10.1016/S0074-6142(09)95006-9.

McComb, H and J West (1931). *List of Seismologic Stations of the World*. 2nd. 82. The National Research Council of The National Academy of Sciences.

McManus, D (May 1987). "Use of Humanitarian Aid Flights to Arm Contras Told". In: *Los Angeles Times*.

McQuarrie, N et al. (2003). "Cenozoic Evolution of Neotethys and Implications for the Causes of Plate Motions". In: *Geophysical Research Letters* 30.20. ISSN: 1944-8007. DOI: 10.1029/2003GL017992.

Mechie, J et al. (July 2019). "Observations of Guided Waves from the Pamir Seismic Zone Provide Additional Evidence for the Existence of Subducted Continental Lower Crust". In: *Tectonophysics* 762, pp. 1–16. ISSN: 0040-1951. DOI: 10.1016/j.tecto.2019.04.007.

Medvedev, SW et al. (1965). "Seismic Intensity Scale Version MSK 1964". In: *International Association of Seismology and Physics of the Earth's Interior*.

Meltzner, AJ et al. (Aug. 2015). "Time-Varying Interseismic Strain Rates and Similar Seismic Ruptures on the Nias–Simeulue Patch of the Sunda Megathrust". In: *Quaternary Science Reviews* 122, pp. 258–281. ISSN: 0277-3791. DOI: 10.1016/j.quascirev.2015.06.003.

Mergili, M and JF Schneider (May 2011). "Regional-Scale Analysis of Lake Outburst Hazards in the Southwestern Pamir, Tajikistan, Based on Remote Sensing and GIS". In: *Natural Hazards and Earth System Sciences* 11.5, pp. 1447–1462. ISSN: 1561-8633. DOI: 10.5194/nhess-11-1447-2011.

Mergili, M et al. (Aug. 2013). "Spatio-Temporal Development of High-Mountain Lakes in the Headwaters of the Amu Darya River (Central Asia)". In: *Global and Planetary Change* 107, pp. 13–24. ISSN: 0921-8181. DOI: 10.1016/j.gloplacha.2013.04.001.

Metzger, S et al. (2020). "Dense GNSS Profiles Across the Northwestern Tip of the India-Asia Collision Zone: Triggered Slip and Westward Flow of the Peter the First Range, Pamir, Into the Tajik Depression". In: *Tectonics* 39.2, e2019TC005797. ISSN: 1944-9194. DOI: 10.1029/2019TC005797.

Metzger, S et al. (Dec. 2021). "Tajik Depression and Greater Pamir Neotectonics From InSAR Rate Maps". In: *Journal of Geophysical Research: Solid Earth* 126.12. ISSN: 2169-9313, 2169-9356. DOI: 10.1029/2021JB022775.

Mikhailova, NN et al. (Apr. 2015). "Central Asia Earthquake Catalogue from Ancient Time to 2009". In: *Annals of Geophysics* 1. ISSN: 15935213. DOI: 10.4401/ag-6681.

Miller, SA et al. (Feb. 2004). "Aftershocks Driven by a High-Pressure CO2 Source at Depth". In: *Nature* 427.6976, pp. 724–727. ISSN: 1476-4687. DOI: 10.1038/nature02251.

Mohadjer, S et al. (Feb. 2016). "A Quaternary Fault Database for Central Asia". In: *Natural Hazards and Earth System Sciences* 16.2, pp. 529–542. ISSN: 1561-8633. DOI: 10.5194/nhess-16-529-2016.

Molinaro, M et al. (2005). "The Structure and Kinematics of the Southeastern Zagros Fold-Thrust Belt, Iran: From Thin-Skinned to Thick-Skinned Tectonics". In: *Tectonics* 24.3. ISSN: 1944-9194. DOI: 10.1029/2004TC001633.

Molnar, P (Feb. 1979). "Earthquake Recurrence Intervals and Plate Tectonics". In: *Bulletin of the Seismological Society of America* 69.1, pp. 115–133. ISSN: 0037-1106. DOI: 10.1785/BSSA0690010115.

Molnar, P and D Qidong (1984). "Faulting Associated with Large Earthquakes and the Average Rate of Deformation in Central and Eastern Asia". In: *Journal of Geophysical Research: Solid Earth* 89.B7, pp. 6203–6227. ISSN: 2156-2202. DOI: 10.1029/JB089iB07p06203.

Molnar, P and P Tapponnier (1975). "Cenozoic Tectonics of Asia: Effects of a Continental Collision". In: *Science* 189.4201, pp. 419–426.

Morishita, Y et al. (Jan. 2020). "LiCSBAS: An Open-Source InSAR Time Series Analysis Package Integrated with the LiCSAR Automated Sentinel-1 InSAR Processor". In: *Remote Sensing* 12.3, p. 424. ISSN: 2072-4292. DOI: 10.3390/rs12030424.

Mosar, J et al. (Jan. 2010). "Cenozoic-Recent Tectonics and Uplift in the Greater Caucasus: A Perspective from Azerbaijan". In: *Geological Society, London, Special Publications* 340.1, pp. 261–280. ISSN: 0305-8719, 2041-4927. DOI: 10.1144/SP340.12.

Mostafaei, H and T Kabeyasawa (2004). "Investigation and Analysis of Damage to Buildings during the 2003 Bam Earthquake". In: *Bull. Earthq. Res. Inst. Univ. Tokyo* 79, pp. 107–132.

Motagh, M et al. (Feb. 2017). "Quantifying Groundwater Exploitation Induced Subsidence in the Rafsanjan Plain, Southeastern Iran, Using InSAR Time-Series and in Situ Measurements". In: *Engineering Geology* 218, pp. 134–151. ISSN: 0013-7952. DOI: 10.1016/j.enggeo.2017.01.011.

Nadim, F et al. (Jan. 2004). "The Bam Earthquake of 26 December 2003". In: *Bulletin of Earthquake Engineering* 2.2, pp. 119–153. ISSN: 1573-1456. DOI: 10.1007/s10518-004-2286-4.

Nealy, JL et al. (Mar. 2017). "The 2008 Wells, Nevada, Earthquake Sequence: Source Constraints Using Calibrated Multiple-Event Relocation and InSAR". In: *Bulletin of the Seismological Society of America* 107.3, pp. 1107–1117. ISSN: 0037-1106. DOI: 10.1785/0120160298.

Neil, EA and GA Houseman (1997). "Geodynamics of the Tarim Basin and the Tian Shan in Central Asia". In: *Tectonics* 16.4, pp. 571–584. ISSN: 1944-9194. DOI: 10.1029/97TC01413.

Niemann, H et al. (Nov. 2006). "Microbial Methane Turnover at Mud Volcanoes of the Gulf of Cadiz". In: *Geochimica et Cosmochimica Acta* 70.21, pp. 5336–5355. ISSN: 0016-7037. DOI: 10.1016/j.gca.2006.08.010.

Nissen, E et al. (Apr. 2016). "Limitations of Rupture Forecasting Exposed by Instantaneously Triggered Earthquake Doublet". In: *Nature Geoscience* 9.4, pp. 330–336. ISSN: 1752-0908. DOI: 10.1038/ngeo2653.

Nissen, E et al. (Sept. 2011). "New Views on Earthquake Faulting in the Zagros Fold-and-Thrust Belt of Iran". In: *Geophysical Journal International* 186.3, pp. 928–944. ISSN: 0956-540X. DOI: 10.1111/j.1365-246X.2011.05119.x.

Nissen, E et al. (2014). "Zagros "Phantom Earthquakes" Reassessed—The Interplay of Seismicity and Deep Salt Flow in the Simply Folded Belt?" In: *Journal of Geophysical Research: Solid Earth* 119.4, pp. 3561–3583. ISSN: 2169-9356. DOI: 10.1002/2013JB010796.

Odonne, F et al. (Dec. 2021). "Surface Structure, Activity and Microgravimetry Modeling Delineate Contrasted Mud Chamber Types below Flat and Conical Mud Volcanoes from Azerbaijan". In: *Marine and Petroleum Geology* 134, p. 105315. ISSN: 0264-8172. DOI: 10.1016/j.marpetgeo.2021.105315.

Oliver-Smith, A (July 2010). "Haiti and the Historical Construction of Disasters". In: *NACLA Report on the Americas* 43.4, pp. 32–36. ISSN: 1071-4839, 2471-2620. DOI: 10.1080/10714839.2010.11725505.

Ori, GG and PF Friend (Aug. 1984). "Sedimentary Basins Formed and Carried Piggyback on Active Thrust Sheets". In: *Geology* 12.8, pp. 475–478. ISSN: 0091-7613. DOI: 10.1130/0091-7613(1984)12<475:SBFACP>2.0.CO;2.

Ou, Q et al. (2020). "Magnitude of the 1920 Haiyuan Earthquake Reestimated Using Seismological and Geomorphological Methods". In: *Journal of Geophysical Research: Solid Earth* 125.8, e2019JB019244. ISSN: 2169-9356. DOI: 10.1029/2019JB019244.

Özdemir, A et al. (2025). "Detecting Millimetric Slow Slip Events Along the North Anatolian Fault With GNSS". In: *Geophysical Research Letters* 52.10, e2024GL111428. ISSN: 1944-8007. DOI: 10.1029/2024GL111428.

Ozkula, G et al. (Oct. 2023). "Field Reconnaissance and Observations from the February 6, 2023, Turkey Earthquake Sequence". In: *Natural Hazards* 119.1, pp. 663–700. ISSN: 1573-0840. DOI: 10.1007/s11069-023-06143-2.

Patyniak, M et al. (2021). "The Pamir Frontal Thrust Fault: Holocene Full-Segment Ruptures and Implications for Complex Segment Interactions in a Continental Collision Zone". In: *Journal of Geophysical Research: Solid Earth* n/a.n/a, e2021JB022405. ISSN: 2169-9356. DOI: 10.1029/2021JB022405.

Pierce, I et al. (2024). "Surface Rupturing Earthquakes of the Greater Caucasus Frontal Thrusts, Azerbaijan". In: *Tectonics* 43.3, e2023TC007758. ISSN: 1944-9194. DOI: 10.1029/2023TC007758.

Planke, S et al. (Dec. 2003). "Mud and Fluid Migration in Active Mud Volcanoes in Azerbaijan". In: *Geo-Marine Letters* 23.3, pp. 258–268. ISSN: 1432-1157. DOI: 10.1007/s00367-003-0152-z.

Platt, JP (1990). "Thrust Mechanics in Highly Overpressured Accretionary Wedges". In: *Journal of Geophysical Research: Solid Earth* 95.B6, pp. 9025–9034. ISSN: 2156-2202. DOI: 10.1029/JB095iB06p09025.

Poblet, J and RJ Lisle (Jan. 2011). "Kinematic Evolution and Structural Styles of Fold-and-Thrust Belts". In: *Geological Society, London, Special Publications* 349.1, pp. 1–24. DOI: 10.1144/SP349.1.

Prados, J (Sept. 2017). *The Ghosts of Langley: Into the Heart of the CIA*. Amberley Publishing Limited. ISBN: 978-1-4456-6793-5.

Rautian, TG et al. (Nov. 2007). "Origins and Methodology of the Russian Energy K-Class System and Its Relationship to Magnitude Scales". In: *Seismological Research Letters* 78.6, pp. 579–590. ISSN: 0895-0695. DOI: 10.1785/gssrl.78.6.579.

Reid, . (1910). "The California Earthquake of April 18, 1906". In: *Report of the state earthquake investigation commission* 2.

Reigber, C et al. (Aug. 2001). "New Space Geodetic Constraints on the Distribution of Deformation in Central Asia". In: *Earth and Planetary Science Letters* 191.1, pp. 157–165. ISSN: 0012-821X. DOI: 10.1016/S0012-821X(01)00414-9.

Reilinger, R et al. (2006). "GPS Constraints on Continental Deformation in the Africa-Arabia-Eurasia Continental Collision Zone and Implications for the Dynamics of Plate Interactions". In: *Journal of Geophysical Research: Solid Earth* 111.B5. ISSN: 2156-2202. DOI: 10.1029/2005JB004051.

Rizza, M et al. (Jan. 2015). "Earthquake Geology of the Bulnay Fault (Mongolia)". In: *Bulletin of the Seismological Society of America* 105.1, pp. 72–93. ISSN: 0037-1106. DOI: 10.1785/0120140119.

Rizza, M et al. (2019). "Rate of Slip From Multiple Quaternary Dating Methods and Paleoseismic Investigations Along the Talas-Fergana Fault: Tectonic Implications for the Tien Shan Range". In: *Tectonics* 38.7, pp. 2477–2505. ISSN: 1944-9194. DOI: 10.1029/2018TC005188.

Roberts, KS et al. (July 2011). "Structural Controls on Mud Volcano Vent Distributions: Examples from Azerbaijan and Lusi, East Java". In: *Journal of the Geological Society* 168.4, pp. 1013–1030. ISSN: 0016-7649. DOI: 10.1144/0016-76492010-158.

Robertson, A et al. (2000). "Tectonics and Magmatism in Turkey and the Surrounding Area". In: *Geol. Soc. London. Spec. Publ.* 173, pp. 97–138.

Robinson, AC et al. (July 2004). "Tectonic Evolution of the Northeastern Pamir: Constraints from the Northern Portion of the Cenozoic Kongur Shan Extensional System, Western China". In: *GSA Bulletin* 116.7-8, pp. 953–973. ISSN: 0016-7606. DOI: 10.1130/B25375.1.

Röhringer, I et al. (Nov. 2012). "The Late Pleistocene Glaciation in the Bogchigir Valleys (Pamir, Tajikistan) Based on 10Be Surface Exposure Dating". In: *Quaternary Research* 78.3, pp. 590–597. ISSN: 0033-5894. DOI: 10.1016/j.yqres.2012.09.002.

Ruch, J et al. (May 2012). "Salt Lake Deformation Detected from Space". In: *Earth and Planetary Science Letters* 331–332, pp. 120–127. ISSN: 0012-821X. DOI: 10.1016/j.epsl.2012.03.009.

Rutte, D et al. (2017a). "Building the Pamir-Tibetan Plateau—Crustal Stacking, Extensional Collapse, and Lateral Extrusion in the Central Pamir: 1. Geometry and Kinematics". In: *Tectonics* 36.3, pp. 342–384. ISSN: 1944-9194. DOI: 10.1002/2016TC004293.

Rutte, D et al. (2017b). "Building the Pamir-Tibetan Plateau—Crustal Stacking, Extensional Collapse, and Lateral Extrusion in the Central Pamir: 2. Timing and Rates". In: *Tectonics* 36.3, pp. 385–419. ISSN: 1944-9194. DOI: 10.1002/2016TC004294.

Sadovsky, MA and IL Nersesov (Aug. 1974). "Forecasts of Earthquakes on the Basis of Complex Geophysisical Features". In: *Tectonophysics*. Focal Processes and the Prediction of Earthquakes 23.3, pp. 247–255. ISSN: 0040-1951. DOI: 10.1016/0040-1951(74)90024-9.

Saks, T et al. (2024). "Acceleration of Abramov Glacier (Pamir-Alay) Retreat since the Little Ice Age". In: *Boreas* 53.3, pp. 415–429. ISSN: 1502-3885. DOI: 10.1111/bor.12659.

Salomon, G et al. (Mar. 2025). "The 2020 Mw 6.4 Koryak Highlands Earthquake Illustrates Hidden Seismic Hazards in the Northern Pacific Cordillera". In: *Geophysical Journal International* 240.3, pp. 2111–2124. ISSN: 1365-246X. DOI: 10.1093/gji/ggaf031.

Savage, JC et al. (2005). "Postseismic Relaxation and Transient Creep". In: *Journal of Geophysical Research: Solid Earth* 110.B11. ISSN: 2156-2202. DOI: 10.1029/2005JB003687.

Scherbaum, F (Dec. 2006). *Of Poles and Zeros: Fundamentals of Digital Seismology*. Springer Science & Business Media. ISBN: 978-0-7923-6835-9.

Schneider, FM et al. (Aug. 2013). "Seismic Imaging of Subducting Continental Lower Crust beneath the Pamir". In: *Earth and Planetary Science Letters* 375, pp. 101–112. ISSN: 0012-821X. DOI: 10.1016/j.epsl.2013.05.015.

Schneider, FM et al. (2019). "The Crust in the Pamir: Insights From Receiver Functions". In: *Journal of Geophysical Research: Solid Earth* 124.8, pp. 9313–9331. ISSN: 2169-9356. DOI: 10.1029/2019JB017765.

Scholz, CH et al. (Feb. 1986). "Scaling Differences between Large Interplate and Intraplate Earthquakes". In: *Bulletin of the Seismological Society of America* 76.1, pp. 65–70. ISSN: 0037-1106. DOI: 10.1785/BSSA0760010065.

Scholz, CH and J Campos (2012). "The Seismic Coupling of Subduction Zones Revisited". In: *Journal of Geophysical Research: Solid Earth* 117.B5. ISSN: 2156-2202. DOI: 10.1029/2011JB009003.

Schultz, RA (May 2000). "Localization of Bedding Plane Slip and Backthrust Faults above Blind Thrust Faults: Keys to Wrinkle Ridge Structure". In: *Journal of Geophysical Research: Planets* 105.E5, pp. 12035–12052. ISSN: 0148-0227. DOI: 10.1029/1999JE001212.

Schurr, B et al. (2014). "Seismotectonics of the Pamir". In: *Tectonics* 33.8, pp. 1501–1518. ISSN: 1944-9194. DOI: 10.1002/2014TC003576.

Schwab, M et al. (2004). "Assembly of the Pamirs: Age and Origin of Magmatic Belts from the Southern Tien Shan to the Southern Pamirs and Their Relation to Tibet". In: *Tectonics* 23.4. ISSN: 1944-9194. DOI: 10.1029/2003TC001583.

Schweitzer, J (Feb. 2001). "HYPOSAT – An Enhanced Routine to Locate Seismic Events". In: *pure and applied geophysics* 158.1, pp. 277–289. ISSN: 1420-9136. DOI: 10.1007/PL00001160.

Schweitzer, J (2018). "User Manual for HYPOSAT 6 and HYPOMOD 2". In: *New Manual of Seismological Observatory Practice 2 (NMSOP2)*, 216 kB, 38 pages. DOI: 10.2312/GFZ.NMSOP-3_PD_11.1.

Segall, P (2010). *Earthquake and Volcano Deformation*. Princeton, N.J: Princeton University Press. ISBN: 978-0-691-13302-7.

Semmane, F et al. (2005). "The 2000 Tottori Earthquake: A Shallow Earthquake with No Surface Rupture and Slip Properties Controlled by Depth". In: *Journal of Geophysical Research: Solid Earth* 110.B3. ISSN: 2156-2202. DOI: 10.1029/2004JB003194.

Şengör, AMC and WSF Kidd (June 1979). "Post-Collisional Tectonics of the Turkish-Iranian Plateau and a Comparison with Tibet". In: *Tectonophysics* 55.3, pp. 361–376. ISSN: 0040-1951. DOI: 10.1016/0040-1951(79)90184-7.

Seong, YB et al. (Mar. 2009). "Quaternary Glaciation of Muztag Ata and Kongur Shan: Evidence for Glacier Response to Rapid Climate Changes throughout the Late Glacial and Holocene in Westernmost Tibet". In: *GSA Bulletin* 121.3-4, pp. 348–365. ISSN: 0016-7606. DOI: 10.1130/B26339.1.

Seton, M et al. (2020). "A Global Data Set of Present-Day Oceanic Crustal Age and Seafloor Spreading Parameters". In: *Geochemistry, Geophysics, Geosystems* 21.10, e2020GC009214. ISSN: 1525-2027. DOI: 10.1029/2020GC009214.

Shah, S (Mar. 2012). "CIA Tactics to Trap Bin Laden Linked with Polio Crisis, Say Aid Groups". In: *The Guardian*. ISSN: 0261-3077.

Shaw, B et al. (Apr. 2008). "Eastern Mediterranean Tectonics and Tsunami Hazard Inferred from the AD 365 Earthquake". In: *Nature Geoscience* 1.4, pp. 268–276. ISSN: 1752-0908. DOI: 10.1038/ngeo151.

Shaw, B and J Jackson (May 2010). "Earthquake Mechanisms and Active Tectonics of the Hellenic Subduction Zone". In: *Geophysical Journal International* 181.2, pp. 966–984. ISSN: 0956-540X. DOI: 10.1111/j.1365-246X.2010.04551.x.

Shean, DE et al. (June 2016). "An Automated, Open-Source Pipeline for Mass Production of Digital Elevation Models (DEMs) from Very-High-Resolution Commercial Stereo Satellite Imagery". In: *ISPRS Journal of Photogrammetry and Remote Sensing* 116, pp. 101–117. ISSN: 0924-2716. DOI: 10.1016/j.isprsjprs.2016.03.012.

Shearer, PM (May 2019). *Introduction to Seismology*. Cambridge University Press. ISBN: 978-1-107-18447-3.

Sherkati, S et al. (Sept. 2005). "Detachment Folding in the Central and Eastern Zagros Fold-Belt (Iran): Salt Mobility, Multiple Detachments and Late Basement Control". In: *Journal of Structural Geology* 27.9, pp. 1680–1696. ISSN: 0191-8141. DOI: 10.1016/j.jsg.2005.05.010.

Sippl, C et al. (Dec. 2013a). "Deep Burial of Asian Continental Crust beneath the Pamir Imaged with Local Earthquake Tomography". In: *Earth and Planetary Science Letters* 384, pp. 165–177. ISSN: 0012-821X. DOI: 10.1016/j.epsl.2013.10.013.

— (Dec. 2013b). "Deep Burial of Asian Continental Crust beneath the Pamir Imaged with Local Earthquake Tomography". In: *Earth and Planetary Science Letters* 384, pp. 165–177. ISSN: 0012-821X. DOI: 10.1016/j.epsl.2013.10.013.

Sippl, C et al. (2013c). "Geometry of the Pamir-Hindu Kush Intermediate-Depth Earthquake Zone from Local Seismic Data". In: *Journal of Geophysical Research: Solid Earth* 118.4, pp. 1438–1457. ISSN: 2169-9356. DOI: 10.1002/jgrb.50128.

Sloan, RA et al. (Apr. 2011). "Earthquake Depth Distributions in Central Asia, and Their Relations with Lithosphere Thickness, Shortening and Extension". In: *Geophysical Journal International* 185.1, pp. 1–29. ISSN: 0956-540X. DOI: 10.1111/j.1365-246X.2010.04882.x.

Smith, N (2006). "There's No Such Thing as a Natural Disaster". In.

Sobel, ER et al. (Apr. 2011). "Late Miocene–Pliocene Deceleration of Dextral Slip between Pamir and Tarim: Implications for Pamir Orogenesis". In: *Earth and Planetary Science Letters* 304.3, pp. 369–378. ISSN: 0012-821X. DOI: 10.1016/j.epsl.2011.02.012.

Sobel, ER et al. (Feb. 2013). "Oceanic-Style Subduction Controls Late Cenozoic Deformation of the Northern Pamir Orogen". In: *Earth and Planetary Science Letters* 363, pp. 204–218. ISSN: 0012-821X. DOI: 10.1016/j.epsl.2012.12.009.

Stanyukovich, K (1997). *In the Mountains of Pamir and Tien-Shan*. InMysl' Publishing House, Moscow.

Storchak, D et al. (Feb. 2015). "The ISC-GEM Global Instrumental Earthquake Catalogue (1900–2009): Introduction". In: *Physics of the Earth and Planetary Interiors* 239, pp. 48–63. ISSN: 00319201. DOI: 10.1016/j.pepi.2014.06.009.

Storchak, DA et al. (Dec. 2017). "Rebuild of the Bulletin of the International Seismological Centre (ISC), Part 1: 1964–1979". In: *Geoscience Letters* 4.1, p. 32. ISSN: 2196-4092. DOI: 10.1186/s40562-017-0098-z.

Storchak, DA et al. (Dec. 2020). "Rebuild of the Bulletin of the International Seismological Centre (ISC)—Part 2: 1980–2010". In: *Geoscience Letters* 7.1, p. 18. ISSN: 2196-4092. DOI: 10.1186/s40562-020-00164-6.

Strom, A and K Abkhmatov (2018). *Rockslides and Rock Avalanches of Central Asia: Distribution, Morphology, and Internal Structure*. Amsterdam, Netherlands ; Cambridge, MA, United States: Elsevier. ISBN: 978-0-12-803204-6.

Stübner, K et al. (Apr. 2021). "Unravelling the Pleistocene Glacial History of the Pamir Mountains, Central Asia". In: *Quaternary Science Reviews* 257, p. 106857. ISSN: 0277-3791. DOI: 10.1016/j.quascirev.2021.106857.

Tadono, T et al. (Apr. 2014). "Precise Global DEM Generation by ALOS PRISM". In: *ISPRS Annals of the Photogrammetry, Remote Sensing and Spatial Information Sciences* II-4, pp. 71–76. ISSN: 2194-9042. DOI: 10.5194/isprsannals-II-4-71-2014.

Takada, Y et al. (Apr. 2009). "Coseismic Displacement Due to the 2008 Iwate-Miyagi Nairiku Earthquake Detected by ALOS/PALSAR: Preliminary Results". In: *Earth, Planets and Space* 61.4, e9–e12. ISSN: 1880-5981. DOI: 10.1186/BF03353153.

Takaku, J et al. (Apr. 2014). "Generation of High Resolution Global DSM from ALOS PRISM". In: *The International Archives of the Photogrammetry, Remote Sensing and Spatial Information Sciences* XL-4, pp. 243–248. ISSN: 1682-1750. DOI: 10.5194/isprsarchives-XL-4-243-2014.

Talebian, M et al. (Dec. 2016). "Active Faulting within a Megacity: The Geometry and Slip Rate of the Pardisan Thrust in Central Tehran, Iran". In: *Geophysical Journal International* 207.3, pp. 1688–1699. ISSN: 0956-540X. DOI: 10.1093/gji/ggw347.

Talebian, M and J Jackson (Mar. 2004). "A Reappraisal of Earthquake Focal Mechanisms and Active Shortening in the Zagros Mountains of Iran". In: *Geophysical Journal International* 156.3, pp. 506–526. ISSN: 0956-540X. DOI: 10.1111/j.1365-246X.2004.02092.x.

Taymaz, T et al. (Aug. 1991). "Active Tectonics of the North and Central Aegean Sea". In: *Geophysical Journal International* 106.2, pp. 433–490. ISSN: 0956-540X. DOI: 10.1111/j.1365-246X.1991.tb03906.x.

Thatcher, W (1993). "The Earthquake Cycle and Its Role in the Long-Term Deformation on the Continental Lithosphere". In: *Annals of Geophysics* 36.2.

Thatcher, W (May 2009). "How the Continents Deform: The Evidence From Tectonic Geodesy*". In: *Annual Review of Earth and Planetary Sciences* 37.Volume 37, 2009, pp. 237–262. ISSN: 0084-6597, 1545-4495. DOI: 10.1146/annurev.earth.031208.100035.

Thomas, JC et al. (1993). "A Paleomagnetic Study of Tertiary Formations from the Kyrgyz Tien-Shan and Its Tectonic Implications". In: *Journal of Geophysical Research: Solid Earth* 98.B6, pp. 9571–9589. ISSN: 2156-2202. DOI: 10.1029/92JB02912.

Thompson, JA et al. (June 2018). "Coarse- versus Fine-Grain Quartz OSL and Cosmogenic 10Be Dating of Deformed Fluvial Terraces on the Northeast Pamir Margin, Northwest China". In: *Quaternary Geochronology* 46, pp. 1–15. ISSN: 1871-1014. DOI: 10.1016/j.quageo.2018.01.002.

Thompson, JA (2013). "Neogene Tectonic Evolution of the NE Pamir Margin, NW China". PhD thesis. United States – California: University of California, Santa Barbara. ISBN: 9781303540912.

Thompson, SC et al. (2002). "Late Quaternary Slip Rates across the Central Tien Shan, Kyrgyzstan, Central Asia". In: *Journal of Geophysical Research: Solid Earth* 107.B9, ETG 7-1-ETG 7–32. ISSN: 2156-2202. DOI: 10.1029/2001JB000596.

Thompson Jobe, JA et al. (Oct. 2018). "Dating Growth Strata and Basin Fill by Combining 26Al/10Be Burial Dating and Magnetostratigraphy: Constraining Active Deformation in the Pamir–Tian Shan Convergence Zone, NW China". In: *Lithosphere* 10.6, pp. 806–828. ISSN: 1941-8264. DOI: 10.1130/L727.1.

Titus, SJ et al. (Sept. 2006). "Thirty-Five-Year Creep Rates for the Creeping Segment of the San Andreas Fault and the Effects of the 2004 Parkfield Earthquake: Constraints from Alignment Arrays, Continuous Global Positioning System, and Creepmeters". In: *Bulletin of the Seismological Society of America* 96.4B, S250–S268. ISSN: 0037-1106. DOI: 10.1785/0120050811.

Tong, D et al. (Aug. 2012). "Fault System, Deformation Style and Development Mechanism of the Bachu Uplift, Tarim Basin". In: *Journal of Earth Science* 23.4, pp. 529–541. ISSN: 1867-111X. DOI: 10.1007/s12583-012-0273-2.

Trifonov, VG (July 1978). "Late Quaternary Tectonic Movements of Western and Central Asia". In: *GSA Bulletin* 89.7, pp. 1059–1072. ISSN: 0016-7606. DOI: 10.1130/0016-7606(1978)89<1059:LQTMOW>2.0.CO;2.

Tsai, CH et al. (2022). "Probing the Upper End of Intracontinental Earthquake Magnitude: A Prehistoric Example From the Dzhungarian and Lepsy Faults of Kazakhstan". In: *Tectonics* 41.10, e2022TC007300. ISSN: 1944-9194. DOI: 10.1029/2022TC007300.

Tucker, BE (Nov. 2004). "Trends in Global Urban Earthquake Risk: A Call to the International Earth Science and Earthquake Engineering Communities". In: *Seismological Research Letters* 75.6, pp. 695–700. ISSN: 0895-0695. DOI: 10.1785/gssrl.75.6.695.

Varum, H et al. (2014). "Structural Behaviour and Retrofitting of Adobe Masonry Buildings". In: *Structural Rehabilitation of Old Buildings*. Ed. by A Costa et al. Berlin, Heidelberg: Springer, pp. 37–75. ISBN: 978-3-642-39686-1. DOI: 10.1007/978-3-642-39686-1_2.

Villaseñor, A and ER Engdahl (Sept. 2005). "A Digital Hypocenter Catalog for the International Seismological Summary". In: *Seismological Research Letters* 76.5, pp. 554–559. ISSN: 0895-0695. DOI: 10.1785/gssrl.76.5.554.

Viltres, R et al. (2022). "Present-Day Motion of the Arabian Plate". In: *Tectonics* 41.3, e2021TC007013. ISSN: 1944-9194. DOI: 10.1029/2021TC007013.

Walker, RT et al. (Sept. 2008). "Active Tectonics of an Apparently Aseismic Region: Distributed Active Strike-Slip Faulting in the Hangay Mountains of Central Mongolia". In: *Geophysical Journal International* 174.3, pp. 1121–1137. ISSN: 0956-540X. DOI: 10.1111/j.1365-246X.2008.03874.x.

Walker, RT et al. (Apr. 2013). "The 2010–2011 South Rigan (Baluchestan) Earthquake Sequence and Its Implications for Distributed Deformation and Earthquake Hazard in Southeast Iran". In: *Geophysical Journal International* 193.1, pp. 349–374. ISSN: 0956-540X. DOI: 10.1093/gji/ggs109.

Walker, RT et al. (May 2015). "Co-Seismic, Geomorphic, and Geologic Fold Growth Associated with the 1978 Tabas-e-Golshan Earthquake Fault in Eastern Iran". In: *Geomorphology*. Geomorphology of Active Faulting and Seismic Hazard Assessment: New Tools and Future Challenges 237, pp. 98–118. ISSN: 0169-555X. DOI: 10.1016/j.geomorph.2013.02.016.

Walker, RT et al. (2017). "The Egiin Davaa Prehistoric Rupture, Central Mongolia: A Large Magnitude Normal Faulting Earthquake on a Reactivated Fault with Little Cumulative Slip Located in a Slowly Deforming Intraplate Setting". In: *Geological Society, London, Special Publications* 432.1, pp. 187–212. ISSN: 0305-8719, 2041-4927. DOI: 10.1144/SP432.4.

Walker, RT et al. (2021). "Slip-Rate on the Main Köpetdag (Kopeh Dagh) Strike-Slip Fault, Turkmenistan, and the Active Tectonics of the South Caspian". In: *Tectonics* 40.8, e2021TC006846. ISSN: 1944-9194. DOI: 10.1029/2021TC006846.

Walsh, D (July 2011). "US-Pakistan Spy Wars Hit Flood Relief as Aid Workers Get Caught in Dragnet". In: *The Guardian*. ISSN: 0261-3077.

Walters, RJ et al. (Oct. 2018). "Dual Control of Fault Intersections on Stop-Start Rupture in the 2016 Central Italy Seismic Sequence". In: *Earth and Planetary Science Letters* 500, pp. 1–14. ISSN: 0012-821X. DOI: 10.1016/j.epsl.2018.07.043.

Wang, J et al. (Apr. 2011). "Quaternary Glacial Geomorphology and Glaciations of Kongur Mountain, Eastern Pamir, China". In: *Science China Earth Sciences* 54.4, pp. 591–602. ISSN: 1674-7313, 1869-1897. DOI: 10.1007/s11430-010-4165-y.

Wang, L et al. (1987). "Long Period Source Parameters of the Wuqia, Xinjiang Earthquake of August 23, 1985 - Results from Inversion of the Records of the IDA Network". In: *Acta Seismologica Sinica* 9.1, pp. 108–111.

Wang, S et al. (Sept. 2022). "Structural Controls on Coseismic Rupture Revealed by the 2020 Mw 6.0 Jiashi Earthquake (Kepingtag Belt, SW Tian Shan, China)". In: *Geophysical Journal International* 230.3, pp. 1895–1910. ISSN: 0956-540X. DOI: 10.1093/gji/ggac159.

Wang, Z and X Wang (2016). "Late Cenozoic Deformation Sequence of a Thrust System along the Eastern Margin of Pamir, Northwest China". In: *Acta Geologica Sinica - English Edition* 90.5, pp. 1664–1678. ISSN: 1755-6724. DOI: 10.1111/1755-6724.12809.

Watson, AR et al. (2022a). "Interseismic Strain Accumulation Across the Main Recent Fault, SW Iran, From Sentinel-1 InSAR Observations". In: *Journal of Geophysical Research: Solid Earth* 127.2, e2021JB022674. ISSN: 2169-9356. DOI: 10.1029/2021JB022674.

Watson, CS et al. (Jan. 2022b). "Analyzing Satellite-Derived 3D Building Inventories and Quantifying Urban Growth towards Active Faults: A Case Study of Bishkek, Kyrgyzstan". In: *Remote Sensing* 14.22, p. 5790. ISSN: 2072-4292. DOI: 10.3390/rs14225790.

Wei, HH et al. (2013). "Tertiary Evolution of the Western Tarim Basin, Northwest China: A Tectono-Sedimentary Response to Northward Indentation of the Pamir Salient". In: *Tectonics* 32.3, pp. 558–575. ISSN: 1944-9194. DOI: 10.1002/tect.20046.

Wescoat, JL (2015). "Political Ecology of Risk, Hazards, Vulnerability, and Capacities". In: *The Routledge Handbook of Political Ecology*. Routledge. ISBN: 978-1-315-75928-9.

Wessel, P et al. (2019). "The Generic Mapping Tools Version 6". In: *Geochemistry, Geophysics, Geosystems* 20.11, pp. 5556–5564. ISSN: 1525-2027. DOI: 10.1029/2019GC008515.

Weston, J et al. (July 2018). "ISC-EHB: Reconstruction of a Robust Earthquake Data Set". In: *Geophysical Journal International* 214.1, pp. 474–484. ISSN: 0956-540X. DOI: 10.1093/gji/ggy155.

Wilkinson, R (2023). "Active Tectonics and Seismic Hazard in Central Asia". DPhil. Oxford: University of Oxford.

Wimpenny, S and CS Watson (Dec. 2020). "gWFM: A Global Catalog of Moderate-Magnitude Earthquakes Studied Using Teleseismic Body Waves". In: *Seismological Research Letters*. ISSN: 0895-0695, 1938-2057. DOI: 10.1785/0220200218.

Wood, H (1921). *A List of Seismologic Stations of the World*. Vol. 2. Bulletin of the National Research Council.

Wright, TJ et al. (2004). "Toward Mapping Surface Deformation in Three Dimensions Using InSAR". In: *Geophysical Research Letters* 31.1. ISSN: 1944-8007. DOI: 10.1029/2003GL018827.

Xu, Y et al. (Apr. 2006). "Analysis of Seismic Activity in the Crust from Earthquake Relocation in the Central Tien Shan". In: *Bulletin of the Seismological Society of America* 96.2, pp. 737–744. ISSN: 0037-1106. DOI: 10.1785/0120030220.

Yablokov, A (Feb. 2001). "The Tragedy of Khait: A Natural Disaster in Tajikistan". In: *Mountain Research and Development* 21.1, pp. 91–93. ISSN: 0276-4741, 1994-7151. DOI: 10.1659/0276-4741(2000)021[0091:TTOKAN]2.0.CO;2.

Yu, C et al. (2017). "Generation of Real-Time Mode High-Resolution Water Vapor Fields from GPS Observations". In: *Journal of Geophysical Research: Atmospheres* 122.3, pp. 2008–2025. ISSN: 2169-8996. DOI: 10.1002/2016JD025753.

Yu, C et al. (2018a). "Generic Atmospheric Correction Model for Interferometric Synthetic Aperture Radar Observations". In: *Journal of Geophysical Research: Solid Earth* 123.10, pp. 9202–9222. ISSN: 2169-9356. DOI: 10.1029/2017JB015305.

Yu, C et al. (Jan. 2018b). "Interferometric Synthetic Aperture Radar Atmospheric Correction Using a GPS-based Iterative Tropospheric Decomposition Model". In: *Remote Sensing of Environment* 204, pp. 109–121. ISSN: 0034-4257. DOI: 10.1016/j.rse.2017.10.038.

Yuan, X et al. (Mar. 2018). *East Pamir Network*. DOI: 10.14470/3U7560589977.

Zech, R et al. (Sept. 2005). "Late Quaternary Glacial and Climate History of the Pamir Mountains Derived from Cosmogenic 10Be Exposure Ages". In: *Quaternary Research* 64.2, pp. 212–220. ISSN: 0033-5894. DOI: 10.1016/j.yqres.2005.06.002.

Zhang, Y et al. (Sept. 2022). "Review of Seismic Risk Mitigation Policies in Earthquake-Prone Countries: Lessons for Earthquake Resilience in the United States". In: *Journal of Earthquake Engineering*. ISSN: 1363-2469.

Zhang, Y et al. (2023). "Strain Accommodation and Seismic Hazards of the Kalpin Fold-And-Thrust Belt, Southwestern Tian Shan Foreland, China: Insights From the 2020 Mw 6.0 Kalpin Earthquake". In: *Journal of Geophysical Research: Solid Earth* 128.3, e2022JB025328. ISSN: 2169-9356. DOI: 10.1029/2022JB025328.

Zhou, Y et al. (Oct. 2016). "Coseismic and Postseismic Displacements from the 1978 Mw 7.3 Tabas-e-Golshan Earthquake in Eastern Iran". In: *Earth and Planetary Science Letters* 452, pp. 185–196. ISSN: 0012-821X. DOI: 10.1016/j.epsl.2016.07.038.

Zhou, Y et al. (Feb. 2018). "Time-Dependent Postseismic Slip Following the 1978 Mw 7.3 Tabas-e-Golshan, Iran Earthquake Revealed by over 20 Years of ESA InSAR Observations". In: *Earth and Planetary Science Letters* 483, pp. 64–75. ISSN: 0012-821X. DOI: 10.1016/j.epsl.2017.12.005.

Zielke, O and JR Arrowsmith (Feb. 2012). "LaDiCaoz and LiDARimager—MATLAB GUIs for LiDAR Data Handling and Lateral Displacement Measurement". In: *Geosphere* 8.1, pp. 206–221. ISSN: 1553-040X. DOI: 10.1130/GES00686.1.

Zubovich, A et al. (2016). "Tectonic Interaction between the Pamir and Tien Shan Observed by GPS". In: *Tectonics* 35.2, pp. 283–292. ISSN: 1944-9194. DOI: 10.1002/2015TC004055.

Zubovich, AV et al. (2010). "GPS Velocity Field for the Tien Shan and Surrounding Regions". In: *Tectonics* 29.6. ISSN: 1944-9194. DOI: 10.1029/2010TC002772.

appendixfigure[figure]

6 | Appendix

6.1 Appendix to Chapter 2: Rupture of the 1949 Khait earthquake on a cryptic fault: implications for earthquake hazard

A1: 1949 digitized arrivals and m_B estimates

Station name	Distance [°]	Azimuth [°]	Comp	Phase	Arrival time	T [sec]	Amp[μm]	m_B
BER	45.283	320.178	Z	P	01:56.0	3	22.02	7.57
BER	45.283	320.178	Z	PP	03:19.0	3	37.59	7.8
BER	45.283	320.178	EW	S	08:36.0	9	107	7.58
BER	45.283	320.178	EW	SS	08:39.0	-	-	
DBN	46.333	308.839	Z	P	02:02.0	3	17.14	7.56
DBN	46.333	308.839	Z	PP	03:50.0	5	21.36	7.33
DBN	46.333	308.839	EW	S	08:54.0	5	30.57	7.39
DBN	46.333	308.839	EW	SS	12:44.0	-	-	
ROM	44.052	292.756	Z	P	01:41.0	5	59.47	7.58
ROM	44.052	292.756	Z	PP	03:05.0	5	32.47	7.51
ROM	44.052	292.756	EW	S	08:19.0	12	253	7.92
HUA	139.672	302.663	Z	Pdiff	13:04.0	9	21	7.37
HUA	139.672	302.663	EW	PP	16:04.0	10	27	7.43
HUA	139.672	302.663	EW	SS	20:32.0	12	54	7.95
PAD	43.613	298.125	Z	P	01:35.0	3	25	7.42
PAD	43.613	298.125	Z	PP	03:26.0	6	39	7.41
PAD	43.613	298.125	EW	S	03:26.0	6	167	7.94
PAS	106.708	7.851	Z	P	07:58.0	5	4.08	7.71
PAS	106.708	7.851	Z	PP	12:09.0	5	19.45	7.99
PAS	106.708	7.851	NS	S	18:28.0	5	44.12	8.15
HAM	43.183	310.326	Z	P	01:48.0	5	51	7.51
HAM	43.183	310.326	Z	PP	03:38.0	5	59	7.6
HAM	43.183	310.326	EW	S	08:28.0	8	102	7.61
LEI	41.963	306.812	Z	P	01:24.0	4	48	7.58
LEI	41.963	306.812	Z	PP	03:04.0	5	78	7.69
LEI	41.963	306.812	EW	S	07:45.0	7	94	7.63
GTT	43.444	307.416	Z	P	01:32.0	4	45	7.55
GTT	43.444	307.416	Z	PP	03:16.0	7	65	7.57
GTT	43.444	307.416	EW	S	03:16.0	9	87	7.49
TLO	56.222	296.554	Z	P	03:17.0	5	13	7.21
TLO	56.222	296.554	Z	PP	04:09.0	5	23	7.56
TLO	56.222	296.554	EW	S	11:06.0	6	45	7.48
COL	72.026	16.328	Z	P	04:58.0	9	34	7.48
COL	72.026	16.328	Z	PP	07:39.0	12	41	7.63
COL	72.026	16.328	NS	S	14:21.0	15	65	7.64
ABU	50.812	73.406	Z	P	02:43.0	9	56	7.49
ABU	50.812	73.406	Z	PP	04:22.0	12	59	7.39
ABU	50.812	73.406	NS	S	10:04.0	16	98	7.39
							Average m_B	**7.59 ± 0.2**
							Median m_B	**7.56 ± 0.2**

A2: 1949 surface wave magnitude estimates

Station (Instrument)	**Period [sec]**	**Amplitude [μm]**	**Ms**
BER	16	623	7.83
DBN	16	282	7.5
ROM	19	647	7.76
HUA	27	86	7.28
PAS	25	145	7.41
HAM	19	600	7.72
LEI	16	617	7.79
GTT	18	1223	8.05
COL	25	588	7.83
ABU	22	1083	7.99
		Median	**7.77 ± 0.2**
		Average	**7.72 ± 0.2**

A3: 1949 scalar moment and moment magnitude M_w estimates for each seismic station. This was done by fitting synthetic seismograms generated from the modelled focal mechanism and varying the seismic moment until the observed and synthetic seismogram amplitudes agreed. A more detailed account of the method can be found in a more detailed account of this method see Kulikova and Krüger (2015) and Ou et al. (2020).

Station	**Lat**	**Lon**	**Mo / Nm**	**M_w**
BER	60.4000	5.3100	2.00E+20	7.5
DBN	52.1000	5.1800	5.72E+20	7.8
ROM	41.9033	12.5133	2.14E+20	7.52
HUA	-12.0384	-75.3228	1.05E+21	7.98
PAD	45.4086	11.8878	5.68E+20	7.8
PAS	34.1485	-118.1711	2.01E+20	7.5
HAM	53.4642	9.925	1.93E+20	7.49
LEI	51.3400	12.3900	1.24E+20	7.36
GTT	51.5500	9.9667	1.76E+20	7.46
TLO	36.4667	-6.2000	4.89E+20	7.76
COL	64.9000	-147.7933	5.20E+20	7.78
ABU	34.8603	135.5739	4.23E+20	7.72
		Average	**3.19±2.5E+20**	**7.64**
		Median	**3.95±2.5E+20**	**7.7**

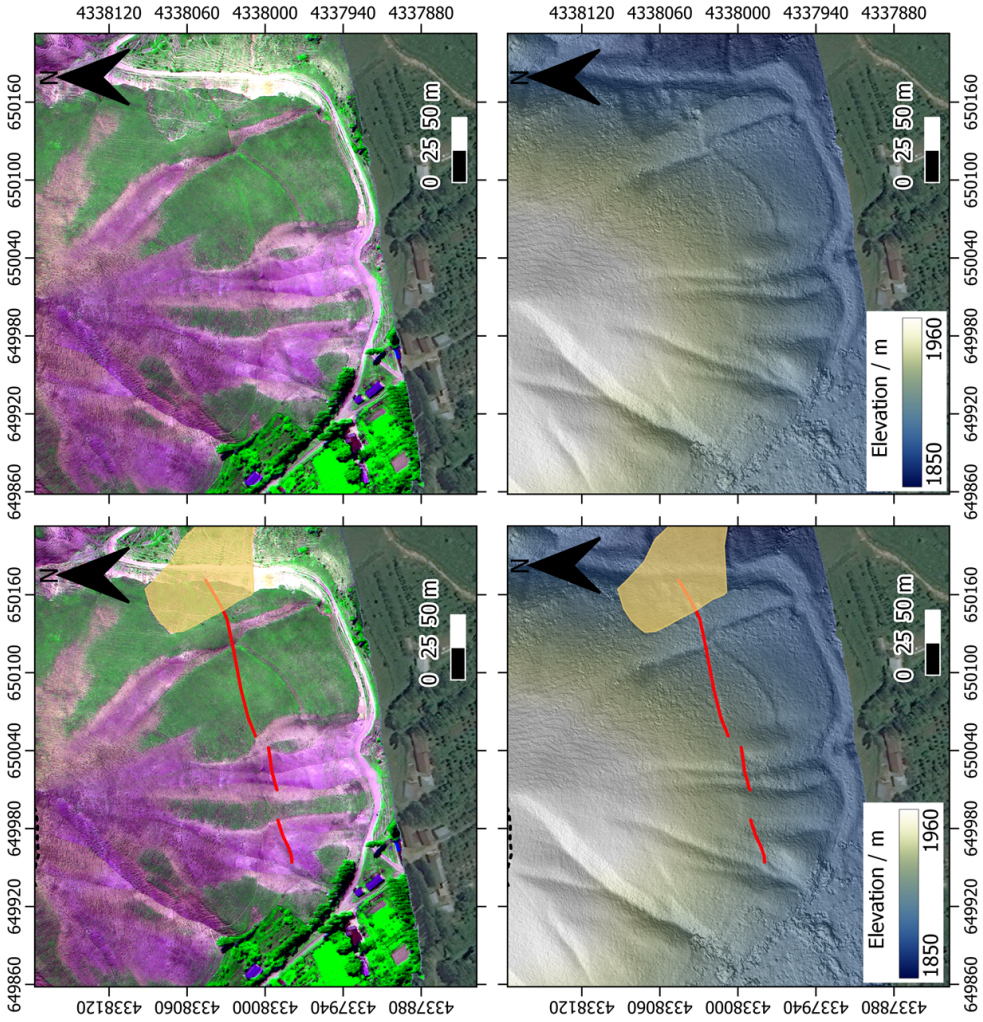

A4: Possible rupture near Khurramshahr, about half way down the Yasman Valley. There is an apparent offset of one drainage to the east of the image of around 6-12 m. This is very close to a recent landslide, so we hypothesise this offset is likely due to land-slip rather than tectonic motions.

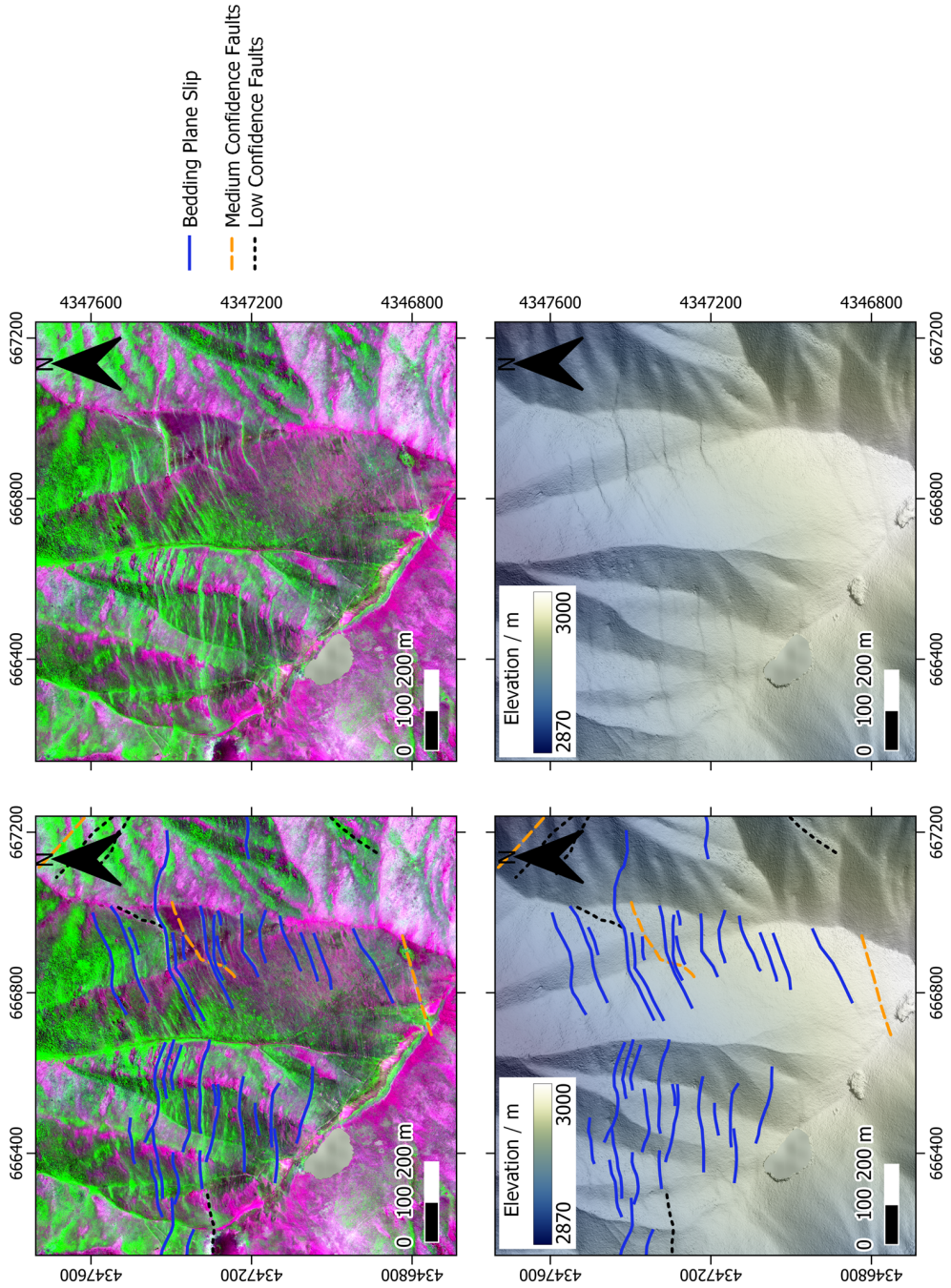

A5: Bedding plane slip north-east of Khait. These parallel, non-branching scarps are colinear with bedding plane measurements identified in VSEGEI geological maps. They are uphill-facing scarps, so unlikely to be due to mass movements. Cross-cutting these are other scarps, which may be tectonic but are perpendicular to our hypothesized fault plane, delinated by the 1949 focal mechanism, and mechanisms relocated with *mloc* (see Fig. 2.1b). Movement on bedding planes may reduce the expression of linear tectonic scarps, explaining why we have been unable to find these along the line marked out in Fig. 2.1b.

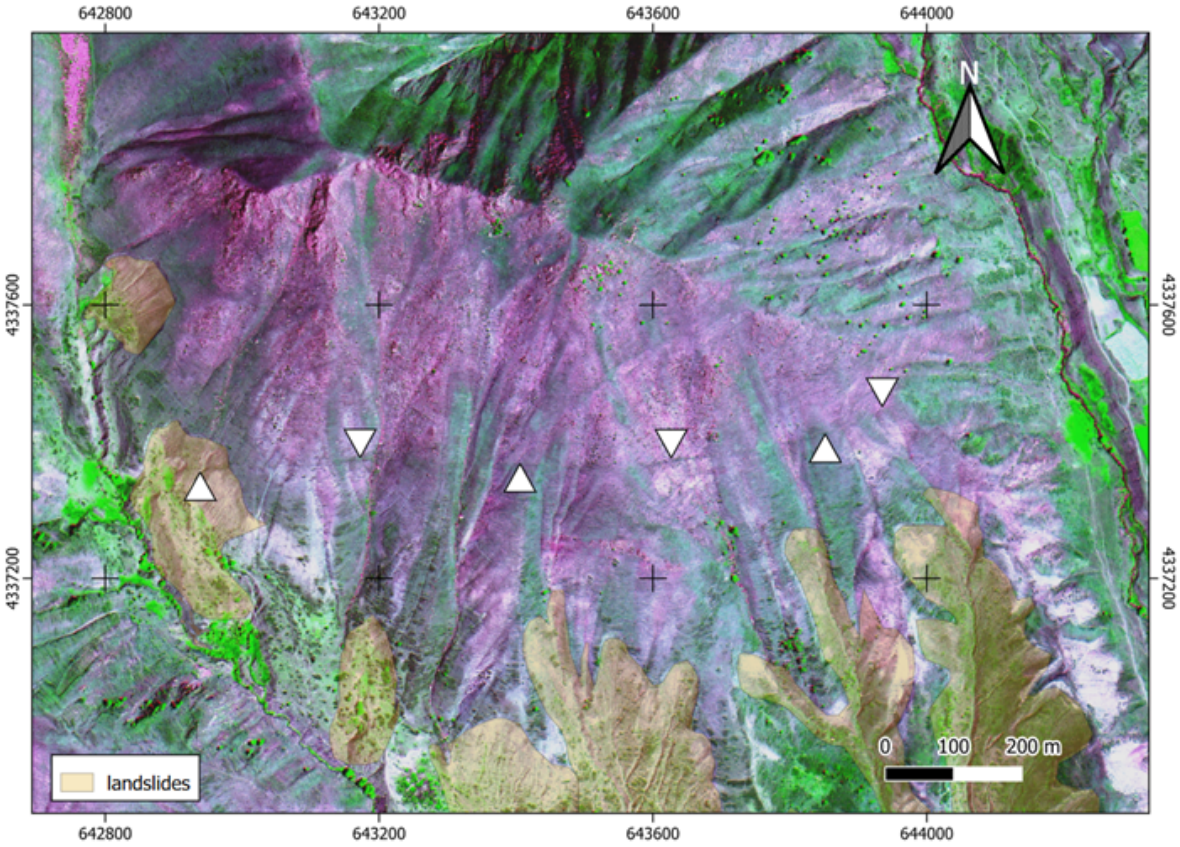

A6: West of Musofiron (Figure 2.6) there are traces visible on the hillside which may be related to the offsets visible in the valley. Offsets are not resolvable in the DEM.

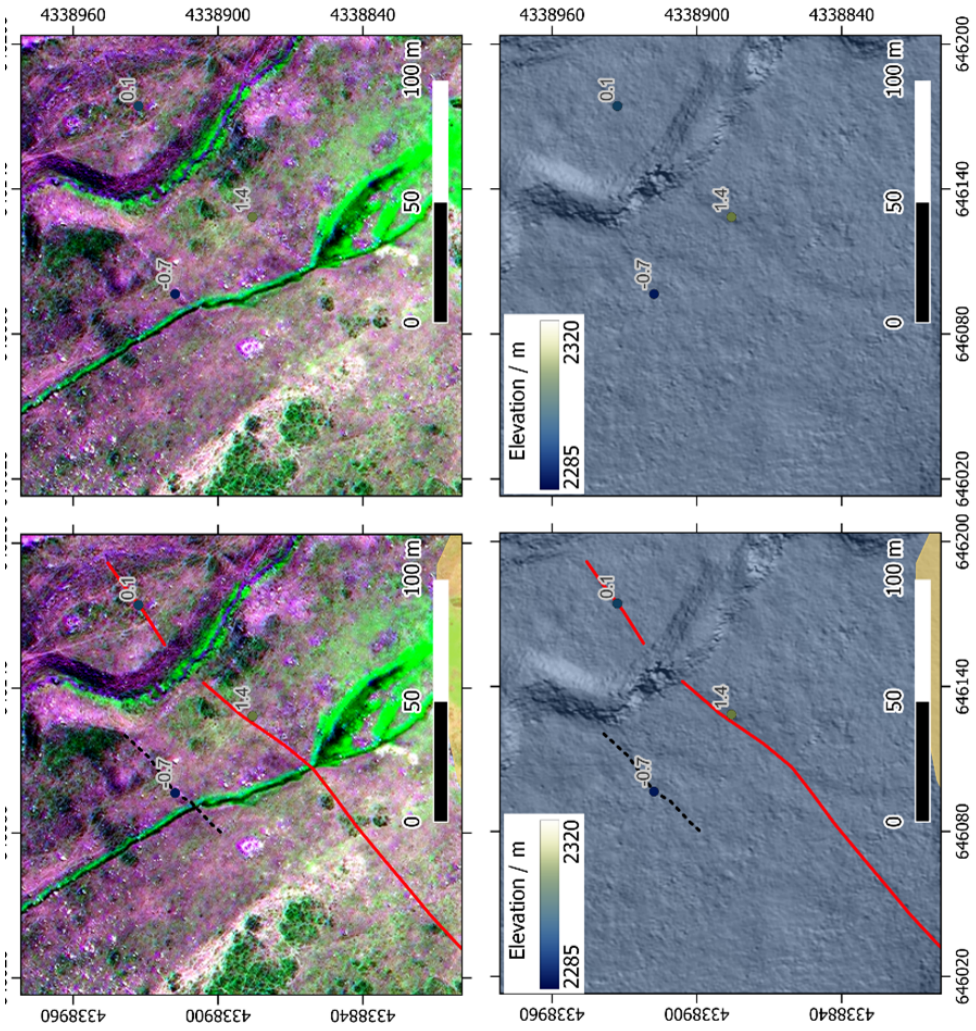

A7: Surface ruptures near Safebod. We interpret the widening of the western stream to be due to crossing the scarp, with deeper incision on the upthrown (northern) side.

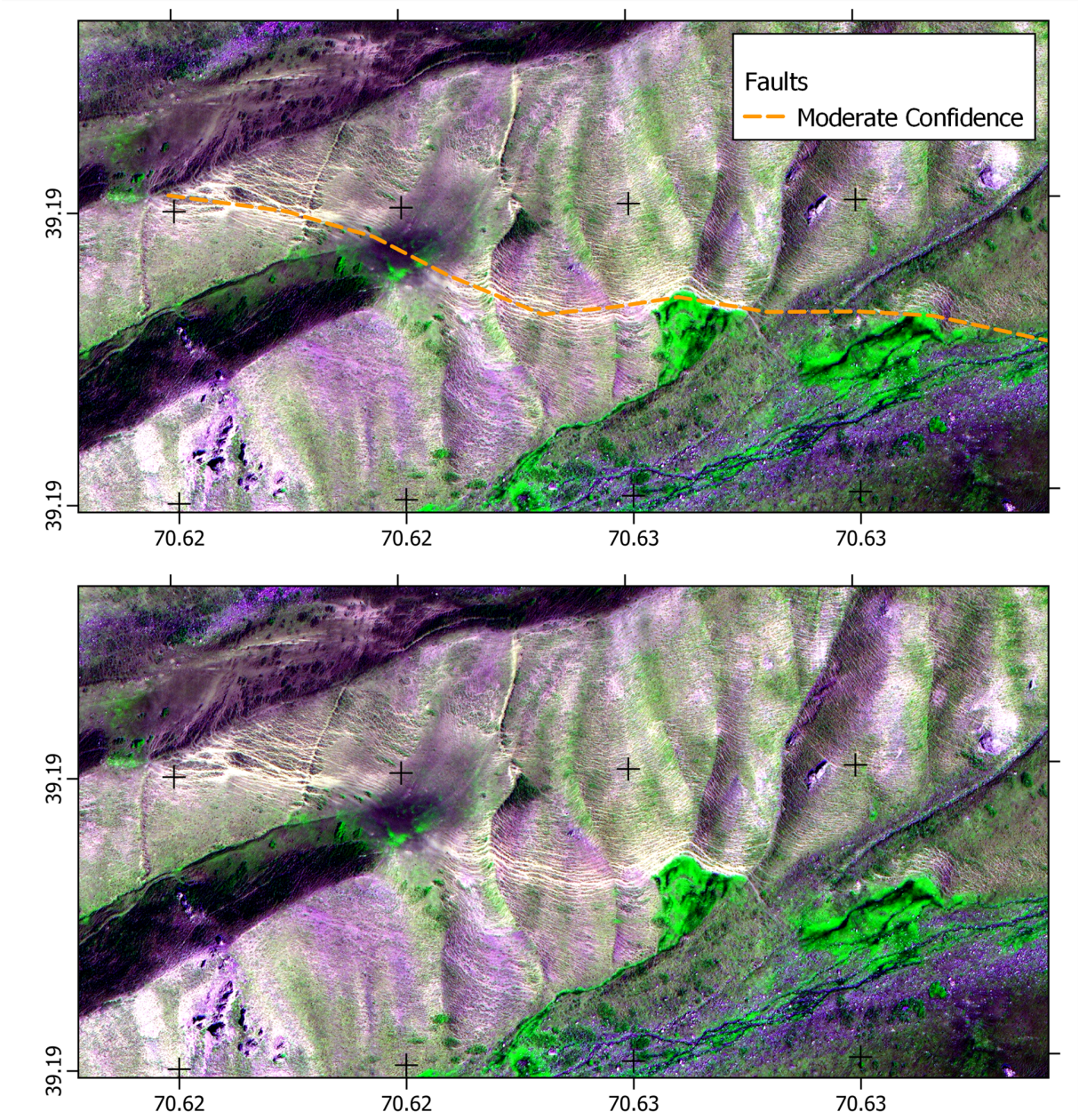

A8: False colour image of fault trace south of Figure 2.6. The NIR band (which picks up vegetation) shows aligned springs, similarly to other fault zones mapped in this study. White lines contouring the topography suggest a track runs through the area, possibly exploiting a fault scarp in the hillside.

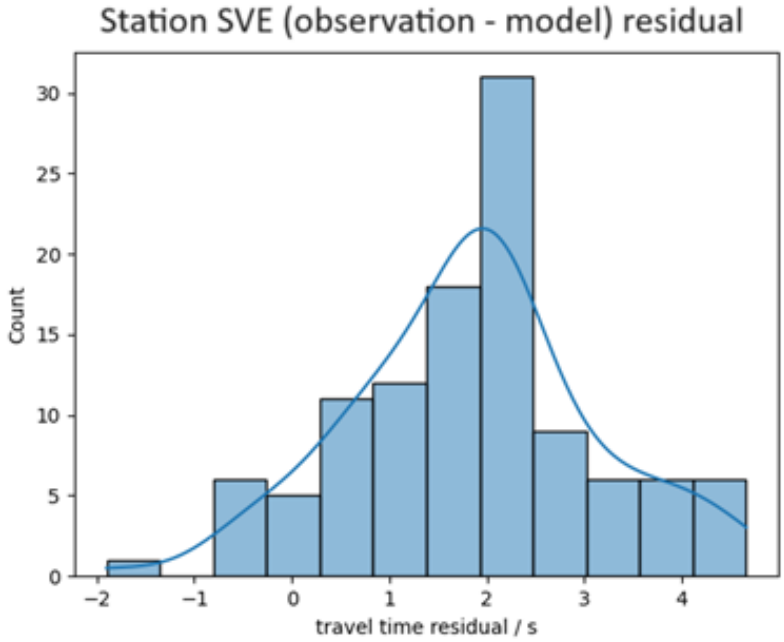

A9: Seismic phase travel time residuals from the modified ak135 velocity model used for the *mloc* relocations. These have a roughly normal distribution, with a mean at around 2s. This represents the systematic errors in the ak135 model caused by regional variations in the seismic velocity structure. See Figure 2.4B.

6.2 Appendix to Chapter 3: Rapid fault creep in the fluid-rich Kura Basin, Azerbaijan, imaged with InSAR

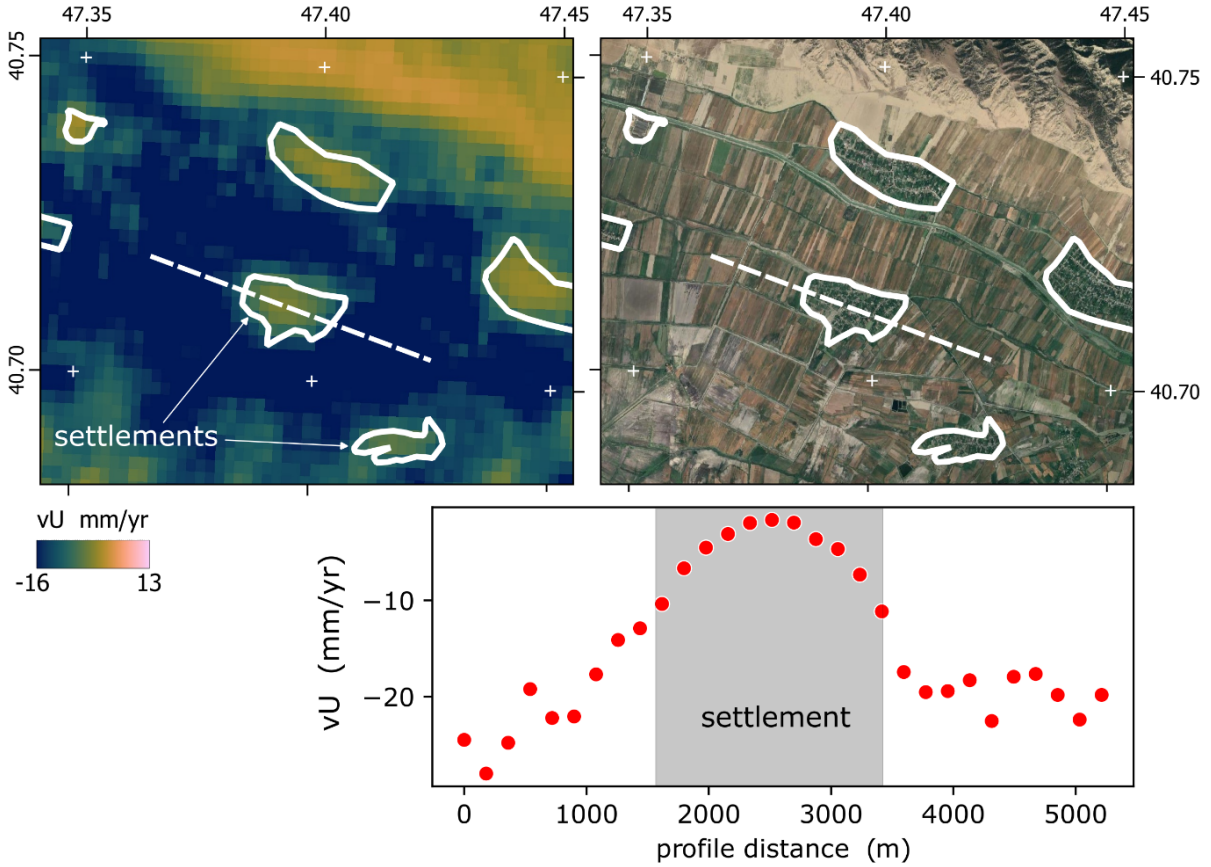

A10: Close up view of the vertical velocity over agricultural land just south of the KFTB. The unmasked vertical velocity field shows the degree to which land use affects the signal. The pixels within the settlement are close to 0 mm/yr, by contrast the surrounding fields show highly negative vertical velocities reaching ∼-20 mm/yr. This can be attributed to phase bias, but also potentially to subsidence from water abstraction for agriculture.

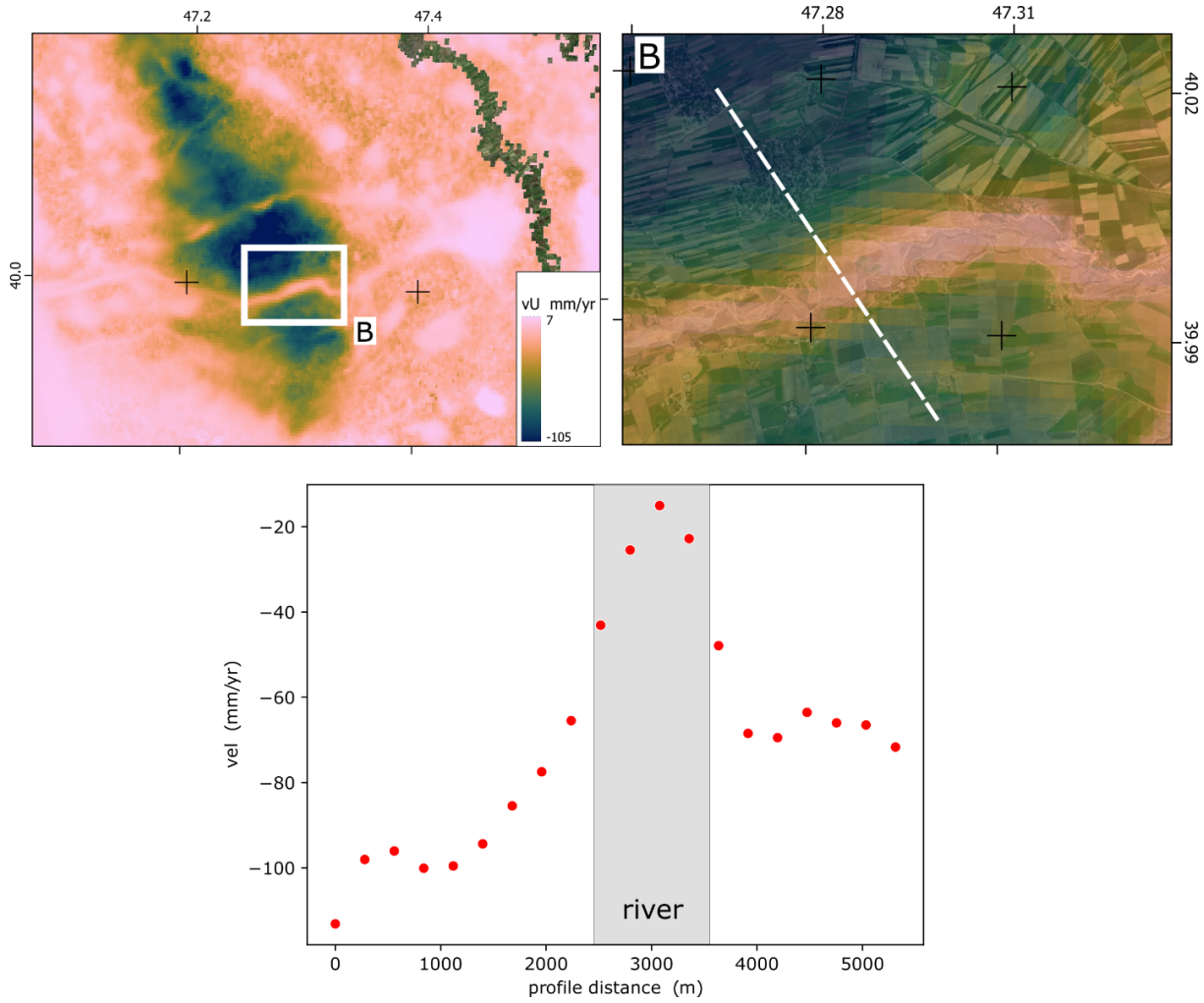

A11: Vertical velocity field near the Lesser Caucasus. We observe an oval region with highly negative vertical velocity (∼100 mm/yr). This region is crossed by lines of higher velocity, which correspond to meandering rivers. This velocity contrast is likely related to the relative lack of vegetation at the river bank compared to the irrigated cropland it crosses, and is a demonstration of the effect of phase bias in the area.

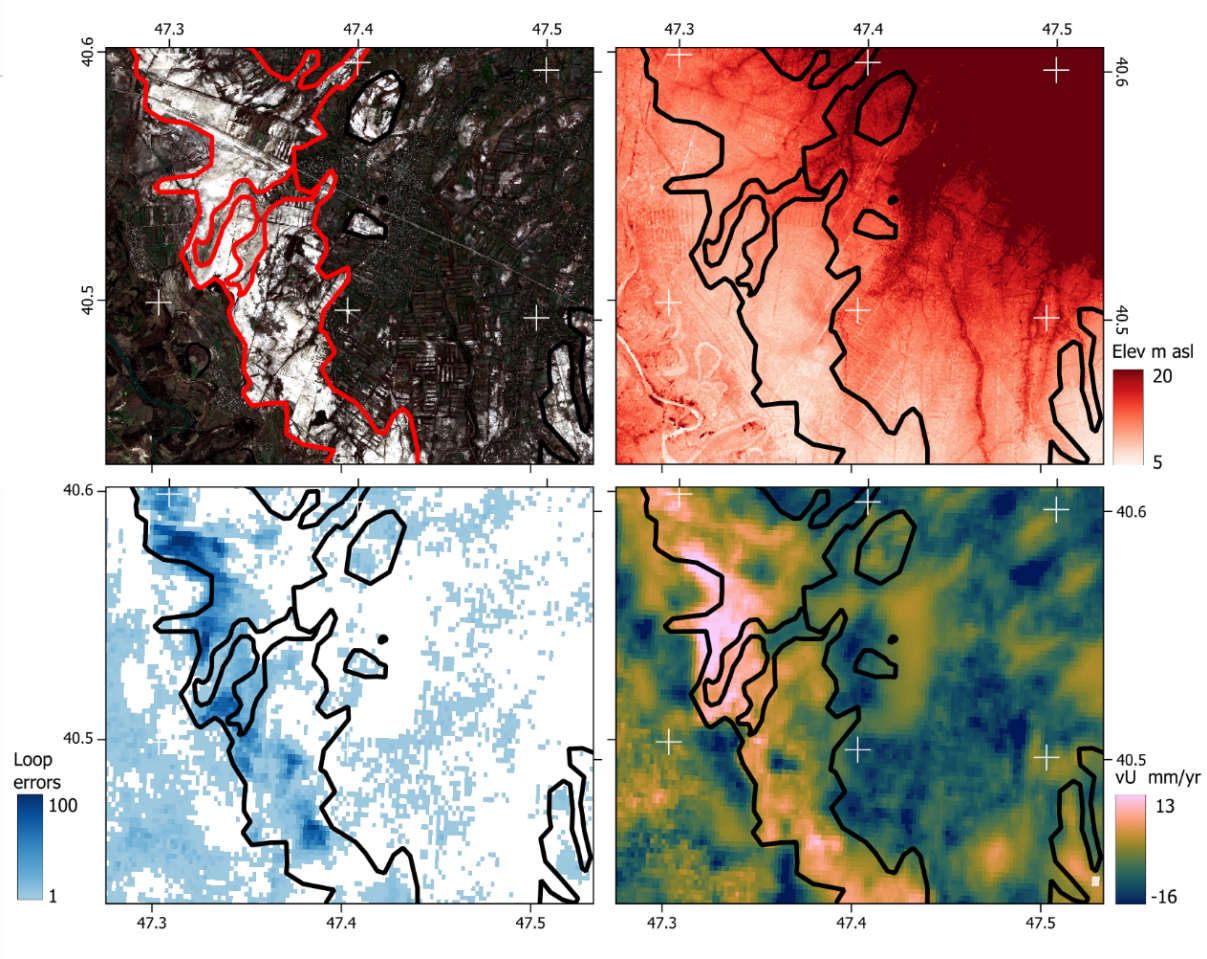

A12: Salt pan uplift in the Kura Basin. The black outline contains a region of highly reflective white material visible in Sentinel 2 True Color optical imagery (top-left). This corresponds roughly to a topographic low (top-right), which we suspect is salt deposition from evaporation. We observe similar highly reflective deposits next to lakes in the region (e.g. 41.0073,46.9348). Within the polygon we find a concentration of loop errors (bottom-left) – showing a propensity for unwrapping errors in this region. Finally, we observe an uplift signal in the InSAR data (bottom-right). Taken together, we suggest this region is undergoing real uplift due to deposition of evaporites, and potentially some false uplift due to unwrapping errors.

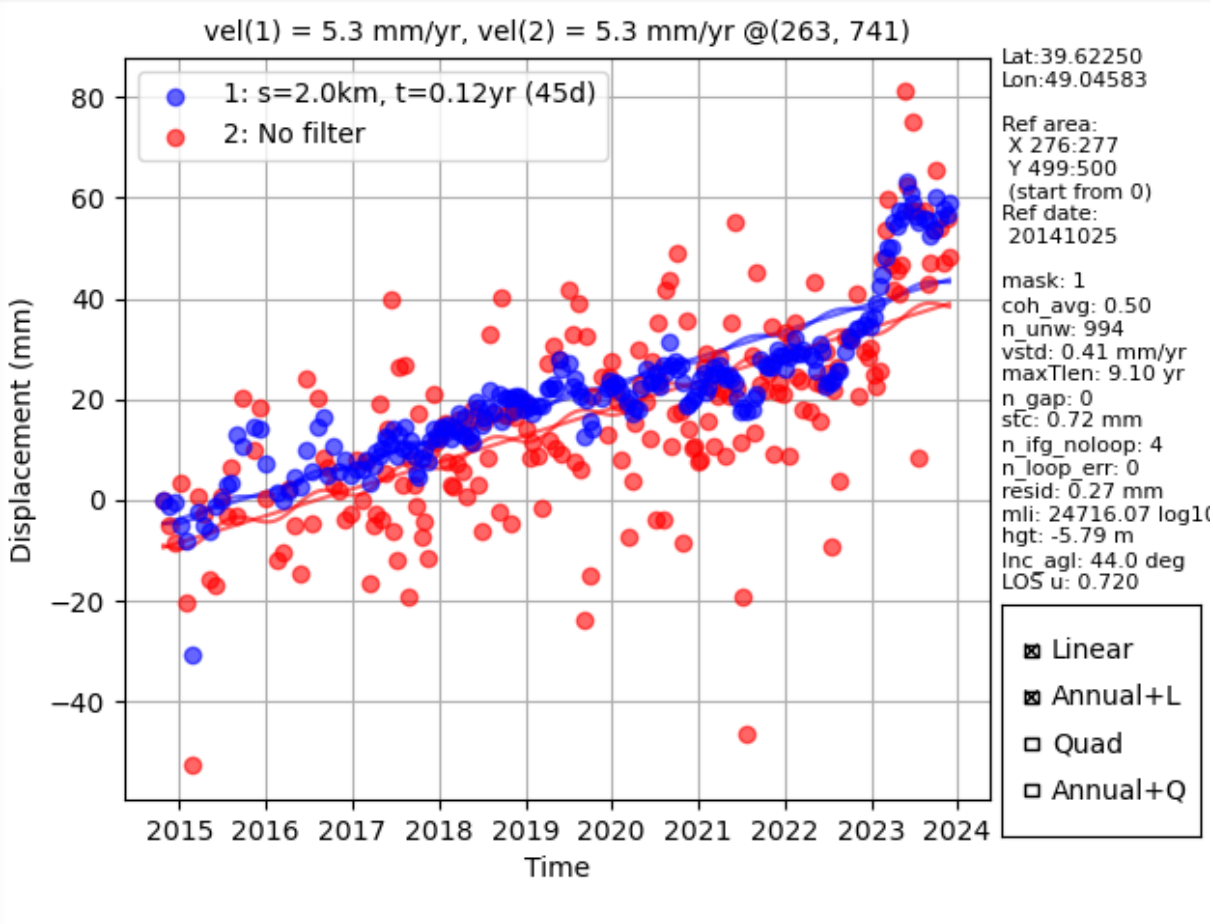

A13: Time series of line-of-sight displacements for 108D pixel centred on the Salyan Fault uplift (Figure 3.8a). The jump in velocity in 2023 is likely related to the M_w 7.8 Kahramanmaraş earthquake in Turkey, around 1000 km away.

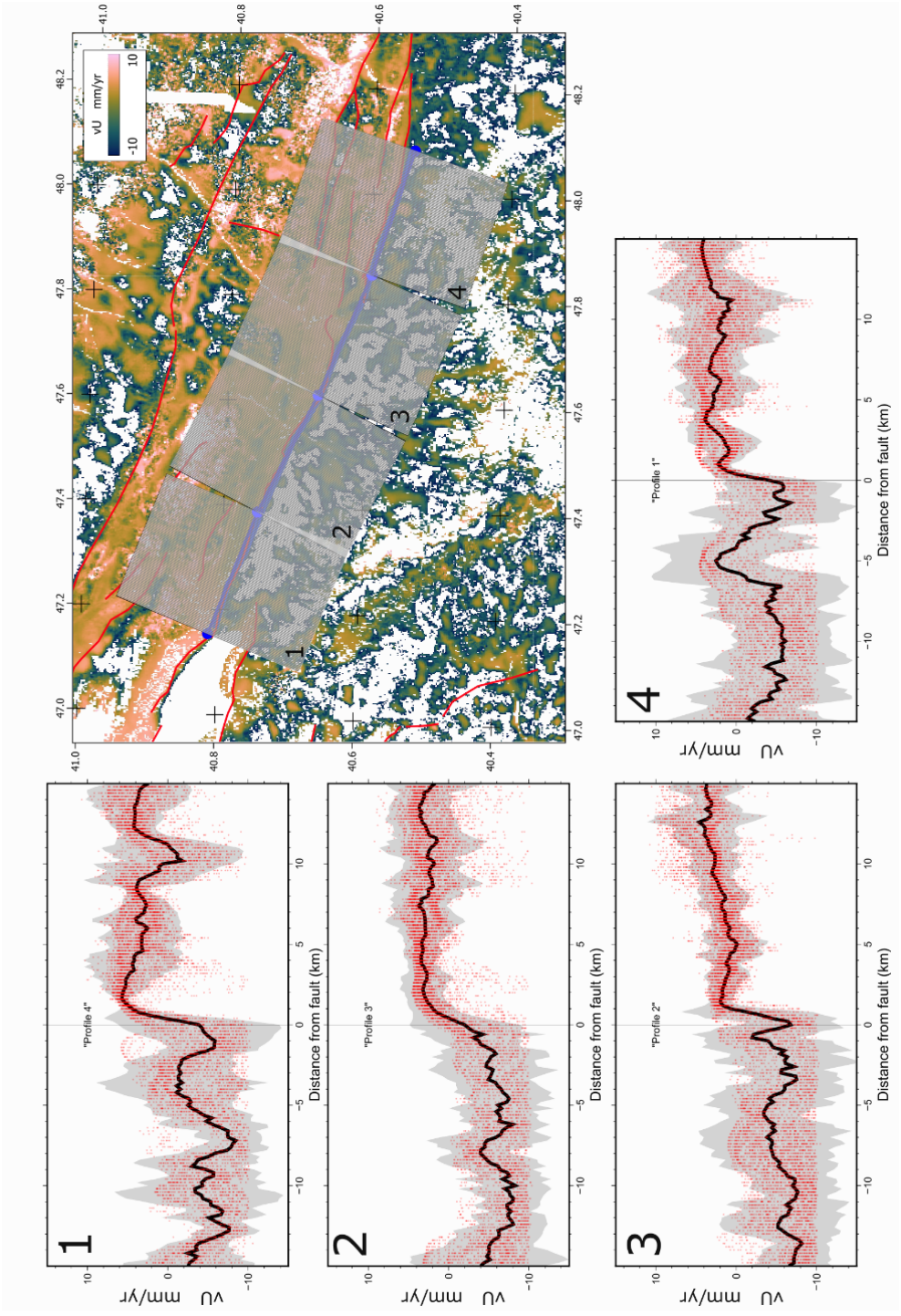

A14: Decomposed vertical velocity for the same region as in Figure 3.9, with a minimum velocity threshold of -10 mm/yr as opposed to -5 mm/yr in the main text. This shows the up-down velocity contrast across the KFTB is still present, but the magnitude is much greater. This is due to the inclusion of pixels affected by phase bias due to agriculture.

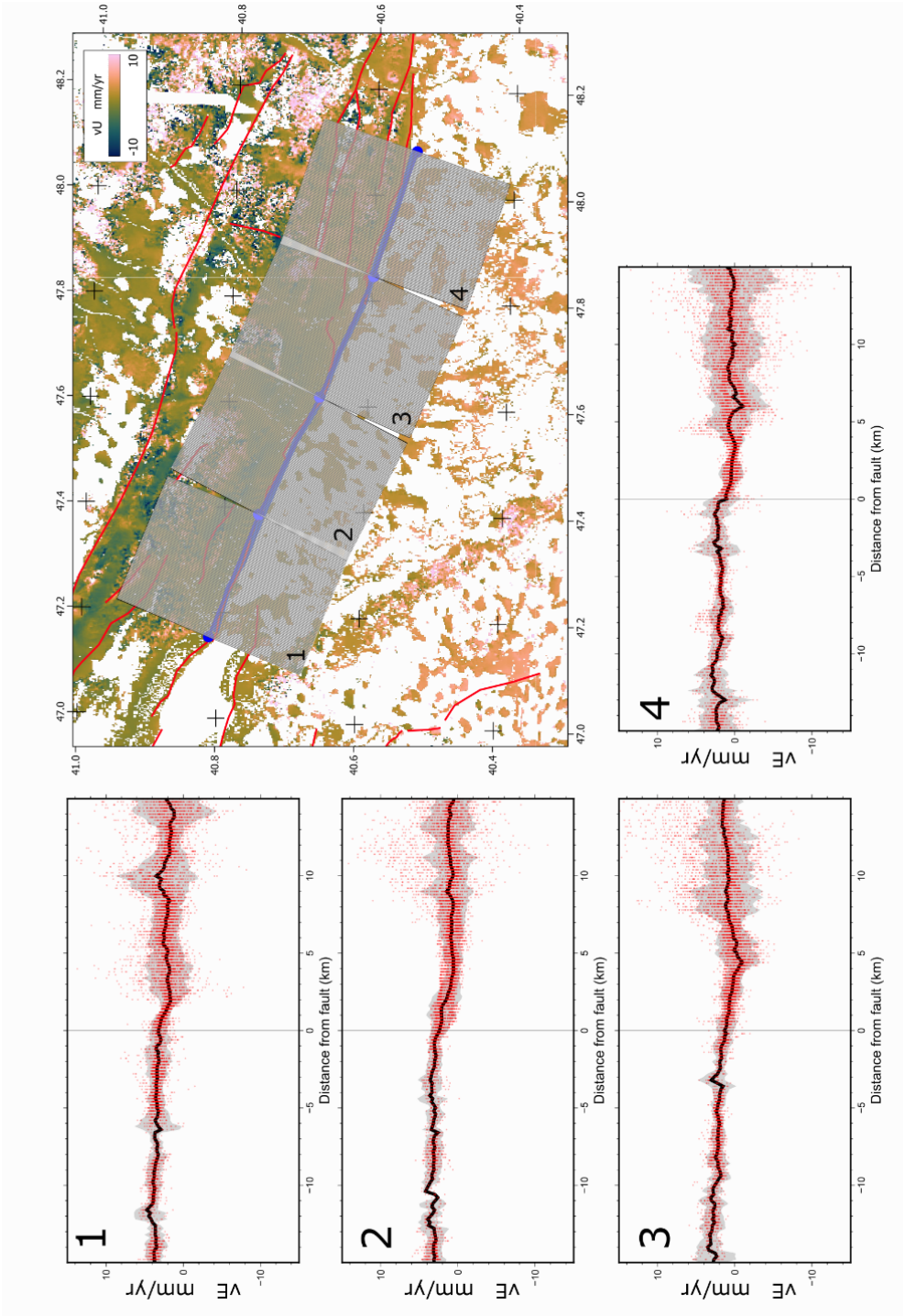

A15: East-west velocity field for the KFTB, using the mask generated by thresholding the up-down velocity at -5 mm/yr and above. There is a slight left-lateral motion visible of 1-2 mm/yr across the fault in all the profiles. This is consistent with GNSS measurements which also show a slight left lateral motion across this fault (Figure 3.2C)

6.3 Appendix to Chapter 4: The 1985 Wuqia Earthquake: rupture beneath the sedimentary cover on a strike-slip transpressive structure

1978 November 1 (1 subevent)
111/52/152/5/976

A6a.

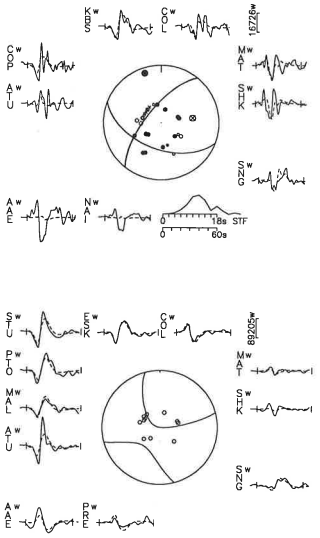

1978 November 1 (3 subevents)
1:70/85/180/8/78
2:108/68/163/9/426
3:116/50/150/10/436

A6b.

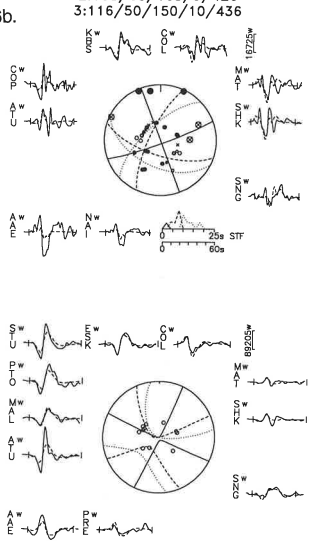

A7. 1982 September 29

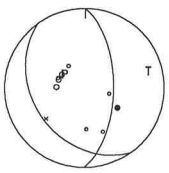

NUR are too small. For a 6° gentler dip of 38°, the synthetic SH phases are too big at COL, too small at NAI, and out of phase at TOL. For a 12° steeper rake of 69°, the synthetic P phase at COL is too big, and the synthetic SH phases at NAI, TOL, KONO, NUR, and GDH are a little too small. For a 12° gentler rake of 45°, the synthetic SH phases at TOL, ESK, KEV, and COL are too big.

1985 August 23 Wuqia earthquake (Fig. A10). 39.43°N, 75.27°E, depth = 18 km, with average solution of strike = 316°, dip = 46°, rake = 160°, M_o = 2.22 × 10^{19} Nm, or consisting of three subevents: strike = 283°, dip = 34°, rake = 142°, M_o = 3.6 × 10^{18} Nm; strike = 326°, dip = 58°, rake = 158°, M_o = 7.9 × 10^{18} Nm; and strike = 309°, dip = 41°, rake = 152°, M_o = 9.9 × 10^{18} Nm.

This is a large earthquake for which the complexity of the signals requires a source more complicated than a point source. We explored a series of possible sources that include a single point source (Fig. A10a), a source with a uniform rupture velocity (Fig. A10b), and multiple sources (Fig. A10c). Definite improvements in matches of synthetic and recorded waveforms can be seen with increasingly complex sources, described by an increasing number of free parameters, but as a result it is difficult to assign uncertainties to all of these parameters.

Note first that the strong P waves at stations to the northwest and the small complex signals at stations to the east and southeast require both that one nodal plane pass near the stations to the east and southeast and that there be a significant strike-slip component. These inferences are corroborated by the amplitudes and shapes of SH phases. Neither the broad pulses for both P and SH to the east and southeast, however, nor the multiple pulses of P at these stations and of SH at stations to the northwest are synthesized well using a point source (Fig. A10a).

After numerous trials and errors we examined systematically rupture propagation toward the northwest, similar to that inferred by Ekström (1987). In Figure A10b we show the matches of recorded and synthetic waveforms for a rupture velocity of 2.5 km/s in the direction 300°. With velocities of 2.0, 2.5, or 3.0 km/s in the direction 300°, the improvement over a point source is noteworthy, including broader synthetic signals to the east and southeast and a better match of the complex P and SH phases to the northwest and east, respectively. In all cases, however, the source time functions appeared to consist of three subevents. Consequently, we then broke the uniform rupture into separate subevents, each describable as point sources. Fixing their locations, we inverted for the source parameters of three subevents. which allowed a still better match to the complexities of P phases to the northwest and SH phases to the southeast. Finally, we inverted for the source parameters of these subevents, including not just strikes, dips, rakes, depths, and seismic moments but also their relative positions and times, to obtain the final fits shown in Figure A10c. The addition of these parameters also yielded improved fits to the complex P phases at stations to the west.

Obviously assigning uncertainties to each of the parameters is hopeless, and to place constraints on some of them, we considered only the point source. First, for an earthquake of this size and for which there are suggestions of surface faulting (Feng and others, 1986), the depth is not a very meaningful quantity. The inversion routine repeatedly returned depths of about 18 km, and we simply accept that the depth was shallower than 25 km but probably not confined to the upper 10 km.

A8a. 1983 December 16
192/53/58/11/58

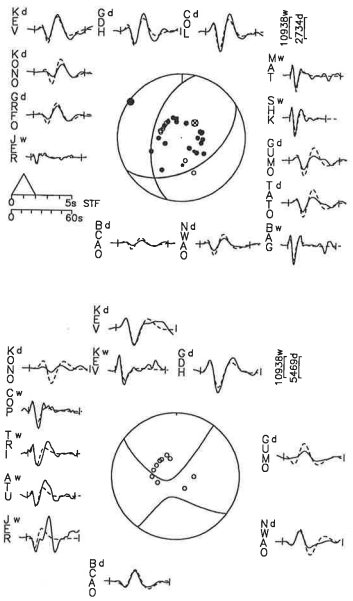

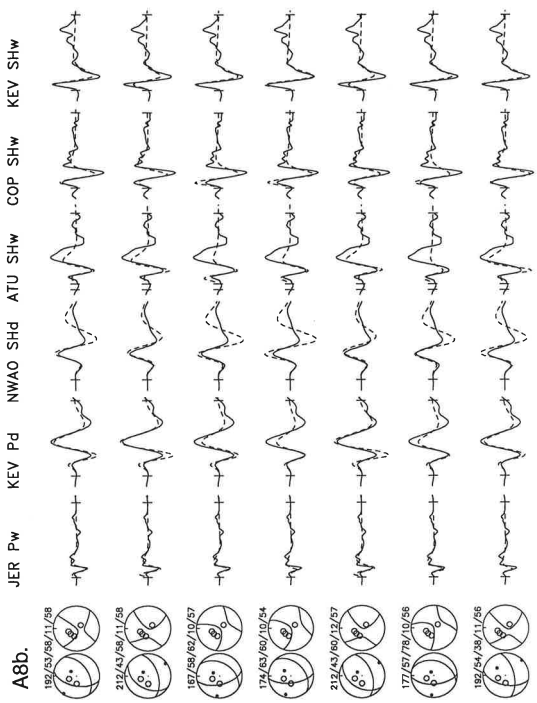

Let us consider the degradation of fits of synthetic and recorded waveforms with systematic variations in the strike, dip, and rake of the northeast-striking plane, which is probably the auxiliary plane. To do this, we used the match with a rupture propagating at 2.5 km/s in the direction N300° to define an acceptably good fit. A more clockwise strike of 85° renders synthetic P waveforms at MUN and LEM too big, pulse widths of synthetic SH waveforms at SNG and LEM too sharp, and SH waveforms at European stations (e.g., VAL) poor. For the more counterclockwise value of 35°, synthetic P waveforms at STU, VAL, ESK, AKU, GDH, and COL fit poorly, and the polarities of synthetic SH phases at SNG and LEM are opposite to those observed. For a steep dip of 78°, synthetic P phases at STU, GDH, and SEO and SH phases at VAL, ESK, and AKU are a little too small. For a gentle dip of 58°, synthetic P phases at MUN and LEM are too big and SH phases at VAL, ESK, AKU, and GUA are too small. For a relatively steep rake of 57°, synthetic SH phases at SEO and SHK are a little too big, and those at VAL, ESK, and AKU are too small. For a relatively gentle value of 32°, the synthetic P waveforms at STU, VAL, GDH, and COL are too small, and SH phases at SNG, LEM, and MUN are a little too big. These ranges of values encompass those given by Ekström (1987) for this earthquake.

1985 September 11 (Fig. A11). 39.36°N, 75.44°E, depth = 7 ± 3 km, strike = 108° + 30°/- 60°, dip = 31° + 7°/-10°, rake = 104° + 25°/-60°.

Obtaining an acceptable solution for this was especially frustrating. Only three P waves could be digitized, and all of them were recorded during noisy periods (Fig. A11a). Waveforms from DAV are notoriously inconsistent (e.g., Chen and others, 1981; Molnar and Lyon-Caen, 1989). Although we plot the recorded and synthetic waveforms from TRI and BAG, we did not rely on them much in constraining the nodal planes. The signal at TRI is superimposed on the coda from another earthquake. Moreover, broad-band signals constructed from digital recordings by Ekström (1987) exhibit similar low signal-to-noise ratios. Because only a couple of other reliable P-wave first motions could be identified with confidence, the fault plane solution is not well constrained by them. The source parameters are constrained largely by SH phases, and they fit two different classes of solution: largely strike-slip displacement on northwesterly or northeasterly trending planes or largely thrust faulting on east-west–trending planes. Ekström (1987) reported the latter type, which we favor, but not with much confidence.

In any case, the SH phases could not be fit as well as we hoped with either type of solution. The double pulse at some European stations (e.g., COP and NUR) has eluded a simple explanation. In addition, our calculated moment is roughly 3 times smaller than Ekström's (1987), which in part is due to his much longer time function but also reflects a difficulty in getting a good fit. Finally, travel time residuals for these phases are also quite large, commonly several seconds, suggesting that either the phases have been misidentified or that the location and origin time are in error. We spent considerable time redigitizing and realigning the recorded waveforms with their synthetic counterparts generated for different fault plane solutions but with no significant improvement in matches.

Notice that a strike of 138°, 30° more clockwise than the "best" value, yields a yet worse fit of P at TRI and SH phases at COL and BAG that are too small and too big, respectively (Fig. A11b). For a strike of 48°, 60° counterclockwise from the "best" strike, P at TRI is

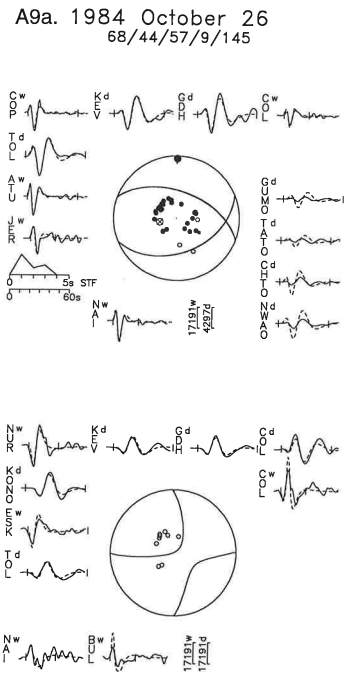

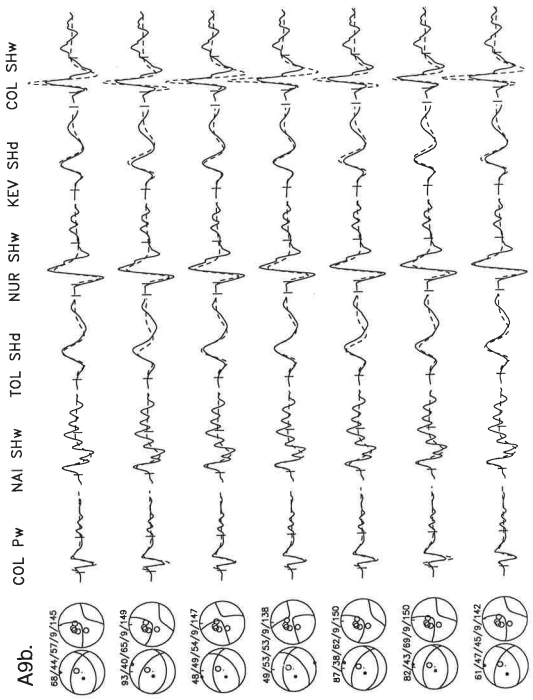

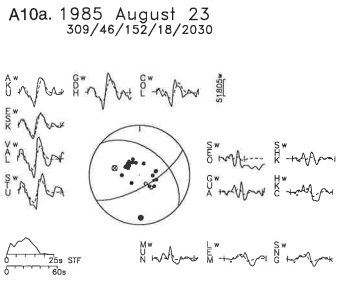

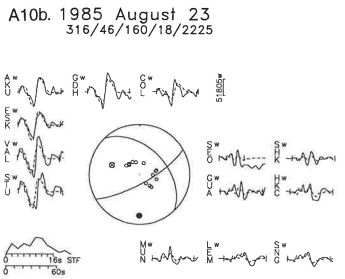

also worse, but at BAG it is better than for the "best," and the synthetic SH at ATU is too big. For a steeper dip of 38°, synthetic P phases at TRI and BAG are too big, and SH phases at ATU, STU, and BAG are too small. For a gentler dip of 21°, the synthetic P at TRI again is too small, but that at BAG fits well, ad SH phases at COL ad BAG are a little too large. For a rake of 129°, 25° larger than the "best," the synthetic P at TRI is too small, the synthetic SH at STU is a little too small, and those COL and BAG are too big. For a rake of only 44°, 60° smaller than the "best," synthetic SH phases at ATU and STU are too big, and that at COL is too small.

1985 October 13 (Fig. A12). 40.32°N, 69.84°E, depth = 15 ± 3 km, strike = 268° + 10°/- 35°, dip = 50° + 7°/- 5°, rake = 77° + 12°/- 8°.

P-wave first motions require a large thrust component but do not place a tight constraint on the orientations of the planes (Fig. A12a). The match of synthetic to recorded seismograms requires that both planes strike roughly east-west to perhaps northeast-southwest.

The strike is not very well constrained (Fig. A12b). A 10° more clockwise strike of 278° yields a synthetic P phase at TRI that is a little too big and synthetic SH phases at COL and TRI that are too small. A 35° more counterclockwise strike of 233°, corresponding also to a 12°

A10c. 1985 August 23
1:282/34/142/18/359
2:326/58/158/19/791
3:309/41/152/18/992

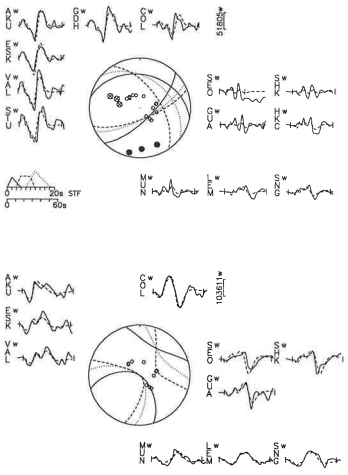

A11a. 1985 September 11
108/31/104/7/81

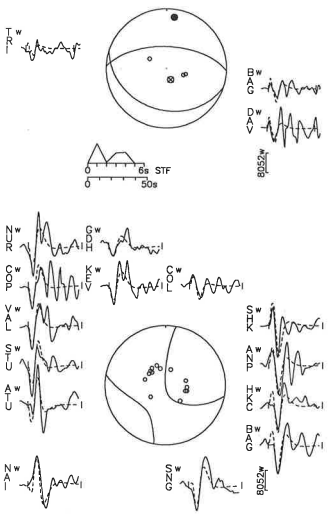

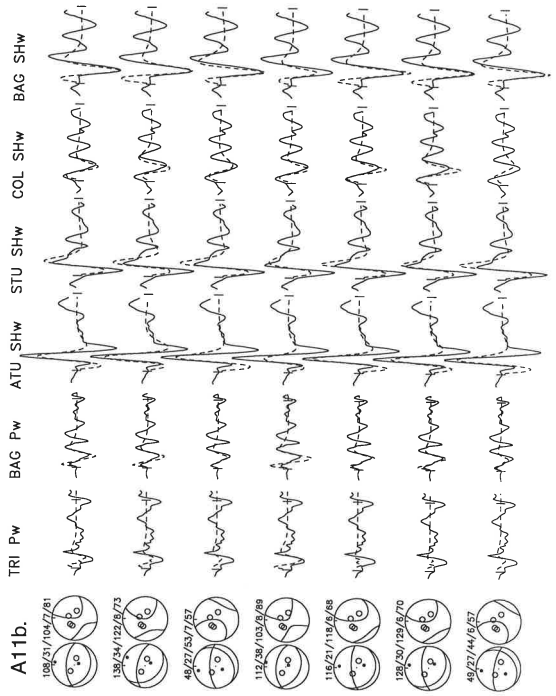

A12a. 1985 October 13
268/50/77/15/40

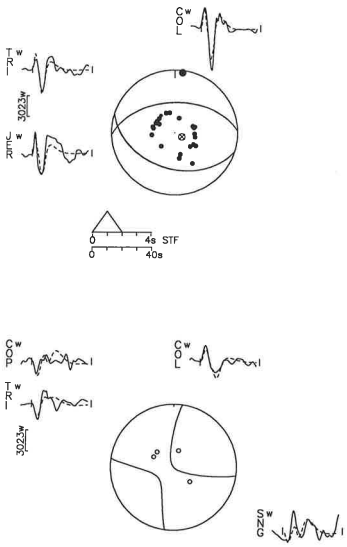

steeper rake of 89°, yields a synthetic SH phase at COP that is too small. A 7° steeper dip of 57° generates a P phase at COL that is too small and a sSH that is too large. A 5° gentler dip makes a P phase at TRI that is a little too big and SH phases at COP, TRI, and COL that are too small. An 8° gentler rake of 69° creases SH phases at COL and TRI that are too small, but also with a large backswing at COL.

REFERENCES CITED

Abers, G., Bryan, C., Roecker, S., and McCaffrey, R., 1988, Thrusting of the Hindu Kush over the southeastern Tadjik Basin, Afghanistan: Evidence from two large earthquakes: Tectonics, v. 7, p. 41–56.

Andrews-Speed, C. P., and Brookfield, M. E., 1982, Middle Paleozoic to Cenozoic geology and tectonic evolution of the northwestern Himalaya: Tectonophysics, v. 82, p. 253–275.

Argand, E., 1924, La Tectonique de l'Asie: International Geological Congress Reports of Sessions, v. 13, p. 170–372.

Artemijev, M. E., and Belousov, T. P., 1983, Recent tectonics and isostasy in the Pamirs, southern Tien Shan and the zone of their junction: Bolletin Geofisica Teoria Applicada, v. 25, p. 401–408.

Baker, D. M., Lillie, R. J., Yeats, R. S., Johnson, G. D., Yousuf, M., and Zamin, A.S.H., 1988, Development of the Himalayan frontal thrust zone: Salt Range, Pakistan: Geology, v. 16, p. 3–7.

Balakina, L. M.,1983, Tectonics and mechanisms of earthquakes (in Russian), *in* Gubin, I. Ye., and Zakharov, S. A., eds., Tectonics of the Tien Shan and Pamir: Moscow, Nauka, p. 24–39.

Baranowski, J., Armbruster, J., Seeber, L., and Molnar, P., 1984, Focal depths and fault plane solutions of earthquakes and active tectonics of the Himalaya: Journal of Geophysical Research, v. 89, p. 6918–6928.

Baratov, R. B., ed., 1976, Separation of stratigraphic and intrusive formations of Tadjikistan (in Russian): Dushanbe, Donish, 268 p.

Bassoulet, J. P., Boulin, J., Colchen, M., Marcoux, J., Mascle, G., and Montenat, C., 1980, L'évolution des domaines téthysiennes au pourtour du bouclier indien du Carbonifère au Cretacé, *in* Géologie des chaines alpines issues de la Tethys: Bureau Recherche Géologie et Miniérs, Mêmoire, Orleans, France, Mèmoire 115, p. 180–198.

Bazhenov, M. L., and Burtman, V. S., 1981, Formation of the Pamir-Punjab syntaxis: Implications from paleomagnetic investigations of Lower Cretaceous and Paleogene rocks of the Pamirs, *in* Contemporary scientific researches in Himalaya: Dehra Dun, India, Bishen Singh Mahendra Pal Sing, p. 71–81.

—— , 1982, The kinematics of Pamir arc: Geotectonics, v. 16 (English translation), p. 288–301.

—— , 1986, Tectonics and paleomagnetism of structural arcs of the Pamir-Punjab syntaxis: Journal of Geodynamics, v. 5, p. 383–396.

—— , 1990 Structural arcs of the Alpine Belt: Carpathians-Caucasus-Pamir (in Russian): Moscow, Nauka, 168 p.

Bekker, Ya. A., Koshlakov, G. V., and Kuznetsov, Ye. S., 1974a, Deep structure of southwest Tadjikistan from geologic and geophysical data (in Russian), *in* Searches for precursors of earthquakes in prediction polygons: Moscow, Nauka, p. 16–23.

Bekker, Ya. A., Koshlakov, G. V., Kuznetsov, E. C., Murchaidze, D. P., and Orlov, E. S., 1974b, Toward the tectonics of the region of the city of Dushanbe (Gissar Valley) from the results of geological-geophysical investigations (in Russian), *in* Searches for precursors of earthquakes in prediction polygons: Moscow, Nauka, p. 24–29.

Bekker, Ya. A., Konovalov, Yu. F., Koshlakov, G. V., and Muchaidze, D. R., 1983, New data about the structure of the earth's crust of Tadjikistan (in Russian), *in* Gubin, I. Ye., and Zakharov, S. A., eds., Tectonics of the Tien Shan and Pamir: Moscow, Nauka, p. 118–123.

Belokopytov, V. A., Guseva, T. V., Lukk, A. A., Skovorodkin, Yu. P., Trapeznikov, Yu. A., and Shevchenko, V. I., 1992, Present-day geodynamics and seismicity in the Garm test area, Tadjikistan: Tectonophysics, v. 202, p. 163–167.

Belousov, T. P., 1976, Tectonic movements of the Pamir in the Pleistocene and Holocene epochs and seismicity (in Russian): Moscow, Nauka, 120 p.

Beloussov, V. V., and 11 others, 1980, Structure of the lithosphere along deep seismic sounding profile: Tien Shan–Pamirs–Karakorum–Himalayas:

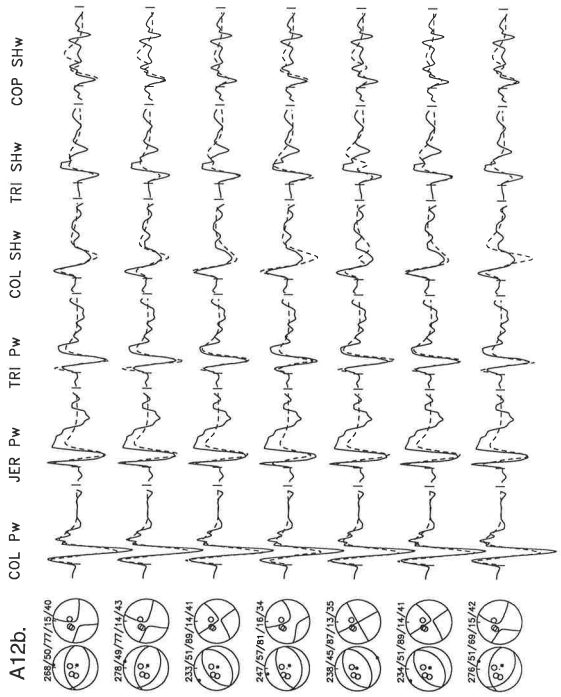

A16: Burtman and Molnar (1993) figures.

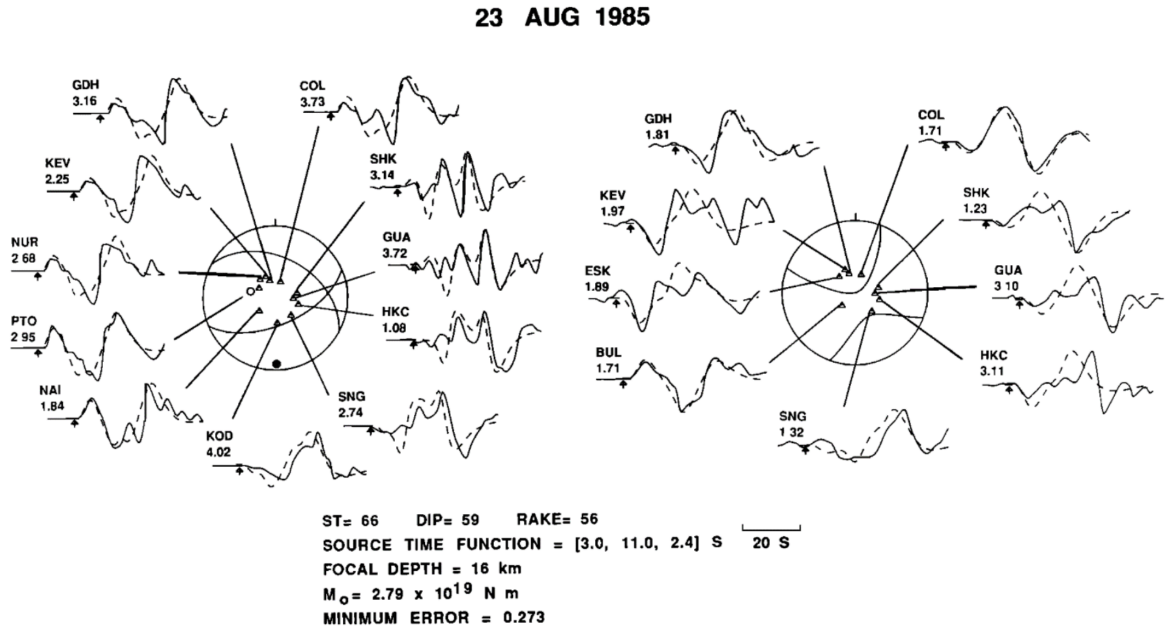

Figure 10a. The long-period waveform inversion result for the main shock of the August 23, 1985, Wuqia earthquake (event 32). For other details, see Figure 4a.

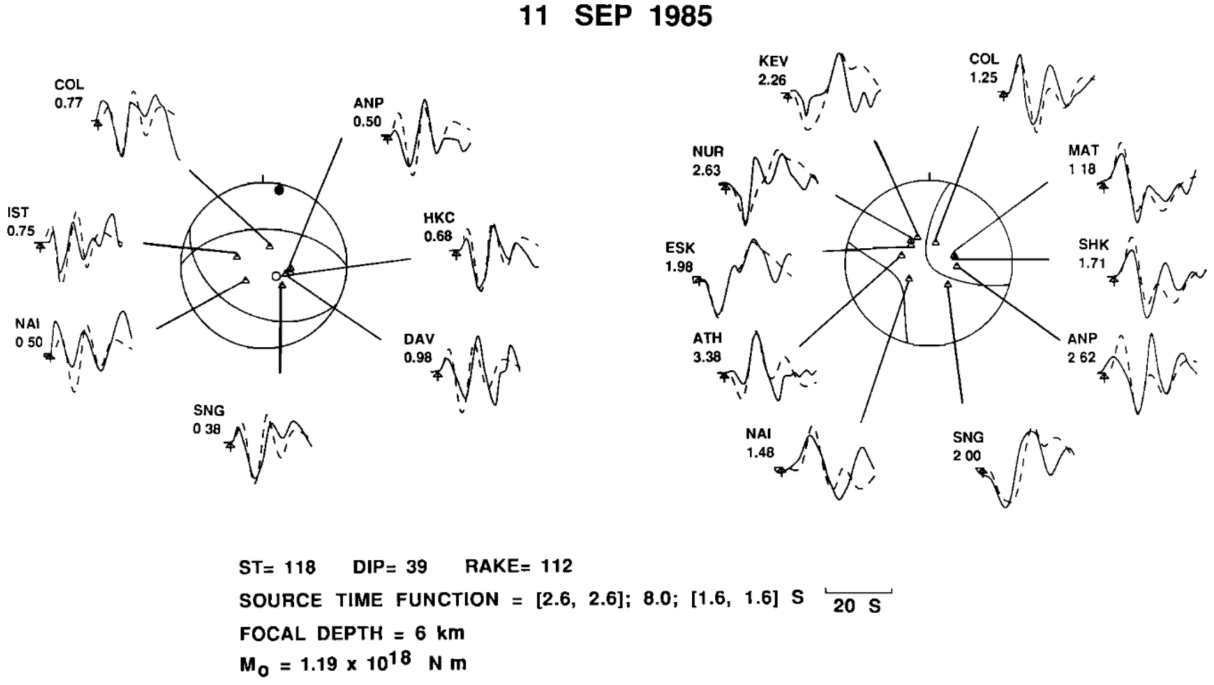

Figure 10b. The matches between long-period observed waveforms and synthetics for the September 11, 1985, event (event 34), the largest aftershock of the Wuqia earthquake. A double source is assumed. The focal depth is determined from the waveform inversion. For other details, see Figure 4a.

A17: Figures taken from Fan et al. (1994). The depth phase arrival for 6 km would be ∼1 second delay, so it is likely that this has been mixed up in the source time function. Given the event has been modelled as a double source, we propose the double source is modelling the depth phase.

A18: Surface rupture measurements compiled by Ainscoe (2018) from Feng et al. (1986) and Feng et al. (1988). Additional measurements from He et al. (2024). Displayed in Figure 4.4 of the main text.

Longitude (°E)	Latitude (°N)	Orientation	Offset (m)	Reference	Notes
75.3806	39.4873	V	1.1	F88	
75.3822	39.4873	V	0.55	F88	
75.3871	39.4821	V	0.34	F88	location approx.
75.4027	39.4802	V	1.1	F88	
75.4084	39.4797	RL	1.55	F88	
75.4117	39.4783	V	1.55	F88	
75.4152	39.4776	V	1.1	F88	
75.4192	39.4765	V	0.38	F88	
75.4226	39.4761	V	0.5	F88	
75.4234	39.4751	V	0.28	F88	
75.4245	39.4737	V	0.22	F88	
75.4247	39.4732	RL	0.7	F88	
75.4254	39.4718	RL	1.3	F88	
75.4267	39.4691	V	0.5	F88	
75.4293	39.4665	RL	1.2	F88	
75.4297	39.4653	V	0.26	F88	
75.4335	39.4638	V	0.75	F88	
75.4386	39.4621	V	1.05	F88	
75.4453	39.4596	V	1.15	F88	
75.4473	39.4582	V	0.92	F88	
75.4499	39.4568	V	0.47	F88	
75.4541	39.449	V	0.29	F88	
75.4552	39.4473	RL	1.25	F88	
75.4554	39.4473	V	1.25	F88	
75.4574	39.443	V	0.17	F88	
75.4508	39.4548	V	0.8	F86	location approx.
75.4518	39.453	RL	1.6	F86	location approx.
75.4519	39.4528	V	0.85	F86	location approx.
75.4559	39.4467	V	0.7	F86	location approx.
75.26305	39.51355	V	1	H24	
75.3593	39.48766	V	2	H24	

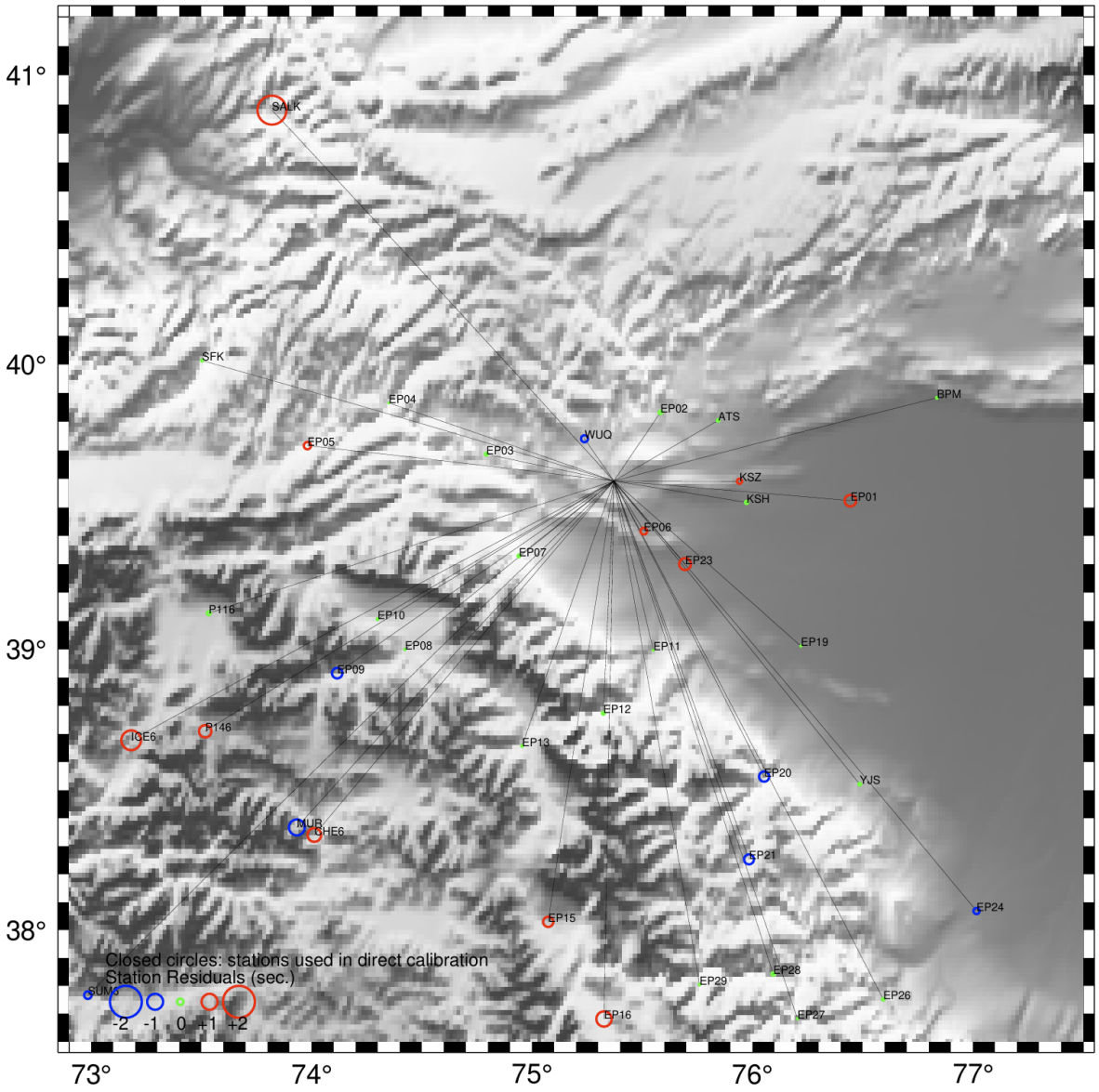

A20: Direct calibration stations used for the *mloc* cluster, most of which are from the 8H seismic network deployed between 2015 and 2017. Residuals are coded by the colour and size of the circles around each station, with the black lines raypaths from hypocentroid to the station. Anomalies appear to not be correlated with distance or azimuth, indicating no bias in the hypocentroid location. The good azimuthal coverage of the stations gives us confidence the hypocentroid is well constrained.

A19: Cumulative scaro height measurements from Ainscoe (2018). From measurement of ALOS AWD30m DEM. T18 is taken from Thompson et al. (2018).

Longitude (°E)	Latitude (°N)	Orientation	Offset (m)	Uncertainty (m)	Reference	Notes
75.2262	39.5365	RL	1.4	±0.5	.	
75.2263	39.5365	RL	1.9	±0.5	.	
75.2263	39.5365	RL	1.8	±0.5	.	
75.2486	39.5203	V	12.9	±3.8	.	
75.2511	39.519	V	34.3	±1.9	.	
75.2547	39.5172	V	19.6	±1.2	.	
75.2571	39.516	V	21.9	±2.0	.	
75.2584	39.5156	V	30.3	±1.2	.	
75.2591	39.5153	V	26.5	±1.6	.	
75.4121	39.4783	V	2.5	±0.9	.	
75.4225	39.4761	V	2.3	±1.1	.	
75.4335	39.4638	V	4.1	±0.7	.	
75.4501	39.4566	V	10.7	±0.7	.	
75.0591	39.5406	V	3.8		T18	
75.1096	39.5843	V	15		T18	location approx.